

NONINVASIVE SENSING TECHNIQUES AND GEOPHYSICAL METHODS FOR CULTURAL HERITAGE AND CIVIL INFRASTRUCTURES MONITORING

GUEST EDITORS: FRANCESCO SOLDVIERI, JEAN DUMOULIN, NICOLA MASINI, AND ERICA UTSI





Noninvasive Sensing Techniques and Geophysical Methods for Cultural Heritage and Civil Infrastructures Monitoring

International Journal of Geophysics

**Noninvasive Sensing Techniques and
Geophysical Methods for Cultural Heritage
and Civil Infrastructures Monitoring**

Guest Editors: Francesco Soldovieri, Jean Dumoulin,
Nicola Masini, and Erica Utsi



Copyright © 2011 Hindawi Publishing Corporation. All rights reserved.

This is a special issue published in "International Journal of Geophysics." All articles are open access articles distributed under the Creative Commons Attribution License, which permits unrestricted use, distribution, and reproduction in any medium, provided the original work is properly cited.

Editorial Board

Jean-Pierre Burg, Switzerland
John F. Cassidy, Canada
Ping Chang, USA
Yun-tai Chen, China
S. Crampin, UK
Robin Crockett, UK
Jack Petrovich Dvorkin, USA
Gary Egbert, USA

Marek Grad, Poland
Hans-Gert Kahle, Switzerland
Masao Kanamitsu, USA
Shuichi Kodaira, Japan
Zdenek Martinec, Czech Republic
Philip Meredith, UK
Steve Milan, UK
C. Papazachos, Greece

Joerg Schleicher, Brazil
Sheng-Rong Song, Taiwan
P. Talwani, USA
Rudolf A. Treumann, Germany
Bjørn Ursin, Norway
Petr Vaníček, Canada
Michael S. Zhdanov, USA
Sergej Zilitinkevich, Finland

Contents

Noninvasive Sensing Techniques and Geophysical Methods for Cultural Heritage and Civil Infrastructures Monitoring, Francesco Soldovieri, Jean Dumoulin, Nicola Masini, and Erica Utsi
Volume 2011, Article ID 487679, 2 pages

Automatic Road Pavement Assessment with Image Processing: Review and Comparison, Sylvie Chambon and Jean-Marc Moliard
Volume 2011, Article ID 989354, 20 pages

Noninvasive Remote Sensing Techniques for Infrastructures Diagnostics, Angelo Palombo, Stefano Pignatti, Angela Perrone, Francesco Soldovieri, Tony Alfredo Stabile, and Simone Pascucci
Volume 2011, Article ID 204976, 9 pages

Road Networks Winter Risk Estimation Using On-Board Uncooled Infrared Camera for Surface Temperature Measurements over Two Lanes, M. Marchetti, M. Moutton, S. Ludwig, L. Ibos, V. Feuillet, and J. Dumoulin
Volume 2011, Article ID 514970, 8 pages

Multidisciplinary Approach to a Recovery Plan of Historical Buildings, Luciana Orlando
Volume 2011, Article ID 258043, 12 pages

A Combined Methodology for Landslide Risk Mitigation in Basilicata Region by Using LIDAR Technique and Rockfall Simulation, G. Colangelo and A. Guariglia
Volume 2011, Article ID 392676, 5 pages

Site Assessment of Multiple-Sensor Approaches for Buried Utility Detection, Alexander C. D. Royal, Phil R. Atkins, Michael J. Brennan, David N. Chapman, Huanhuan Chen, Anthony G. Cohn, Kae Y. Foo, Kevin F. Goddard, Russell Hayes, Tong Hao, Paul L. Lewin, Nicole Metje, Jen M. Muggleton, Adham Naji, Giovanni Orlando, Steve R. Pennock, Miles A. Redfern, Adrian J. Saul, Steve G. Swingler, Ping Wang, and Christopher D. F. Rogers
Volume 2011, Article ID 496123, 19 pages

Application of the Cylindrical Wave Approach to the Simulation of Buried Utilities, Fabrizio Frezza, Lara Pajewski, Cristina Ponti, and Giuseppe Schettini
Volume 2011, Article ID 974518, 8 pages

Multitemporal Satellite Images for Knowledge of the Assyrian Capital Cities and for Monitoring Landscape Transformations in the Upper Course of Tigris River, Giuseppe Scardozzi
Volume 2011, Article ID 917306, 17 pages

Integrated Methodologies for the 3D Survey and the Structural Monitoring of Industrial Archaeology: The Case of the Casalecchio di Reno Sluice, Italy, Gabriele Bitelli, Giorgia Gatta, Valentina Alena Girelli, Luca Vittuari, and Antonio Zanutta
Volume 2011, Article ID 874347, 8 pages

Data Fusion for Electromagnetic and Electrical Resistive Tomography Based on Maximum Likelihood, Sven Nordebo, Mats Gustafsson, Therese Sjöden, and Francesco Soldovieri
Volume 2011, Article ID 617089, 11 pages

Review of Environmental and Geological Microgravity Applications and Feasibility of Its Employment at Archaeological Sites in Israel, Lev V. Eppelbaum
Volume 2011, Article ID 927080, 9 pages

Postprocessing of Infrared Reflectography to Support the Study of a Painting: The Case of Vivarini's Polyptych, Laura Fragasso and Nicola Masini

Volume 2011, Article ID 738279, 8 pages

Ground Penetrating Radar in Dam Monitoring: The Test Case of Acerenza (Southern Italy), A. Loperte, M. Bavusi, G. Cerverizzo, V. Lapenna, and F. Soldovieri

Volume 2011, Article ID 654194, 9 pages

From Geophysics to Microgeophysics for Engineering and Cultural Heritage, P. L. Cosentino, P. Capizzi, R. Martorana, P. Messina, and S. Schiavone

Volume 2011, Article ID 428412, 8 pages

Distributed Strain Measurement along a Concrete Beam via Stimulated Brillouin Scattering in Optical Fibers, Romeo Bernini, Aldo Minardo, Stefano Ciaramella, Vincenzo Minutolo, and Luigi Zeni

Volume 2011, Article ID 710941, 5 pages

Editorial

Noninvasive Sensing Techniques and Geophysical Methods for Cultural Heritage and Civil Infrastructures Monitoring

Francesco Soldovieri,¹ Jean Dumoulin,² Nicola Masini,³ and Erica Utsi⁴

¹ *Istituto per il Rilevamento Elettromagnetico dell'Ambiente, Consiglio Nazionale delle Ricerche, Via Diocleziano 328, 80 124 Napoli, Italy*

² *Monitoring, Assessment and Computational Science Department (MACS), French Institute of Science and Technology for Transport, Development and Networks (IFSTTAR), Route de Bouaye, CS4, 44344 Bouguenais, France*

³ *Istituto per i Beni Archeologici e Monumentali, CNR, C.da S. Loja, 85050 Tito Scalco (PZ), Italy*

⁴ *Utsi Electronics Ltd., Cambridge CB22 7NZ, UK*

Correspondence should be addressed to Francesco Soldovieri, soldovieri.f@irea.cnr.it

Received 24 January 2012; Accepted 24 January 2012

Copyright © 2011 Francesco Soldovieri et al. This is an open access article distributed under the Creative Commons Attribution License, which permits unrestricted use, distribution, and reproduction in any medium, provided the original work is properly cited.

This special issue presents a good and interesting review of the state of art and novel methodologies, instrumentation, and data-processing approaches to perform non- or minimally destructive investigations with a specific focus to the applicative field of the cultural heritages and critical infrastructure monitoring. In addition, it is concerned with some interesting theoretical and “in real world” examples of how the integration between the classical geophysical techniques with new emerging surface and subsurface-sensing techniques enables a multidepth, multiresolution, and multiscale monitoring.

P. L. Cosentino et al. present the new concept of “microgeophysics” of relevant interest in both the fields of the civil engineering and cultural heritage studies. In particular, the paper is concerned with research efforts in the field of the instrumentation and methodologies so to gain the relevant applicative advantages of time reduction without any loss of information, by taking care to the adoption of multichannel systems.

L. Fragasso and N. Masini present a very interesting use of the infrared reflectography in cultural heritage; in particular, the survey regards the assessment of the polyptych panel attributed to Vivarini’s workshop conserved in the “Sigismondo Castromediano” Museum in Lecce. An effort has been made in processing the IR images through Principal Component Analysis and spectral indices able to give information about different pictorial drafting and restoration works.

L. N. Eppelbaum gives an interesting review of the microgravity investigations with a focus to archaeological applications, which is a very challenging research field. In particular, an advanced methodology based on gravity anomalies analysis and 3D modelling is presented with the aim to delineate ancient targets. The performed model computations indicate that microgravity investigations might be successfully applied at least in 20–25% of archaeological sites in Israel.

Orlando et al’s paper is concerned with the application of a multisensing approach based on geology, GPS, surveys of cracking, boreholes, seismic refraction and electrical resistivity tomography—to image the shallow stratigraphy and hypothesize the cause of instability of an historical centre. The synergy due to the combination of different geophysical surveys permits to depict underground features at small and medium scale.

The paper from G. Scardozzi et al. regards the contribution of the high-resolution multitemporal optical satellite imagery for change detection of a territory with a focus to the modifications that affected archaeological features and the landscape. In particular, the investigation was focused to five great Assyrian capital cities (Ashur, Kar-Tukulti-Ninurta, Kalhu, Dur-Sharrukin, and Nineveh, in northern Iraq) by using very high-resolution satellite images taken between 2001 and 2007 and panchromatic photographs taken by U.S. spy satellites operating between 1965 and 1969.

The paper by G. Bitelli et al. is an example of integrated surveying and monitoring activities for the control of an ancient structure, the Casalecchio di Reno sluice, located near Bologna, Italy, representing a case of “industrial archaeological site.” Classical topography, high-precision spirit levelling, terrestrial laser scanning, digital close-range photogrammetry, and thermal imagery were used to monitor the stability and the movements of the structure. In addition, the creation of a 3D model of the structure was achieved and permitted to compare two situations, before and after the serious damages suffered by the sluice. Also, an analysis of the whole sluice, carried out at a regional scale, was done via the use of aerial photogrammetry.

The paper by R. Bernini et al. is concerned with the application of a new diagnostic technique for long-range strain and temperature monitoring, exploiting a distributed fiber-optic sensor portable system based on Brillouin scattering. The experiment in laboratory has demonstrated the effectiveness of this novel technique as a structural assessment tool by measuring the strain on a 4 m long concrete beam and detecting the formation of a crack in the beam resulting from the external applied load.

Paper by A. Loperte et al. deals with an interesting case of use of the Ground Penetrating Radar (GPR) in monitoring of critical infrastructure by a high-resolution diagnostics. In particular, in this paper, the application of GPR has permitted the monitoring and diagnostics of one of the largest dams in the Basilicata region (Southern Italy) for safety management; in fact, the investigation had the aim to detect and localize underground sandstone banks that are potential ways of flow of water below the dam.

Paper by M. Marchetti et al. is concerned with the study of the performance of an infrared camera for the determination of ice road susceptibility, to build a new winter risk index, to improve the measurements rate, and to analyze its consistency with seasons and infrastructures environment. The comparison of this technique with the classical radiometer sensing technique shows a good effectiveness of the IR technique with promising perspectives.

Paper by S. Chambon et al. regards the use of automatic analysis of optical images for crack detection on the French national roads. The work gives three main contributions as: a state of the art of the image-processing tools applied to civil engineering, an approach based on multi-scale extraction and a Markovian segmentation for a fine-defect detection in pavement surface, the design and the validation of a protocol for evaluating the road pavement crack detection.

Paper by A. Palombo et al. regards an experiment at Montagnole site performed in the framework of FP7 ISTIMES project. Ground-based microwave radar interferometer and high-frequency InfraRed Thermography (IRT) were used at the same time to detect and characterize the dynamic displacement of a 16 m concrete beam affected by high-energy direct impacts of an iron ball weighting few tons. The results achieved by the two techniques were compared in terms of frequency analysis and show a very good correlation, which makes confident about the reliability of the diagnosis results.

The paper by G. Colangelo and A. Guariglia discusses a hazard assessment strategy and risk mitigation for rock-falls in a section of a national road, along the coast of Maratea (Southern Italy), using LIDAR technique and spatial modelling. The results represent a valid cognitive support to choose the most appropriate technical solution for topography strengthening and an example of good practice for the cooperation between innovative technologies and field emergency management.

The paper by S. Nordebo et al. represents a methodological contribution to the data fusion problem, which is of great interest in the integration of different techniques for critical infrastructure monitoring. In particular, it is presented a maximum likelihood-based approach to data fusion for electromagnetic (EM) and electrical resistive (ER) tomography. As a multiphysics problem formulation with applications in geophysics, the problem of tunnel detection based on EM and ER tomography is studied in this paper.

The paper by L. Pajewski et al. falls in the framework of the research activities for the development of physical-based data processing for GPR measurements. The effectiveness of the full-wave technique for the solution of the two-dimensional plane-wave scattering problem is shown for a set of perfectly conducting and dielectric cylinders buried in a dielectric half-space, or in a finite-thickness slab. In particular, metallic pipes and air cavities are simulated as buried utilities.

The last paper by A. C. D. Royal et al. presents the progress of a research project that aims to develop a multisensor geophysical platform that can improve the probability of detection of the infrastructure buried beneath the carriageway. The multisensor platform is being developed in conjunction with a knowledge-based system that aims to provide information on how the properties of the ground might affect the sensing technologies being deployed. The fusion of data sources (sensor data and utilities record data) is also being researched to maximize the probability of location. This paper describes the outcome of the initial phase of testing along with the development of the knowledge-based system and the fusion of data to produce utility maps.

*Francesco Soldovieri
Jean Dumoulin
Nicola Masini
Erica Utsi*

Research Article

Automatic Road Pavement Assessment with Image Processing: Review and Comparison

Sylvie Chambon and Jean-Marc Moliard

Departement of MACS, Institut Français des Sciences et Technologies des Transports, de l'Aménagement et des Réseaux (IFSTTAR), 44341 Bouguenais Cedex, France

Correspondence should be addressed to Sylvie Chambon, schambon@enseiht.fr

Received 31 January 2011; Revised 21 May 2011; Accepted 6 June 2011

Academic Editor: Jean Dumoulin

Copyright © 2011 S. Chambon and J.-M. Moliard. This is an open access article distributed under the Creative Commons Attribution License, which permits unrestricted use, distribution, and reproduction in any medium, provided the original work is properly cited.

In the field of noninvasive sensing techniques for civil infrastructures monitoring, this paper addresses the problem of crack detection, in the surface of the French national roads, by automatic analysis of optical images. The first contribution is a state of the art of the image-processing tools applied to civil engineering. The second contribution is about fine-defect detection in pavement surface. The approach is based on a multi-scale extraction and a Markovian segmentation. Third, an evaluation and comparison protocol which has been designed for evaluating this difficult task—the road pavement crack detection—is introduced. Finally, the proposed method is validated, analysed, and compared to a detection approach based on morphological tools.

1. Introduction

The evaluation of road quality is an important task in many countries, like in France, where the national roads are inspected each three years in order to estimate the needed reparations. To estimate the quality, these aspects can be taken into account: the adherence, the microtexture, the macrotexture, and the surface degradations. Before 1980, all these inspections were accomplished manually. Since 1980, this task can be automated with noninvasive techniques to be more comfortable, less dangerous for employees and users of the road but also more efficient and less expensive than manual methods. Many systems have been proposed, based on ground-penetrating radar [1] or laser system [2]. However, for noninvasive evaluation of surface degradations, the recent research results seem more promising with optical image-processing approaches for these reasons [3]:

- (1) The acquisition systems based on optical devices are easier to design and to use than other kinds of systems (they are less sensitive to movement and to vibrations than other systems).
- (2) They also allow a dense acquisition (each millimeter), that is, the acquisition can be realized for the whole

road surface, whereas for the other systems, like laser, the measurements are available every 4 millimeters at normal speed (90 km/h).¹

- (3) The measurement of the defects is more precise than with other systems because, as explained in (2), enough information is available.
- (4) Even if the images are not always well contrasted, they are more contrasted than the images/signals that can be given by other devices, that is, the ratio between noise and signal is greater with optical sensor than with other kind of sensors.

Nowadays, many acquisition systems are available [3, 4], see Table 1 (interested readers can find details about the evaluation of such systems in [5, 6]). Moreover, to the best of our knowledge, many methods for semiautomatic detection of road defects can be found in the literature but only one is commercialized (by INO²). Among all the existing approaches, it is difficult to know which one is the most adapted to the task and what is the actual method that is the most used. This is why the first goal of this paper is to present a state of the art of assessment methods in noninvasive control based on image processing.

TABLE 1: The quality evaluation systems of the road pavement based on optical devices L, CLS, LC, and IPT mean, respectively, that the described system involves a laser, a controlled lighting system, a linear camera and/or some image processing tools. The first set corresponds to systems without image processing tools. While the second group of systems are able to provide nondense measurement, the third group of systems can give a dense evaluation of the quality of the road.

Name	Year	Country	L	CLS	LC	IPT
ADDA, automated distress data acquisition	1991	USA			—	
ACM, automated crack monitor	1991	USA			—	
SIRANO	1991	France			—	
HARRIS, Highways Agency Road Research Information System ^a	1999	UK	—		—	
ADA, automated distress analyser ^b	2007	USA	—		—	
AIGLE RN ^c	2008	France		—		
AMAC ^d	2004	France	—	—	—	—
Profilograph and laser ^e	2007	Danemark	—	—	—	
REAL, road excellent automatic logging ^f	1992	Japan	—	—	—	—
ARAN, automatic road analyser and then FuGro ADVantage ^g	1993/2003	Canada	—	—		—
PAVUE ^h	1999	Sweden		—		—
RoadCrack ⁱ	2008	Australia		—	—	—

^ahttp://www.trl.co.uk/facilities/mobile_test_equipment/highways_agency_road_research_information_system.htm.

^b<http://www.waylink.com/>.

^chttp://www.cete-normandie-centre.equipement.gouv.fr/IMG/pdf/15-AigleRNpress_cle243947.pdf.

^d<http://www.vecetra.fr/sites/fr/materiels-et-solutions/auscultations-des-chaussees/amac.html>.

^e<http://www.greenwood.dk/road.php>.

^f<http://www.pasco.co.jp/eng/solutions/geospatial/ground/>.

^g<http://www.roadware.com>.

^h<http://rst.ramboll.se/en/produkter/rst%20pavue.aspx>.

ⁱ<http://www.csiro.au/solutions/psaa.html>.

The detection of crack is difficult in the context of road surface evaluation because the signal to detect is weakly represented (1.5% of the whole image) and weakly contrasted (the road possesses a texture that hides the crack). Recent methods have shown their limits; the detection contains a lot of false detections (induced by the particular texture of the road), and the detection is not enough precise (the given result is a region of detection and not the skeleton with the width of the crack). The main default of the existing methods is the fact that the specific geometry of the crack—it is a thin and linear object—is not taken into account. In consequence, the second aim of this work is to introduce a new method that takes into account some geometric properties of the cracks.

Even if this problem is hard and very important in the field of civil engineering, as far as we are concerned, there is no protocol for evaluating and for comparing existing methods, and it is difficult to know what kind of methods has to be chosen for this task. In consequence, with the multiple methods proposed in the literature, it seems important to evaluate and to compare the various methods in order to validate previous work and to identify the approaches that can be employed and/or the methods that need improvements. So, the third aspect discussed in this paper is the introduction of such a protocol.

In consequence, the objectives are as follows: first, to give a state of the art of the existing methods in noninvasive control based on image processing for estimating the quality of the road surface, second, to present our method, and, third, to introduce a protocol of evaluation and comparison that allows to highlight the advantages and drawbacks of each method.

2. Automatic Road Crack Detection

In the literature, many methods have been introduced to detect thin objects in textured images, like that in medical imagery, for the detection of blood vessels [27], and satellite imagery, for road network detection [28]. Since 1990, algorithms have been proposed for the semiautomatic detection of road cracks (interested readers can see [29] for details about road imaging systems and their limits). For the detection of cracks, three components have to be taken into account

- (1) *acquisition* (see Table 2 for details),
- (2) *storage, and*
- (3) *image processing*.

In this paper, only the last step is studied, but the choices for the two first steps are important for the success of the image treatment. Moreover, most of the references are given in the field of road quality assessment, but some of them come from different applications, like cracks and defects in concrete (for bridges or pipelines), on ceramics or on metallic surfaces (for industrial applications). For road cracks, most of the time, these hypotheses can be exploited.

- (1) *Photometric hypotheses*

- (H_{p_1}) The crack pixels are darker than the road pixels.
- (H_{p_2}) The gray-level distributions of road crack and road surface are independent.

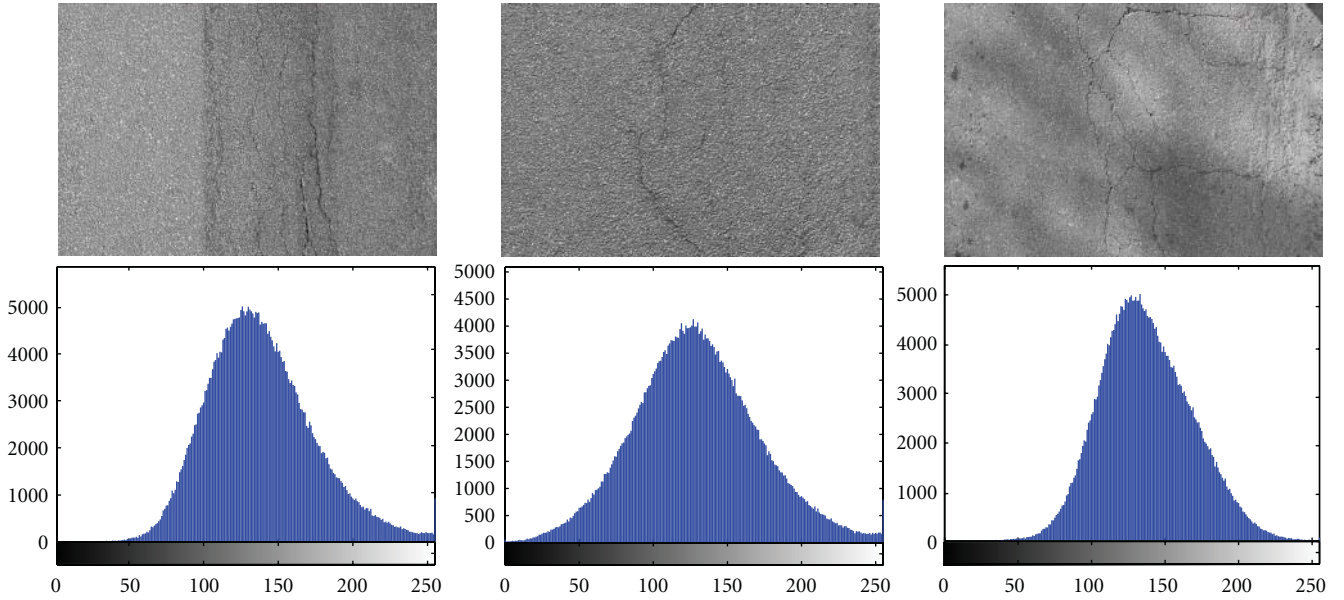


FIGURE 1: Examples of histograms (second row) of images (first row) with cracks. These histograms contain only one mode, and it is impossible to separate the gray-level distribution of cracks from the gray-level distribution of the road pavement.

TABLE 2: The imaging systems. For each kind of configuration, the given details are the orientation of the sensor (O.) that can be perpendicular or not to the road plane, the number of sensors, the presence (—) or not of a laser, the presence (—) or not of overlapping images (R.) between the different acquisitions. For the sensors, we distinguish 2D sensors (CCD, charged couple device) from 1D sensor (linear camera coupled with laser).

O.	Sensor	Laser	R.	Citations
⊥	1 (2D sensor)			[7–17]
⊥	1 (2D sensor)	—		[18, 19]
⊥	More than one (2D sensors)			[20, 21]
⊥	More than one (1D sensors)			[22, 23]
⊥	More than one (2D sensors)		—	[24, 25]
∠	More than one (2D sensors)		—	[26]

(2) Geometric hypotheses

(H_{g_1}) A crack is a thin continuous object.

(H_{g_2}) A crack is a set of connected segments with different orientations.

(H_{g_3}) A crack does not have a constant width on the whole length.

(3) Photometric and geometric hypotheses

(H_{pg_1}) The points inside a crack can be considered as points of interest, from a photometric and/or a geometric point of view.

These different hypotheses can be complementary, like (H_{p_1}) and (H_{p_2}) or (H_{g_1}) and (H_{g_3}), but some of them are opposite, like (H_{g_1}) and (H_{g_2}). The hypothesis (H_{pg_1}) combines two kinds of constraint because the definition of a point of

interest (POI), that is, a significant point in a scene, can be expressed both with photometric constraints (some hypotheses about the distribution of gray levels near POI can be made) and geometric constraints (a point of interest can be a corner, an edge, or any kind of geometric structure).

In the field of image processing, the semiautomatic methods and the automatic detection approaches are considered, and these five families can be distinguished, see Table 3.

- (1) Based on *histogram* analysis (hypotheses H_{p_1} and H_{p_2}), these methods are the most ancient and the most popular. They use a thresholding based on an histogram analysis [7, 30, 31], with Gaussian hypotheses [9] and/or an adaptive or a local thresholding [32, 33]. These approaches are simple and not time consuming, but they also give many false detections. In fact, these methods assume that the two gray level distributions (the road pavement distribution and the crack distribution) can be separated based on a global level statistics (histogram³). In Figure 1, we can see that most of the time, this hypothesis is not valid.
- (2) Based on *mathematical morphological tools* [15, 33–38] (hypotheses H_{p_1} and H_{g_1}), an initial thresholding is needed, and the results contain less false detections than methods based on histogram analysis. However, the major drawback of this kind of techniques is that the quality of the results is highly dependent on the parameter choices.
- (3) Based on a *learning* phase in order to alleviate the problems of the two first groups of methods [39, 40] (hypotheses H_{p_1} and H_{p_2}), most of the approaches are based on neural networks [8, 41, 42]. The drawback is the learning step that cannot allow a fast and fully automatic analysis.

TABLE 3: The classification of existing methods for crack detection (or detection of thin objects in textured images) into five different families. For each family, the hypotheses used by the methods of the family are specified.

Histogram (H_{p_1}, H_{p_2})	Learning (H_{p_1}, H_{p_2})	Morphology (H_{p_1}, H_{g_1})	Filtering ($H_{p_1}, H_{g_1-g_3}$)	Model-based ($H_{p_1}, H_{g_1-g_3}, H_{pg_1}$)
[7, 9, 11, 12, 14, 20, 22, 30–32, 35, 57–62]	[8, 10, 13, 21, 39–42, 63–65]	[15, 23, 33, 34, 36, 37, 66–69]	[17, 25–28, 38, 43, 44, 46–54, 70, 71]	[16, 24, 45, 55, 56, 72, 73]

- (4) Based on *filtering*, the most recent ones (hypotheses H_{p_1} , H_{g_1} , and H_{g_3}). Edge extraction by filtering with fixed scale is not adapted to the task of the detection of road cracks because the width of the crack is not constant, and this is why many methods are based on wavelet detections [17, 25, 43, 44] with adaptive filtering [27, 45, 46] (these approaches will be detailed in the Section 4), contourlets [47], Gabor's filters [48], finite impulse response filter (FIR) [26], and methods using models based on partial differential equations (PDE) [49, 50]. Some techniques also use autocorrelation filtering [51, 52] (a similarity score is estimated between some targets that simulate cracks and all the targets of the original image). An other kind of algorithms is based on texture analysis [53, 54] (the crack is considered as a noise inside a texture).
- (5) Based on an analysis of a *model* [55, 56] (hypotheses H_{p_1} , $H_{g_1-g_3}$, and H_{pg_1}). Most of these approaches are based on a local analysis versus a global analysis in order to take into account the local properties and the global properties of a crack, by multiscale analysis of texture combined with an algorithm of minimal path [55] or by local detection of points of interest combined with geodesic contours [56].

In conclusion, we can notice the following.

- (i) Many methods have been proposed, but the problem is not still solved. The results contain many false positives, and the detections are incomplete. Moreover, most of the existing techniques can give interesting results for only one given class of road pavement, that is, the performance of the method is dependent on the road texture.
- (ii) Methods based on histogram study, even those that are local, do not express correctly the problem, that is, they do not take into account geometric characteristics of the cracks and photometric characteristics of the road pavement.
- (iii) Learning methods are efficient, but the learning step is expensive (the time and the investments from the users that are not expert in image processing).

For all these reasons, even if learning methods have been used in our previous work, this paper focuses on the presentation of two methods proposed to alleviate the limits of the old ones by obtaining a dense detection with a low rate of false detections.

3. Proposed and Compared Methods

Before introducing the proposed method, we briefly present the preliminary works that motivate and justify our proposition. First of all, a neuron-based method has been tested [13], on the real images of size 768×512 presented in Section 4.2. Results are interesting, but learning methods are not easy to use for a nonspecialist in image processing, and the users have to spend a lot of time for setting the parameters and for building the database for the learning step before using the method. The main goal is to propose a system that facilitates the work of users and not a system that induces a lost time by including a learning phase and a maintenance each year in order to maintain the performances of the system.⁴ In consequence, we have now focused our work on methods that allow automatic processing, and, in particular, we present two approaches as follows.

- (1) The first, *Morph*, belongs to the families (1) and (2) because it combines thresholding and refinement by morphological analysis.
- (2) The second, *GaMM*, of families (4) and (5), is based on the advantage of multiscale analysis and local modelling of the crack.

Morph has been proposed before *GaMM* and is quite equivalent to the method presented in [15]. The contributions of this section are about *GaMM*; we propose a new model for the sites and the potentials used in the Markovian model. The advantages of this new method will be illustrated with qualitative and quantitative results in Section 5.

3.1. Morphological Method (*Morph*). The chosen approach is based on hypotheses H_{p_1} , H_{g_1} , and H_{g_3} , and it follows these steps.

- (1) Preprocessing of the images: to reduce the influence of the texture and to increase the contrast between the road pavement and the crack.
- (2) Binarization by thresholding (the threshold is different in the various variant, and a local threshold can be used).
- (3) Refinement by closing.
- (4) Segmentation with shape analysis.
- (5) Extraction of the characteristics of the cracks.

For step (1), three variants are developed, based on the combination of these local tools: an erosion in gray levels, a conditional median filtering, a histogram equalization, a mean filtering (these preprocessings are detailed in Section 5.1).

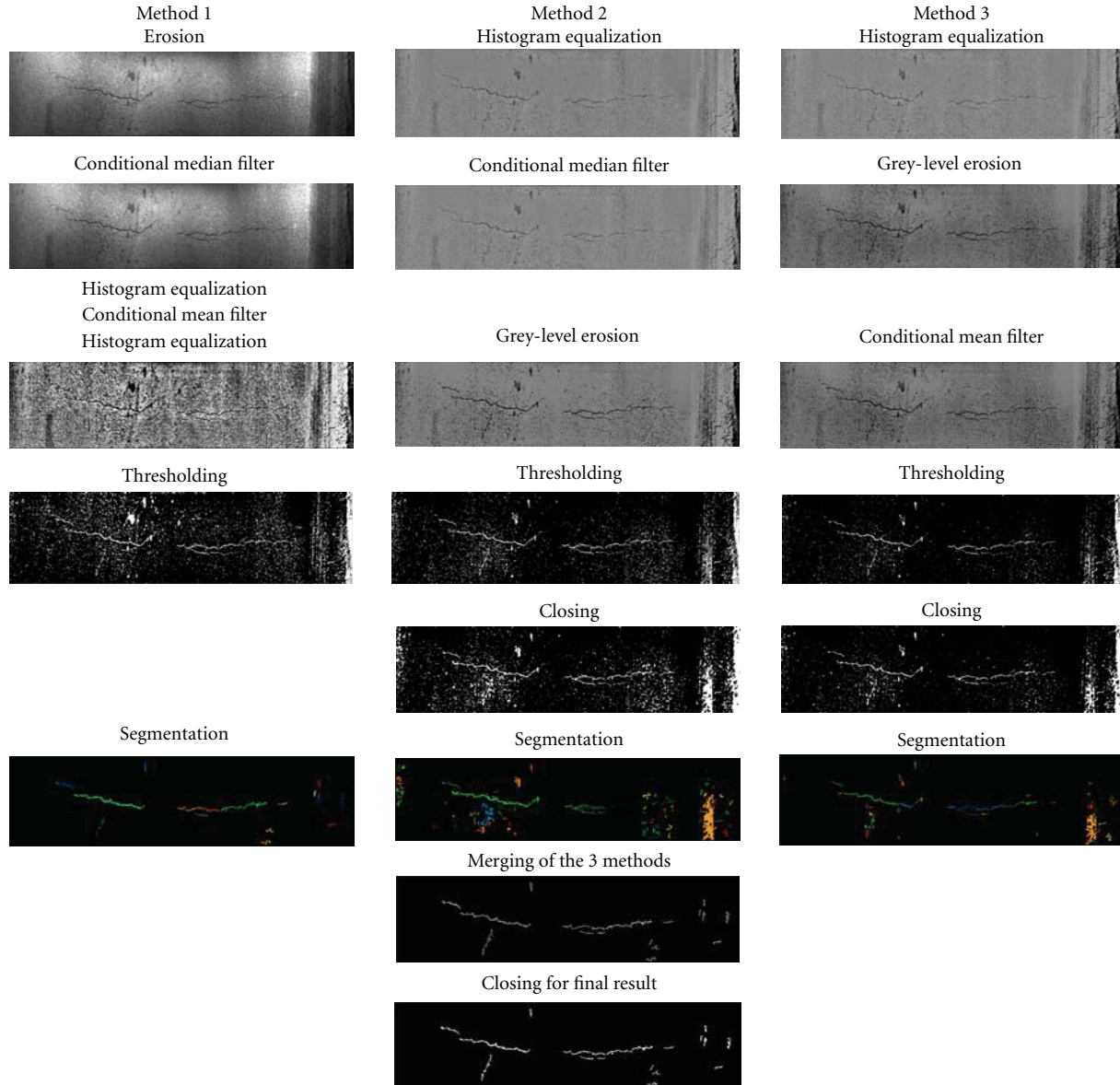


FIGURE 2: The different steps of the method *Morph*. The conditional filtering is applied when the gray level is higher than 40 (to prevent the removal of the crack). The last step is proposed in order to reduce false detections and to complete the detection.

The step (4) is realised in two stages. First, a labeling by analysis of the connected components is realized. Second, the size and the shape of each component is determined in order to remove components which have a shape that is not similar to a crack; the shape of a crack has to be a thin object. It induces constraints on the width w and the height h of the component. More precisely, from an expert point of view, a crack is not significant if $h < 50$ cm, but we can suppose that we manage to detect only a small part of the crack, and this constraint becomes $h < 7.5$ mm. Moreover, the mean width and the maximal width of the crack have to respect these rules: $w_{\min} < 3$ mm and $w_{\max} < 6.5$ mm. All these thresholds are empirically set. In Figure 2, we illustrate the kind of results obtained at each step for the 3 variants. The next step

of the method *Morph* merges the 3 results (with a weighted sum, and the weights are chosen with a learning phase). The final stage refines the result by computing the closing in gray levels of the fusion result.

3.2. Adaptive Filtering and Markovian Modelling (GaMM).

More recently, our work focused on the field of wavelet decomposition. As it is difficult to chose the mother wavelet⁵ well adapted to the detection of road cracks, the adaptive filter theory seems convenient, and, in particular, it allows to build a mother wavelet adapted to our task. We present the first step of the algorithm based on adaptive filtering (hypotheses H_{p_1} and H_{g_3}) and the second stage on Markovian segmentation that can take into account the particular geometry of the crack (H_{g_2} and H_{g_3}).

Input
Road images
Initialization
Number of scales and angles
Steps
(1) For each scale do
(1a) For each direction do
 Estimate Adaptive Filter (AF)
(1b) Merge AF in all the directions
(2) For each scale do
(2a) Initialization of the sites (Markov)
(2b) While not (stop condition) do
 Updating of the sites
(3) Fusion of the results on each scale

ALGORITHM 1: The studied algorithm for the method based on adaptive filtering and segmentation by Markovian modelling. The step (1) leads to a binary image using adaptive filtering, while step (2) refines this result with a Markovian modelling.

3.2.1. Algorithm. The goal of this algorithm, presented in Algorithm 1, is to obtain, step (1), a binarization (black pixels for the background and white pixels for the cracks) and a refinement of this detection by using a Markovian segmentation, step (2). Using adaptive filtering is important in order to allow the detection of the crack with nonconstant width (hypothesis H_{g_3}).⁶ The number of scales for the adaptive filtering has to be chosen and depends on the resolution of the image. By supposing a resolution of 1 mm per pixel, by choosing 5 scales, a crack with a width from 2 mm to 1 cm can be detected. Moreover, the number of directions (for the filtering) also has to be chosen, and it seems natural to take these four directions: $[0, \pi/4, \pi/2, 3\pi/4]$ that correspond to the four usual directions used for crack classification. The adaptive filtering is applied in each scale, each direction, and then all the results are merged on each scale (mean of the coefficients). The results of this filtering is the initialization of the Markovian segmentation step.

3.2.2. Adaptive Filtering. Some details are provided in order to realize step (1a) and (1b) in Algorithm 1. The $\psi \in \mathcal{L}^2(\mathbb{R}^2)^7$ function is a wavelet if

$$\int_{\mathbb{R}^2} \frac{|\Psi(\mathbf{x})|^2}{\|\mathbf{x}\|^2} d\mathbf{x} < \infty, \quad \text{with } \mathbf{x} = (i, j), \quad (1)$$

where Ψ is the Fourier transform of ψ . Equation (1) induces that $\int_{\mathbb{R}^2} \psi(\mathbf{x}) d\mathbf{x} = 0$. The wavelet family is defined for each scale s and for each position \mathbf{u} , by

$$\psi(\mathbf{x}) = \frac{1}{2} \psi \left(R^\theta \left(\frac{\mathbf{x} - \mathbf{u}}{s} \right) \right), \quad (2)$$

where R^θ is a rotation of angle θ .

One of the main difficulties for applying a wavelet decomposition is the choice of the mother wavelet ψ . Numerous functions are used in the literature: the Haar wavelet, the Gaussian derivatives, the Mexican hat filter, the Morlet wavelet. It is very hard to determine which one is the best

for a given application. In the case of crack detection, two elements are present: the crack (if there is a crack) and the background (the road surface can be viewed as a repetitive texture). The goal of the crack detection is to recognize a signal (its shape is known up to a factor) mixed with a noise whose characteristics are known. Consequently, adaptive filtering is well designed for the problem: extracting singularities in coefficients estimated by a wavelet transform. If \mathbf{s} is a discrete and deterministic signal with $\mathbf{s} = (s_1 \cdots s_N)$, N the number of samples, and $\mathbf{z} = (z_1 \cdots z_N)$ is a noisy observation of \mathbf{s} , \mathbf{b} is supposed to be an additive noise: $\mathbf{z} = \mathbf{s} + \mathbf{b}$. The main hypothesis is that this second-order noise is centered and stationary, with the autocorrelation function ϕ_{bb} of terms $\phi_{bb(i,j)} = \phi_{bb|i-j}$, independent of the signal \mathbf{s} . The adaptive filter \mathbf{h} of \mathbf{s} is defined by

$$\mathbf{h} = \phi_{bb}^{-1} \mathbf{s}. \quad (3)$$

The crack signal depends on the definition of the crack. In this paper, like in most of the papers of this domain, crack pixels correspond to black pixels surrounded by background pixels (road pixels). This is why, in [46], a crack is a piecewise constant function f , defined for each position $x \in \mathbb{R}$ by:

$$f(x) = \begin{cases} -a & \text{If } x \in \left[-\frac{T}{2}, \frac{T}{2}\right], \\ 0, & \text{elsewhere,} \end{cases} \quad (4)$$

where the factor a and the threshold T have to be determined. It does not correspond to a realistic representation of the crack. Because of subsampling, lights, and orientation of the camera, the signal is more like a Gaussian function with zero mean

$$f(x) = -ae^{-(1/2)(x/\sigma)^2}, \quad (5)$$

where a is the size of the crack and depends on σ , the deviation of the Gaussian law, that is, $a = 1/\sigma\sqrt{(2\pi)}$. Consequently, the term σ allows to fix the width of the crack (like threshold T in (4)). Finally, for step (1), \mathbf{h} is estimated for each of the 5 scales, as explained in the beginning of Section 3.2.1, and ϕ_{bb} is interpolated in order to have the same size. Then the filter is rotated in order to cover the 4 orientations.

3.2.3. Segmentation. The goal of this part is to extract shapes, that is, cracks, using the detection maps estimated at the first stage of the algorithm (step (2a) of Algorithm 1). For the first step of segmentation (initialization), the sites are of size 3×3 , consequently, a regular grid is considered in the image. In [46], four configurations are possible and represented in Figure 3 (the part inside the rectangle with low gray levels). The initialization of the sites is based on the configuration that maximizes the coefficients obtained with the adaptive filtering. More formally, if we denoted $\gamma_{2,0}$, $\gamma_{2,\pi/4}$, $\gamma_{2,\pi/2}$, and $\gamma_{2,3\pi/4}$, the four configurations, the best configuration γ_{best} is:

$$\gamma_{\text{best}} = \arg \max_{\alpha \in [0, \dots, 3\pi/4]} m_{2,\alpha} \quad (6)$$

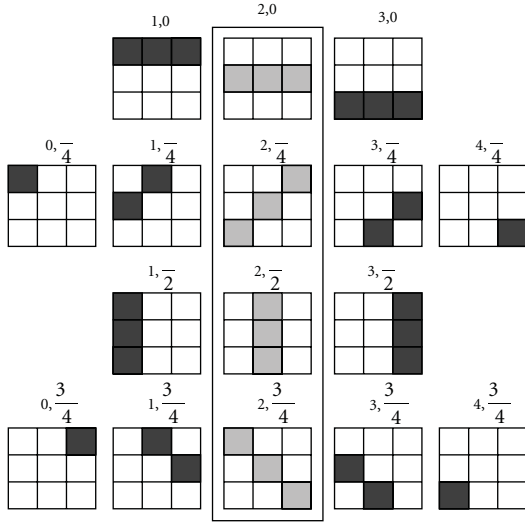


FIGURE 3: The sixteen configurations in order to improve the modeling of sites. The four initial configurations proposed in [46] are in the bold rectangle, the sites are represented by the clearer gray levels, and, for the proposed configurations, the sites are represented by the darker gray levels.

where $m_{2,\alpha}$ is the mean of the coefficients on the considered configuration $\gamma_{2,\alpha}$. These four configurations do not represent all the possibilities and are not realistic configurations. In fact, all these four configurations are centered, whereas it is possible to have some noncentered configurations. Consequently, we use the set of sixteen configurations illustrated in Figure 3 (all the presented sites). By modifying the number of configurations, we need to adapt the initialization of sites, and (6) becomes

$$\gamma_{\text{best}} = \arg \max_{i \in [0;4], \alpha \in [0, \dots, 3\pi/4]} m_{i,\alpha}, \quad (7)$$

where $m_{i,\alpha}$ is the mean of the coefficients on the considered configuration $\gamma_{i,\alpha}$.

The image is considered as a finite set of *sites* denoted $\mathcal{S} = \{s_1, \dots, s_N\}$. For each site, the *neighborhood* is defined by: $\mathcal{V}_s = \{s' \mid s \notin \mathcal{V}_{s'} \ \& \ s' \in \mathcal{V}_s \Rightarrow s \in \mathcal{V}_{s'}\}$. A *clique* c is defined as a subset of sites in \mathcal{S} whose every pair of distinct sites are neighbors.

These random fields are considered as follows.

- (1) The observation field $Y = \{y_s\}$ with $s \in \mathcal{S}$. Here, y_s is the mean of the coefficients on the site.
- (2) The descriptor field $L = \{l_s\}$ with $s \in \mathcal{S}$. If there is a crack $l_s = 1$ elsewhere $l_s = 0$.

At each iteration, a global cost, or a sum of potentials that depends on the values of the sites and the links between neighborhoods, is updated. This global cost takes into account the coefficients of the sites (computed from the coefficients estimated during the first part of the algorithm: adaptive filtering) and the configurations of each site and its neighbor sites (the 8 neighbors). More formally, the global

TABLE 4: The function u_2 used in [46]. This table presents the values $u_2(s', s)$ for the sites in low gray levels in Figure 3. In our experiments, like the authors, we have chosen $\beta_1 = -2$, $\beta_2 = -1$, and $\beta_3 = 2$.

	$\gamma_{2,0}$	$\gamma_{2,\pi/4}$	$\gamma_{2,\pi/2}$	$\gamma_{2,3\pi/4}$
$\gamma_{2,0}$	β_1	β_2	β_3	β_2
$\gamma_{2,\pi/4}$	β_2	β_1	β_2	β_3
$\gamma_{2,\pi/2}$	β_3	β_2	β_1	β_2
$\gamma_{2,3\pi/4}$	β_2	β_3	β_2	β_1

cost is the sum of all the potential functions of the sites. This potential function contains two terms as follows.

$$u_s = \alpha_1 u_1(s) + (1 - \alpha_1) \sum_{s' \in \mathcal{V}_s} u_2(s, s'). \quad (8)$$

The first term, u_1 , corresponds to the *data term*, and it evaluates how a site is similar to a crack from a photometric point of view (hypotheses H_{p_1} and H_{p_2}). This term is based on the results given by the adaptive filtering. The second term, u_2 , represents the *constraints* induced by the neighbors of the site. More precisely, it estimates the consistency between a site and each neighbor site, and it takes into account the geometric hypotheses H_{g_2} and H_{g_3} . The choice of the value α_1 depends on the importance of each part of (8), and it will be discussed in Section 5.1.1.

The function u_1 is given by,

$$u_1(y_s, l_s = 1) = \begin{cases} e^{\xi_1(k-y_s)^2} & \text{If } y_s \geq k, \\ 1 & \text{elsewhere,} \end{cases} \quad (9)$$

$$u_1(y_s, l_s = 0) = \begin{cases} e^{\xi_2(y_s-k)^2} & \text{If } y_s < k, \\ 1 & \text{elsewhere.} \end{cases}$$

The parameters ξ_1 , ξ_2 , and k have to be fixed.⁸ For the definition of u_2 , we have to determine the number of cliques. In [46], 4 cliques are possible and the 8-connexity is considered. The potential function proposed in the precedent work only considers the difference of orientations between two neighborhoods and not the position between the two sites of the clique, see Table 4. Some cases are not penalized with the old configuration. For example, these two unfavorable cases are not penalized as follows:

- (i) two sites with the same orientation but with no connection between them,
- (ii) two sites with the same orientation, but their position makes them parallel.

This is why, with the sixteen configurations that are presented in Figure 3, the potential has to take into account the differences of orientations between two sites (there are 16×16 possibilities) and the position of the two sites (there is 8 possibilities because we consider the 8 neighbors). Consequently, the new potential function u_2 follows these two important rules.

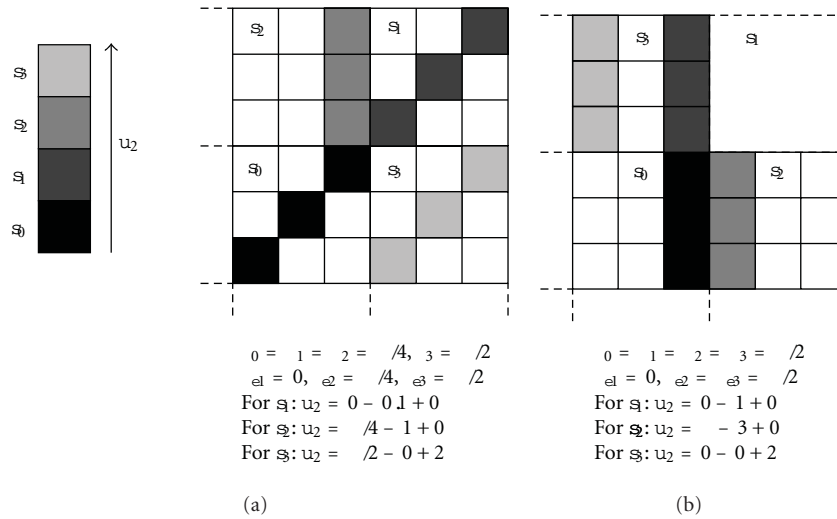


FIGURE 4: Examples of the function u_2 . These two examples of sites with their respective neighbors show the behavior of the potential u_2 with the two considered aspects: orientation and distance. In example (a), with the help of the orientation term, the configuration s_3 is penalized and, s_2 is less penalized than s_3 . In example (b), with the help of the two terms about the distance, the site s_3 is penalized, compared to s_1 . On the contrary, the particular case of s_2 is favorable, and it compensates the penalty given by the orientations.

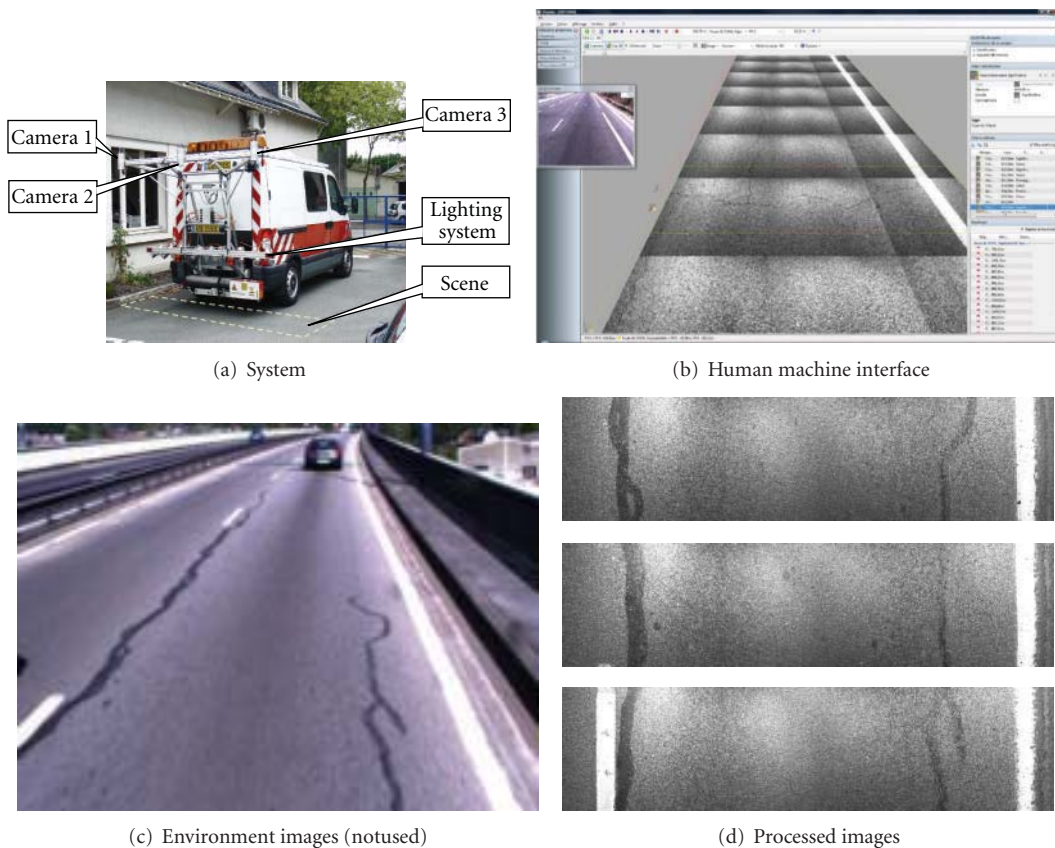


FIGURE 5: The acquisition system used for the evaluation. In (a), the acquisition system is illustrated whereas in (b) it shows the user interface. In (c, d), an example of the final images is given. In (d), we can see the road that is visible in (c). The processing is done 1 meter by 1 meter, that is, independently on each image presented in (d). The surface contains two reparations of vertical cracks. In some cases, the 3 sensors do not have the same settings, and the global illuminations are different, so it can generate some “false cracks”. This aspect has been easily taken into account in a preprocessing step by eliminating the junction area in the region of interest.

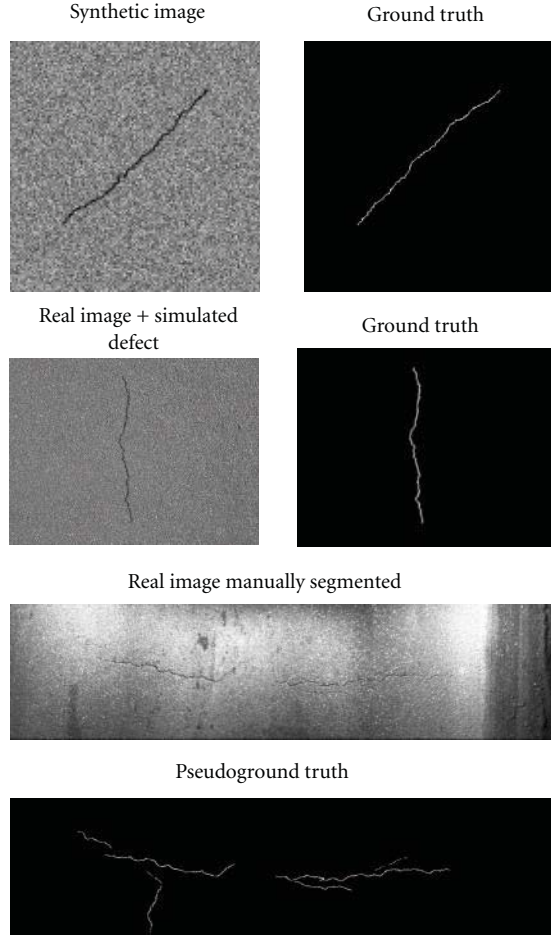


FIGURE 6: Examples of the images tested.

- (R₁) The lower the difference of orientations between two sites, the lower the potential.
- (R₂) The lower the distance between two sites, the lower the potential (in this case, the distance means the minimal distance between the extremities of the two segments).

More formally, if

- (i) d denotes the Euclidean distance between the two closest extremities of the sites, with $d \in [0, d_{\max}]$,⁹
- (ii) θ_1 and θ_2 are the orientations of, respectively, $s = \{p_i\}_{i=1 \dots N_s}$, and $s' = \{p'_i\}_{i=1 \dots N'_s}$ where, p_i , respectively p'_i , is the pixel i of the N_s , respectively N'_s , pixels that composes the site s , respectively s' ,
- (iii) θ_e is the angle between the two sites; the u_2 function is defined by

$$u_2(s', s) = \alpha_2 \left(\frac{|2\theta_e - \theta_1 - \theta_2|}{2\pi} \right) + (1 - \alpha_2) \left(\frac{J(\text{NbC}) \min_{i,j} (d(s_i, s'_j))}{d_{\max}} - \frac{\text{NbC}}{3} \right), \quad (10)$$

where NbC indicates the number of connected pixels between the two sites s and s' , and $J(x)$ equals 1 if $x = 0$ and 0 elsewhere. The first term is induced by the rule about the orientations, (R₁). This term equals zero when the sites have the same orientation, and this orientation is the same as the orientation between the sites, that is, $\theta_e = \theta_2 = \theta_1$. This first term penalizes the configurations where the sites do not have the same orientation but also the particular case where they are parallel, see example (a) in Figure 4. The second term and the third term express the rule (R₂) about the distances. Two aspects have to be distinguished: the number of connected pixels, when the sites are connected, and, on the contrary, that is, when the sites are not connected, the distance between the sites. It allows to give low influence at disconnected sites and also to increase the cost of sites that are parallel but connected, see example (b) in Figure 4. To study the influence of all these terms, the equation has been normalized, and the different terms have been weighted (using α_2 , the choices for α_2 will be discussed in Section 5.1.1).

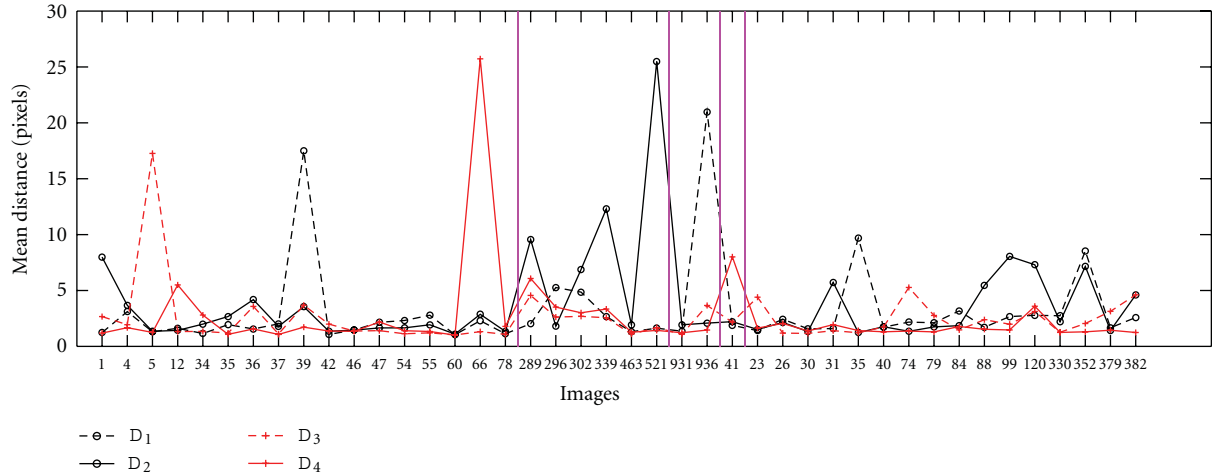
4. Evaluation Protocol

For the evaluation of automatic crack detection by image processing methods, to the best of our knowledge, no evaluation and comparison protocol has been proposed in the community. However, in all the countries, for estimating the quality of the road surface, it is important to know exactly the size and the width of defects, that is, to detect precisely the defect. This is why it seems important to characterize quantitatively the performances of the methods. For building this kind of protocol, it is necessary, first, to choose the tested images, second, to choose how to build reference segmentations, and, third, to determine the criteria used for the quantitative analysis. For estimating the reference segmentations, two approaches can be used

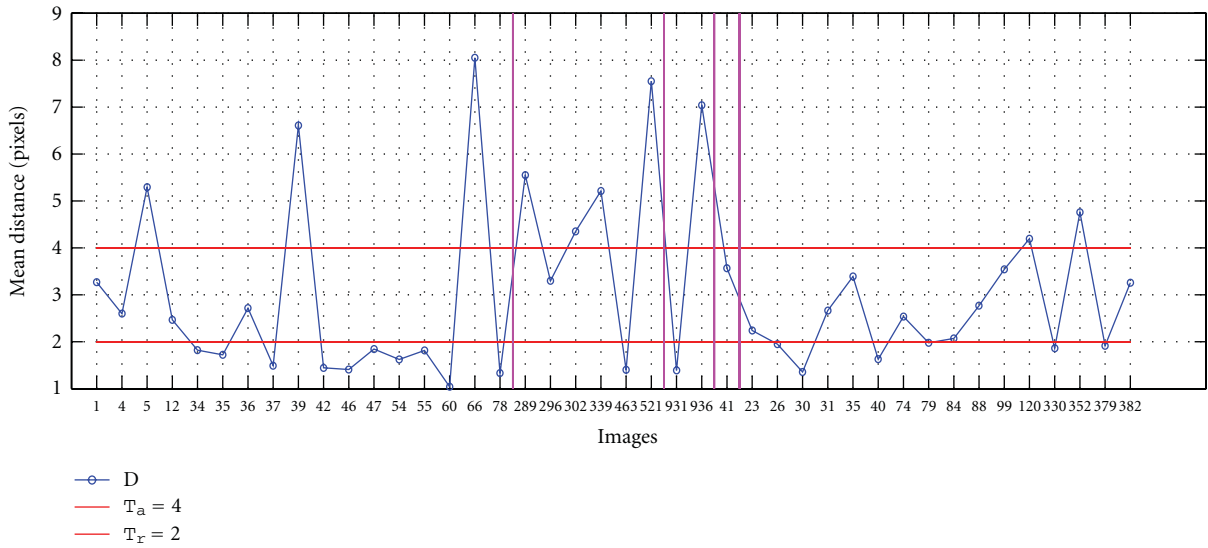
- (1) *To compute synthetic images with synthetic defects.* The exact position of the defects is known, and the reference segmentations can be considered as ground truth.
- (2) *To propose reliable segmentations of real images.* It supposes that we are able to provide a segmentation that is reliable enough to be employed as a reference. For evaluation, these segmentations can be called "pseudoground truth."

The two solutions are studied, and, we explain how the manual segmentations (that are our references) are computed. Before, we briefly describe the acquisition system.

4.1. Acquisition. The acquisition system used for the dataset of our experiments is described in Figure 5. It contains 4 video cameras with 3 sensors in gray levels in the backside of the car and 1 color in front of the car. The first camera is



(a)



(b)

FIGURE 7: The variations between each manual segmentations that are used for building pseudoground truth. The first graph represents for each operator (one curve for one operator) and each image (x -coordinates), cf. Figure 16 for the corresponding images, the mean distance, D_i , $i \in \{1, 2, 3, 4\}$. The second graph presents D , cf. Section 4.3 and Table 5. This graph allows us to distinguish the different categories of images (red axes): *reliable* ($D < T_r$), *moderately reliable* ($T_r \leq D < T_a$), *ambiguous* ($T_a \leq D$). In the two graphs, the purple axes represent the five different samples of images (each sample corresponds to a kind of road pavement). The first ones were acquired with a static system whereas the four others were acquired with a dynamic system.

needed to determine the environment conditions (weather, location, traffic) whereas the three other ones are used for the crack detection. The resolution of this one is smaller than the 3 others, and; moreover, the optical axis is not perpendicular to the road surfaces, on the contrary of the 3 others. The 3 cameras have been physically synchronized directly during the acquisition. To be independent of the illumination problems, nine stroboscopic lights have been added. The position of the lights is perpendicular to the road plane, and they are distant from the surface of 1 meter. The light power has been chosen in order to not deteriorate the visualisation of the road pavement and the defects.

4.2. *Reference Images.* The most difficult is to propose images with a reference segmentation. On the first hand, we introduce synthetic images with a simulated crack (the size of these images is 256×256).¹⁰ As shown in Figure 6, the result is not realistic enough. It does not seem realistic because the contrast is too important between the road and the crack. Moreover, the interruptions of the crack, the changes in the direction, the presence of many paths, and so forth, in the default, are not simulated. In order to be more realistic, it seems that we have to design and to implement a complex heuristic to simulate the crack, and it represents too much effort for having only a synthetic default. This is why, on

the other hand, we have simulated different defects on real images that previously contain no defect (the size of these images are 768×512 and 1920×480). The result is more realistic, but the shape and the photometric aspect of the cracks (which are randomly chosen) does not seem realistic enough. This is why it appears important to propose a set of real images (size 768×512 and 1920×480) with manual segmentations that are reliable enough to be considered as reference segmentations. To summarize, the two first kinds of images allow to propose an exact evaluation and to illustrate theoretically the behavior of the method whereas the last kind of images allows to validate the work on real images with a pseudoground truth.

4.3. Reference Segmentations. For real images, we briefly explain how the manual segmentations are validated. Four experts have manually segmented the images with the same tools¹¹ and in the same conditions. Then, the four segmentations are merged, following these rules.

- (1) A pixel marked as a crack by more than two experts is considered as a crack pixel.
- (2) Every pixel marked as a crack and next to a pixel kept by step (1) or (2) is also considered as a crack.

The second rule is iterative and stops when no pixel is added. Then, the result is dilated with a squared structuring element of size 3×3 . To evaluate the reliability of the reference segmentations, we estimate, first, the percentage of covering between each operator and, second, the mean distance, D , between each pixel (detected by only one expert and not kept in the reference image) and the reference segmentation.

Table 5 shows some results for 5 of the 42 images manually segmented. We have distinguished 5 families: the first one contains images acquired in static whereas the four other ones are acquired in dynamic. Moreover, we have 4 different kinds of road pavement acquired in dynamic. The 5 images have been taken in order to show results on each of these families. We can notice that the first 2 images are the most reliable because the mean error is less than 2 pixels. The precision of these results is satisfactory. On the contrary, the last 3 images show the important variabilities between operators and how it is difficult to extract a segmentation for these images and, in particular, in the image 936, where the error is due to a bad interpretation of one of the four operators who finds a defect that does not exist.

By analyzing the results for the criterion D , presented in Table 5, we can classify the 42 tested images in 3 categories, that is, images with the following.

- (1) A *reliable* segmentation: the criterion $D < T_r$. It means that all the operators have built segmentations that are quite near to each other.
- (2) A segmentation that is *moderately reliable*: the criterion $T_r \leq D < T_a$. It means that some parts of the crack are not easy to segment, and there are local errors.
- (3) An *ambiguous segmentation*: the criterion $D \geq T_r$. It clearly shows that the images are difficult to segment,

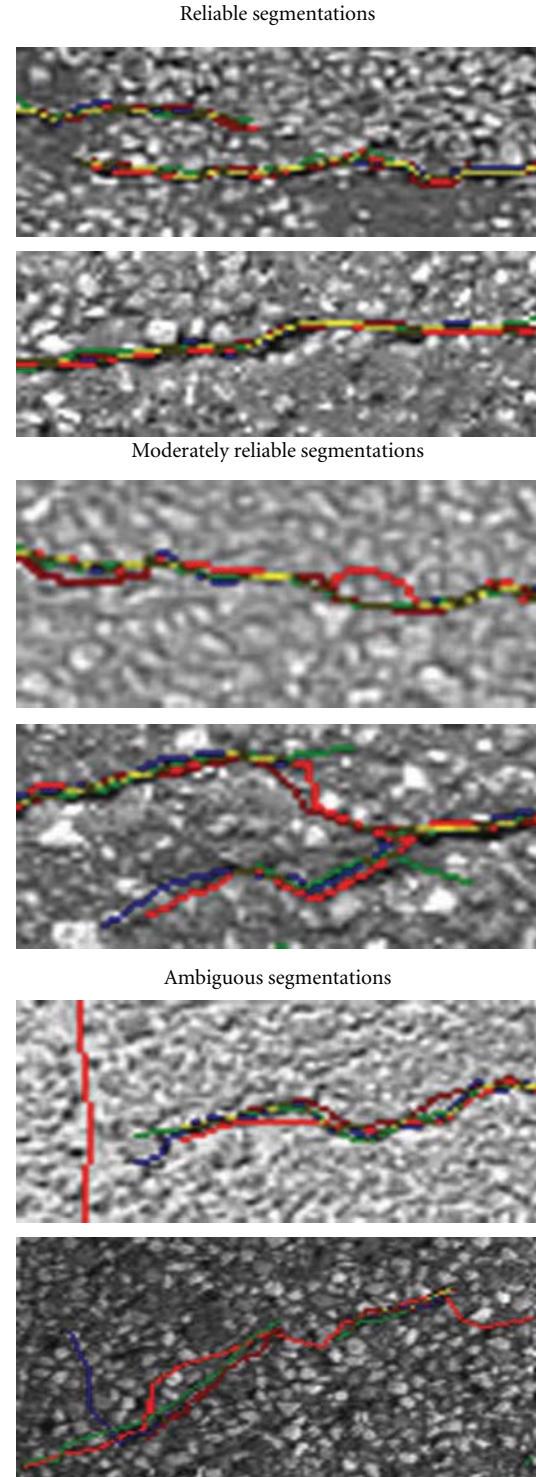


FIGURE 8: The levels of difficulties of the tested images. On these images, we present the four manual segmentations. The codes are red (light and dark), blue, green, for each of the four operators. The parts in yellow correspond to the parts of the cracks detected by more than one operator. There are two examples per category of segmentation. To better visualize, only a part of the images is shown. In the ambiguous images, we clearly see the mistake of the operator in dark red.

TABLE 5: The comparison of the 4 manual segmentations for estimating the final reference segmentations. For each image, we specify: the percentage of pixels in the whole image that are preserved as crack pixels in the final reference segmentation (F), the percentage of recovering between 2, 3 and 4 manual segmentations and the sum of these 3 percentages (S). For all the crack pixels that are not preserved in the final reference segmentation, the mean distance to this segmentation is given (D).

Images	F (%)	2 (%)	3 (%)	4 (%)	S (%)	D (pix)
42 	0.4	26.69	14.59	4.2	45.48	1.45
463 	0.17	23.46	5.95	0.39	29.8	1.4
936 	0.41	23.52	7.41	0.9	31.83	7.05
41 	0.33	22.64	7.31	1.33	31.28	3.56
88 	1.44	22.74	8.23	1.23	32.2	2.76

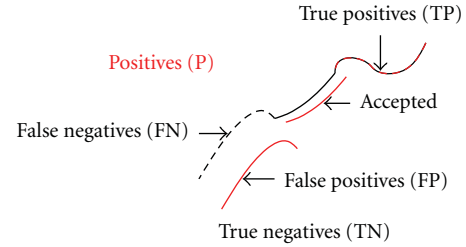
and, in most of the cases, it means that some parts are detected as a crack whereas they are not and reversely.

The threshold have been empirically chosen: $T_r = 2$ and $T_a = 4$. In Figure 7, first, we present the mean distance, D_i , $i \in \{1, 2, 3, 4\}$, between the final reference segmentation, S_r , and each manual segmentation, S_i (obtained with each operator), and, second, the criterion D for each real image of our protocol. The first graph illustrates how it is important to combine the four manual segmentations instead of using only one manual segmentation. Indeed, we can notice that each operator, alternately, gives an interpretation that is different from the three others. The second graph explains how the thresholds are chosen for determining the detections that are “accepted” for the evaluation, see Section 4.4 for explanations about accepted detections.

The three categories of reference segmentations are illustrated in Figure 8. Overall, the four segmentations are near to each other, and, if the segmentations are combined, it permits to detect the width of the crack. However, these examples also present some difficulties of the crack segmentation: areas where the cracks are less visible and regions where the texture elements that have the same size and/or the same gray levels as the crack pixels. Thus, in some cases, one operator extends the crack or gives a different shape. In some extreme cases, the operator can even confound a crack and another object of the scene (a piece of wood, e.g.). In another way, these examples highlight the interest in combining different segmentations in order to obtain reference segmentations as reliable as possible.

4.4. Criteria of Efficiency. In this section, we introduce how the reference segmentation and the estimated segmentation are compared. In Figure 9, we present common evaluation criteria that are used for segmentation evaluation:

- (1) the percentage of correct detections (true positives) (TP),
- (2) the percentage of false positives (FP),



Sensitivity	$\frac{TP}{TP+FN}$	Proportion of good detections
Specificity	$\frac{TN}{TN+FP}$	Proportion of nondetected pixels
Similarity coefficient or DICE similarity	$\frac{2TP}{FN+TP+P}$	Ratio between good detections and nondetections

FIGURE 9: The evaluation criteria. In this figure, two segmentations of the same crack are represented the black line corresponds to a manual (or reference) segmentation, and the red line is an estimated segmentation. The goal is to evaluate the quality of the estimated segmentation that corresponds to the positives (P). All the non-selected pixels that do not correspond to the crack are called the true negatives (TN). The piece of line with the two colors (red and black) are the correct detections or true positives (TP). In this table, different criteria are introduced, but, in this work, we have used the DICE because this coefficient well represents what we want to measure: the quality of the detection against the percentage of the crack that is detected, in order to determine how to reduce false detections whilst increasing the density.

- (3) the percentage of false negatives (FN), and
- (4) the similarity coefficient (DICE).

This last criterion seems to be the most significant because it evaluates the ratio between the FP and the FN , and it resumes the results of all the criteria. Moreover, it directly expresses what is important to evaluate: how the method can reduce errors of detection whilst increasing the density of good detections.

For real images, the detections that are “accepted” have been added in order to tolerate a small error on the localization of crack pixels. This criterion is needed because perfect detection seems, for the moment, difficult to reach, see the results in Table 5. In consequence, these accepted pixels have been included in the estimation of the similarity coefficient or DICE. The threshold for accepted detections equals 0 for synthetic images whereas it depends on the mean distances, see D in Table 5, for the real images.

5. Experimental Results

In this section, two aspects are studied and presented:

- (1) the evaluation of the method based on an adaptive filtering and a Markovian modelling in order to

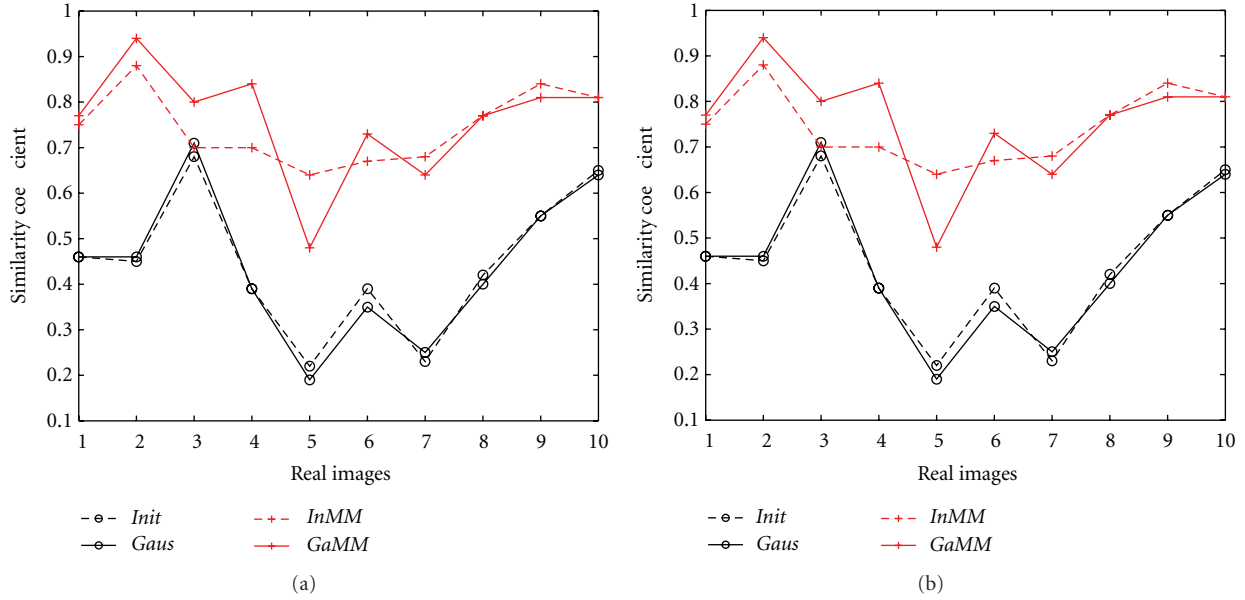


FIGURE 10: The variations of the similarity coefficients (given in Figure 9) for the 4 variants. The first graph shows the results for synthetic images (the first 3 ones are obtained from real images with simulated defect), and the second graph presents the results with real images. The good performances of the methods *InMM* and *GaMM* can be noticed.

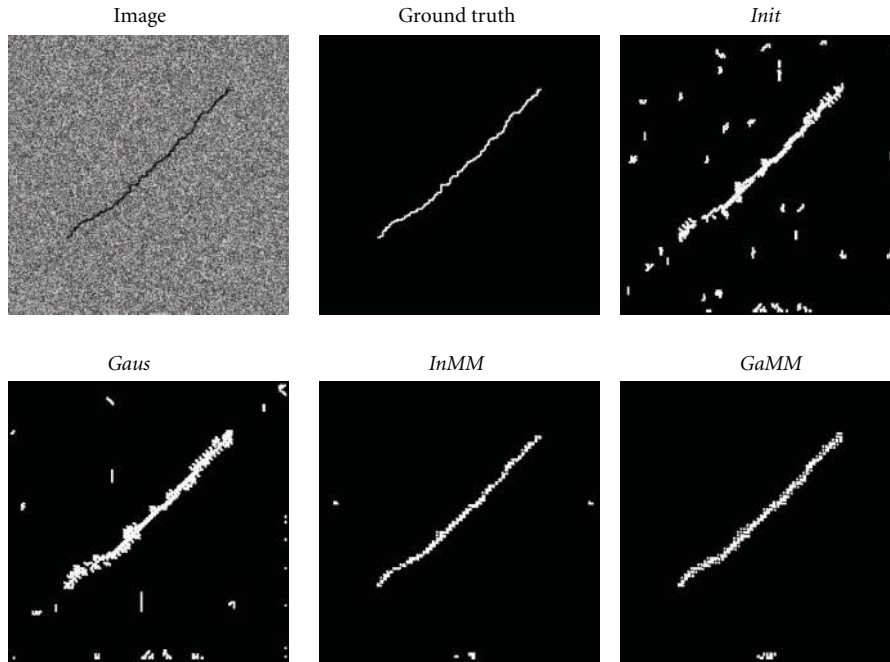


FIGURE 11: The segmentation results on some synthetic images presented in Figure 6. These are the results obtained with the four variants, and they show how the method *GaMM* gives the clearest result. We can also notice the good results of the method *InMM*.

characterize its behavior, to estimate the best parameters and to determine the best variant;

(2) the comparison to the *Morph* method.

5.1. Adaptive Filtering and Markovian Modelling. We want to determine, first, how to fix the different parameters, second,

the preprocessing steps that are necessary, and, finally, which variant is the most efficient. In consequence, these points have been studied.

(i) Parameter values. The weights α_1 , (8), and α_2 , (10), are tested from 0 to 1 with a step of 0.1.

(ii) *Preprocessings*. These preprocessings have been experimented to reduce noises induced by texture, to increase the contrast of the defect and to reduce the light halo in some images as follows.

- (1) *Threshold*. This preprocessing has been proposed in order to reduce the light halo in the last 4 images presented in Figure 6 and in all the images of the last four categories in Figure 7. Each pixel lower than a given threshold is replaced by the local average of the gray levels.
- (2) *Smoothing*. A mean filter of size 3×3 is applied to reduce the granularity of the texture.
- (3) *Erosion*. An erosion (in gray level) with a square structuring element of size 3×3 is also applied to reduce the granularity of the texture.
- (4) *Restoration*. It combines the advantages of all the previous methods in three steps: a histogram equalization, a thresholding (like *Threshold*), and an erosion (like *Erosion*).

In order to preserve the crack signal, each pixel under a given threshold is not filtered.¹²

(iii) *Algorithm variants*. Four variants are compared as follows.

- (1) *Init*. This is the initial method proposed in [46].
- (2) *Gaus*. This variant supposes that the distribution of the gray levels inside a crack follows a Gaussian function, see Section 3.2.2.
- (3) *InMM*. This is the initial version with an improvement of the Markovian modelling (new definition of the sites and of the potential function), see Section 3.2.3.
- (4) *GaMM*. This is the method *Gaus* with the new Markovian modelling.

(iv) *Comparison*. We have compared this method with the method based on morphological tools and that is quite similar to [15], *Morph*.

5.1.1. *Influence of Parameters*. Among all the results, two conclusions can be done.

- (1) For each variant and each preprocessing, the weights between the term for adaptive filtering and the term for the Markovian modelling should be the same, see (8), that is, $\alpha_1 = 0.5$. However, when the weight given to adaptive filtering is the largest, the quality of the results is lower than that when it is the reverse. It means that in this kind of application, the geometric information is more reliable than the photometric information. It seems coherent with the difficulties induced by the acquisition.
- (2) For the Markovian modelling, we have noticed that the results are the best when the weights are the same between the orientation term and the distance term,

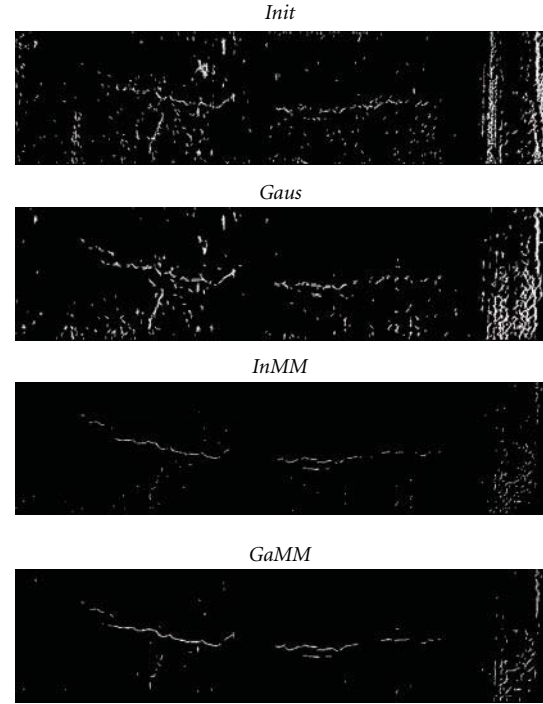


FIGURE 12: The segmentation results on some real images. These are the results obtained with the real images presented in Figure 6. The method *InMM* obtains the clearest detection (i.e., with less false detection), but we can also notice the good quality of the detection map with the method *GaMM*.

see (10), that is, $\alpha_2 = 0.5$. However, better results are obtained when the weight of the orientation is greater than the weight of the distance one instead of the reverse. It means that the orientation characteristics are more reliable than the distance ones, and this remark is coherent with the fact that cracks present strong spatial constraints. Moreover, it is also linked with the difficulties induced by the acquisition (the lighting system makes the photometric information less reliable).

5.1.2. *Preprocessing*. These tests have been done with real images, because the synthetic images do not need preprocessings. These conclusions can be made for the needed preprocessing per method:

- (i) *Init*: restoration;
- (ii) *Gaus*: restoration;
- (iii) *InMM*: threshold;
- (iv) *GaMM*: erosion.

However, for the first dataset (acquired with lighting conditions more comfortable than the lighting conditions of the next 4 ones), the preprocessing is not significant for increasing the quality of the results. Moreover, with the new Markovian modelling, the preprocessing step does not significantly increase the quality of the results.

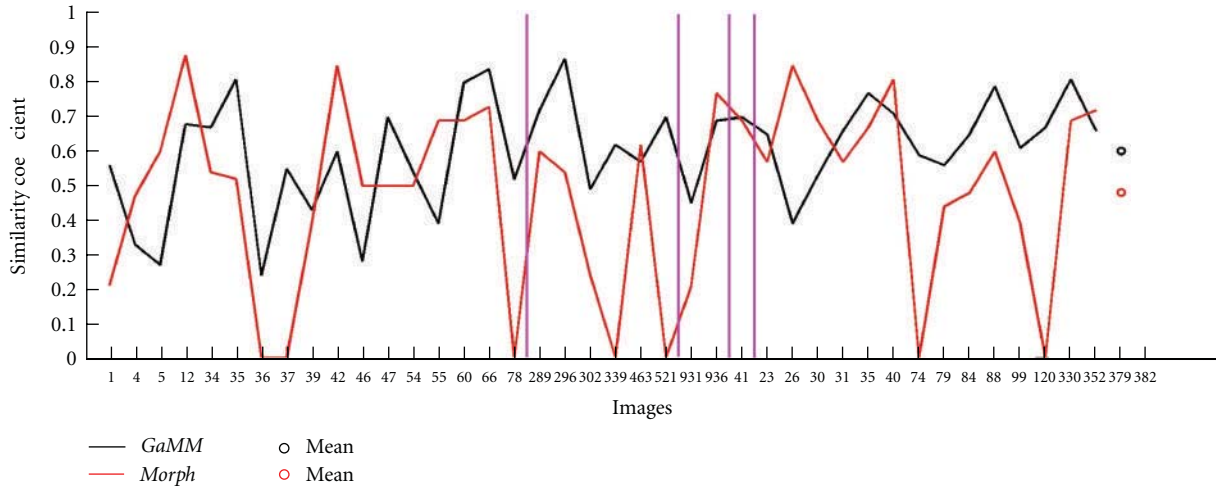


FIGURE 13: The comparison of the similarity coefficients between *GaMM* and *Morph*. The purple axes correspond to the five sets of tested images. For the first set that corresponds to real images with no illumination problems, the results are mixed whereas, for the four other sets, *GaMM* is the best. The mean of this criterion is 0.6 (variance = 0.0257) for *GaMM* whereas it is 0.49 (variance = 0.0750) for *Morph*. However, this method has one step of characterization of the cracks (not introduced in *GaMM*), and this step can remove cracks that do not respect the characteristics of a cracks (in length, size, and shape). This step contributes to reduce errors, but, in some difficult cases, it decreases the performances of the detection, compared to *GaMM*.

5.1.3. Variants. The results are presented for

- (1) synthetic images,
- (2) real images.

For the first category, the ground truth is available whereas, for the second category, a pseudoground truth is used and the detections which are accepted are taken into account in the evaluation, that is, a threshold is applied to the distance between the segmentation estimated by the evaluated method and the pseudoground truth segmentation. The thresholds applied on the distance for the accepted detections are determined with the results given in Table 5, column *D*.

In Figure 10, the evolution of the similarity coefficients, or DICE, is presented for the 11 synthetic images, in Figure 10(a), and 10 of the real images, in Figure 10(b). With synthetic images, the method *GaMM* is clearly the best for most of the images. However, for one image (the fifth), the results are worse than the results of the method *Gaus*, but they are still correct (DICE = 0.72). On the contrary, for the most difficult images (the 3 first ones that contain a real road background), the method *GaMM* obtains acceptable results (DICE > 0.5) whereas the other methods are not efficient at all. Illustrations are given in Figures 11 and 12; they show how the method *GaMM* can reduce false detections.

5.2. Results and Comparison with *Morph*. Finally, we have compared the results of *GaMM* on each of the complementary dataset (32 images) with *Morph*. The mean DICE is 0.6 with *GaMM* whereas it is 0.49 with *Morph*, see Figure 13. It shows how *GaMM* can outperform *Morph*. However, if we compare image per image, the results show that in 50% of the cases *GaMM* is the best, see illustrations of these results

in Figures 14 and 15. More precisely, *GaMM* seems more efficient with *ambiguous* images, whereas *Morph* is the best with *reliable* images. Finally, we can also precise the execution time for the two methods: about 1 minute for *GaMM* and 5 seconds for *Morph* with a processor Intel core 2 duo of 2 GHz. These execution times give only some indications because the implementation, in particular for *GaMM*, has not been optimized.

6. Conclusions

In conclusion, this paper gives a review about image-processing methods for the crack detection of road pavement. It can help the researchers who want to choose and to adapt an auscultation method to the constraints of the transport structure that is studied (it depends on the quality of the surface, the needs of the auscultation). Moreover, a new method for the detection of road cracks has been introduced, and we have presented a new evaluation and comparison protocol for automatic detection of road cracks. As far as we are concerned, we proposed real images with ground truth for the first time in the community. Actually, this dataset is available on this website: <http://perso.lpc.fr/sylvie.chambon/FISSURES/>. The new method, *GaMM*, has been validated by the proposed protocol and compared to a previous one, *Morph*. This evaluation shows the complementarity of the two methods: the *Morph* method obtains more true positives than the *GaMM* method whereas this one reduces the percentage of false positives.

Our first improvements of this work will focus on the evaluation and comparison protocol. We want to increase our data set by taking into account the different qualities of

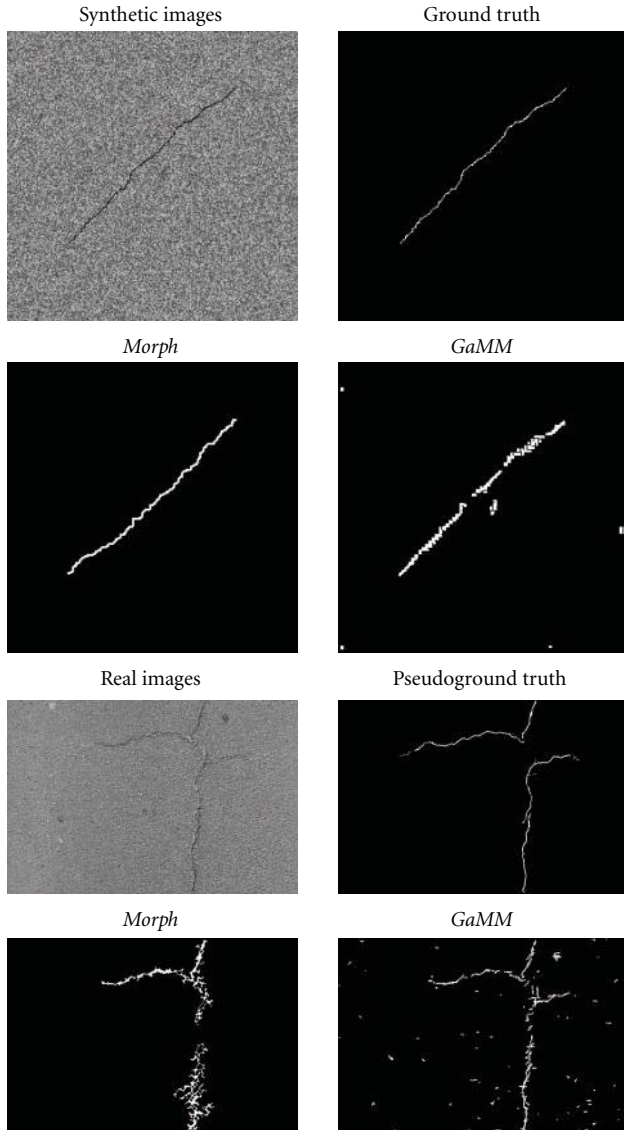


FIGURE 14: The differences between *Morph* and *GaMM*. Examples with synthetic images and real ones. *Morph* is more efficient than *GaMM* with simple synthetic images whereas *GaMM* has a better behavior with real images.

road surface or road texture (because for the moment, each proposed method seems very dependent on the quality of the road texture). In a second step, our future work will include new experiments about the acquisition system. Indeed, the acquisitions, and the results obtained with the acquisition system presented have shown its limits for example, in Figure 6, some parts of the crack are not “visible.” It comes from the fact that, to highlight the crack, it depends on the orientation of the lights and of the sensors. Using one single sensor and one light always in the same position/orientation, we can sometimes miss some defaults in the acquisition. So, it seems important to study other kinds of systems to improve the quality of the automatic treatments. Finally, we want to improve the *GaMM* method by adding the extraction of the crack characteristics, like that in *Morph*.

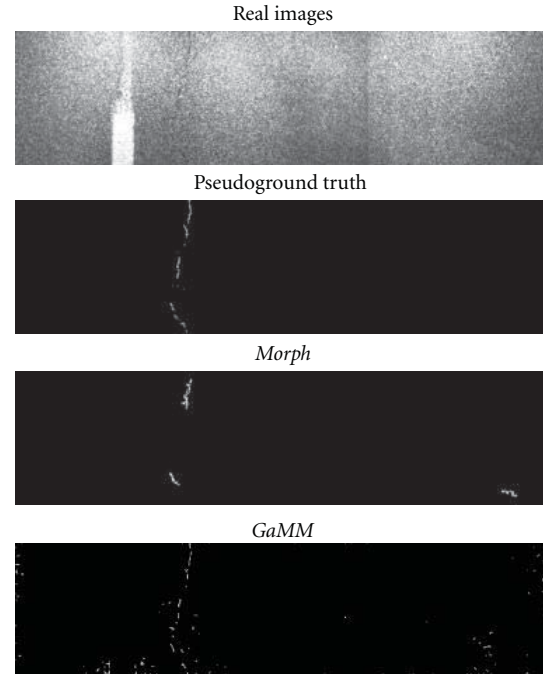


FIGURE 15: The differences between *Morph* and *GaMM*. Examples with real images acquired on a vehicle. The detection with *GaMM* is more complete than the detection with *Morph*.

Endnotes

1. It has been determined from the most recent systems.
2. <http://www.ino.ca/fr-CA/Realisations/Description/projct-p/systeme-laser-mesure-fissures.html>.
3. This separation would be possible based on local statistical analysis around the crack.
4. This maintenance is necessary because the conditions and the systems of acquisition can changed every year, and the road pavement also evolves.
5. It is useful for generating the wavelet family for multi-scale analysis.
6. This hypothesis is realistic for this application.
7. \mathcal{L}^2 is the square integrable space.
8. The choice of k is related to the maximal number of pixels that belong to a crack (it depends on the resolution of images and hypothesis about the size and the configuration of the cracks). We have chosen k in order to consider at most 5% of the image as a crack. Moreover, our experiments have brought us to take $\xi_1 = \xi_2 = 100$.
9. As the sites are of size 3×3 , $d_{\max} = 5\sqrt{2}$.
10. The road is a random texture, that is, each intensity is randomly chosen by supposing a uniform distribution of intensities in $[0; 255]$. Then, the user gives the position of the beginning, the length, and the orientation (vertical, horizontal, or oblique) of the crack. The crack

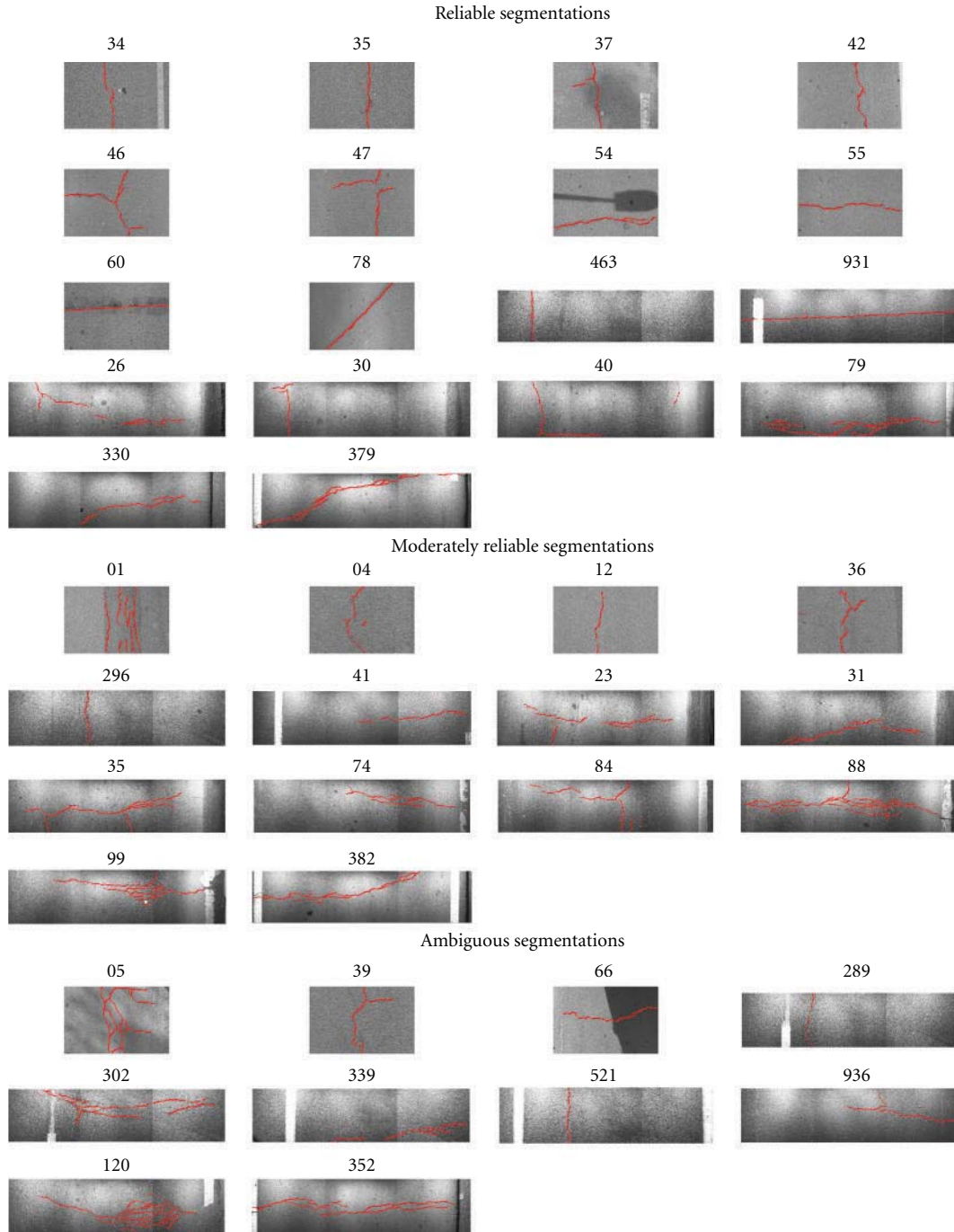


FIGURE 16: The reference segmentations (or pseudoground truth) used in our evaluation protocol for real images. In each original image, the reference segmentation is highlighted in red. Visually, these manual segmentations seem correct and useful for being the reference segmentations in our comparison protocol.

points are built by randomly selecting the next point in the neighborhood and the intensity in $[0; 100]$.

11. We use a “home-made” software that proposes an interface that helps the person to segment the default. The principle is that the user has to select points on the crack. These points have to be close enough (from 5 to 20 pixels of distance). Then, the path between two close points is automatically detected by using a simple heuristic; the

path that minimizes the mean intensity is selected. The interface is complete enough to allow the displacement of the points, and the removing of some points, the removing of some cracks. The user can also select the width of the path (crack). Some filters are also proposed to improve the contrast between the crack and the road in order to help the user.

12. Experimentally, this threshold equals 40.

References

- [1] R. Forest and V. Utsi, "Non destructive crack depth measurements with ground penetrating radar," in *Proceedings of the 10th International Conference Ground Penetrating Radar (GPR '04)*, pp. 799–802, 2004.
- [2] L. D. Payne, "Automating road surface analysis," in *Proceedings of the ACM/SIGAPP Symposium on Applied Computing (SAC '92)*, pp. 944–950, 1992.
- [3] B. Schmidt, "Automated pavement cracking assessment equipment—state of the art," Tech. Rep. 320, Surface Characteristics Technical Committee of the World Road Association (PIARC), 2003.
- [4] Y. Adachi, "Monitoring technologies for maintenance and management of urban highways in Japan—a case of hanshin expressway public corporation," in *Sensing Issues in Civil Structural Health Monitoring*, F. Ansari, Ed., pp. 13–22, Springer, New York, NY, USA, 2005.
- [5] A. Mraz, M. Gunaratne, A. Nazef, and B. Choubane, "Experimental evaluation of a pavement imaging system: Florida department of transportation's multipurpose survey vehicle," *Journal of the Transportation Research Board—Transportation Research Record*, vol. 1974, pp. 97–106, 2006.
- [6] I. Sokolic, "Criteria to evaluate the quality of pavement camera systems in automated evaluation vehicles," Master report, Departement of Civil and Environmental Engineering, College of Engineering, 2003.
- [7] J. J. Acosta, L. Adolfo, and R. L. Mullen, "Low-cost video image processing system for evaluating pavement surface distress," *Journal of the Transportation Research Board—Transportation Research Record*, vol. 1348, pp. 63–72, 1992.
- [8] M. S. Kaseko and S. G. Ritchie, "A neural network-based methodology for pavement crack detection and classification," in *Proceedings of the Annual Meeting of Transportation Research Record*, vol. 1, no. 1, pp. 275–291, 1993.
- [9] H. N. Koutsopoulos and A. B. Downey, "Primitive-based classification of pavement cracking images," *Journal of Transportation Engineering*, vol. 119, no. 3, pp. 402–418, 1993.
- [10] J. Chou, W. A. O'Neill, and H. Cheng, "Pavement distress evaluation using fuzzy logic and moment invariants," *Journal of the Transportation Research Board—Transportation Research Record*, no. 1505, pp. 39–46, 1995.
- [11] A. Georgopoulos, A. Loizos, and A. Flouda, "Digital image processing as a tool for pavement distress evaluation," *ISPRS Journal of Photogrammetry and Remote Sensing*, vol. 50, no. 1, pp. 23–33, 1995.
- [12] S. Jitprasithsiri and H. Lee, "Development of a digital image processing algorithm to compute a unified crack index for salt lake city," in *Proceedings of the Annual Meeting of Transportation Research Record*, 1996, paper 960889.
- [13] D. Meignen, M. Bernadet, and H. Briand, "One application of neural networks for detection of defects using video data bases: identification of road distresses," in *Proceedings of the 8th International Workshop on Database and Expert Systems Applications*, pp. 459–464, 1997.
- [14] H. D. Cheng and M. Miyojim, "Novel system for automatic pavement distress detection," *Journal of Computing in Civil Engineering*, vol. 12, no. 3, pp. 145–152, 1998.
- [15] N. Tanaka and K. Uematsu, "A crack detection method in road surface images using morphology," in *Proceedings of the Workshop on Machine Vision Applications*, pp. 154–157, 1998.
- [16] T. Tomikawa, "A study of road crack detection by the meta-genetic algorithm," in *Proceedings of the IEEE Conference on Africa, AFRICON*, vol. 1, pp. 543–548, 1999.
- [17] J. Zhou, P. Huang, and F.-P. Chiang, "Wavelet-based pavement distress classification," *Journal of the Transportation Research Board—Transportation Research Record*, no. 1940, pp. 89–98, 2005.
- [18] T. Fukuhara, K. Terada, M. Nagao, A. Kasahara, and S. Ichihashi, "Automatic pavement-distress-survey system," *Journal of Transportation Engineering*, vol. 116, no. 3, pp. 280–286, 1990.
- [19] S. A. Guralnick, E. S. Suen, and C. Smith, "Automating inspection of highway pavement surfaces," *Journal of Transportation Engineering*, vol. 119, no. 1, pp. 1–12, 1993.
- [20] K.-M. Chua and L. Xu, "Simple procedure for identifying pavement distresses from video images," *Journal of Transportation Engineering*, vol. 120, no. 3, pp. 412–431, 1994.
- [21] H. C. Rughooputh, S. D. Rughooputh, and J. M. Kinsler, "Automatic inspection of road surfaces," in *Proceedings of the Machine Vision Applications in Industrial Inspection VIII*, SPIE, Ed., vol. 3966, pp. 349–356, 2000.
- [22] J. Pynn, A. Wright, and R. Lodge, "Automatic Identification of cracks in road surfaces," in *Proceedings of the International Conference on Image Processing and Its Applications*, vol. 2, pp. 671–675, 1999.
- [23] C. Rasse, V. Leemans, M.-F. Destain, and J.-C. Verbrugge, "Application of image analysis to the identification and rating of road surface distress," in *Bearing Capacity of Roads, Railways and Airfiels*, A. G. Correia and F. E. Branco, Eds., pp. 61–68, Swets and Zeitlinger, 2002.
- [24] K. C. P. Wang and W. Gong, "Automated pavement distress survey: a review and a new direction," in *Proceedings of the Pavement Evaluation Conference*, pp. 21–25, 2002.
- [25] K. C. P. Wang, G. Li, and W. Gong, "Wavelet-based pavement distress image edge detection with "À trous" algorithm," in *Proceedings of the Annual Meeting of Transportation Research Record*, vol. 2024, pp. 73–81, 2007.
- [26] P. Delagnes and D. Barba, "A markov random field for rectilinear structure extraction in pavement distress image analysis," in *Proceedings of the International Conference on Image Processing*, vol. 1, pp. 446–449, 1995.
- [27] S. Chaudhuri, S. Chatterjee, N. Katz, M. Nelson, and M. Goldbaum, "Detection of blood vessels in retinal images using two-dimensional matched filters," *IEEE Transactions on Medical Imaging*, vol. 8, no. 3, pp. 263–269, 1989.
- [28] D. Geman and B. Jedynak, "An active testing model for tracking roads in satellite images," *IEEE Transactions on Pattern Analysis and Machine Intelligence*, vol. 18, no. 1, pp. 1–14, 1996.
- [29] C. Scheffy and E. Diaz, "Asphalt concrete fatigue crack monitoring and analysis using digital image analysis techniques," in *Proceedings of the Accelerated Pavement Testing International Conference*, 1999.
- [30] D. S. Mahler, Z. B. Kharoufa, E. K. Wong, and L. G. Shaw, "Pavement distress analysis using image processing techniques," *Microcomputers in Civil Engineering*, vol. 6, no. 1, pp. 1–14, 1991.
- [31] E. Teomete, V. R. Amin, H. Ceylan, and O. Smadi, "Digital image processing for pavement distress analyses," in *Proceedings of the Mid-Continent Transportation Research Symposium*, p. 13, 2005.
- [32] D. Darwin, M. N. Abou-Zeid, and K. W. Ketcham, "Automated crack identification for cement paste," *Cement and Concrete Research*, vol. 25, no. 3, pp. 605–616, 1995.
- [33] H. Elbehiery, A. Hefnawy, and M. Elewa, "Surface defects detection for ceramic tiles using image processing and morphological techniques," in *Proceedings of the World Academy of*

- Science, Engineering and Technology (PWASET '05)*, vol. 5, pp. 158–162, 2005.
- [34] C. Bhagvati, M. M. Skolnick, and D. A. Brivas, "Gaussian normalization of morphological size distributions for increasing sensitivity to texture variations and its application to pavement distress classification," in *Proceedings of the IEEE Computer Society Conference on Computer Vision and Pattern Recognition*, pp. 700–703, 1994.
- [35] M. Coster and J.-L. Chermant, "Image analysis and mathematical morphology for civil engineering materials," *Cement and Concrete Composites*, vol. 23, no. 2, pp. 133–151, 2001.
- [36] A. Ito, Y. Aoki, and S. Hashimoto, "Accurate extraction and measurement of fine cracks from concrete block surface image," in *Proceedings of the Annual Conference of the Industrial Electronics Society*, vol. 3, pp. 2202–2207, 2002.
- [37] S. Iyer and S. K. Sinha, "A robust approach for automatic detection and segmentation of cracks in underground pipeline images," *Image and Vision Computing*, vol. 23, no. 10, pp. 921–933, 2005.
- [38] H. Oliveira and P. L. Correia, "Automatic road crack segmentation using entropy and image dynamic thresholding," in *Proceedings of the European Signal Processing Conference*, 2009.
- [39] H. Oliveira and P. L. Correia, "Supervised strategies for cracks detection in images of road pavement flexible surfaces," in *Proceedings of the European Signal Processing Conference*, 2008.
- [40] H. Oliveira and P. L. Correia, "Identifying and retrieving distress images from road pavement surveys," in *Proceedings of the 1st Workshop on Multimedia Information Retrieval: New Trends and Challenges, International Conference on Image Processing*, 2008.
- [41] J. Chou and H. D. Cheng, "Pavement distress classification using neural networks," in *Proceedings of the IEEE Transactions on Systems, Man and Cybernetics*, vol. 1, pp. 397–401, 1994.
- [42] C.-J. Hsu, C.-F. Chen, C. Lee, and S.-M. Huang, "Airport pavement distress image classification using moment invariant neural network," in *Proceedings of the Asian Conference on Remote Sensing*, vol. 1, pp. 216–220, 2001.
- [43] I. Abdel-Qader, O. Abudayyeh, and M. E. Kelly, "Analysis of edge-detection techniques for crack identification in bridges," *Journal of Transportation Engineering*, vol. 17, no. 4, pp. 255–263, 2003.
- [44] C. Boukouvalas, F. De Natale, G. De Toni et al., "ASSIST: automatic system for surface inspection and sorting of tiles," *Journal of Materials Processing Technology*, vol. 82, no. 1, pp. 179–188, 1998.
- [45] S. Chambon, P. Subirats, and J. Dumoulin, "Introduction of a wavelet transform based on 2d matched filter in a markov random field for fine structure extraction: application on road crack detection," in *Proceedings of the IS&T/SPIE Electronic Imaging—Image Processing: Machine Vision Applications II*, 2009.
- [46] P. Subirats, J. Dumoulin, V. Legeay, and D. Barba, "Automation of pavement surface crack detection with a matched filtering to define the mother wavelet function used," in *Proceedings of the European Signal Processing Conference*, 2006.
- [47] C.-X. Ma, "Pavement distress detection based on nonsampled contourlet transform," in *Proceedings of the International Conference on Computer Science and Software Engineering (CSSE '08)*, pp. 28–31, 2008.
- [48] F. S. Abas and K. Martinez, "Classification of painting cracks for content-based analysis," in *Proceedings of the SPIE, Annual Symposium Electronic Imaging: Machine Vision Applications in Industrial Inspection XI*, vol. 5011, pp. 149–160, 2003.
- [49] B. Augereau, B. Tremblais, M. Khoudeir, and V. Legeay, "A differential approach for fissures detection on road surface images," in *Proceedings of the International Conference on Quality Control by Artificial Vision*, 2001.
- [50] N. Nishimura and S. Kobayashi, "A boundary integral equation for an inverse problem related to crack detection," *International Journal for Numerical Methods in Engineering*, vol. 32, no. 7, pp. 1371–1387, 1991.
- [51] H. Lee and H. Oshima, "New crack-imaging procedure using spatial autocorrelation function," *Journal of Transportation Engineering*, vol. 120, no. 2, pp. 206–228, 1994.
- [52] J. Shirataki and T. Tomikawa, "A study of road crack detection by image processing," Part B. Science and Technology 24, pp. 67–71, Kanagawa Institute of Technology, 2000.
- [53] M. Petrou, J. Kittler, and K. Y. Song, "Automatic surface crack detection on textured materials," *Journal of Materials Processing Technology*, vol. 56, no. 1–4, pp. 158–167, 1996.
- [54] K. Y. Song, M. Petrou, and J. Kittler, "Wigner based crack detection in textured images," in *Proceedings of the International Conference on Image Processing and Its Applications*, pp. 315–318, 1992.
- [55] T. S. Nguyen, M. Avila, S. Begot, F. Duculty, and J.-C. Bardet, "Automatic detection and classification of defect on road pavement using anisotropy measure," in *Proceedings of the European Signal Processing Conference*, pp. 617–621, 2009.
- [56] S. Chambon, "Detection of points of interest for geodesic contours: application on road images for crack detection," in *Proceedings of the International Conference on Computer Vision Theory and Applications (VISAPP '11)*, Algarve, Portugal, 2011.
- [57] H. D. Cheng, J.-R. Chen, C. Glazier, and Y. G. Hu, "Novel approach to pavement cracking detection based on fuzzy set theory," *Journal of Computing in Civil Engineering*, vol. 13, no. 4, pp. 270–280, 1999.
- [58] Y. Huang and B. Xu, "Automatic inspection of pavement cracking distress," *Journal of Electronic Imaging*, vol. 15, no. 1, 2006.
- [59] D. H. Kil and F. B. Shin, "Automatic road-distress classification and identification using a combination of hierarchical classifiers and expert systems-subimage and object processing," in *Proceedings of the International Conference on Image Processing*, vol. 2, pp. 414–417, 1997.
- [60] K. R. Kirschke and S. A. Velinsky, "Histogram-based approach for automated pavement-crack sensing," *Journal of Transportation Engineering*, vol. 118, no. 5, pp. 700–710, 1992.
- [61] H. N. Koutsopoulos and I. El Sanhoury, "Methods and algorithms for automated analysis of pavement images," *Journal of the Transportation Research Board—Transportation Research Record*, vol. 1311, pp. 103–111, 1991.
- [62] H. G. Zhang and Q. Wang, "Use of artificial living system for pavement distress survey," in *Proceedings of the Annual Conference of the IEEE Industrial Electronics Society*, pp. 2486–2490, 2004.
- [63] J. Bray, B. Verma, X. Li, and W. He, "A neural network based technique for automatic classification of road cracks," in *Proceedings of the International Joint Conference on Neural Networks*, pp. 907–912, 2006.
- [64] D. Corso, R. Fioravanti, and S. Fioravanti, "Morphological analysis of textured images for identification of thin structures," in *Proceedings of the 20th International Conference on Acoustics, Speech, and Signal Processing*, vol. 4, pp. 2359–2362, 1995.

- [65] S. G. Ritchie, M. Kaseko, and B. Bavarian, "Development of an intelligent system for automated pavement evaluation," *Journal of the Transportation Research Board—Transportation Research Record*, vol. 1311, pp. 112–119, 1991.
- [66] H. D. Cheng, X. Jiang, J. Li, and C. Glazier, "Automated real-time pavement distress analysis," *Journal of the Transportation Research Board—Transportation Research Record*, vol. 1655, pp. 55–64, 1998.
- [67] J. Dumoulin, P. Subirats, V. Legay et al., "Progressive automation of pavement surface distress by imaging techniques," in *Proceedings of the Final Seminar of the 11A025 Research Project*, 2005.
- [68] M. Mustaffara, T. C. Ling, and O. C. Puan, "Automated Pavement Imaging Program (APIP) for pavement cracks classification and quantification—a photogrammetric approach," in *Proceedings of the Congress of the International Society for Photogrammetry and Remote Sensing*, vol. WG IV/3, 2008.
- [69] S. Sorncharean, "Crack detection on asphalt surface image using enhanced grid cell analysis," in *Proceedings of the 4th IEEE International Symposium on Electronic Design, Test and Applications*, pp. 49–54, 2008.
- [70] N. Coudray, A. Karathanou, and S. Chambon, "Multi-resolution approach for fine structure extraction—application and validation on road images," in *Proceedings of the 5th International Conference on Computer Vision Theory and Applications (VISAPP '10)*, 2010.
- [71] B. Tremblais and B. Augereau, "A fast multi-scale edge detection algorithm," *Pattern Recognition Letters*, vol. 25, no. 6, pp. 603–618, 2004.
- [72] S. Chambon, "Detection of road cracks with multiple images," in *Proceedings of the 5th International Conference on Computer Vision Theory and Applications (VISAPP '10)*, 2010.
- [73] S. Chambon, C. Gourraud, J.-M. Moliard, and P. Nicolle, "Road crack extraction with adapted filtering and markov model-based segmentation—introduction and validation," in *Proceedings of the 5th International Conference on Computer Vision Theory and Applications (VISAPP '10)*, 2010.

Research Article

Noninvasive Remote Sensing Techniques for Infrastructures Diagnostics

Angelo Palombo,¹ Stefano Pignatti,¹ Angela Perrone,¹ Francesco Soldovieri,² Tony Alfredo Stabile,³ and Simone Pascucci¹

¹ *Consiglio Nazionale delle Ricerche, Istituto di Metodologie per l'Analisi Ambientale (IMAA), 85050 Tito Scalo, Italy*

² *Consiglio Nazionale delle Ricerche, Istituto per il Rilevamento Elettromagnetico dell'Ambiente (IREA), 80127 Naples, Italy*

³ *Dipartimento di Scienze Fisiche, Università degli Studi di Napoli Federico II, 80126 Naples, Italy*

Correspondence should be addressed to Angelo Palombo, palombo@imaa.cnr.it

Received 15 February 2011; Revised 15 April 2011; Accepted 25 May 2011

Academic Editor: Nicola Masini

Copyright © 2011 Angelo Palombo et al. This is an open access article distributed under the Creative Commons Attribution License, which permits unrestricted use, distribution, and reproduction in any medium, provided the original work is properly cited.

The present paper aims at analyzing the potentialities of noninvasive remote sensing techniques used for detecting the conservation status of infrastructures. The applied remote sensing techniques are ground-based microwave radar interferometer and InfraRed Thermography (IRT) to study a particular structure planned and made in the framework of the ISTIMES project (funded by the European Commission in the frame of a joint Call "ICT and Security" of the Seventh Framework Programme). To exploit the effectiveness of the high-resolution remote sensing techniques applied we will use the high-frequency thermal camera to measure the structures oscillations by high-frequency analysis and ground-based microwave radar interferometer to measure the dynamic displacement of several points belonging to a large structure. The paper describes the preliminary research results and discusses on the future applicability and techniques developments for integrating high-frequency time series data of the thermal imagery and ground-based microwave radar interferometer data.

1. Introduction

During the last decades, the advances in nondestructive electromagnetic sensing techniques (optical, thermal, and microwave) operating at different spectral, spatial and time scales make a multidepth, multiresolution and multiscale diagnostics and monitoring activities thus to be used for the status assessment of existing structures [1].

These nondestructive techniques are primarily suited for the detection and characterisation of alterations and defects in the near surface of structures [2] and for the displacement monitoring and verification of the structural integrity of buildings and structures [3, 4].

As regards the sensing techniques used for this study, the thermal camera technology is a non-destructive investigation technique commonly used in different applications and in particular in the infrastructures and architectural heritage diagnostics [5]. Thermal imagery is used to identify sub-surface ununiformities since the heat flow from the surface

to the inner structure is affected by the defects and inhomogeneities present in the structure. The InfraRed Thermography (IRT) analysis allows diagnostic results ranging from qualitative characterization (e.g., detection) to quantitative analysis (e.g., inhomogeneities characterization). It is worth noting that the application of IRT for detecting and characterizing defects in construction materials can be quite complicated as different physical properties affecting the thermal and optical properties of the structure [6] have to be considered. Among them, the most important are the conductivity, the diffusivity, and the specific heat of the investigated material, whereas the spectral properties such as emissivity, absorption, reflection, and transmission play a key role on the heat distribution in the material. Other properties/characteristics that influence the thermal behaviour of a material are related to its porosity, volumetric mass, and water content.

Furthermore, the use of high-frequency imagery thermal camera gives the opportunity of measuring full field

deformation and vibration characteristics (i.e., frequency and attenuation). From these measurements different modal parameters of the structure (e.g., natural frequencies, mode shapes, and damping ratios) can be extracted and displayed and used for the definition of a baseline set of dynamic characteristics of the structure. This kind of analysis can be subsequently used for the structural health monitoring and the application of vibration-based damage detection techniques (see e.g., [7, 8]).

For the present study, we used high-frequency imagery (HFI) acquisitions for the retrieving of fast displacements and vibrations in the structure.

On the other hand, concerning the microwave interferometry technology applied in this study, it has proven to be a powerful remote sensing tool for vibration measurement of structures [9]. It was recently applied for tracking the vibration of bridges excited by vehicular traffic [8, 10] to monitor the displacements of heritage architectural structures such as the two bell towers,

Giotto's Tower and Arnolfo's Tower, in Florence [11] or the Tower of Pisa [12], for deflection measurements on vibrating stay cables [13], and for in-field dynamic monitoring of engineering structures [4, 14]. All these studies have been carried out by the use of an innovative noncontact microwave interferometer, named IBIS-S (Image By Interferometric Survey of Structures), manufactured by the Italian company IDS S.p.A. This innovative radar system has been also applied for this study and it is based on the Stepped-Frequency Continuous Wave (SF-CW) technique [15] and on the Differential Interferometric technique [16]. The former providing the system with a range resolution capability and the latter allowing the system to evaluate the displacement response of each target detected in the illuminated scenario. IBIS-S sensor is fast and easy to be installed, allowing to operate in all weather conditions, both day and night, even at a significant distance and without the need of installing and wiring sensors. A further advantage obtained by the IBIS-S instrument is the direct measurement of the displacement of a large number of targets simultaneously, in real-time, and with high accuracy.

In this paper, the application of different sensors and methodologies to several noninvasive infrastructures near surface diagnostics is presented. The analysis of acquired data on different structures and materials included also time series recorded by the thermal camera and radar on several points of a test bed cement beam.

2. Data and Methods

2.1. Test Beds. The data for this study were acquired in Montagnole (French Alps) site in an innovative facility owned by LCPC (Laboratoire Central des Ponts et Chaussées), that is one of the ISTIMES partners.

The Montagnole test site is mainly used to certify metallic protection nets that are used in mountains to prevent catastrophic rockslides. For ISTIMES project, it was exploited as a purely research-oriented facility to verify the behaviour of noninvasive sensing techniques during the progressive

damage of an on purpose built concrete beam structure. In particular, the experiment has regarded the progressive damage, in different stages, of a concrete beam by means of falling blocks thus allowing the different techniques to be tested in the presence of hazards.

In the Montagnole experiment an iron ball of 2.5 Tons was used (Figure 1(a)) and for this study we analyze only the four falling actions where the ball has impacted directly on the beam. In particular, drops 1 to 3 have been performed from an altitude of 1 m with respect to the beam and drop 4 from a 5 m of height. The last drop (i.e., number 4) was used to study and diagnose the significant structural damage as induced by a heavy direct impact of the ball onto the armed concrete beam in order to understand the progressive energy release. Therefore, for this experiment, we assumed that such drop rate was convenient to have a refined monitoring of the beam at the beginning and at the end of each daily experiment session.

2.2. Data. For this study we used the following instrumentation for a rapid and noninvasive diagnostic of the infrastructure status. Specifically, as regards the IRT instrumentation, we used a FLIR SC7900-VL thermal camera (LWIR; 7.7–11.5 μm), whereas an IBIS-S microwave radar interferometer operating in the Ku frequency band with a central frequency of 16.75 GHz was used for the microwave interferometry.

The FLIR camera features has a “snap shot” integration range from 10 μs to 10 ms, which incorporates a high quantum efficiency MCT focal plane array thus ensuring a very high-spectral resolution with a Noise Equivalent Temperature Difference (NETD) <25 mK. The frame rates are up to 200 FPS (frames per second) in full frame mode (320×256) and 6000 FPS in subwindowing mode. In this study, we used the following optimal configuration of the LWIR camera: 160×128 frames, thus allowing 800 FPS.

The IBIS-S microwave radar consists of a sensor module installed on a tripod with a 3D rotating head. An USB interface allows the connection with a control PC, which is used to configure the acquisition parameters, to view in real time the first results, and to perform the storage of the measurements. The two horn antennas transmit the electromagnetic signals in the frequency band of 16.75 ± 0.30 GHz and receive the echoes from the target. Sensor module and PC are connected to a battery unit.

IBIS-S system can provide a range resolution of 0.5 m, a displacement sensitivity of 0.01 mm, a maximum operational distance of 500 m, and a maximum sampling frequency of 200 Hz [17].

2.3. Methods

2.3.1. HFI Thermal Imagery. In the survey of measurements on the Montagnole test site, we took advantage of the thermal camera (LWIR) to obtain very high-frequency thermal imagery on the concrete beam during the direct impact of the falling blocks. The FLIR camera was mounted on a tripod at about 40 m (i.e., in box 3) and 70 m (i.e., near box 5) of distance from the beam. Box 3 was used for the first three

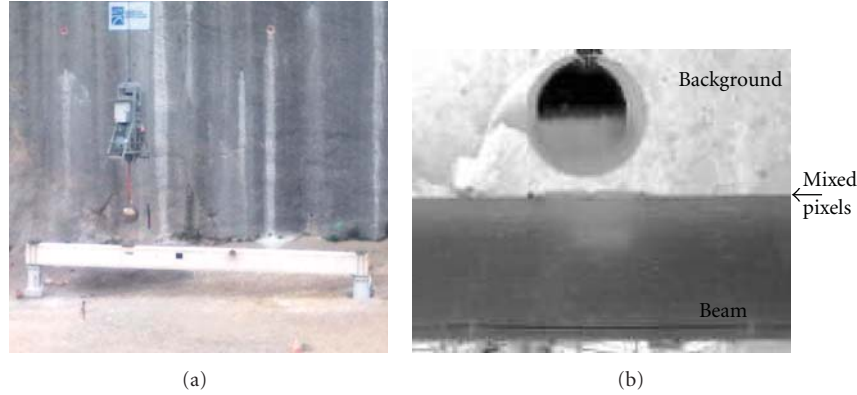


FIGURE 1: (a) Picture of the experimental site with the heavy load (iron ball) suspended at the height of 1 m over the beam. (b) Example of a frame acquired by HFI FLIR camera. The frame depicts the heavy load just before the impact on the concrete beam. The black arrow indicates the mixed pixels (i.e., background and beam) used for calculating the oscillation frequency after the impact.

drops (height of the falling ball of 1 m); for the drop 4 (height of the falling ball of 5 m), due to safety reasons, the camera was installed near the box 5 (70 m). For all the drops, the acquisition time was of 46 s for a total of 37000 frames.

The thermal imagery acquisitions were used to calculate the beam oscillation frequency as derived from the difference between the beam temperature and the background temperature (see Figure 1(b)).

The method is based on the presence of mixed pixels composed by both the beam and the background as shown by the black arrow in Figure 1(b), labelled as *i-pixel*. The *i-pixel* temperature measured by the FLIR camera accounts for the time-varying temperature relative to the beam and the background. The following equations were used to retrieve the beam oscillation:

$$\begin{aligned} c_1 T_b + c_2 T_t &= T_m, \\ c_1 + c_2 &= 1, \end{aligned} \quad (1)$$

where, c_1 and T_b are the fraction of the *i-pixel* occupied by the background and its temperature, respectively; c_2 and T_t are the fraction of the *i-pixel* occupied by the beam and its temperature, respectively. T_m is the temperature measured by the camera for the *i-pixel*.

The first equation of (1) represents the linear mixing of the temperatures of the beam and the background, the second is the constrain used for the total pixel fraction. The T_b and T_t temperatures, which are unknowns in (1), can be extracted from the temperature values of the neighbouring pixels of the *i-pixel*. The neighbouring pixels used for calculating T_b and T_t have to be pure pixels (i.e., made up of only beam or target).

In (1), c_2 represents the oscillation quantity expressed in terms of pixel fraction that varies from 0 to 1. Moreover, when c_2 oscillation reaches values near to the maximum and minimum, this represents situations in which the amplitude of oscillation is close to or greater than the maximum measurable for a pixel, respectively. In the case that a pixel is not sufficient to encompass the oscillation, it is possible to solve the problem by considering, using the sum of

the neighbouring pixels, “equivalent pixels” having a larger dimension compared to the original one.

2.3.2. Ground-Based Microwave Radar Interferometer. IBIS-S is based on two well-known radar techniques: the Stepped-Frequency Continuous Wave (SF-CW) and the Differential Interferometric [12, 18].

The SF-CW technique allows the system to resolve the scenario in the range direction [15, 19], that is, to detect the position of target surfaces placed at different distances from the sensor. It is based on the synthesis and transmission of a burst of N monochromatic pulses equally and incrementally spaced in frequency (with fixed frequency step of Δf) leading to a work bandwidth B :

$$B = (N - 1)\Delta f, \quad (2)$$

The N monochromatic pulses sample the scenario in the frequency domain similarly to a short pulse with a large bandwidth B . In a SF-CW radar, the signal source dwells at each frequency $f_x = f_0 + k\Delta f$ ($k = 0, 1, 2, \dots, N-1$), the single tone signal is sufficiently long to allow the echoes backscattered by the target to reach the receiver. Hence, the duration of each monochromatic pulse (T_{pulse}) depends on the maximum distance (R_{max}) to be observed in the scenario and is given by,

$$T_{\text{pulse}} \geq \frac{2R_{\text{max}}}{c}, \quad (3)$$

where c represents the velocity of the light.

At each sampled time instant, both I (In-phase) and Q (Quadrature) components of the received signals are acquired so that the resulting data consist of a vector of N complex samples, representing the frequency response measured at N discrete frequencies.

By taking the Inverse Discrete Fourier Transform (IDFT) the radar response is reconstructed in the time domain: each complex sample in this domain represents the signal (echo) from a range (distance) interval of length $cT_{\text{pulse}}/2$.

The amplitude range profile of the radar echoes is then obtained by calculating the magnitude of each bin of

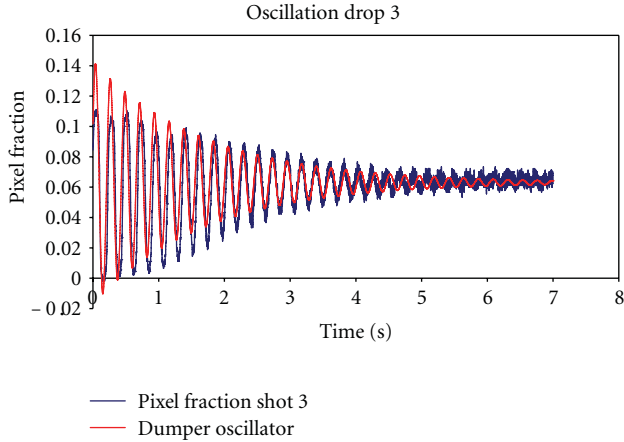


FIGURE 2: The graph shows the under-damping decay attained for the fraction of the i -pixel occupied by the beam (i.e., blue line C_2) used for the Montagnole experiment. Red line depicts the theoretical dumper oscillator calculated from the parameters of Table 1.

the IDFT of acquired vector samples. This range profile gives a one-dimensional mapping of scattering objects in the “view space” as function of their relative distance from the sensor.

The differential interferometric technique allows the system to measure the displacements of the structure illuminated by the antenna main beam by comparing the phase information of the backscattered electromagnetic waves collected at different times (see, e.g., [16]).

Generally speaking, when a target surface moves with respect to the sensor module (emitting and back-receiving the electromagnetic wave) at least a phase shift arises between the signals reflected by the target surface at different times. Hence, the displacement of the investigated object is determined from the phase shift measured by the radar sensor at the discrete acquisition times. The radial displacement d_p (i.e., the displacement along the direction of wave propagation) and the phase shift $\Delta\varphi$ are linked by the following:

$$d_p \propto \frac{\lambda}{4\pi} \Delta\varphi, \quad (4)$$

where λ is the wavelength of the probing electromagnetic signal.

The radar emits a series of electromagnetic waves for the entire measurement period and processes phase information at regular time intervals to find any displacement occurring between one emission and the next one. It is worth underlining that the interferometric technique in (4) provides a measurement of the displacement along the line of sight for all the range bins of the structure illuminated by the antenna beam; once d_p has been evaluated, the vertical displacement d can be easily found by making some geometric projections.

IBIS-S system was applied in both Montagnole and Musmeci test beds. In the first case it was installed on a hill at a height of about 15 m from the ground level and at a distance of about 70 m from the target. In order to improve the accuracy and the signal-to-noise ratio of the measurements, a corner reflector was fixed on the beam. To acquire the

measurements a range sampling frequency of 200 Hz and an acquisition time of about 60 s for each drop were used.

In the Musmeci test bed IBIS-S system was placed just under the bridge deck with a perpendicular direction at a distance of about 30 m. A sampling frequency of about 100 Hz and an acquisition time of about 5 minutes were applied.

In both cases the use of IBIS-S system allowed the dynamic monitoring of the investigated target without any contact between the sensor and the investigated target. This characteristic was very useful in Montagnole test bed where very restricted security conditions were required in order to carry out the experiment.

3. Results and Discussion

3.1. HFI Results. For Montagnole experiment, the drops of the heavy iron ball on the beam were used as mechanical solicitation to measure the dynamic response of the beam. For this study we used a simple model by considering the behaviour of the beam as the one of a damped harmonic oscillator. The equation describing the oscillation is

$$z(t) = A_0 e^{-\zeta\omega_0 t} \sin\left(\sqrt{1 - \zeta^2}\omega_0 t + \varphi\right), \quad (5)$$

where A_0 is the amplitude and φ the phase that dictates the initial conditions, ω_0 is the undamped angular frequency of the oscillator and ζ is damping ratio that are given, respectively, by:

$$\omega_0 = \sqrt{\frac{k}{m}}, \quad (6)$$

$$\zeta = \frac{c}{2m\omega_0},$$

where k is the elastic constant, m is the mass, and c is the viscous damping coefficient.

The value of ζ determines the behaviour of the system in fact, the damped harmonic oscillator can be (a) for $\zeta > 1$, the system is represented by exponentially decays; (b) for $\zeta = 1$, the system returns to equilibrium as quickly as possible without oscillating; (c) for $\zeta < 1$, the system is represented by an underdamped harmonic oscillator (Figure 2).

The quantity that describes the beam oscillation is the c_2 value represented in (1). This value was calculated for all the frames of each acquisition performed on the beam. Figure 2 depicts the comparison between the quantity c_2 (blue line) calculated for the third drop and the theoretical underdamped harmonic oscillator (red line) that approximates the c_2 oscillations. The parameters used for evaluating the underdamped harmonic oscillation, that is, those that better approximates the c_2 oscillation, are reported in Table 1.

Moreover, in order to obtain the resonance frequencies of the beam we applied the Fast Fourier Transform (FFT) on the quantity c_2 evaluated for the four drops. Figure 3 depicts the time behaviour of the c_2 for the four drops, whereas Figure 4 reports the amplitude of the FFT of c_2 . Table 2 shows the oscillation frequencies of the two most significant FFT coefficients.

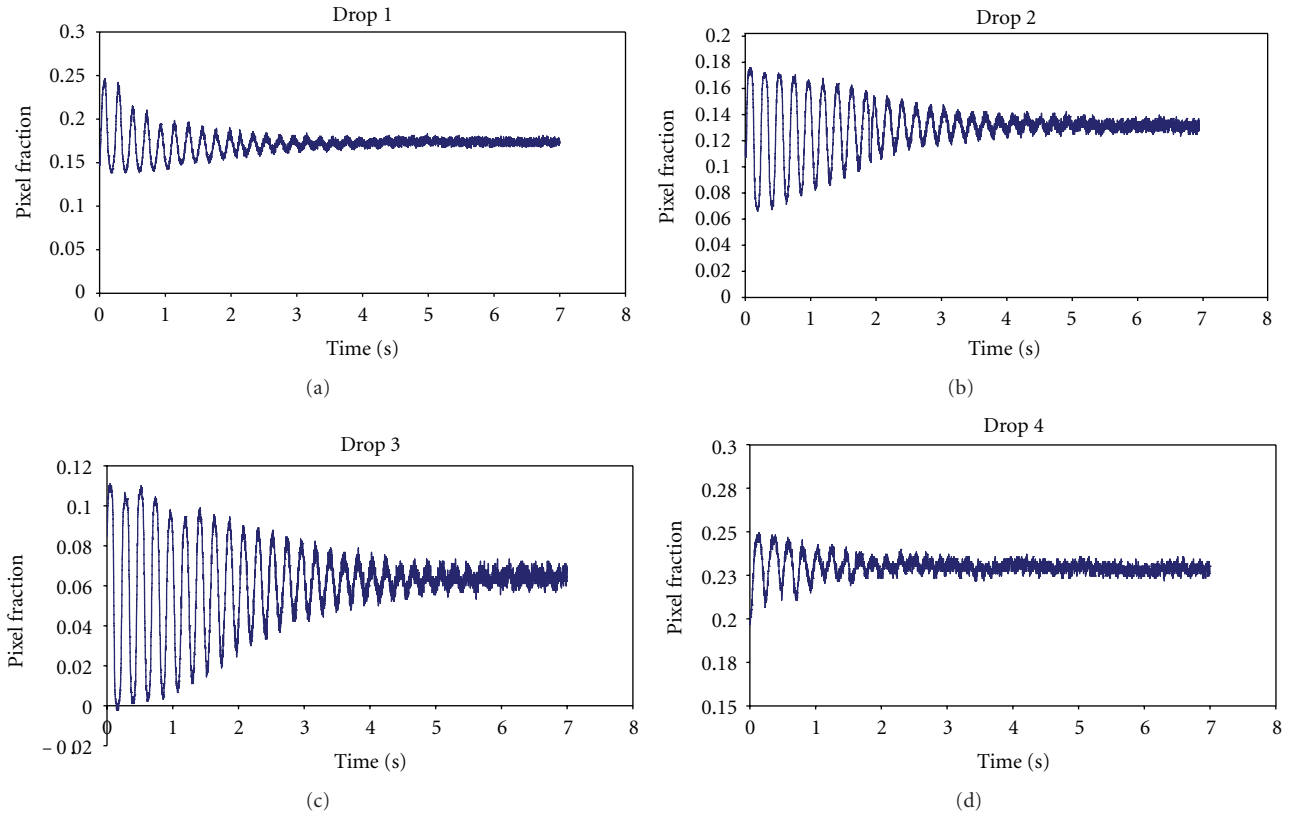


FIGURE 3: The graphs show the underdamped decay attained for the fraction of the i -pixel occupied by the beam used for the four Montagnole drops.

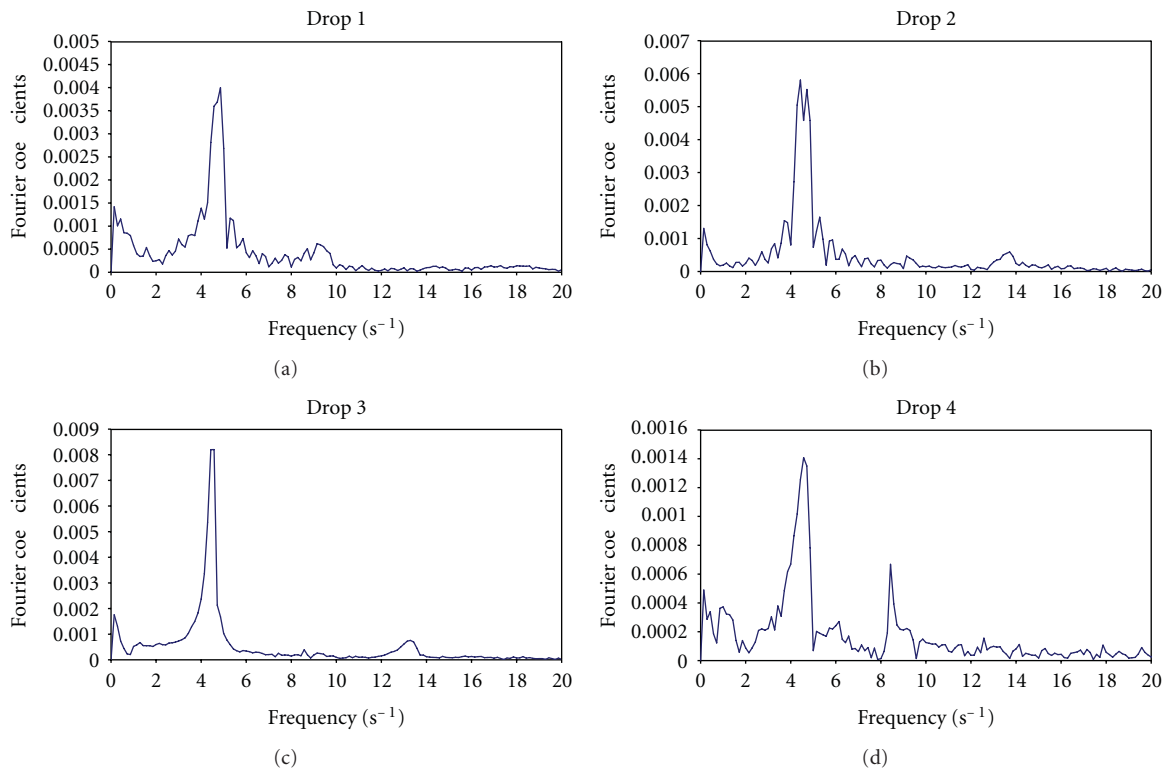


FIGURE 4: FFT absolute coefficients relative to the c_2 oscillations.

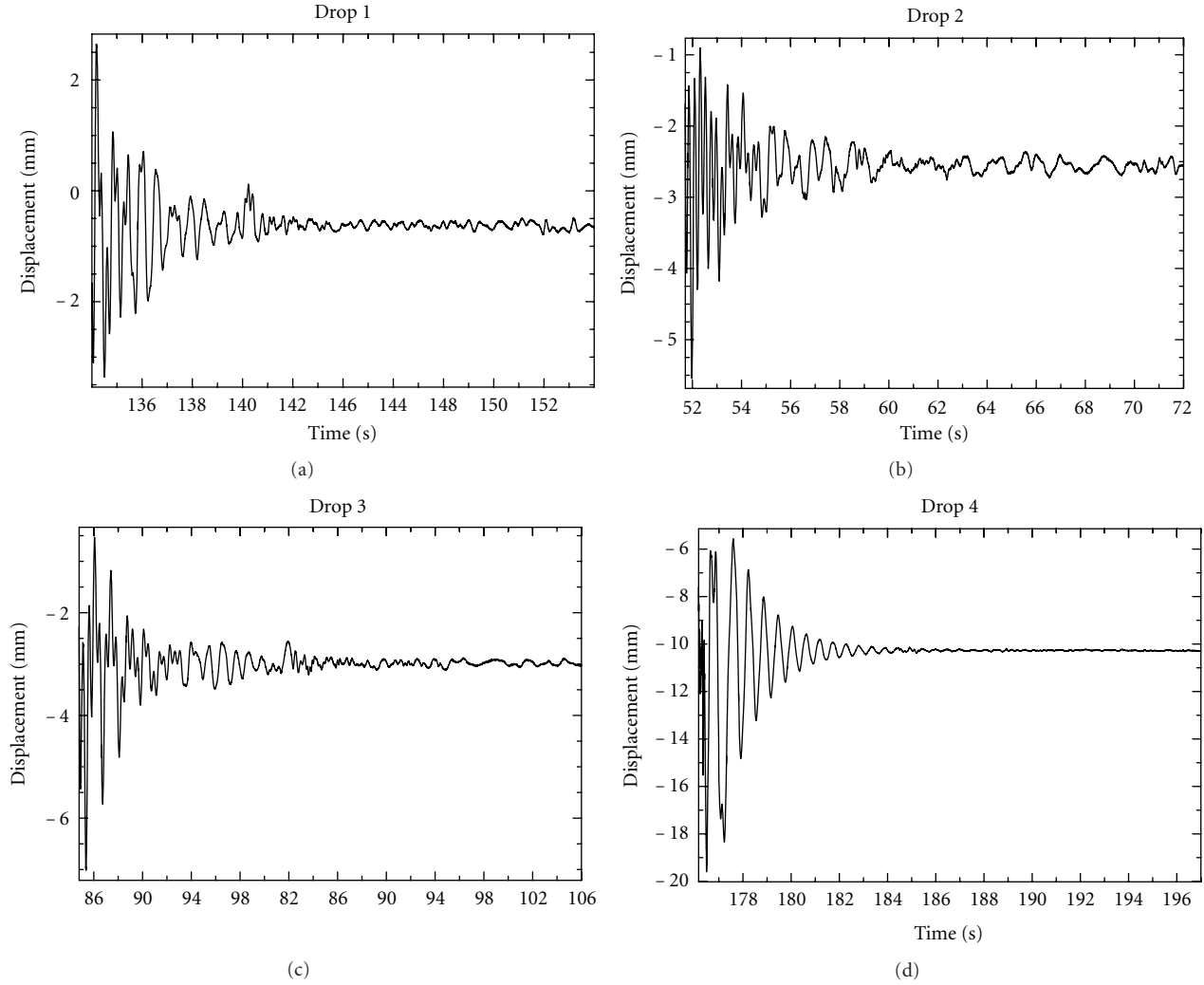


FIGURE 5: The graphs show the time domain response of the beam after each drop. A time window of about 20 s was considered.

TABLE 1: Parameters used for calculating the underdamped harmonic oscillator from (5).

A_0	0.700
φ	1.1
ω_0	28.049
ζ	0.021
Freq.	4.5 Hz

TABLE 2: Significant oscillation frequencies of the beam under the four direct impacts.

Drop	First frequency (Hz)	Secondary frequency (Hz)
1	4.7	9.3
2	4.5	13.7
3	4.5	13.2
4	4.6	8.4

3.2. *Ground-Based Microwave Radar Interferometer Results.* IBIS-S data acquired in Montagnole test site were processed by using the commercial IBIS DATA VIEWER (IBISDV) software. The software works by using MATLAB libraries and is based on (i) Inverse Discrete Fourier Transform (IDFT), and (ii) Differential Interferometric technique.

The IBIS-S results allowed the measure of the dynamic response in time and frequency domain of the beam affected by the direct impact of the heavy iron ball.

Figures 5 and 6 show the response in time and frequency domain of the beam oscillation, due to the direct

impact of the heavy iron ball, for the four drops, respectively.

In the time domain a window of about 20 sec after each direct impact was considered in order to study the dynamic behaviour of the beam. The results show a negative line of sight (LOS) permanent displacement for each drop. In particular, the displacement increases from the first to the last drop as reported in Table 3.

The different LOS permanent displacement could be due to a combination between horizontal and vertical movement of the beam towards the IBIS-S sensor after each drop. This

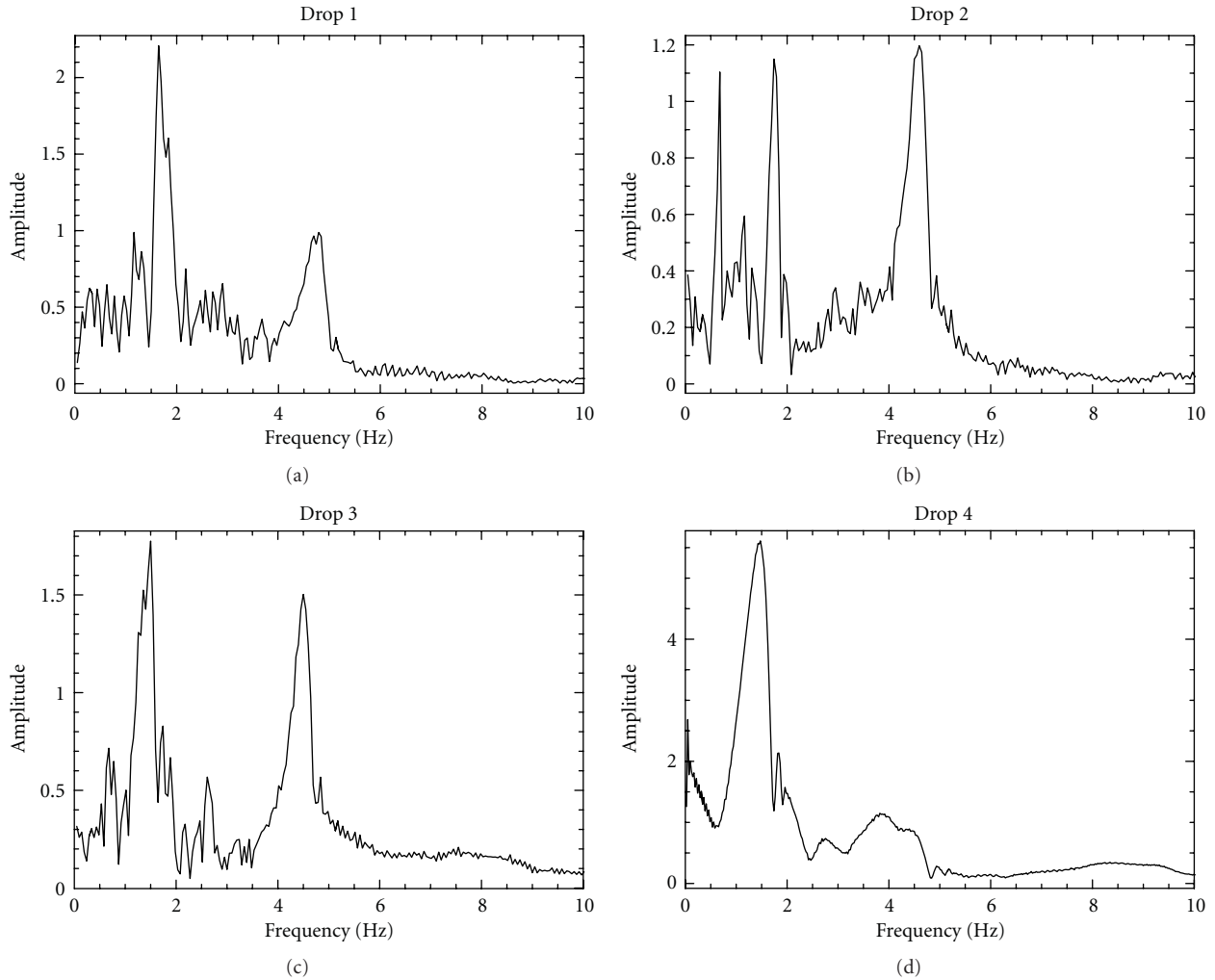


FIGURE 6: The graphs report the frequency domain response of the beam during the four drops, a frequency range up to 10 Hz is considered.

TABLE 3: LOS permanent displacements of the beam after each drop.

Drop number	Permanent displacement (mm)
1	-0.5
2	-2.5
3	-3.0
4	-10.0

displacement is less than 3 mm and grows slightly for the first three drops where the falling block conditions (drop height equal to 1 m) are the same. The permanent displacement is amplified after the fourth drop where the iron ball falls from 5 m height.

Before applying the Fourier Transform to the signals of Figure 5, the mean value and the linear trend were removed from the signal in the selected window. The amplitude of the spectra in a frequency range up to 10 Hz is reported in Figure 6. For all the drops, two main resonant peak frequencies arise, the first one at about 1.5 Hz and the second one at about 4.5 Hz. As can be argued from Table 4, both

TABLE 4: Oscillation frequencies of the beam under the four direct impacts measured by Ground-based microwave radar interferometer.

Drop	First frequency (Hz)	Secondary frequency (Hz)
1	1.6	4.8
2	1.6	4.6
3	1.4	4.5
4	1.4	3.8

the main resonant peak frequencies decrease after any direct impact of the iron ball on the beam.

4. Conclusions

The proposed multitechniques approach, which is the main aim of the ISTIMES Project, can be useful to individuate suitable parameters which will allow a continuous and/or rapid remote control of the condition of infrastructures to plan appropriate interventions for their conservation. This is even more important when analyzing complex structures

TABLE 5: Comparison between the oscillation frequencies measured by HFI and GB microwave Radar with the relative percentage difference.

Drop	HFI (HZ)	GB microwave radar (Hz)	Relative percentage difference
1	4.7	4.8	2.1
2	4.5	4.6	2.2
3	4.5	4.5	0.0
4	4.6	3.8	17.4

where the use of a single diagnostic tool can provide results leading to ambiguous interpretations.

However, it is difficult to have at disposal a complete setup of instruments measuring the same parameter, for example, as in this case where HFI thermal imagery and ground-based (G-B) microwave radar were applied to study the dynamic behaviour of a beam affected by changeable strains.

G-B microwave radar was applied with the aim of measuring the dynamic displacement of the beam. This technique provided good results, giving information about the behaviour of the target investigated in time and frequency domains. In particular, it allowed the estimation of the displacement affecting the beam after each drops and the measurement of the main frequencies characterizing the structure. Two main peaks at different frequencies were highlighted; both the frequencies decrease after the two last drops due to the increase of the number of severe cracks observed on the beam. The cracks damaging the beam have induced a loss of stiffness with a consequent raise of the period of the eigen modes and a decrease of the eigen-frequencies.

HFI thermal imagery camera was applied with the aim of measuring the structure oscillations by high frequency analysis. Also in this case, the results allowed to discriminate two main peaks at different frequencies after each drop. The first peak measured by HFI at around 4.5 Hz is comparable with the second peak measured by G-B radar. However, HFI frequencies do not highlight a decrease after the last drop as well as the G-B results (see Table 5). This could be explained considering the different line of view of the two techniques; indeed, G-B microwave radar was placed at a different height respect to the HFI camera and it observed the beam by a specific angle. HFI thermal camera was placed at the same height of the beam and it observed the target perpendicularly. Moreover, the information provided by G-B microwave radar is related to displacement of the beam along the line of sight, while the information from HFI camera is related to the displacement of the beam in the plane perpendicular to the sensor. The comparison between HFI and G-B results also suggests that G-B radar better points out the low peak frequencies, whereas the HFI thermal camera highlights the high frequencies.

About the lowest frequencies retrieved by G-B radar (see Table 4), two possible explanation could be given as: a vibration mode of the beam or the main oscillation frequency of dropping machinery after each drop.

Future work will be focused on (a) laboratory and field measurements to better understand the different results attained by the HFI and GB microwave Radar (b) a numerical modelling of the beam to estimate its main frequencies, and (c) the development and analysis of the integration of the data acquired by different sensor technologies on infrastructures in order to evaluate their effectiveness and suitability for this kind of application.

Acknowledgment

The research leading to these results has received funding from the European Community's Seventh Framework Programme (FP7/2007–2013) under Grant Agreement no. 225663 Joint Call FP7-ICT-SEC-2007-1.

References

- [1] C. Kohl, M. Krause, C. Maierhofer, K. Mayer, J. Wöstmann, and H. Wiggerhauser, "3D-visualisation of NDT data using a data fusion technique," *Insight*, vol. 45, no. 12, pp. 800–804, 2003.
- [2] Ch. Maierhofer, R. Arndt, M. Röllig et al., "Application of impulse-thermography for non-destructive assessment of concrete structures," *Cement and Concrete Composites*, vol. 28, no. 4, pp. 393–401, 2006.
- [3] M. Proto, M. Bavusi, R. Bernini et al., "Transport infrastructure surveillance and monitoring by electromagnetic sensing: the ISTIMES project," *Sensors*, vol. 10, no. 12, pp. 10620–10639, 2010.
- [4] S. Rödelsperger, G. Läufer, C. Gerstenecker, and M. Becker, "Monitoring of displacements with ground-based microwave interferometry: IBIS-S and IBIS-L," *Journal of Applied Geodesy*, vol. 4, no. 1, pp. 41–54, 2010.
- [5] J. R. Brown and H. R. Hamilton, "Quantitative infrared thermography inspection for FRP applied to concrete using single pixel analysis," *Construction and Building Materials*. In press.
- [6] S. Pascucci, C. Bassani, A. Palombo, M. Poscolieri, and R. Cavalli, "Road asphalt pavements analyzed by airborne thermal remote sensing: preliminary results of the venice highway," *Sensors*, vol. 8, no. 2, pp. 1278–1296, 2008.
- [7] S. W. Doebling, C. R. Farrar, M. B. Prime, and D. Shevitz, *Damage identification and health monitoring of structural and mechanical systems from changes in their vibration characteristics: a literature review*, Los Alamos National Laboratory, 1996.
- [8] C. Gentile and G. Bernardini, "Output-only modal identification of a reinforced concrete bridge from radar-based measurements," *NDT and E International*, vol. 41, no. 7, pp. 544–553, 2008.
- [9] C. R. Farrar, T. W. Darling, A. Migliori, and W. E. Baker, "Microwave interferometers for non-contact vibration measurements on large structures," *Mechanical Systems and Signal Processing*, vol. 13, no. 2, pp. 241–253, 1999.
- [10] M. Pieraccini, F. Parrini, M. Fratini, C. Atzeni, P. Spinelli, and M. Micheloni, "Static and dynamic testing of bridges through microwave interferometry," *NDT and E International*, vol. 40, no. 3, pp. 208–214, 2007.
- [11] M. Pieraccini, M. Fratini, D. Dei, and C. Atzeni, "Structural testing of Historical Heritage Site Towers by microwave remote sensing," *Journal of Cultural Heritage*, vol. 10, no. 2, pp. 174–182, 2009.

- [12] C. Atzeni, A. Bicci, D. Dei, M. Fratini, and M. Pieraccini, "Remote survey of the leaning tower of pisa by interferometric sensing," *IEEE Geoscience and Remote Sensing Letters*, vol. 7, no. 1, Article ID 5290014, pp. 185–189, 2010.
- [13] C. Gentile, "Application of microwave remote sensing to dynamic testing of stay-cables," *Remote Sensing*, vol. 2, no. 1, pp. 36–51, 2010.
- [14] M. Pieraccini, F. Parrini, M. Fratini, C. Atzeni, and P. Spinelli, "In-service testing of wind turbine towers using a microwave sensor," *Renewable Energy*, vol. 33, no. 1, pp. 13–21, 2008.
- [15] J. D. Taylor, Ed., *Ultra-Wideband Radar Technology*, CRC Press, 2001.
- [16] F. M. Henderson and A. J. Lewis, Eds., *Manual of Remote Sensing. Principles and Applications of Imaging Radar*, John Wiley & Sons, New York, NY, USA, 1998.
- [17] C. Gentile and G. Bernardini, "An interferometric radar for non-contact measurement of deflections on civil engineering structures: laboratory and full-scale tests," *Structure and Infrastructure Engineering*, vol. 6, no. 5, pp. 521–534, 2010.
- [18] G. Bernardini, G. De Pasquale, A. Bicci et al., "Microwave interferometer for ambient vibration measurement on civil engineering structures: 1. Principles of the radar technique and laboratory tests," in *Experimental Vibration Analysis for Civil Engineering Structures (EVACES '07)*, Porto, Portugal, October 2007.
- [19] M. Pieraccini, M. Fratini, F. Parrini, G. Macaluso, and C. Atzeni, "High-speed CW step-frequency coherent radar for dynamic monitoring of civil engineering structures," *Electronics Letters*, vol. 40, no. 14, pp. 907–908, 2004.

Research Article

Road Networks Winter Risk Estimation Using On-Board Uncooled Infrared Camera for Surface Temperature Measurements over Two Lanes

M. Marchetti,¹ M. Moutton,¹ S. Ludwig,¹ L. Ibos,² V. Feuillet,² and J. Dumoulin³

¹ CETE de l'Est-ERA 31, 71 rue de la Grande Haie, Tomblaine 54510, Nancy, France

² CERTES, Université Paris-Est, 61 avenue du Général de Gaulle, 94010 Créteil Cedex, France

³ IFSTTAR, Université Nantes Angers Le Mans, Route de Bouaye, CS4, 44344 Bouguenais Cedex, France

Correspondence should be addressed to M. Marchetti, mario.marchetti@developpement-durable.gouv.fr

Received 18 February 2011; Revised 17 May 2011; Accepted 18 May 2011

Academic Editor: Nicola Masini

Copyright © 2011 M. Marchetti et al. This is an open access article distributed under the Creative Commons Attribution License, which permits unrestricted use, distribution, and reproduction in any medium, provided the original work is properly cited.

Thermal mapping has been implemented since the late eighties to establish the susceptibility of road networks to ice occurrence with measurements from a radiometer and some atmospheric parameters. They are usually done before dawn during wintertime when the road energy is dissipated. The objective of this study was to establish if an infrared camera could improve the determination of ice road susceptibility, to build a new winter risk index, to improve the measurements rate, and to analyze its consistency with seasons and infrastructures environment. Data analysis obtained from the conventional approved radiometer sensing technique and the infrared camera has shown great similarities. A comparison was made with promising perspectives. The measurement rate to analyse a given road network could be increased by a factor two.

1. Introduction

Thermal mapping, invented in the seventies, has been implemented since the late eighties to measure road pavement temperature along with some other atmospheric parameters to establish the susceptibility of road network to ice occurrence [1–11]. Measurements are mainly done using a vehicle circulating on the road network in given road weather conditions (clear weather, cloudy, wet pavement, etc.), though the dry pavement is the most common situation. These measurements are both used for the determination of a winter risk based on the comparison of road surface temperature with dew point over the road network, and as an input for road weather forecast models based on energy balance. If the dew point temperature is below road surface temperature there is a risk of ice occurrence and therefore a loss of grip for circulating vehicles. Some numerical models could be an alternative to determine pavement temperature [12–15] at a local scale, though some measurements will still be necessary to check the relevance and the consistency of these numerical tools.

Road surface temperature is mainly obtained with an infrared radiometer providing measurements at a given spatial frequency whatever the speed of the vehicle was due to its insertion in traffic flow. The device is either installed outside or inside the vehicle. To avoid too much influence of the sun, and to see the thermal behavior of the pavement enhanced, thermal mapping is usually done before dawn during wintertime, that is when the energy accumulated by the road during daytime is mainly dissipated (by radiation, by conduction, and by convection) and before the road structure starts a new cycle. The length of a road network ranges between a few hundred of kilometres and up to several thousands kilometres when it comes to multiple lanes highways and an analysis in the two directions of a road.

This analysis is mainly done when a new road network is built, when some major pavement changes are made, or when modifications in the road surroundings took place that might affect the thermal heat balance. This helps road managers to install sensors to monitor road status on specific locations identified as dangerous, or simply to install specific road signs. A set of road events are collected by the operator

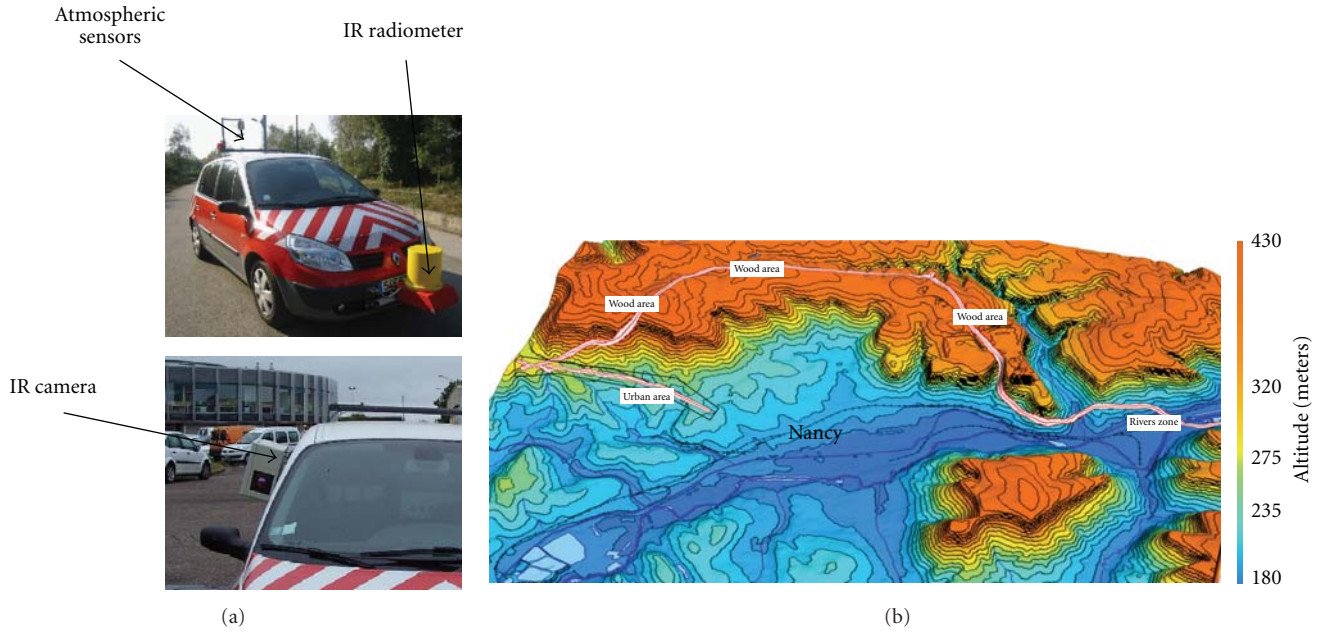


FIGURE 1: Vehicle for thermal mapping (a); map of the road network investigated (from 180 m (blue) to 430 m (red) (b).

(presence of bridges, urban areas, woods on road sides, pavement nature changes, etc.) that might help in the analysis of road thermal response.

Measurements are run at speeds allowed on the road networks, and in our case the maximum speed was 70 km/h. They are anyhow time consuming. Indeed, a whole road network can hardly be analysed at once and has to be partitioned in stretches that could be done in the open time window to avoid temperature artefacts due to a rising sun.

The LRPC Nancy has been using a vehicle for thermal mapping early after the technique appeared. The vehicle is illustrated on Figure 1. Although the whole device has great performances, such radiometer could only analyse one lane at a time. Furthermore, measurements being run before dawn, all road events are usually obtained making measurements during daytime. The road surface temperature obtained is then used to establish a rough cooling speed, aspect not detailed in this work. A map of the road network investigated is also presented in Figure 1 in order to localize urban zones, woods, rivers, some bridges, and so forth, and the type of road (highways, roads, and urban streets).

The objective of this work was to establish if the implementation of an infrared camera on a thermal mapping vehicle could improve the determination of road network susceptibility to ice occurrence. The device would provide the same information as conventional thermal mapping with a radiometer. The field of the camera will embrace several lanes, improving the measurement rate. Such camera could ease the detection and the quantification of transverse thermal gradients between lanes or within a lane. The thermal image would allow analysing the relevance of local specific winter risk. It will allow obtaining information on local thermal behavior of the road surroundings. Some difficulties have to be faced with an infrared camera, such

TABLE 1: Characteristics of PRT5 radiometer.

Detector type	Bolometer detector
Spectral bandwidth	9.5–11.5 μm
Thermal range	–40°C to +70°C
Sensitivity	0.1°C below 0°C, 0.05°C above 0°C
Accuracy	$\pm 0.5^\circ\text{C}$
FOV	20°
Time response	50 ms
NET	0.005°C for a time response of 50 ms on a body at 25°C

as a proper focus over the whole image, the choice of emissivity value of road pavements, though also present with radiometers, the presence of thermal signatures of passing vehicles, and the data volume. The analysis of road surface temperature obtained from the radiometer and the infrared camera has shown great similarities. Comparison was made on an area located between the wheel tracks. Promising perspectives appeared to increase by a factor two the measurement rate to analyse a given road network.

2. Description of the Experimental Devices

2.1. Infrared Radiometer PRT5 and Atmospheric Parameters. The infrared radiometer is a PRT5 from Barnes pyrometer, with a 20° FOV. It was mounted on the front bumper of a car, in a compartment whose temperature is regulated around 18°C. The compartment is located at about 40 cm above the road surface. The characteristics of the radiometer are given in Table 1. In our study, and because of its sensitivity,

TABLE 2: Characteristics of FLIR S65 camera.

Detector type	Microbolometer detector uncooled IRFPA of 320 × 240 sensitive elements
Spectral bandwidth	7.5–13 μm
Thermal range used	−40°C to +120°C
Sensitivity (NETD)	0.08°C
Accuracy	±2% of the measurement
FOV	24° × 18° (H × V) (focal lens 35 mm)
IFOV	1.3 mrad
Image acquisition frequency	Max 1.6 Hz (see text for details)
Video output	Up to 50 Hz non interlaced

its accuracy, and its NET, this radiometer was chosen as a reference for data analysis.

During the measurements, usual atmospheric parameters such as air temperature, relative humidity, and atmospheric pressure were monitored. Measurements were provided by a SSBC probe designed to be installed on moving vehicles, including aircrafts wings [16].

2.2. Infrared Camera FLIR S65 and Thermal Images. A FLIR S65 camera was used. This camera has an uncooled 320 × 240 FPA detector in band III. The camera was installed in a compartment attached to a window on the right side of the vehicle. It was plugged to a computer through an IEEE1394 firewire interface. The camera was turned on at least 30 minutes before starting the measurements to make sure the whole electronic system has reached a thermal equilibrium. The characteristics of the camera are summarized in Table 2.

The camera field of view (FOV) was such that each thermal image would embrace several elements of the scene, from the road pavement and up to the sky. In such configuration, the road is analyzed at a near grazing angle. A diffusive mirror was installed in the FOV of the camera, along with a surface painted with Nextel 811-21, whose emissivity is considered as stable and equal to 0.97 [17]. The Nextel paint could be used for a temperature reference if necessary. Emissivity of the mirror has been determined to 0.063 [18]. The mirror was used for environment radiative corrections. Its position in the FOV of the camera induces a blurring of the edges of the mirror. This mirror was large enough to consider that pixels in the middle could be used for these radiative corrections.

Due to the grazing angle, the measurement area for the infrared camera was located ahead of the radiometer one. There is so a distance offset between the temperature measurements obtained from the radiometer and the one from the infrared camera, data being acquired at the same time. This offset obviously depends on the area of interest selected in the thermal image for further investigation. The farther the area from the front of the vehicle, the greater the offset. In the configuration chosen for the data acquisition,

the distance offset was of 12 m. So as to properly compare data from the infrared radiometer and the camera, the temperature measured by the camera for a given distance d will correspond to the one given by the radiometer for the distance $d + 12$ m.

Thermal images obtained with the camera were analyzed with ThermaCam Researcher 2.9. Several regions of interest (ROI) were defined on the mirror, on the Nextel coating, and on the road pavement. This last one was such that no thermal interference due to circulating vehicles was included in the region of interest. A sketch of the instruments configuration along with an infrared image is given in Figure 2. This value is the distance between the point where the radiometer is making a measurement and the middle of the pavement ROI.

2.3. Data Acquisition. Data acquisition for atmospheric parameters is performed every 3 m with a speed of 70 km/h using a software interface developed under LabVIEW. Pavement emissivity was first supposed to be equal to one and to behave as a black body. A set of road events are collected by the operator (presence of bridges, urban areas, woods on road sides, etc.) that might help in the analysis of road thermal response.

A software interface for data acquisition, also developed under LabVIEW using a specific FLIR SDK toolkit, was made. The code was written to proceed in a snapshot mode for thermal images acquisition. To cope with the camera time integration and limit data transfer, thermal images were only acquired every 12 m, whatever the speed of the vehicle, the speed staying below 70 km/h depending on limits due to traffic and using FLIR native format. This corresponds to a variable time frequency, its maximum being 1.6 Hz, and ease the data treatment because of dense traffic flow. Despite the snapshot function, the microbolometer matrix and the whole electronic part of the infrared camera have an integration time of a few milliseconds. This time caused a slight blur in the thermal images when the vehicle is moving (trace behind object over a few pixels). This aspect is compensated by a choice of ROI whose size exceeds the blur effect. All the atmospheric parameters measured by the different sensors such as air temperature and relative humidity were used as input parameters for the infrared camera when recording thermal images. The software interface is given in Figure 3.

2.4. Road Network Pavement. The road network chosen for the test was almost 30 km long. It included several configurations, from single lane road to multiple lanes highway, passing above and below bridges, with and without trees on the roadside. Measurements were run without sun radiation to avoid artefacts, with a light cloud cover. The vehicle remained in the right lane when the driving was done on highway. A large distance with the vehicle right before was maintained to avoid its thermal signature.

In such a configuration, there were many variations in the materials that could be used for road pavement manufacturing. Furthermore, due to aging pavement and repairs, a wide variety of situations were met along these 30 km. Therefore, a fixed and constant emissivity value could hardly

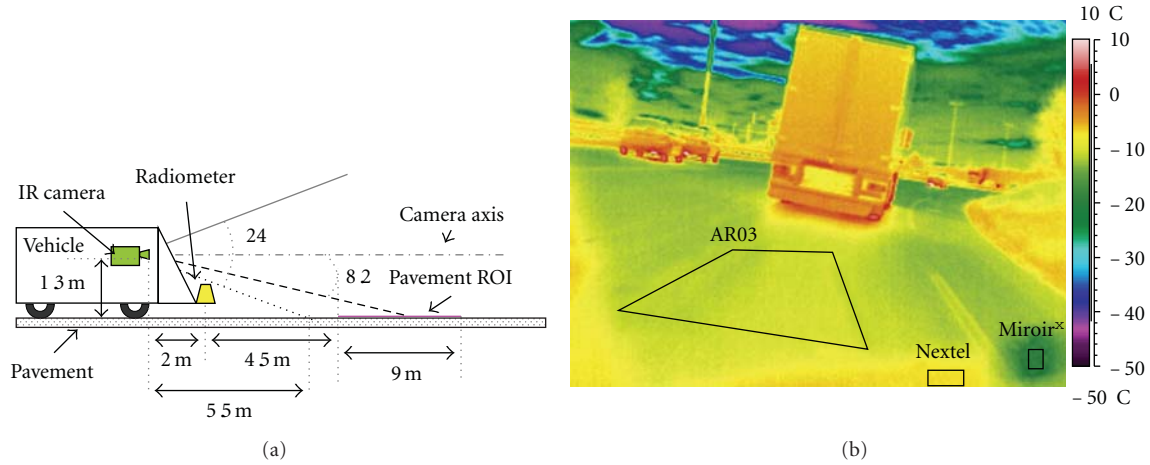


FIGURE 2: Sketch of instruments configuration (a) and thermal image from the vehicle with ROI (b).

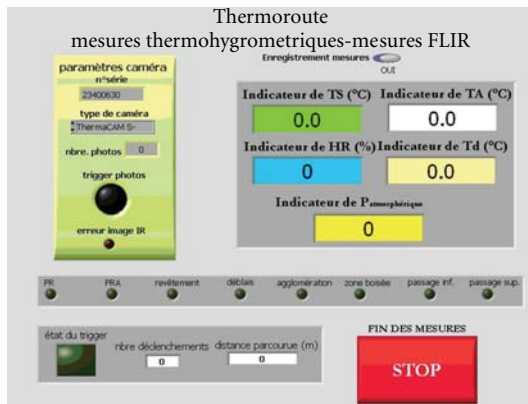


FIGURE 3: Software interface for data acquisition with atmospheric and infrared parameters.

be defined. The pavement emissivity could be considered as close to 1 for measurement close to the normal of the surface [17, 19]. Based on the literature [20–22], the emissivity decreases when the observation angle gets closer to 90° (with respect to the normal of the analysed surface). Nevertheless, considering the specularity of the pavement materials and the grazing angle, a correction is expected if a large difference is observed between radiometer and infrared camera data.

3. Results and Discussion

3.1. Thermal Mapping Improvement with the Infrared Camera. Pavement temperatures obtained with the infrared radiometer along with the ones from the camera were strongly different before any treatment and environment corrections. The camera temperatures were significantly colder. Nevertheless, the pavement temperature profiles were equivalent. Furthermore, in both cases, major elements of the road environment such as bridges were properly detected by both instruments. The thermal amplitude of surface temperature was larger with the camera (11°C) than it was with the radiometer (6°C).

The radiance balance of the whole system could be written as

$$L_{\text{measured}} = \tau_{\text{atmosphere}} \cdot \varepsilon_{\text{pavement}} \cdot L_{\text{pavement}} + \tau_{\text{atmosphere}} \cdot (1 - \varepsilon_{\text{pavement}}) \cdot L_{\text{environment}} + (1 - \tau_{\text{atmosphere}}) \cdot L_{\text{atmosphere}} \quad (1)$$

with τ being the atmospheric transmission coefficient [0 to 1] and L the radiance in $\text{W} \cdot \text{m}^{-2} \cdot \text{sr}^{-1}$ and ε being the emissivity [0 to 1].

In the chosen configuration the distance between the road and the infrared camera is around a few tens of meters for the most distant point where a measurement is done. Neither clouds, nor fog were present during the measurements. The atmospheric transmission coefficient $\tau_{\text{atmosphere}}$ was then considered as equal to one. The transmission attenuation due to relative humidity of atmosphere and of its other component could therefore be neglected [21–23].

The radiance from the environment was obtained thanks to the mirror installed in the field of view of the infrared camera. All bodies in the environment of the thermal scene are considered as emitting infrared radiation as blackbodies. Thus, the radiance measured on the diffusive mirror surface allows computing a mean radiant temperature $T_{\text{environment}}$ taking into account the influence of the surrounding environment on the road surface. As described in the previous paragraphs, measurements were done with the camera having a grazing angle with respect to pavement surface. In such a situation, the emissivity is below the conventional 0.95 to 0.98 value for nonmetallic materials in general and asphalt concrete in particular [17, 19]. An emissivity value of 0.77 was selected, consistent with the literature [22]. Such a choice was made to fulfill the grazing angle situation. It is also based on the assumption that asphalt concrete emissivity did not depend on the asphalt concrete nature. Therefore, infrared flux variations detected by the camera are only due to temperature variations. This assumption is consistent with the fact that the pavements encountered over the whole

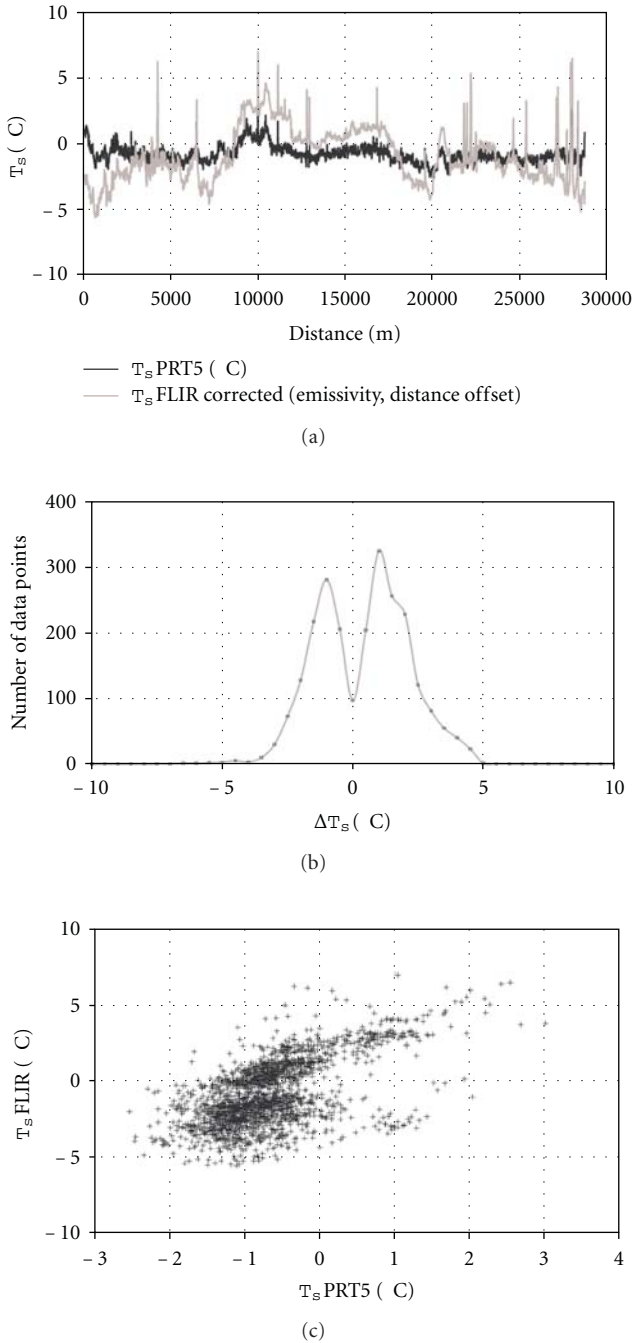


FIGURE 4: Temperature measurements as a function of distance (emissivity and distance offset corrections completed) (a), pavement temperature difference ΔT_s (b), and surface temperature correlation between the two instruments (c).

itinerary were all aged ones, with close structures. It also allowed getting temperature measurements from the infrared camera matching the values from the PRT5 radiometer chosen as a reference. Thus, pavement temperature with an environment correction could be obtained

$$T_{\text{measured}}^4 = \epsilon_{\text{pavement}} \cdot T_{\text{pavement}}^4 + (1 - \epsilon_{\text{pavement}}) \cdot T_{\text{environment}}^4 \quad (2)$$

Once the radiative correction completed, a second one was performed to take into account the distance offset, as illustrated in Figure 2 where the measurement with the infrared camera is ahead of the one of the radiometer. Results of the good concordance between the temperatures issued from both instruments once included these corrections are presented in Figure 4(a).

With this set of corrections, the distribution of pavement temperature difference ΔT_s between the two infrared instruments was established. It is represented in Figure 4(b). The distribution is centered above 0°C, and the average difference was around 0.1°C, with a standard deviation of 1.8°C. This distribution reflects the surface temperature measurements, where surface temperature obtained with the infrared camera is either above or below the one given by the radiometer. The data analysis indicated that T_s (radiometer) was below T_s (FLIR) when the sky view factor was large and close to the half space above the vehicle. In the other cases, the road environment was such that part of the itinerary was partly shaded during daylight either because of the topography or because of the proximity of trees and buildings. Based on the values given in Tables 1 and 2, data were clearly within the sensitivity and accuracy of the instruments. According to Figure 4(c), there is no clear correlation between surface temperatures obtained from the radiometer and the infrared camera, though two sets of data points could be observed. This absence of clear consistency could be attributed to several factors. First of all the two instruments do not have the same accuracy and the same spectral band. This could induce some discrepancies in the measurements. The second aspect is the emissivity correction with the camera because of the grazing angle. An emissivity distribution over the region of interest, and not only a single value as performed in a first approximation, could improve the matching between the curves of Figure 4(a). This is still based on the assumption that asphalt concrete emissivity was only a function of the observation angle. The last aspect deals with the way the influence of the surrounding environment has been considered. A mirror was installed in the field of view of the camera. But its orientation provided information on the space located behind the camera and the vehicle (see Figure 1). So once the vehicle gets closer and farther of a bridge, the environment correction is not properly taken into account. The environmental correction could therefore be improved, introducing in the FOV of the infrared camera a mirror properly orientated.

3.2. Winter Risk Index, Consistency with Seasons, and Infrastructure Environment. Many possibilities exist in the calculation of the winter risk (WR) of an itinerary. One commonly employed possibility consists in using the average parameters of the itinerary (air temperature T_a , relative humidity HR, pavement temperature T_s , and dew point T_d) and analyse how far or close the measurements are from these averages. Indeed, when surface temperature is below the dew point, condensation could occur. And if surface temperature is below 0°C, some slipperiness might appear, and generating a danger for road users. WR is the sum of two risks, one

on surface temperature, and a second one on dew point. WR was then defined in this study according to (3), for each data point, giving more weight to the variation of surface temperature. With such definition, a risk exists each time the surface temperature drops below the dew point, with a negative surface temperature. The greater the difference in such configuration, the greater the winter risk WR

$$WR = 2 \cdot WR(T_s) + WR(T_d),$$

with

$$WR(T_s) = \begin{cases} 0, & \text{if } -0.5^\circ\text{C} \leq T_s - T_{s, \text{average}} < 0^\circ\text{C}, \\ 1, & \text{if } -1^\circ\text{C} \leq T_s - T_{s, \text{average}} < -0.5^\circ\text{C} \dots, \end{cases}$$

$$WR(T_d) = \begin{cases} 0, & \text{if } 0^\circ\text{C} \leq T_d - T_{d, \text{average}} < 0.5^\circ\text{C}, \\ 1, & \text{if } 0.5^\circ\text{C} \leq T_d - T_{d, \text{average}} < 1^\circ\text{C} \dots \end{cases} \quad (3)$$

Such a method to evaluate the winter risk is not optimum. Indeed, the choice of average values could hide specificities of a given itinerary. Furthermore, if you consider two stretches of a same itinerary, studied at two distinct moments in a same season, such calculation would not allow concatenating the two stretches. The conventional winter risk was then calculated using pavement temperature measurements of the PRT5 radiometer as usually done, and with data from the infrared camera, once the emissivity and distance offset correction done. The global WR shape was respected, though values were clearly different from one instrument to the next. Such difference has to be moderated because of the method chosen for WR calculation. WR is greatly sensitive to the average obtained. In the case of the PRT5 radiometer, the average temperature is slightly above -0.7°C , while it is near -1.3°C in the case of the FLIR camera. Average value for dew point is the same in both cases. Therefore, a difference will appear in the conventional WR evaluation.

Measurement with the infrared camera was based on many elements from the road environment, enhancing the thermal amplitude of the ROI. The one used for pavement temperature had a given spatial extent. And due to the grazing angle, pavement points farther from the vehicle appeared colder than the ones near the vehicle. A temperature difference up to 2°C was recorded along thermal images based on Figure 2 pavement ROI. This might also contributed to increase the thermal amplitude within the ROI. This could be corrected considering an emissivity distribution within the ROI instead of attributing a constant emissivity. Indeed, emissivity drops quickly when it comes to such low observation angles (below 10°). So, once the average pavement temperature was calculated for WR, variations around it were enhanced with the infrared camera and this clearly affected the conventional WR, which appeared greater than the one obtained with the radiometer.

Although this calculation is extremely common, some limits could be easily raised. As illustrated on Figure 4(b), the pavement temperature distributions from both instruments are greatly different though Gaussian in both cases. WR

is therefore greatly sensitive to the average temperature obtained. If one itinerary section is studied one day, and a part of this same itinerary section the very same day along with another road stretch, the WR over the common part might not give the same weather risk. Indeed, average values used for the WR risk calculations would be different. Moreover, considering the average parameters of the itinerary could be considered as far-fetched since the temperature balance in any location is the result of its local environment and not of the situation several kilometres before and ahead. The other drawback of such consideration is the consistency of winter risk with seasons and infrastructure environment. The risk should be greater in wintertime than in other seasons, though the condensation risk exists in any season. But using average parameters of the whole itinerary does neither reflect such seasonal modifications, nor the effect of bridges commonly known as colder than the rest of the surface pavement on a road because of a greater convective effect.

To evaluate a more appropriate WR calculation and its consistency with seasons and roads environment, the 30 km long road stretch described in 2.4 was monitored during a whole year, at least once a month. WR was then calculated considering a moving average of the surface temperature over 250 meters before and after each measurement data point. The average temperature for dew point was unchanged. WR was then defined as

$$WR = 2 \cdot WR(T_s) + WR(T_d),$$

with

$$WR(T_s) = \begin{cases} 0, & \text{if } -0.5^\circ\text{C} \leq T_s - T_{s, \text{moving average}} < 0^\circ\text{C}, \\ 1, & \text{if } -1^\circ\text{C} \leq T_s - T_{s, \text{moving average}} < -0.5^\circ\text{C} \dots, \end{cases}$$

$$WR(T_d) = \begin{cases} 0, & \text{if } 0^\circ\text{C} \leq T_d - T_{d, \text{average}} < 0.5^\circ\text{C}, \\ 1, & \text{if } 0.5^\circ\text{C} \leq T_d - T_{d, \text{average}} < 1^\circ\text{C} \dots \end{cases} \quad (4)$$

Then comparison of WR established in a conventional way, according to (3), with a WR calculated using moving average for the same data points is presented in Figures 5(a) and 5(b) in the case of the analysis of data recorded during winter. Then, so as to study the season impact, the WR calculation with a moving average was performed over several months. Figures 5(c) and 5(d) are illustrating this WR during spring and summer months.

A great difference could be noticed between the WR results obtained through the two methods, the conventional one, and with the moving average. In the case of the moving average, the WR amplitude decreases, as spring and then summer get closer. There is always a residual risk since, as indicated before, water condensation over a pavement surface is always possible. The most noticeable point is that the highest values of WR are always obtained at the same locations whatever the season considered for the computation. The other aspect is the consistency of WR established with a moving average with infrastructure environment. Bridges beginnings and ends were plotted in

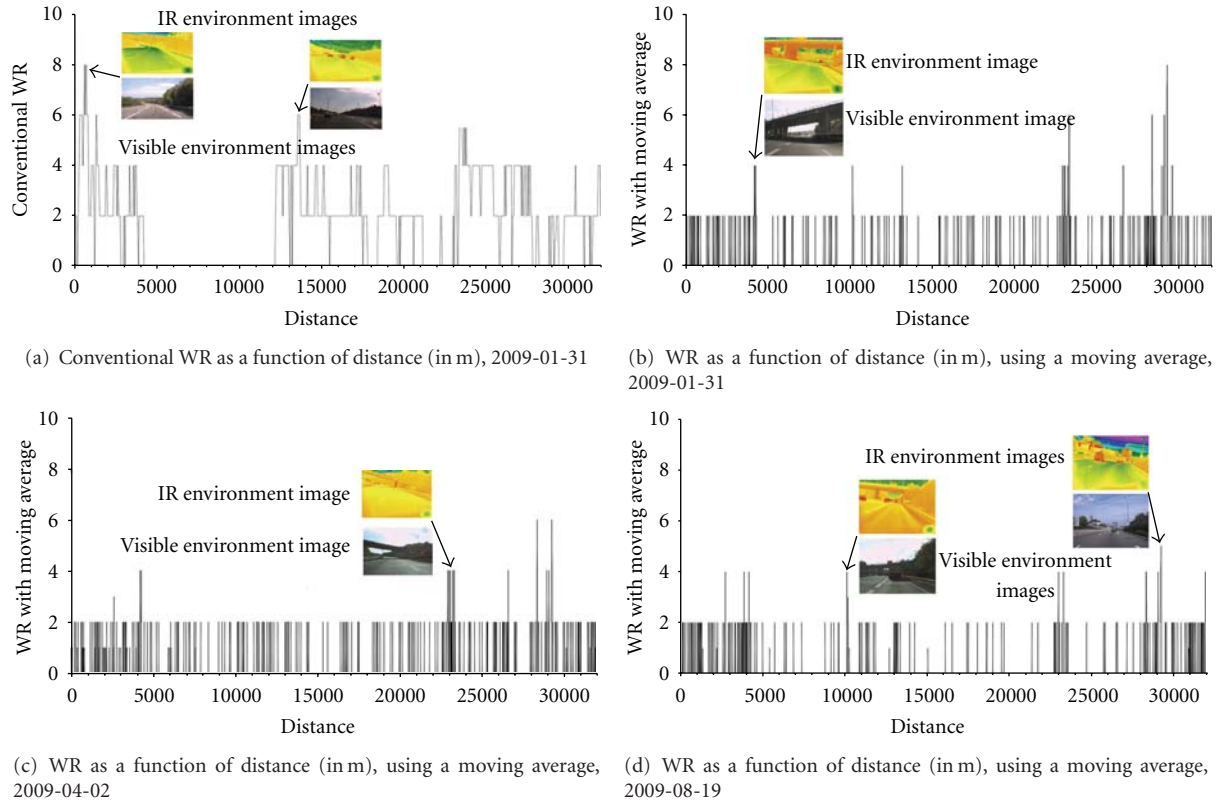


FIGURE 5: Winter risk indexes of the same road stretch at different seasons; IR and visible images corresponding to road points with highest WR values are provided.

Figure 5. Intense WR is always located on bridges present along the itinerary. Furthermore, woods on roadside are source of large relative humidity. They enhance the water condensation and here again the risk was greater in these locations. These locations were indicated with a risk and could be related to the presence of a forest (high relative humidity), or to the fact that the topography does not allow a large insulation (see Figure 1(b)). In the case of conventional WR, largest values could not be correlated to a specific infrastructure and were obtained in open spaces. Some additional calculations were run using another moving average, with 125 m before and after each measurement data point. The WR profile obtained was the same as the ones presented in Figure 5, but with different intensities. This could be easily explained by the moving average changes induced in $T_{s, average}$ and $T_{d, average}$ upon which the WR is based. The choice of the moving average would have to be such that it will properly include specific singularities of the itinerary, without getting a too detailed level that would be useless for road managers.

4. Conclusion

The first objective of the work was to establish the possibility to implement an infrared camera on a thermal mapping vehicle. The second one was to study the consistency of a new winter risk calculation with seasons and infrastructure environment. To do so, two instruments were selected. They

consisted in a conventional PRT 5 radiometer, and a FLIR S65 camera. A 30 km long itinerary was chosen, including different road configurations (highways, urban area, bridges, trees, etc.). The infrared camera was installed on the vehicle in such a way that an emissivity correction was necessary, along with a distance offset one, measurements from the camera being ahead the ones obtained from the radiometer. A LabVIEW interface was developed for data acquisition, including atmospheric parameters and infrared images. This road stretch was monitored at least once a month over several months.

Road surface temperatures analysis obtained from the radiometer and the infrared camera have shown great similarities. Comparison was made on an area located between the wheel tracks. Once emissivity and distance correction performed, there was a good agreement between the surface temperature measurements. Data from the infrared camera indicated greater thermal amplitude. This could be explained by the grazing angle that should induce an emissivity correction with a distribution over the region of interest, and not only a single value as performed in a first approximation. The environment correction has also to be optimized to properly take into account the part located ahead of the vehicle and the camera. The winter risk calculation was conducted according to a very traditional and simplistic way. Because of the greater thermal amplitude obtained with the camera, a larger winter risk was deduced along the network with respect to the one obtained with the radiometer.

A new winter risk calculation, based on the moving average of surface temperature was implemented. This winter risk index has shown a great consistency with respect to infrastructure environment, such as bridge presence and woods on roadside. As spring and summer get closer, the winter risk intensity is reduced. This new index could replace the former one based on the average value of parameters over the whole itinerary. The length of data considered for computing moving average values has however to be defined more precisely. It could be expected that this parameter should depend on the road environment (urban situation or surrounding woods for instance).

As a conclusion, the feasibility of performing thermal mapping with an infrared camera was established. This would improve the performance by measuring pavement temperatures in several lanes at the same time. The position of the camera has to be optimized according to its field of view. Although the thermal images acquisition frequency is comfortable, a reduction would ease data analysis. This could be performed acquiring data from the sole region of interest instead of the whole image, reducing its volume. A compromise has to be found to get information about road surroundings, to avoid radiation from passing vehicles. One major aspect would be to either avoid a grazing observation angle, or to set an emissivity distribution correction over the region of interest. The infrared camera would also ease the implementation of the winter risk index based upon a moving average value of surface temperature, using an appropriate camera field of view that would take into account the appropriate region of interest.

References

- [1] J. E. Thornes, *The prediction of ice formation on motorways in Britain*, Ph.D. thesis, Department of Geography, University of London, London, UK, 1984.
- [2] J. E. Thornes, "Thermal mapping and road-weather information systems for highway engineers," in *Highway Meteorology*, A. H. Perry and L. J. Symons, Eds., pp. 39–67, Spon Press, London, UK, 1991.
- [3] T. Gustavsson and J. Bogren, "Infrared thermography in applied road climatological studies," *International Journal of Remote Sensing*, vol. 12, no. 9, pp. 1811–1828, 1991.
- [4] D. G. Belk, *Thermal mapping for a highway gritting network*, Ph.D. thesis, University of Sheffield, Sheffield, UK, 1993.
- [5] J. Shao, P. J. Lister, and H. B. Pearson, "Thermal Mapping: reliability and repeatability," *Meteorological Applications*, vol. 3, pp. 325–330, 1996.
- [6] J. Shao, J. C. Swanson, R. Patterson, P. J. Lister, and A. N. McDonald, "Variation of winter road surface temperature due to topography and application of Thermal Mapping," *Meteorological Applications*, vol. 4, no. 2, pp. 131–137, 1997.
- [7] T. Gustavsson, "Thermal mapping—a technique for road climatological studies," *Meteorological Applications*, vol. 6, no. 4, pp. 385–394, 1999.
- [8] L. Chapman, J. E. Thornes, and A. Bradley, "Modelling of road surface temperature from a geographical parameter database: part 2: numerical," *Meteorological Applications*, vol. 8, no. 4, pp. 421–436, 2001.
- [9] L. Chapman and J. E. Thornes, "A geomatics-based road surface temperature prediction model," *Science of the Total Environment*, vol. 360, no. 1–3, pp. 68–80, 2006.
- [10] L. Chapman and J. E. Thornes, "Small-scale road surface temperature and condition variations across a road profile," in *Proceedings of the 14th International Road Weather Conference (SIRWEC '08)*, Prague, Czech Republic, May 2008.
- [11] L. Chapman and J. E. Thornes, "The influence of traffic on road surface temperatures: implications for thermal mapping studies," *Meteorological Applications*, vol. 12, no. 4, pp. 371–380, 2005.
- [12] L. Chapman and J. E. Thornes, "A geomatics-based road surface temperature prediction model," *Science of the Total Environment*, vol. 360, no. 1–3, pp. 68–80, 2006.
- [13] J. Bogren, T. Gustavsson, and S. Lindqvist, "A description of a local climatological model used to predict temperature variations along stretches of road," *Meteorological Magazine*, vol. 121, no. 1440, pp. 157–164, 1992.
- [14] J. Norrman, "Slipperiness on roads—an expert system classification," *Meteorological Applications*, vol. 7, no. 1, pp. 27–36, 2000.
- [15] D. Bouris, T. Theodosiou, K. Rados, M. Makrogianni, K. Koutsoukos, and A. Goulas, "Thermographic measurement and numerical weather forecast along a highway road surface," *Meteorological Applications*, vol. 17, no. 4, pp. 474–484, 2010.
- [16] <http://www.forumgraphic.eu/prod/index.php/Mesure/sonde-basse-couche.html>.
- [17] L. Ibos, M. Marchetti, A. Boudenne, S. Dacru, Y. Candau, and J. Livet, "Infrared emissivity measurement device: principle and applications," *Measurement Science and Technology*, vol. 17, no. 11, pp. 2950–2956, 2006.
- [18] S. Dacru, L. Ibos, Y. Candau, and S. Mattei, "Improvement of building wall surface temperature measurements by infrared thermography," *Infrared Physics and Technology*, vol. 46, no. 6, pp. 451–467, 2005.
- [19] M. Marchetti, L. Ibos, V. Muzet et al., "Emissivity measurements of road materials," *Quantitative InfraRed Thermography Journal*, vol. 1, no. 1, pp. I.2.1–I.2.7, 2004.
- [20] X. P. V. Maldague, *Theory and Practice of Infrared Technology for Nondestructive Testing*, John Wiley & sons, New York, NY, USA, 2001.
- [21] G. Gaussorgues, "La thermographie infrarouge," *Techniques et Documentation (France)*, pp. 386, 1981.
- [22] *Handbook of Military Infrared Technology*, Office of Naval Research Department of the Navy, Washington, DC, USA, 1965.
- [23] J. Dumoulin, V. Boucher, and F. Greffier, "Numerical and experimental evaluation of road infrastructure perception in fog and/or night conditions using infrared and photometric vision systems," in *Infrared Spaceborne Remote Sensing and Instrumentation XVII*, vol. 7453 of *Proceedings of SPIE*, San Diego, Calif, USA, August 2009.

Research Article

Multidisciplinary Approach to a Recovery Plan of Historical Buildings

Luciana Orlando

Dipartimento di Ingegneria Civile, Edile e Ambientale, Sapienza Università di Roma, Via Eudossiana 18, 00184 Roma, Italy

Correspondence should be addressed to Luciana Orlando, luciana.orlando@uniroma1.it

Received 17 February 2011; Accepted 23 May 2011

Academic Editor: Francesco Soldovieri

Copyright © 2011 Luciana Orlando. This is an open access article distributed under the Creative Commons Attribution License, which permits unrestricted use, distribution, and reproduction in any medium, provided the original work is properly cited.

The paper emphasizes the advantages of employing multiple data techniques—geology, GPS, surveys of cracking, boreholes, seismic refraction and electrical resistivity tomography—to image the shallow stratigraphy and hypothesize the cause of instability of an urban area. The study is focused on the joint interpretation of the crack pattern, topographic monitoring and the features of the underground, to define the area affected by instability and the direction of ground motion with the objective to advance a hypothesis on the cause of the instability of the area and to depict the main features. Borehole stratigraphies for a univocal interpretation of the lithology of electrical and seismic data and electrical resistivity tomography to constrain the interpretation of the lateral velocity variations and thickness of seismic bedrock were used. The geophysical surveys reveals to be complementary in the depicting of underground features. The study is approached at small and medium scale.

1. Introduction

Over the past 10 years, buildings in the centre of the village of Roccapinalveti, located in central Italy (Figure 1(a)), have shown progressive damage on a time lapse of 7 years. The instability revealed itself suddenly, and with time the increment of damage decreased until becoming null. In most cases, the instability was revealed via cracks and fractures in the walls and floors of buildings, as well as in the roads (Figure 2). The cracks have a displacement of less than 0.1 to 2 cm, and most are located at the building-to-road contact (Figure 2(b)). The buildings, built in the late nineteenth century through today and with different materials and techniques, have all suffered the same sort of damage. Initially, many buildings were reclaimed with micropiles and resined but without any restoration plan based on objective data. Following restoration, some of the buildings have been affected by further instability. Thus, the municipality recognized the need to perform a detailed study of the instability phenomena; this study was conducted from 2004 to 2009.

For an exhaustive analysis of the area affected by instability, a multidisciplinary approach is generally considered in

order to constrain the data interpretation. The data can be used for a joint interpretation [1–4] or for a joint inversion [5–9]. The first is often highly dependent on the experience of interpreter, and the second depends heavily on the algorithms, the quality of data, and so forth. In literature we often find that the joint inversion is performed with some parameters constrained (speed, thickness, resistivity, etc.) and/or using an iterative processes based on more data. In any case, a joint inversion can be very complex to apply for a large number of investigations and to a wide and complex subsoil.

Due to the complexity of the phenomena of instability and of the geological setting of the area, knowledge of topography, morphology, geology, hydrogeology, slit image, and so forth, of fundamental importance for the remediation plan, was considered. Direct and indirect surveys were planned, processed, and interpreted, jointly, in such a way as to obtain information needed to design the remediation plan. In detail, direct and indirect methods were applied, such as mapping of cracks, boreholes, geology, GPS monitoring, electrical resistivity tomography, and seismic refraction. All the data were interpreted jointly to reduce the intrinsic uncertainty of

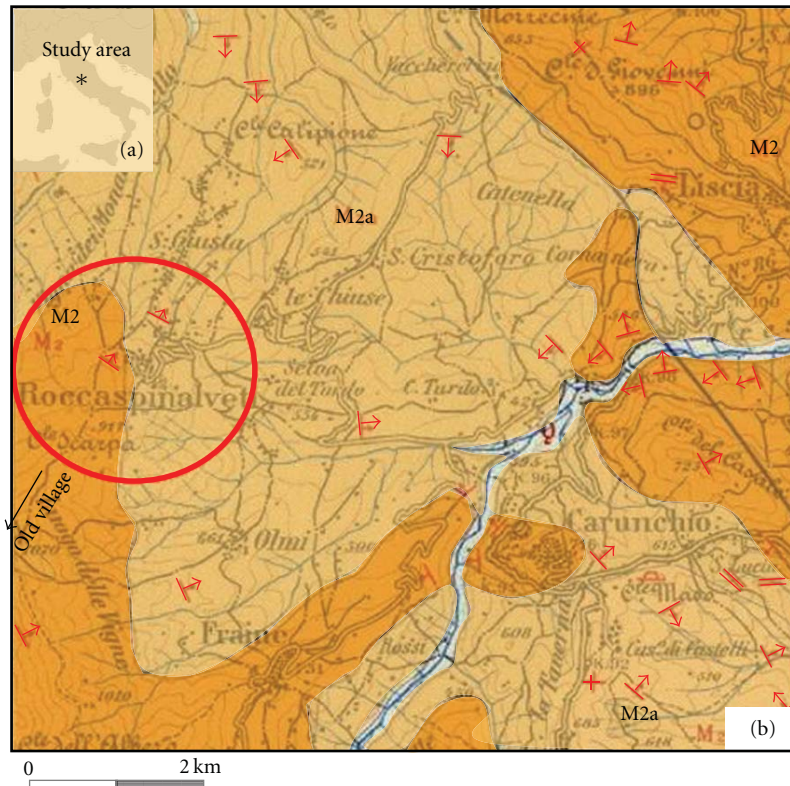


FIGURE 1: Study area location (a). The geological map (b) shows two outcropping formations *Miocene in age*: a flysch complex formed by a succession of calcareous sandstone, dense marl, clayey-marl-clay strata (M2), and a complex formed by a succession of clayey-sand and marl strata (M2a). The red arrows indicate the faults and the black arrow indicates the location of the old village 3 km from the present one.

each method and to reach the following main objectives:

- (1) stratigraphy of the near surface sediments,
- (2) determination of intensity and direction of the main ground motion,
- (3) identification of the cause of instability.

The paper is mainly focused on the acquisition and joint interpretation of data rather than on the advanced inversion.

2. Survey Methods

The study of an urbanized area affected by instability problems is not a simple task. Geological evidence is often masked by structures that severely constrain the planning, location, and quality of the data. In such cases, geophysical methods can be applied, using special precautions to overcome problems due to environmental noise, road surface, hidden outcropping formations, fill material, small dimensions of walking areas, and so forth.

In this study, collection and joint analysis of all the existing data, the choice of the most suitable surveys, their accurate application and inversion, and a joint interpretation of the results were used to find a first answer to the starting questions concerning the geological setting of the unstable area and the most likely causes of the instability. The planning of the survey is shown in the flow chart of Figure 3.

The study was executed in three main steps: first, the morphology and geologic and cracks maps were analyzed (step 1); on the basis of these data, the boundary of the area affected by instability was outlined and the most suitable survey methods were defined (step 2); at the end the area was surveyed, the data were processed, and the results were interpreted jointly (step 3) with the aim of depicting the stratigraphy of the near surface soil and advancing a scenario of the cause of instability.

Below I describe each step in detail.

2.1. Step 1. Step 1 includes

- (i) geo-hydro-morphology analysis,
- (ii) crack surveys.

This step has the objective of planning topographic monitoring, geophysical surveys, and boreholes.

2.1.1. Geo-Hydro-Morphology. The village is 690–770 m above sea level, on a slope varying from 2% to 10% (north west-south east) (Figure 4). Large-scale topography shows numerous nicks from landslides that have occurred in the past (dotted lines in the figure); in fact, a landslide in the mid-eighteenth century induced the population to migrate to the present-day village location (750 m above s.l.) from



FIGURE 2: Photo images of cracks in the floor (a), road (b), ceiling (c), and building walls (d).

the old one, which was 1100 m above s.l. and 3 km SW of today's village (Figure 1(b)).

The geological map (Figure 1(b)) shows that the village is located across two formations of *Miocene* age: a flysch complex formed by a sequence of calcareous sandstone, dense marl, clayey-marl-clay strata (M2) and a complex formed by a sequence of clayey-sand and marl strata (M2a). Such sequences can be over 100 m thick.

Excavation for building foundations has shown that, near the surface, the soil is formed by landfill deposits, clay of variable thicknesses, and marl.

In recent years the area has been affected by long periods of drought. Two points for pumping water have been activated in the proximity of a severely damaged building. These coeval events lead us to endorse the hypothesis that the instability could have been caused by compaction of sediments due to water table drawdown.

2.1.2. Crack Survey. The crack survey was based on interviews with householders, photographs, displacement measurements, and mapping on the cadastral map of the cracks visible in the roads and buildings. This approach was very time-consuming but fundamental in determining the direction of ground motion, because it allowed me to identify three main patterns of cracks and to outline the instability area where the surveys were focused.

Each pattern, formed by cracks more or less parallel to each other was marked with A, B and C in Figure 5(a).

Pattern A (Figure 5(a)) runs parallel to the road, and the cracks are located both inside the buildings and on the road. The main cracks have caused the detachment of the footpath from the buildings (Figure 2(b)). Pattern B (Figure 5(a)) is perpendicular to the A and C patterns and crosses roads and buildings (Figure 2(d)). Pattern C runs almost parallel to A and is nearly perpendicular to B. This pattern was the most difficult to characterise as some of the buildings exhibit heavy damage while the roads are little affected. A careful analysis of the crack locations, and the setting of the area, led us to suppose that stress had induced a viscous deformation of roads that, in this area, are built on embanked materials.

From the analysis of crack map two main findings were established. First, most damaged buildings lie on the rupture alignments while the buildings fully located within the area surrounded by the rupture patterns A, B and C show either no cracks or only small ones. This indicates that the whole area located within the rupture alignments is not exposed to differential movement. The second finding is that the degree of damage is unrelated to age, materials, and techniques of construction as I have found no correlation between degree of damage and these building characteristics.

2.2. Step 2. In the second step, the most suitable techniques for outlining the study area were selected: reconstruction

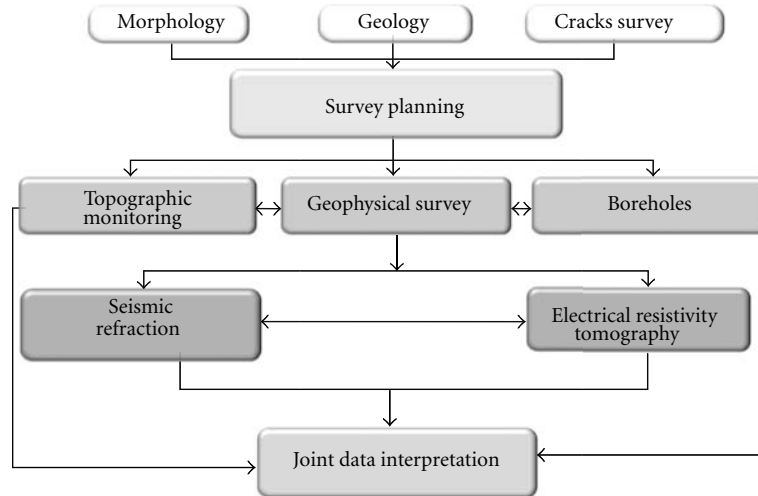


FIGURE 3: Flow chart of the surveys performed in the study area.

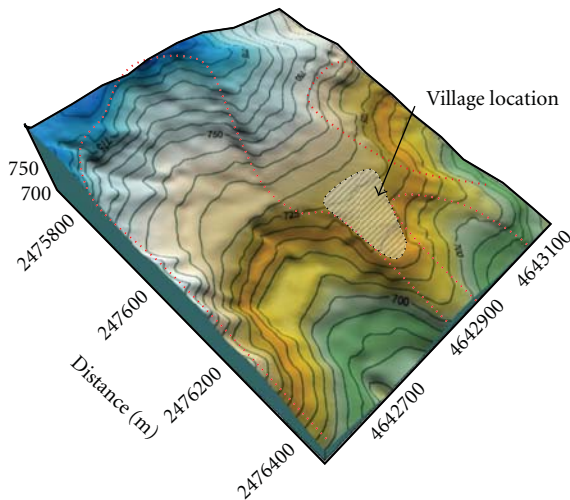


FIGURE 4: Morphology of the area. Dotted lines outline niches induced by landslides that occurred in the past.

of the geological setting and monitoring terrain movement over time. The topographic survey was chosen to assess the magnitude and terrain ground motion over time, boreholes to establish stratigraphy and constrain the ambiguity of the geophysical data interpretation in terms of thickness of strata and lithology, and seismic refraction and electric resistivity tomography to give lateral continuity to borehole stratigraphy in terms of geometries and lithologies. Seismic refraction and electric resistivity tomography were selected because I think that they are the most suitable, well-tested, and robust geophysical methods to outline the near surface stratigraphy.

2.2.1. Topographic Monitoring. The topographic measurements were performed on 7 GPS points (Figure 5(b)). The measurement points were equipped with brass pins inserted into holes drilled in the ground. The GPS (TopCon) RTK

instrument was slotted onto these pins. The measurements were repeated 3 times in one year.

The GPS measurements indicate the following:

- (1) Instability induces mainly vertical movement. The maximum value detected at point A (Figure 5(b)) was about 2 cm in six months.
- (2) Only at point A, a significant lateral movement of about 4-5 cm was recorded, its direction is NNW to SSE, more or less parallel to the pattern of cracks A and C patterns (Figure 5(a)).
- (3) The greatest displacements occurred in the summer season.

These results, combined with those obtained from the crack analyses, are consistent with the hypothesis of compaction of the near surface layers, consequent with lowering of the water table during long periods of drought and activation of two pumping points in the most unstable area (crack pattern A).

2.2.2. Boreholes. Two continuous coring boreholes (BH1 and BH2) and one destructive borehole (Sm1) (white squares in Figure 5(c)) were drilled. The borehole stratigraphies indicate that the first 24 m of soil can be divided into two units: Unit A near the surface consisting of landfill clay deposits and clay interbedded with thin calcarenite layers, and Unit B, formed by fairly dense silty-marl strata.

In detail:

BH1 Borehole. The borehole BH1 is 24 m deep. Unit A extends from 0 to 13.7 m: from the top to 0.7, it consists of landfill clay deposits and from 0.7 to 13.7 m of silty-clay, which becomes slightly sandy between 4 and 13.7 m. At 3.5–5 m, the silty-clay layer incorporates a humus organic soil related to ancient groundcover. This unit also includes thin calcarenite levels that become slightly sandy at 4–13.7 m.



FIGURE 5: (a) Location of main crack patterns lying more or less normal to each other, the buildings with the greatest damage are marked with stars. (b) White circles and stars indicate location of topographic survey: stars indicate steady points and circles unsteady ones. Orange lines are the location of seismic refraction surveys. (c) Borehole locations are indicated with white squares and electric resistivity tomography with green and orange dot lines.

Unit B, from 13.7 to 24 m, consists of water-saturated silty clay with small marl content. The water table was 13 m deep.

BH2 Borehole. This borehole is 15 m deep. Unit A, 9.3 m thick, consists, from 0 to 1.5 m, of clay landfill deposits and silty-clay rich in carbonaceous fragments; clay and thin fractured limestone layers lie in the distance from 1.5 to 6.6 m, and calcarenite from 6.6 m to 9.3 m. Unit B consists mainly of dense silty-clay marl from 9.3 to 15 m. Water eruption during drilling suggests the presence of a water overpressured layer.

Sm3 Borehole. This borehole consists of Unit A from 0 to 6 m of depth and Unit B from 6 m to 8 m. The stratigraphy was based on wash sample analysis.

The water table in the study area is located in Unit A at a depth from 1 to 13 m.

3. Step 3

The well-tested and robust geophysical methods seismic refraction and electrical resistivity tomography for the near-

TABLE 1

Channel	24
Line length	69 m
Receiver offset	3 m
Shot offset	-50, 0, 17.25, 34.5, 51.75, 69, 119 m
Receiver frequency	7 Hz

surface investigation were selected to depict the geometry assessment and P wave velocity of the near-surface geological layers.

3.1. Seismic Refraction. The area was surveyed with 11 refraction seismic profiles located along the roads (Figure 5(b)) for a total length of 759 m with 2 overlapping receivers for lines in succession. The acquisition parameters are listed in Table 1.

The problem of the receiver coupling was overcome using receivers equipped with a metallic plate coupled to the road with mortar. The trigger was a receiver, and the source a dropped weight of 700 kg that was dropped onto the ground by a forklift.

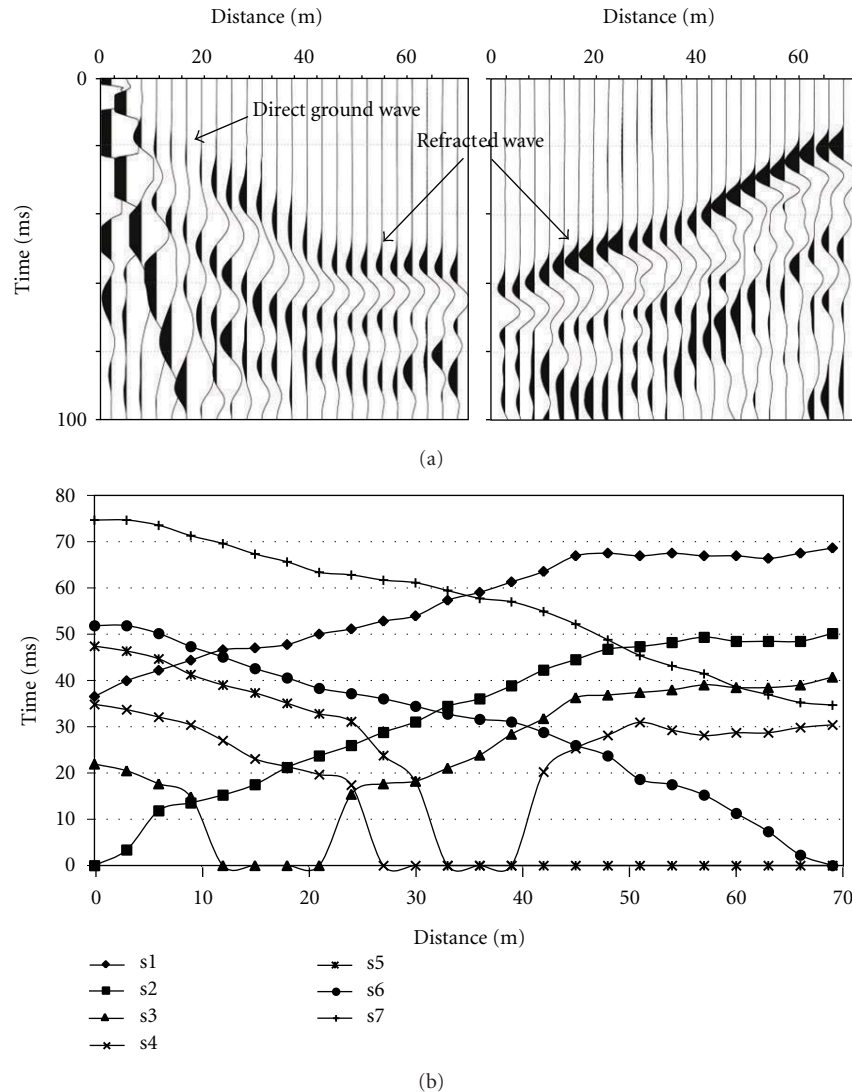


FIGURE 6: (a) Shots, s1 and s6, of seismic refraction line 8. (b) First arrivals of line 8.

The first arrivals were picked by hand and rechecked several times to improve accuracy. In Figure 6(a), shots s2 and s7 of line 8 are shown. The most important problem encountered was due to the direct wave that, for some shots, travelled through the road concrete.

The inversion was checked using the delay time method [10, 11] integrated, in the case of more than one layer, with the method proposed by Bernabini [12] and seismic refraction tomography based on the SIRT (Simultaneous Iterative Reconstruction Technique) algorithm [13, 14]. The tests showed that the delay time method gave more consistent results with the borehole stratigraphy than the seismic tomography method because of the small number of shots for each line, the lack in some shots of the direct ground wave, and the lateral velocity variation of the bedrock.

The first arrivals were used (see an example in Figure 6(b)) for the calculation of P wave velocities and delay times. The former were used to draw the seismic refraction stratigraphy (Figures 7(a), 7(c), 7(e), and 8(a)).

Seismic refraction allowed me to survey the first 1–10 m of soil investigating three layers (Figures 7(a), 7(c), 7(e), and 8(a)). On the basis of the stratigraphy of boreholes, the seismic velocities were interpreted in terms of lithologies (Figure 5(b)) as described below.

- (1) The near surface weathered layer (A1), with velocity of about 500 m/s and thickness from 0.5 to 7 m, was linked to the upper part of Unit A drilled with boreholes, which consists of clay-filled deposits.
- (2) The second seismic layer (A2), with velocity of about 1000–1100 m/s and thickness from 0.5 up to 14 meters, was linked to the lower part of Unit A formed by silty-clay deposits.
- (3) The third seismic layer (B), with velocity of 1000–2300 m/s, was linked to Unit B formed by fairly dense silty-marl.

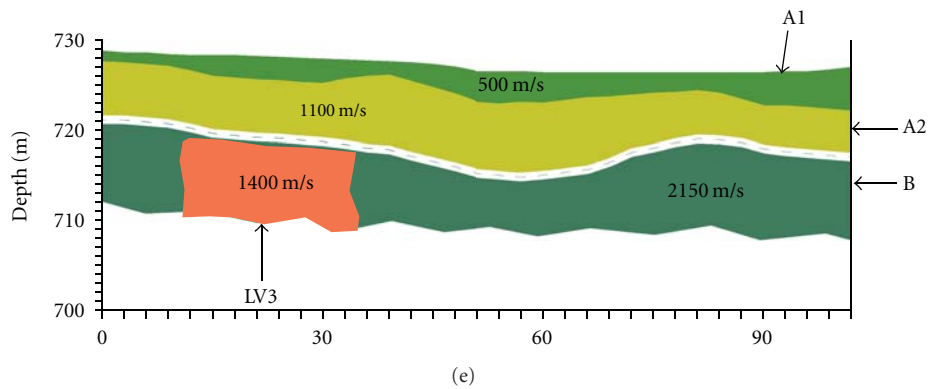
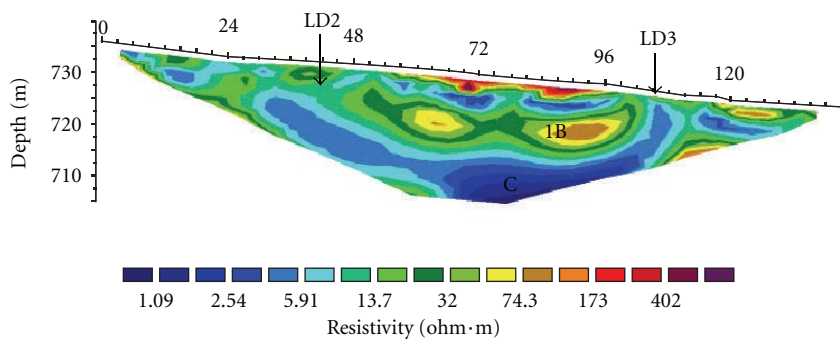
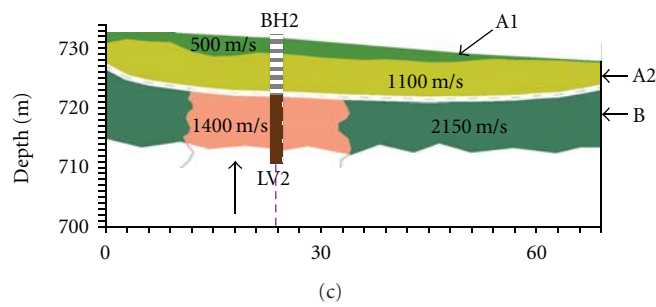
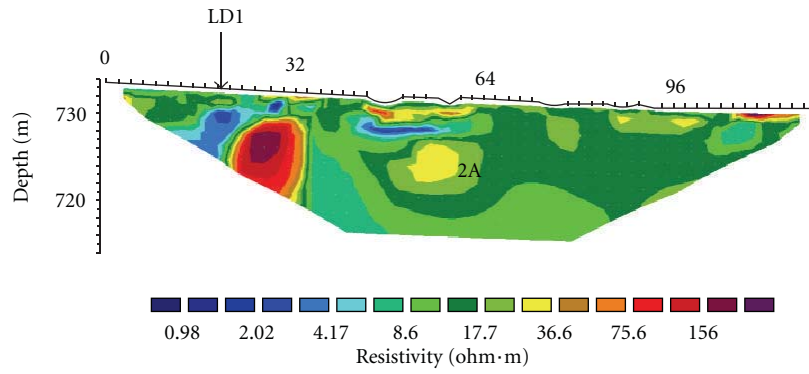
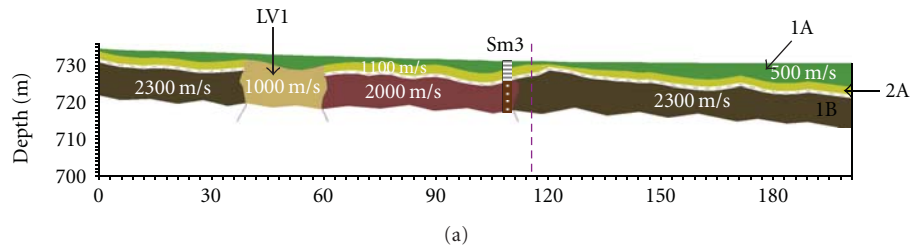


FIGURE 7: Continued.

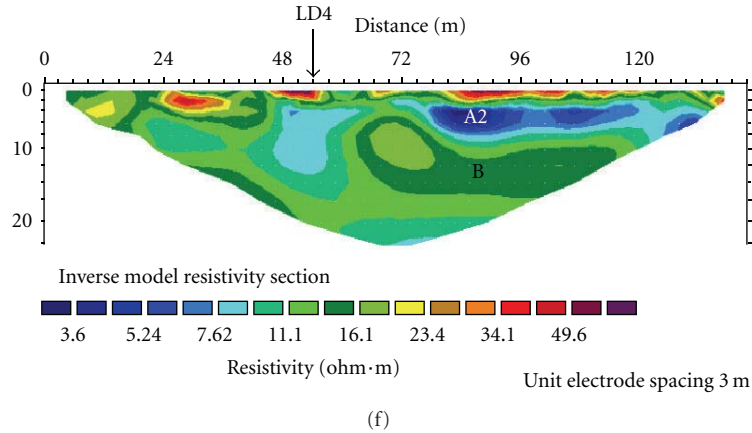


FIGURE 7: Seismic refraction profiles ((a), (c) and (e)) detect three layers, the first two (A1 and A2) related to Unit A and the third to Unit B drilled by boreholes; LV indicates low-velocity zones. Electrical resistivity tomography profiles ((b), (d) and (f)) detect four layers, the first two related to Unit A, the third to Unit B, and the fourth (C) to a non drilled shale layer. LD indicates lateral discontinuity of marl formation. Profile locations appear in Figure 5.

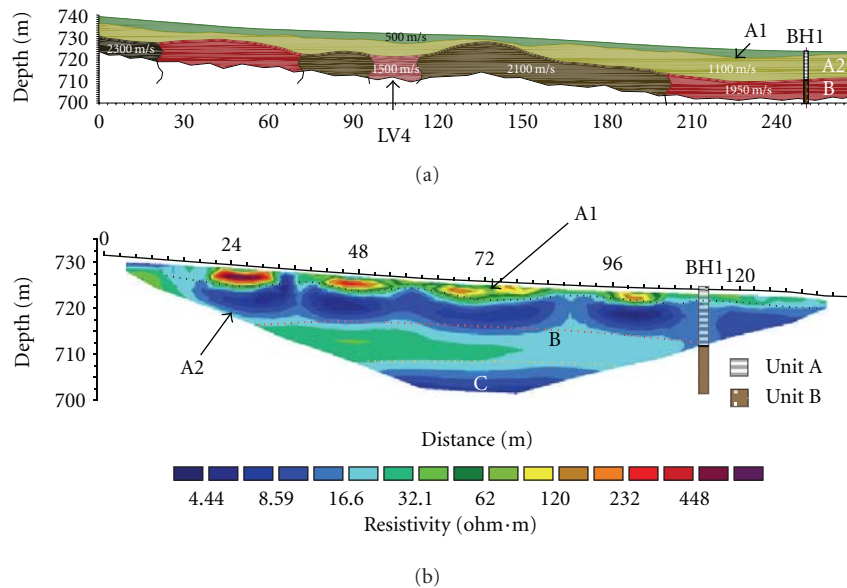


FIGURE 8: (a) Seismic refraction profile detects two layers of Unit A and the top of Unit B; LV indicates a low-velocity zone. (b) Electrical resistivity tomography profile detects Units A and B and a non drilled shale layer. LD indicates lateral discontinuity of marl formation. Profile locations appear in Figure 5.

The third layer is characterised by marked lateral changes in P wave velocity, varying between 1000 and 2300 m/s. The main low-velocity zones in Figures 7(a), 7(c), 7(e) and 8(a) are marked with capital letters LV followed by a number. The couple of seismic profiles with crack locations of Figure 5(a) show a good overlap of the low-seismic-velocity zones with patterns of cracks: in detail, pattern B crosses the profile of Figure 7(a) in correspondence with the LV1 zone, pattern C crosses profiles of Figures 7(c) and 7(e) in correspondence with the LV2 and LV3 zones respectively.

Because of the lateral velocity changes, I realised that this layer could not be considered bedrock for the remediation plan and that the low velocity zones should be studied in

greater detail because low velocities can be due to both rupture zones and to lateral lithology changes.

The ambiguity of the interpretation of low velocity zones of seismic bedrock suggested that I should investigate the area with electrical resistivity tomography (ERT).

3.2. Electrical Resistivity Tomography. The area was surveyed with 9 electrical resistivity tomography (ERT) profiles (Figure 5(c)) during two campaigns. Profiles 1–6 (green lines in Figure 5(c)) were acquired in the first campaign and located more or less in the same position as the seismic refraction profiles with the objective to use the data for a joint interpretation. The profiles 7–9 (dot lines in Figure 5(c))

TABLE 2

ERT Survey	
Instrument	Syscal Pro Switch-IRIS Corporation
Electrode	48
Electrode offset	2 m lines 1–3; 3 m lines 4–
Spread	Wenner, Schlumberger, pole-dipole

were acquired in a second campaign with the objective to increase the depth of investigation. They were located on a slope outside the urban area where the topographic level was lower than the others and pole-dipole spread was used to increase the depth of investigation for comparable line length, which was constrained by the available space.

In the urban area the electrodes were coupled with the sedimentary formation, drilling the insulated paving with holes 40–70 cm deep and 2 cm in diameter. The acquisition parameters are listed in Table 2. The electrode spread of lines 1–3 was 2 m and for all the others 3 m. The 2–3 m spread was chosen on the basis of seismic refraction results that indicated a bedrock at 2–12 m.

The data were processed with the well-tested smoothness-constrained least-squares approach [15, 16] that seeks the theoretical solution which best fits with the actual data. Minimization error was obtained from a Gauss-Newton algorithm based on an iterative process. The inversion was started from a homogeneous model, taking into account the actual topography along the profile that was modelled with model blocks with a moderately damped distorted grid.

ERT profiles investigated a depth of about 20–25 m, detecting 4 main electrolayers (Figures 7(b), 7(d), 7(f) and Figure 8(b)). Starting from the topographic surface, the four layers are characterized by resistivities of 60, 10, 20–40, and 10 $\Omega \cdot m$, respectively. From the correlation of ERT stratigraphy with core boreholes the ERT data were interpreted as described below.

- (1) The first two electrolayers are related to Unit A, where the first electrolayer (A1) consists of reworked material including asphalt and utilities and the second one (A2) of shale.
- (2) The third electro-layer is related to Unit B, which is formed mainly by shale-marl. The resistivity features of this layer show us that it is a few meters thick and laterally discontinuous.
- (3) The fourth layer, marked C in Figures 7 and 8, is not univocally interpretable in terms of lithology because it was not drilled by boreholes. Taking into account the resistivity value of this layer, that is equal to the second one, and the large-scale geological map, which indicates that the study area consists of a succession of shale and marl, I advanced the hypothesis that this layer (marked C in Figures 7 and 8) could be formed by shale-clay.

A perspective mapping of the 4 lines (Figure 9) acquired on the sloping area (Figure 5(c)) shows a shallow subsurface with the same features as the urban area. Here the marl

is laterally discontinuous and probably dips in the same direction as the topography. From the ERT images, the discontinuous marl layer is merged into a shale formation. The main lateral discontinuities of marl in Figures 7(b), 7(d), 7(f), and 8(b) are marked with capital letters LV (lateral discontinuity) followed by a number. Coupling the marl lateral discontinuities with pattern of cracks, I observed that the crack pattern B crosses the profile 7B in correspondence with discontinuity LD1; the crack pattern C crosses the profiles 8D and F in correspondence with LD2 and LD4.

The ERT data confirm that the near surface formation is formed by a shale-marl succession, as indicated by the large-scale geological map, and that the marl layer cannot be considered bedrock for the remediation plan because of its lateral discontinuity and its small thickness.

4. Joint Interpretation

In Figure 10, a synthesis of the data interpretation is shown. The crack survey detected three main patterns of cracks with directions perpendicular to each other. The cracks bound the unstable area. The GPS shows that, in the unstable area, the vertical component of the soil displacement is more prevalent than the horizontal. The direction of the horizontal component is indicated by the arrow in Figure 10. These results agree with the hypothesis that the instability is due to the compacting of near-surface strata caused by the water table drawdown following long periods of drought and the pumping of water in the proximity of two restructured buildings.

The correlation of the seismic with the electrostratigraphy of profiles acquired in the same position shows a good overlap of the geometries of the first three layers as shown in Figures 7 and 8. Combining ERT and seismic refraction data, the subsurface sedimentary structures up to 15–20 m, which consist of 4 layers, were reconstructed with good accuracy. The stratigraphy was investigated with the same resolution by both geophysical surveys. The lithology of each layer was defined by correlation of geophysical data with coring borehole stratigraphies. In detail, starting from the topographic surface, the first layer (A1 in Figures 7 and 8) is linked to the weathered layer that consists of fill materials including utilities. This layer is characterized by a resistivity greater than 60 $\Omega \cdot m$ and a P wave velocity of 400–500 m/s. The second layer, with resistivity of about 10 $\Omega \cdot m$ and P wave velocity of 1100 (A2 in Figures 7 and 8), is shale that includes thin layers of limestone and sandstone. From BH2 borehole I knew that some thin permeable layers are filled by overpressured water. Layer 3 was drilled by boreholes and detected with seismic refraction and ERT. This layer consists of fairly dense shale-marl and is characterized by a resistivity of 20–40 $\Omega \cdot m$ and velocity from 1000 to 2300 km/s. Below the marl, ERT detected Unit C (Figures 8(b), 8(c), and 8(e)) with a resistivity of 10 $\Omega \cdot m$ that I interpreted as shale.

Combining the ERT and seismic data I constrained the interpretation of low-velocity zones (LV) detected by seismic reflection asserting that the low-velocities are due to lateral discontinuities of marl. The map location of the main low velocity zones of Figure 10 shows that they are positioned

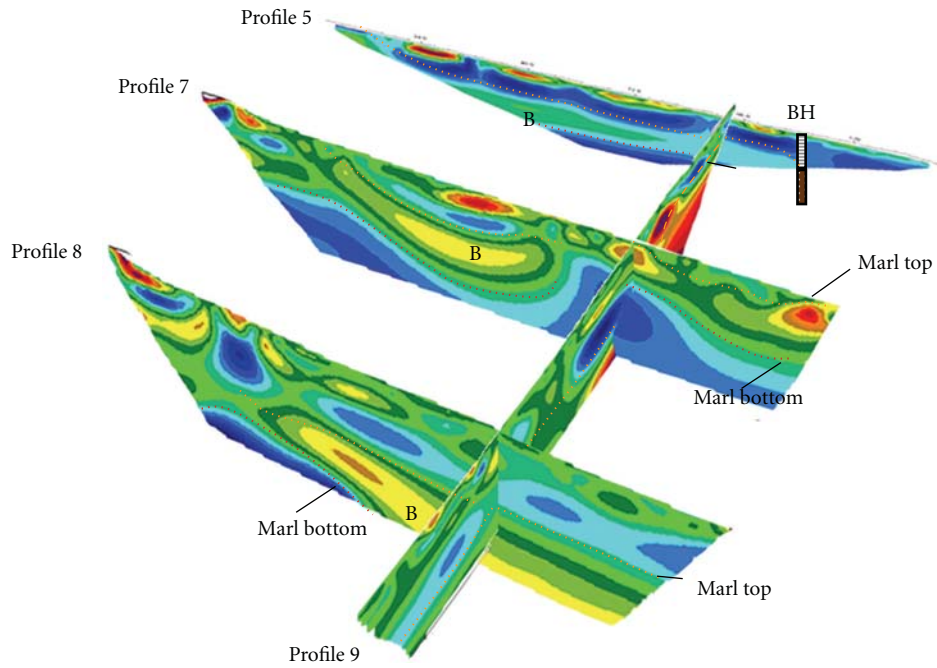
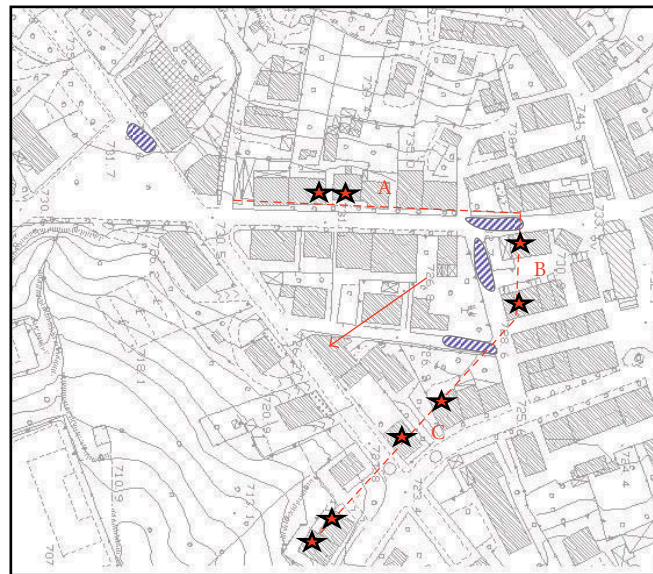


FIGURE 9: Perspective map of ERT profiles located in sloping area. Profile location in Figure 5(c).



-  Low velocity zones
-  Movement direction
-  Damaged buildings
-  Rupture alignments

FIGURE 10: Location of main rupture zones, buildings affected by marked damage, and low-velocity zones detected by seismic refraction. The arrow indicates the main direction of movement in the area and the dashed lines the rupture alignments.

near the crack pattern B. From geophysical investigations, I can infer that the marl layer, although characterized by high seismic velocity (1900–2200 m/s), cannot be regarded as bedrock for planning of environmental recovery of the area because of its lack of lateral continuity. Furthermore, since the lateral discontinuities are located in correspondence of fractures, I can assert that the detachments occurred in the greatest weakness zones of the subsoil.

The buried organic humus layer at a depth of 3.5–5 m detected by borehole BH1 and the marl that is laterally discontinuous and embedded into shale led us to suppose that the near-surface units probably consist of non-*in-situ* formations mobilized by a past landslide.

5. Discussion and Conclusion

In this paper, I have proposed a multidisciplinary approach to perform an exhaustive analysis of an area affected by instability problems for solving two main problems: to depict the stratigraphy of the near surface sediments and to advance a hypothesis on the cause of instability. The former was the more difficult issue because both landslide and terrain compacting can induce ground motion which is the cause of building damage.

The study has shown that, for urban sites characterized by a complex geology, many ambiguities of data interpretation can be overcome with a joint interpretation of data performed with direct and indirect methods. In this particular case the difficulties in solving the problems were due to both the complexity of the geology and the urbanization of the area that have not fostered an optimal survey plan. Therefore, the planning of the surveys was the result of a complex process that started from the initial knowledge of the soil and was improved over time with newly acquired knowledge of the setting of the study area.

This study made me realize the importance of the mapping with fractures visible on the road and buildings and the interviews with the owners. The mapping of the fractures allowed me to separate the unstable from the stable area, observe an organic unity in the distribution of fractures, and conclude that the degree of damage to buildings is independent of their age; the interview with the owners allowed me to reconstruct the evolution of instability.

The joint interpretation of the direct and indirect surveys resulted in establishing boundaries of the area affected by instability phenomena, defining the main direction of ground motion, and depicting the stratigraphy of the first 10–20 of soil.

The electrical imaging, in addition to confirming the results obtained by seismic, allowed me to remove the uncertainty in the interpretation of the low velocities of seismic bedrock, because the images clearly show that low velocities occur in zones where the marl was absent. This result allowed me to assert that the marl layer cannot be considered bedrock for the recovery plan. Seismic refraction is shown to be a useful tool with which to infer the P velocity of the formation and the ERT for lithological characterization of formations that are not drilled.

The joint analysis of the data did not allow me to uniquely identify the cause of instability, because the evidence can be justified both by the reactivation of an old landslide and by the compaction of sediments. In detail, the stratigraphy and morphology could lead to hypothesize that the area has been affected by reactivated landslides, while the topographic survey and the long period of drought that occurred just before the instability problem could lead to hypothesize that the instability was due to the compaction of the near surface sediments. Unfortunately, this problem is inherent in the combined use of direct and indirect methods currently available that allow us to photograph the effects of instability and the soil stratigraphy in a time period that is often too short to understand the phenomena and to reduce the ambiguity in determining the causes of instability in a complex situation. Speculatively, I advance the hypothesis that the urban area was built on an old landslide and that the recent instability that occurred within a period of 5–7 years has been caused by compaction of surface sediments. Despite this, the results obtained from the joint interpretation of direct and indirect surveys, can be considered absolutely necessary for effective restoration planning of the area.

For more exhaustive results, the study could be approached with topographic survey and water table monitoring over an extended period of time and involve other disciplines such as GIS and geostatistical methods [17–19] for a classification of the land in additional susceptibility domains.

Acknowledgments

This research was supported by the municipality of Roccaspinale, Italy. The author would like to thank engineers Emliano Olivetti and Alessandra Di Battista for their help in the acquisition and processing of the data and Professor M. Crespi (Sapienza University of Rome) for his help with the topographic results.

References

- [1] E. Cardarelli, C. Marrone, and L. Orlando, "Evaluation of tunnel stability using integrated geophysical methods," *Journal of Applied Geophysics*, vol. 52, no. 2-3, pp. 93–102, 2003.
- [2] K. Koch, J. Wenninger, S. Uhlenbrook, and M. Bonell, "Joint interpretation of hydrological and geophysical data: electrical resistivity tomography results from a process hydrological research site in the Black Forest Mountains, Germany," *Hydrological Processes*, vol. 23, no. 10, pp. 1501–1513, 2009.
- [3] L. Orlando and G. Pelliccioni, "P and PS data to reduce the uncertainty in the reconstruction of near-surface alluvial deposits (Case study—Central Italy)," *Journal of Applied Geophysics*, vol. 72, no. 1, pp. 57–69, 2010.
- [4] H. J. Mauritsch, W. Seiberl, R. Arndt, A. Römer, K. Schneiderbauer, and G. P. Sendhofer, "Geophysical investigations of large landslides in the Carnic Region of southern Austria," *Engineering Geology*, vol. 56, no. 3-4, pp. 373–388, 2000.
- [5] E. Cardarelli, M. Cercato, and G. Di Filippo, "Assessing foundation stability and soil-structure interaction through integrated geophysical techniques: a case history in Rome (Italy)," *Near Surface Geophysics*, vol. 5, no. 2, pp. 141–147, 2007.

- [6] D. Colombo and M. de Stefano, "Geophysical modeling via simultaneous joint inversion of seismic, gravity, and electromagnetic data: application to prestack depth imaging," *Leading Edge*, vol. 26, no. 3, pp. 326–331, 2007.
- [7] M. Dobroka, A. Gyulai, T. Ormos, J. Csokas, and L. Dresen, "Joint inversion of seismic and geoelectric data recorded in an underground coal mine," *Geophysical Prospecting*, vol. 39, no. 5, pp. 643–665, 1991.
- [8] L. A. Gallardo and M. A. Meju, "Characterization of heterogeneous near-surface materials by joint 2D inversion of dc resistivity and seismic data," *Geophysical Research Letters*, vol. 30, no. 13, pp. 1–4, 2003.
- [9] W. Hu, A. Abubakar, and T. M. Habashy, "Joint electromagnetic and seismic inversion using structural constraints," *Geophysics*, vol. 74, no. 6, pp. R99–R109, 2009.
- [10] L. Gardner, "An area plan of mapping subsurface structure by refraction shooting," *Geophysics*, vol. 4, pp. 247–250, 1939.
- [11] F. S. Grant and G. F. West, *Interpretation Theory in Applied Geophysics*, McGraw-Hill, New York, NY, USA, 1965.
- [12] M. Bernabini, "Alcune considerazioni sui rilievi sismici a piccole profondità," *Bollettino di Geofisica Teorica e Applicata*, vol. 26, pp. 106–118, 1965.
- [13] D. L. Lager and R. J. Lytle, "Determining a subsurface electromagnetic profile from high-frequency measurements by applying reconstruction-technique algorithms," *Radio Science*, vol. 12, no. 2, pp. 249–260, 1977.
- [14] K. A. Dines and R. J. Lytle, "Computerized geophysical tomography," *Proceedings of the IEEE*, vol. 67, no. 7, pp. 1065–1073, 1979.
- [15] A. C. Tripp, G. W. Hohmann, and C. M. Swift, "Two-dimensional resistivity inversion," *Geophysics*, vol. 49, no. 10, pp. 1708–1717, 1984.
- [16] M. H. Loke and R. D. Barker, "Rapid least-squares inversion of apparent resistivity pseudosections by a quasi-Newton method," *Geophysical Prospecting*, vol. 44, no. 1, pp. 131–152, 1996.
- [17] A. Carrara, M. Cardinali, R. Detti, F. Guzzetti, V. Pasqui, and P. Reichenbach, "GIS techniques and statistical models in evaluating landslide hazard," *Earth Surface Processes and Landforms*, vol. 16, no. 5, pp. 427–445, 1991.
- [18] F. Guzzetti, A. Carrara, M. Cardinali, and P. Reichenbach, "Landslide hazard evaluation: a review of current techniques and their application in a multi-scale study, Central Italy," *Geomorphology*, vol. 31, no. 1–4, pp. 181–216, 1999.
- [19] N. Santacana, B. Baeza, J. Corominas, A. de Paz, and J. Marturiá, "A GIS-based multivariate statistical analysis for shallow landslide susceptibility mapping in La Pobla de Lillet Area (Eastern Pyrenees, Spain)," *Natural Hazards*, vol. 30, no. 3, pp. 281–295, 2003.

Research Article

A Combined Methodology for Landslide Risk Mitigation in Basilicata Region by Using LIDAR Technique and Rockfall Simulation

G. Colangelo¹ and A. Guariglia²

¹ Department of Infrastructure and Civil Protection, C.so Garibaldi 139, 85100 Potenza, Italy

² GEOCART, Engineering Company, Viale del Basento 120, 85100 Potenza, Italy

Correspondence should be addressed to G. Colangelo, gerardo.colangelo@regione.basilicata.it

Received 30 March 2011; Accepted 18 May 2011

Academic Editor: Francesco Soldovieri

Copyright © 2011 G. Colangelo and A. Guariglia. This is an open access article distributed under the Creative Commons Attribution License, which permits unrestricted use, distribution, and reproduction in any medium, provided the original work is properly cited.

Rockfalls represent a significant geohazards along the SS18 road of Basilicata Region, Italy. The management of these rockfall hazards and the mitigation of the risk require innovative approaches and technologies. This paper discusses a hazard assessment strategy and risk mitigation for rockfalls in a section of SS118, along the coast of Maratea, using LIDAR technique and spatial modelling. Historical rockfall records were used to calibrate the physical characteristics of the rockfall processes. The results of the simulations were used to define the intervention actions and engineering strategy for the mitigation of the phenomena. Within two months, 260 linear meters of high-energy rockfall barriers for impact energies up to 3000 kJ were installed. After that, according to road authority, the SS18 road was opened in a safe condition. The results represent a valid cognitive support to choose the most appropriate technical solution for topography strengthening and an example of good practice for the cooperation between innovative technologies and field emergency management.

1. Introduction

The geology, relief, neotectonics, climate, and vegetation of Basilicata make the region vulnerable to landslides, but the number of reported landslides in the region has increased over recent centuries, and this has been interpreted as a result of changes in land use [1]. The main typologies of landslide in Basilicata Region are represented principally by earth flow, rock fall and complex landslide due to the combination of movement. The landslide phenomena involved buildings and infrastructures constructed on the slopes. The risk for people and assets needed the intervention of the endusers involved in the risk management and, in particular, the inspection of Regional Department of Infrastructure and Civil Protection (RDICP). In many involved areas (roads, buildings, etc.) and for many families evacuation decrees have been issued in order to allow the damage valuation. The complexity of the phenomena demanded a multidisciplinary approach based on the integration of all the data (direct and indirect)

acquired in the affected areas. An important contribution to obtain high-resolution information on the geomorphology can be provided by LiDAR technique (light detection and ranging). The LiDAR is an active high-resolution technology capable to provide accurate three-dimensional topography measurements. Many examples of the LiDAR application are reported in the literature [2, 3]. In many cases the results of its application allowed to reconstruct the geometry of the slope, to locate the source area of rockfall, and so forth. By using airborne full-waveform laser scanning, some LiDAR have been performed in some damaged areas of the Basilicata region.

In this paper we present the results of Rasi rockfall landslide, located at the western side of Maratea town. Airborne LiDAR data acquisition was carried out on February 2010 for Rasi and surrounding areas. The LiDAR technique allowed us to obtain DTM with a high resolution of 0.25 m. The area have been preliminary studied and rockfall source area have been individuated by the technical staff of the RDICP.

At the same time, the information coming from the airborne LiDAR have been very useful in the phases of the valuation damage and to design engineering solution [4].

2. Geological Setting

The investigated areas are located in Basilicata Region, along the west zone of southern Apennines chain. The latter is mainly composed of sedimentary cover of platform and deep water environments, scraped off from the former Mesozoic Ligurian ocean, from the western passive margin of the Adriatic plate and from the Neogene-Pleistocene foredeep deposits of the active margin. From west to east, the main Mesozoic domains are as follows: (1) the internal oceanic to transitional Liguride-Sicilide basal domains (internal nappes), (2) the Apennine carbonate platform, (3) the Lagonegro-Molise basins, and (4) the Apulian carbonate platform [5].

Maratea area is characterized by carbonate rocks outcrop. They belong to the Bulgheria-Verbicario and Alburno-Cervati Units and exhibit heavy fracturing and occasional karstification. The structural setting depends on the overthrusting of carbonate rocks of the Bulgheria-Verbicario Unit on the clayey-marly made of the plastic soils of the Liguride Unit [6].

On February 2010 a rockfall event occurred to Maratea town in the Rasi area. The rockfall was caused by the high state of fracturing of the outcrops dolomite limestone rocks. After an impact on the material poured out on the debris, the blocks have determined a real discharge of debris on the SS18 road (Figure 1).

The debris on the slope was characterized by elements of different size ($0.5\text{--}1\text{ m}^3$). A part of the debris has stopped its course on SS18 road while another part of debris with highest volume has continued its race for rolling up to the next portion and the lower wooded slopes until sea.

Historical rockfall records were used to calibrate the physical characteristics of the rockfall processes [7]. In the study area was carried out a field measurements to define the geomechanical properties of rock outcrops [8].

3. LIDAR Technique and Modelling

After the closing of the SS18 by ANAS road authority, for the complexity of the phenomena and for the changing of the morphology of the slope, the RDICP needed to have detailed information to evaluate appropriate strategy. To this aim a high-resolution scanning airborne topographic LiDAR was deployed.

3.1. Survey System. The system is characterized by a Flight Management System-CCNS (computer-controlled navigation system), by a Riegl LMS-Q560 high-resolution laser measurement system, by a sensor system control and data logging unit (LMcontrol), DigiCAM-medium-format airborne digital camera system.

A peculiar characteristic of Riegl LMS-Q560 is the "Full Waveform" recording that guarantees a vertical resolution less than 50 cm if compared to noncontinuous lasers



FIGURE 1: Rockfall on SS18 road located in the Rasi area.

(4 echoes) characterized by a vertical resolution higher than 1.20 cm. The flight plan is characterized by flight level of 500 m, speed 50 knots, and pulse repetition rate 240 KHz and 45 flight lines with side overlap of 60%. Double refinement with crossed lines and side overlap of 80% has been measured. The point density is 25 pt/sqm on the whole area and 200 pt/sqm on area affected by landslides, the photo with ground sample has a distance <10 cm.

3.2. Laser Data Processing. The laser data have to be processed to produce a cloud of points preclassified.

For each pulse the system records the full waveform that have to be analyzed to obtain the echoes. Afterward each echo has to be georeferenced through the GPS-INS information.

The Full waveform was processed or decomposed into a sum of components or echoes (that can be unlimited) where each component represents the target shoot. The amplitude of each component is recorded as intensity with a dynamic range of 16 bits (65.536 colors). In addition, the Echo digitization with subsequent full-waveform analysis provides much more information on the target characteristics compared to conventional laser ranging systems. For each echo are associated the range, the echo width, and the amplitude.

3.3. Rockfall Modeling. Rockfalls 2D-3D numerical simulations were carried out using two different methods in order to forecast the velocities, the bounce heights, and the possible impact energy on the dynamic barriers.

In particular, due to computational cost of 3D simulations, they have been used only to define the main trajectories of the rockfall. To refine the results obtained by the previous simulations, a 2D model has been introduced.

The 3D model used for the computation of the trajectories of rockfalls considers the blocks like point block that have an impact on an elevation attributed plane. This plane is formed by a grid of tridimensional nodes that form a triangular mesh which represents the entire area between the launch and the stopping of the blocks.

The elements of the grid have been defined so that, in the inside of the perimeter, the inclination and the direction of the slope together with the physical parameters of the model (Table 1), defined as ratio of the post- and pre-impact energy, can be considered constants.

TABLE 1: Physical parameters used in the model.

Material	Coefficients		Friction angle
	Rn	Rt	θ
Bedrock outcrops	0.35 ± 0.04	0.85 ± 0.04	28 ± 2
Talus cover	0.40 ± 0.04	0.80 ± 0.04	28 ± 2
Talus with vegetation	0.32 ± 0.04	0.45 ± 0.04	28 ± 2
Asphalt	0.40 ± 0.04	0.90 ± 0.04	30 ± 2

The definition of the launch area assumes a previously analysis of the launch niche so that for every block a launch velocity as a function of the initial route along the wall can be defined.

This model also carries out the analysis for the positioning and sizing of protective works. The initial computation verifies that the block knocks against the barrier and does not climb over it, so it verifies that the impact kinetic energy of the block can be completely absorbed by the protective work.

This model for the computation of trajectories of rock falls is mostly used for the design of embankments as protective works because, thanks to their high expansion, the embankments can be able to intercept a great number of blocks before requiring maintenance interventions or reconstruction, and assure a remarkable absorption energy, typically generated by long fall routes.

The trajectory of the block can be determined by using the motion equations of a block. Referred to as cartesian orthogonal axis system these equations are as follows:

$$\begin{aligned} s &= v \cdot t + s_0, \\ z &= -\frac{1}{2} \cdot g \cdot t^2 + v_z \cdot t + z_0, \end{aligned} \quad (1)$$

where v = block velocity; t = time; g = gravitational constant; s = crossed space.

In this way the trajectory of the motion results to be formed by a series of parabolas drawn from the launch point to the impact points on the slope, in the initial phase of the motion, and between two consecutive impact points on the slope, or at the foot, until the stopping point.

By indicating with v_n and v_t the components (normal and tangential) of the velocity before the impact, v'_n and v'_t after the impact can be calculated using the following relations:

$$\begin{aligned} v'_n &= v_n \cdot l_n, \\ v'_t &= v_t \cdot l_t, \end{aligned} \quad (2)$$

where l_n and l_t are the restitution coefficients, varying in the interval 0-1 [9].

About 2D simulations, a lumped-mass method used to design safe slopes. Based on a statistical analysis of fall paths in 2D, it calculates trajectories and rebound energy for falling blocks as well as velocity and height for any point of a slope. It also estimates the location of the fall-path endpoint, which is the most significant factor affecting safety.

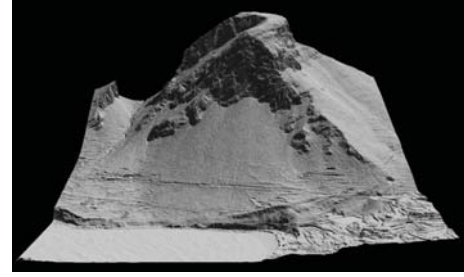


FIGURE 2: High-resolution DTM obtained by airborne full-waveform laser scanning.

In this code every rock is modelled as an infinitely small particle. Rock size is thus not considered, but the equations used in the sliding algorithm reflect shapes that are circular.

Since each rock is infinitely small there is no interaction between particles, only with segments of slope, so each rock behaves as if participating alone in the simulation.

This means that noncleaned catch benches are not well reflected in the code unless the debris slope is explicitly modelled as part of the slope.

RocFall 4.0 is a more or less raw model of the mechanical process of a rockfall, as it does not take into account block shape, size, or angular momentum. Nevertheless, it has the important advantages that its calculations include statistical distributions of the parameters and that it operates very rapidly. In a mining exploitation it is impossible to know falling block shape and size in advance; nonetheless, this code is appropriate for the purpose of modelling rockfall in quarries, given that it is not that difficult to assume statistical distributions for restitution coefficients and friction angles [10].

4. Analysis of the Results

The information associated with the geological, geomorphological, and impact signs along the slope allowed us to define the geomechanic parameters used for the modelling.

During the first part of the emergency the removal of instable blocks on the slope permitted us to have information to support for the back analysis. In fact during these operations, it was possible to following the real trajectory of the blocks and the bounce height envelope. At the same time, a DTM with 0.25 m of accuracy was produced on the area along SS18 road close to the Maratea coast (Figure 2).

The DTM associated with the simulations had a dual use, both during the emergency and in the phase of design engineering solution.

In particular, during the emergency, dangerous areas were detected and possible order families evacuation decrees were individuated. Moreover, thanks to the high detail of the DTM unstable blocks on difficult as vertical portion of the slope were identified and removed by the climbers. After the emergency phase was concluded, there was the necessity to put some protective barrier on the slope. To this aim, a set of simulated trajectory on DTM with the barrier was produced. So, in a first step an incremental Delaunay triangulation was performed on DTM model to produce a 3-dimensional simulations of the possible paths of the rockfall (Figure 3).

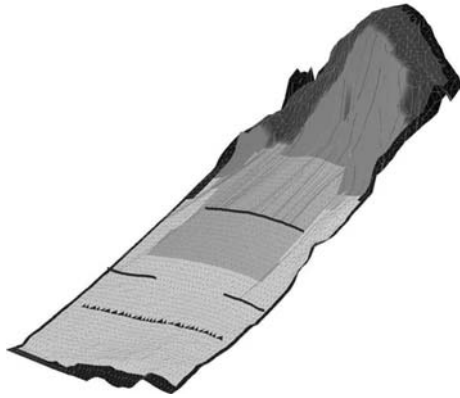


FIGURE 3: 3D simulations of the possible paths of the rockfall.

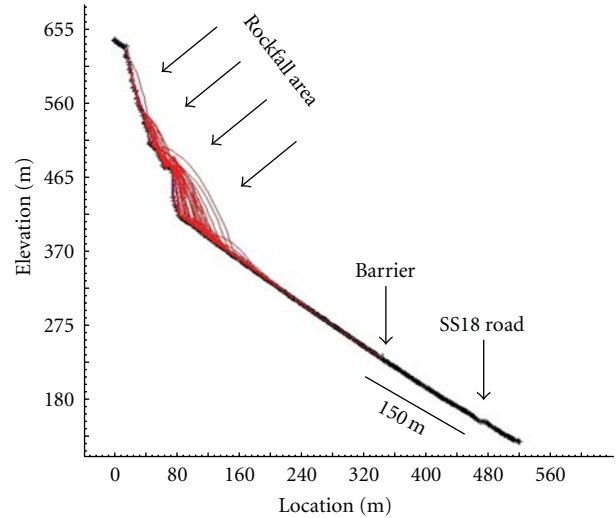


FIGURE 5: Example of the various rockfall layouts for profile n.10 with trajectory and protective barrier.

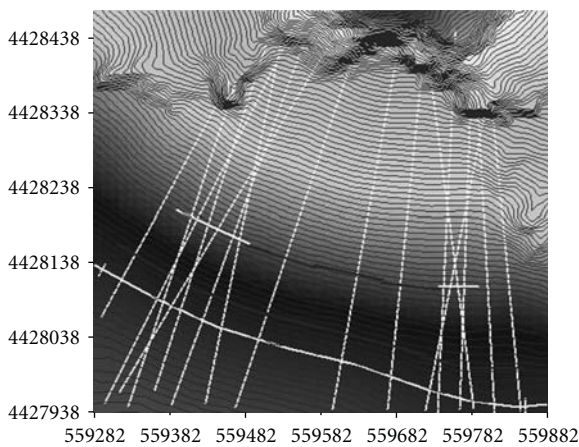


FIGURE 4: Location of the simulation profiles. Sections and SS18 road are indicated on the map. The area inside the rectangle represents the unstable part of the slope.

The 3D project setting is characterized by 100 number of rock blocks with a volume of $2 \pm 1 \text{ m}^3$, mass of 2.400 kg/m^3 .

In a second step, to have more information on the single path, some 2-dimensional simulations of the trajectory of the rockfall, along some well-established profiles were performed.

The rockfall event has interested an area of 40.000 m^2 located in the upper part of the slope. So, along the slope, 16 profiles have been located to effectuated 2D simulations (Figure 4).

The 2D project setting is characterised by 500 number of rocks with a volume of $2 \pm 1 \text{ m}^3$ and a mass of 2.400 kg/m^3 , normal and tangential coefficients are the same reported on Table 1. The results of the simulations (Figure 5) were used to design dynamic barriers (Figure 6).

Within two months 260 linear meters of high-energy rockfall barriers for impact energies up to 3000 kJ and $h = 5.00 \text{ m}$ were installed. After that, according to ANAS road authority, the SS18 road was opened in a safe condition.

5. Conclusions

A new approach has been applied for investigating rockfall landslides in Basilicata Region. In particular an airborne

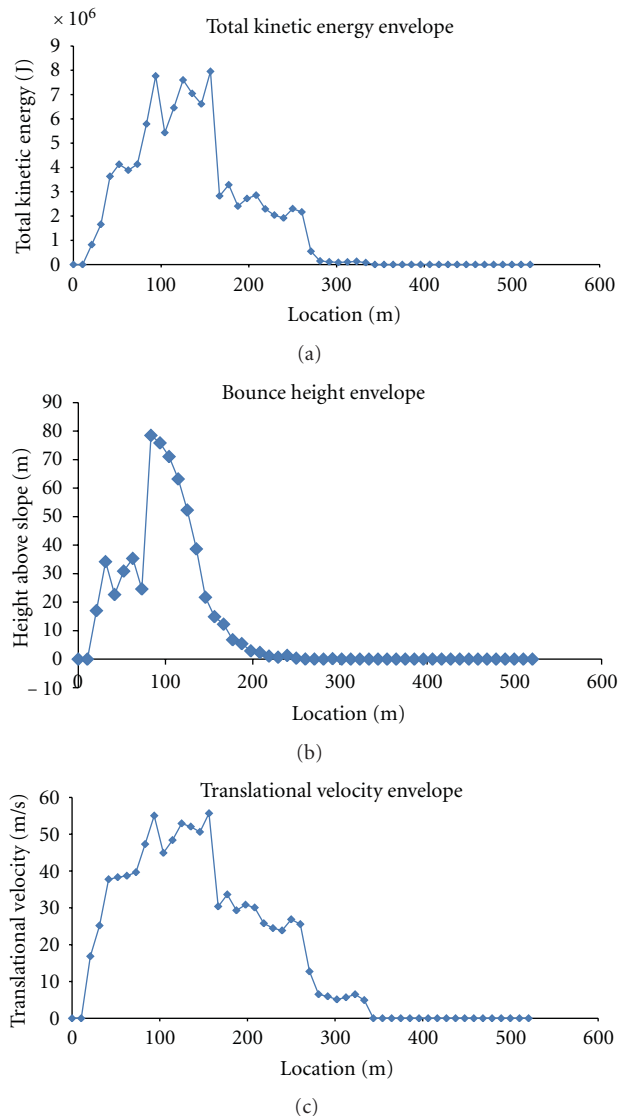


FIGURE 6: Example of analysis along the profile n.10.

LiDAR technique has been used to study the morphology of the area through a high-resolution DTM.

The main objectives of RDICP were the safety of the peoples and the way to follow the evolution of the event with simulation models.

Geological, geomorphological, and impact signs along the slope have been used for the back analysis.

Subsequently, a high-resolution DEM has been used to obtain simulation about the trajectory of the landslide blocks.

The simulations allowed us to design the protective barriers for the mitigation of the phenomena. The information obtained by the application of indirect surveys appeared to be particularly useful for the endusers involved in the risks management. In particular, taking into account the frequency of landslide events, the obtained data could give a valid contribution regarding the damage valuation and the intervention actions.

The DTM associated with the simulations had a dual use, both during the emergency and in the phase of design engineering solution.

This approach, fast and economic, gives us an interpretative tool to evaluate possibly evacuation decrees through the simulations of the trajectories and a second time to design the intervention actions for the mitigation of the phenomena.

Acknowledgments

Thanks to V. Mancusi, A. Lanotte, L. Laurino, and V. Cavallo for the technical support during the field emergency management, GeoAmbiente s.r.l. for the availability during the different phases of the work, and A. Vicari for the useful suggestions on the paper.

References

- [1] O. Stuart, "20th-Century urban landslides in the basilicata region of Italy," *Environmental Management*, vol. 17, no. 4, pp. 433–444, 1993.
- [2] M.-H. Derron and M. Jaboyedoff, "LiDAR and DEM techniques for landslides monitoring and characterization," *Natural Hazards and Earth System Science*, vol. 10, no. 9, pp. 1877–1879, 2010.
- [3] W. H. Schulz, "Landslide susceptibility revealed by LiDAR imagery and historical records, Seattle, Washington," *Engineering Geology*, vol. 89, no. 1-2, pp. 67–87, 2007.
- [4] L. R. Alejano, B. Pons, F. G. Bastante, E. Alonso, and H. W. Stockhausen, "Slope geometry design as a means for controlling rockfalls in quarries," *International Journal of Rock Mechanics and Mining Sciences*, vol. 44, no. 6, pp. 903–921, 2007.
- [5] D. Scrocca, E. Carminati, and C. Doglioni, "Deep structure of the southern Apennines, Italy: thin-skinned or thick-skinned?" *Tectonics*, vol. 24, no. 3, pp. 1–20, 2005.
- [6] M. Polemio and G. D'Ecclesiis, "Aquifer vulnerability in Maratea Mountains (southern Italy)," *Geografia Fisica e Dinamica Quaternaria*, vol. 20, no. 1, pp. 113–117, 1997.
- [7] C. Mallardo, "Frane da crollo nel territorio comunale di Maratea (PZ)," *Geologia Territorio e Ambiente*, vol. 2, pp. 3–6, 2002.
- [8] G. Spilotro, A. Petraglia, and V. Pizzo, "Relazione generale strada statale N18 'tirrena inferiore,'" *Assistenza Tecnica per l'acquisizione ed il trattamento dei dati necessari alla zonazione della pericolosità e del rischio di caduta massi lungo il tratto di strada compreso tra i km 220+600 e 243+670*. ANAS, Compartimento Regionale della Viabilità, Potenza, 2009.
- [9] GeoRock3D 2009. Geostru, Ver.1.rev.70.
- [10] Rocscience, *Rocfall, Statistical Analysis of Rockfalls*. Ver. 4.042, 2004.

Research Article

Site Assessment of Multiple-Sensor Approaches for Buried Utility Detection

Alexander C. D. Royal,¹ Phil R. Atkins,² Michael J. Brennan,³ David N. Chapman,¹ Huanhuan Chen,⁴ Anthony G. Cohn,⁴ Kae Y. Foo,² Kevin F. Goddard,⁵ Russell Hayes,¹ Tong Hao,¹ Paul L. Lewin,⁵ Nicole Metje,¹ Jen M. Muggleton,³ Adham Naji,⁶ Giovanni Orlando,⁶ Steve R. Pennock,⁶ Miles A. Redfern,⁶ Adrian J. Saul,⁷ Steve G. Swingler,⁵ Ping Wang,⁵ and Christopher D. F. Rogers¹

¹ School of Civil Engineering, University of Birmingham, Birmingham B15 2TT, UK

² School of Electronic, Electrical and Computer Engineering, University of Birmingham, Birmingham B15 2TT, UK

³ Institute of Sound and Vibration Research, University of Southampton, Southampton SO17 1BJ, UK

⁴ School of Computing, University of Leeds, Leeds LS2 9JT, UK

⁵ School of Electronics and Computer Science, University of Southampton, Southampton SO17 1BJ, UK

⁶ Department of Electronic and Electrical Engineering, University of Bath, Bath BA2 7AY, UK

⁷ Department of Civil and Structural Engineering, University of Sheffield, Sheffield S10 2TN, UK

Correspondence should be addressed to Alexander C. D. Royal, a.c.royal@bham.ac.uk

Received 12 February 2011; Accepted 15 April 2011

Academic Editor: Erica Utsi

Copyright © 2011 Alexander C. D. Royal et al. This is an open access article distributed under the Creative Commons Attribution License, which permits unrestricted use, distribution, and reproduction in any medium, provided the original work is properly cited.

The successful operation of buried infrastructure within urban environments is fundamental to the conservation of modern living standards. Open-cut methods are predominantly used, in preference to trenchless technology, to effect a repair, replace or install a new section of the network. This is, in part, due to the inability to determine the position of all utilities below the carriageway, making open-cut methods desirable in terms of dealing with uncertainty since the buried infrastructure is progressively exposed during excavation. However, open-cut methods damage the carriageway and disrupt society's functions. This paper describes the progress of a research project that aims to develop a multi-sensor geophysical platform that can improve the probability of complete detection of the infrastructure buried beneath the carriageway. The multi-sensor platform is being developed in conjunction with a knowledge-based system that aims to provide information on how the properties of the ground might affect the sensing technologies being deployed. The fusion of data sources (sensor data and utilities record data) is also being researched to maximize the probability of location. This paper describes the outcome of the initial phase of testing along with the development of the knowledge-based system and the fusing of data to produce utility maps.

1. Introduction

The preservation of buried infrastructure within the urban landscape is of fundamental importance if modern living is to be maintained. Failure to maintain the buried infrastructure can rapidly result in breakdown of utility service provision; yet traditional open-cut methods used to repair and replace the buried utilities are inherently disruptive to society's functions and damaging to the carriageway (beneath which the utilities are commonly buried), and

potentially the buried infrastructure itself. A recent UK study estimated that street works cost the UK £7bn in lost revenues annually; comprising £5.5bn in social costs and £1.5bn in direct damages [1]. Open-cut practices deployed within the carriageway constitute a significant proportion of this work, and hence cost. Trenchless technology could be used in place of open-cut methods when installing or repairing the buried infrastructure, although concerns over the risk of damaging existing adjacent utilities have limited the uptake of these techniques (particularly those that excavate, displace,

or otherwise disturb the ground). These risks partially stem from the inability to precisely locate all buried utilities below the carriageway without some form of proving excavation. Mapping the Underworld (MTU) is a research initiative that aims to research and develop the tools necessary to locate all utilities below the carriageway and record their position, thereby promoting the use of trenchless technology. One of the MTU research projects focuses on developing a prototype multisensor platform that can be used to improve the probability of complete detection of all buried utilities below the carriageway.

2. Development of MTU Multisensor Device

The MTU initiative is an umbrella for several EPSRC-funded projects that collectively aim to research and develop the tools necessary to locate, position, and electronically record the buried utilities, in the context of UK practices. Projects include the development of resonant RFID tags, which can be affixed to new utilities, or retrofitted to existing utilities during periods of maintenance and repair, that improve detection rate of the buried utilities when using Ground Penetrating Radar (GPR) [2]; the development of surveying techniques to permit the accurate positioning of utilities in heavily built up urban environments (so-called “urban canyons” where traditional GPS can struggle to operate); the development of a database that integrates existing electronic and paper records denoting utilities locations across the utilities industry [3]. The MTU initiative also includes the research and development of a multisensor device, a platform that will employ four geophysical location technologies previously identified in a feasibility study [4] as being potentially complementary and which, when intelligently combined, should improve the probability of utility detection. The four sensing technologies comprise GPR, vibro-acoustics, low-frequency electromagnetic fields (LFEM), and passive magnetic fields (PMF).

The creation of the MTU multisensor device is a novel undertaking [4]: the authors are not aware of a platform previously created using these four sensing technologies, and indeed a number of the sensing technologies are being developed from first principles for this project. However, the construction of the multisensor device in itself does not represent the sea change that the MTU initiative aims to achieve; prototype multisensor devices have been created in the past and utility location companies may also deploy multiple geophysical detection technologies sequentially on a site when the situation demands it. Empirical experiences from the utility location industry would suggest the deployment of a geophysical device, or a suite of devices, without prior knowledge of the site in question makes detection of all utilities difficult in all but the simplest of ground conditions and utility layouts. The ground-breaking aspect of this MTU project arises from how the device is to be deployed and how the data are analysed (Figure 1). The project considers two additional streams of information that could potentially be used to enhance the data acquired by the multisensor device: the ground conditions encountered on site and the existing electronic utility location records. This information will be

incorporated into the surveying protocols developed for the prototype device to optimise deployment and to increase the probability that all buried utilities are located.

It is well understood that the ground conditions can have a significant effect upon the performance of the geophysical location technologies employed to find the buried utilities, therefore in conjunction with the multisensor device, research is being undertaken into both the relationship between the geotechnical properties and corresponding geophysical properties of various soils, and changes in geophysical properties for various soils with the seasons (or more precisely recent weather conditions) to provide the foundations for the development of a soil evaluation knowledge-based system. This will be used to inform the surveyor of potential problems for one or more of the sensing technologies on the site and facilitate the optimisation of the deployment of the device on the site. In addition to the focus on ground conditions, research is being undertaken to incorporate existing utility position records into the process. Records tend to exist for utilities buried on a given site (presuming that the utilities present do not predate the keeping of modern records), and whilst these records are neither always accurate in the locations they report nor complete, they do provide an indication of what should be encountered when surveying the site. Research undertaken in the VISTA project [3] has led to the development of a common database for the utility sector and new research is underway to use data held on the VISTA database to improve surveying practices. Not only could the information held on the database act as a primer, giving an indication of what to expect when surveying the site, during the desk study, but it could also be used as a first approximation of layout and fused with the data emanating from the multisensor device to produce a probability map for the layout of the utilities. Such an approach should increase the likelihood of detection. Furthermore, fusing the data together could also highlight discrepancies within the electronic record, thereby facilitating the updating of the records to improve the electronic resource for future use.

The MTU multisensor device project is a four-year research programme funded by the UK's Engineering and Physical Sciences Research Council (EPSRC) and commenced in January 2009. The sensing technologies for the project are all being developed specifically for the project, either from first principles (LFEM and PMF) or as fundamental enhancements of the existing state of the art. By the end of 2010 the majority of the sensing technologies had been developed to a point where testing in field conditions could be undertaken and the results from the initial tests are described herein with the aim of drawing the first raft of important conclusions for those working in this topic area.

2.1. The Sensing Technologies

2.1.1. Ground Penetrating Radar. GPR, reckoned by many to be the mainstay of the shallow geophysical techniques used to detect buried utilities, is being developed for two applications in the MTU project. The first application is a traditional

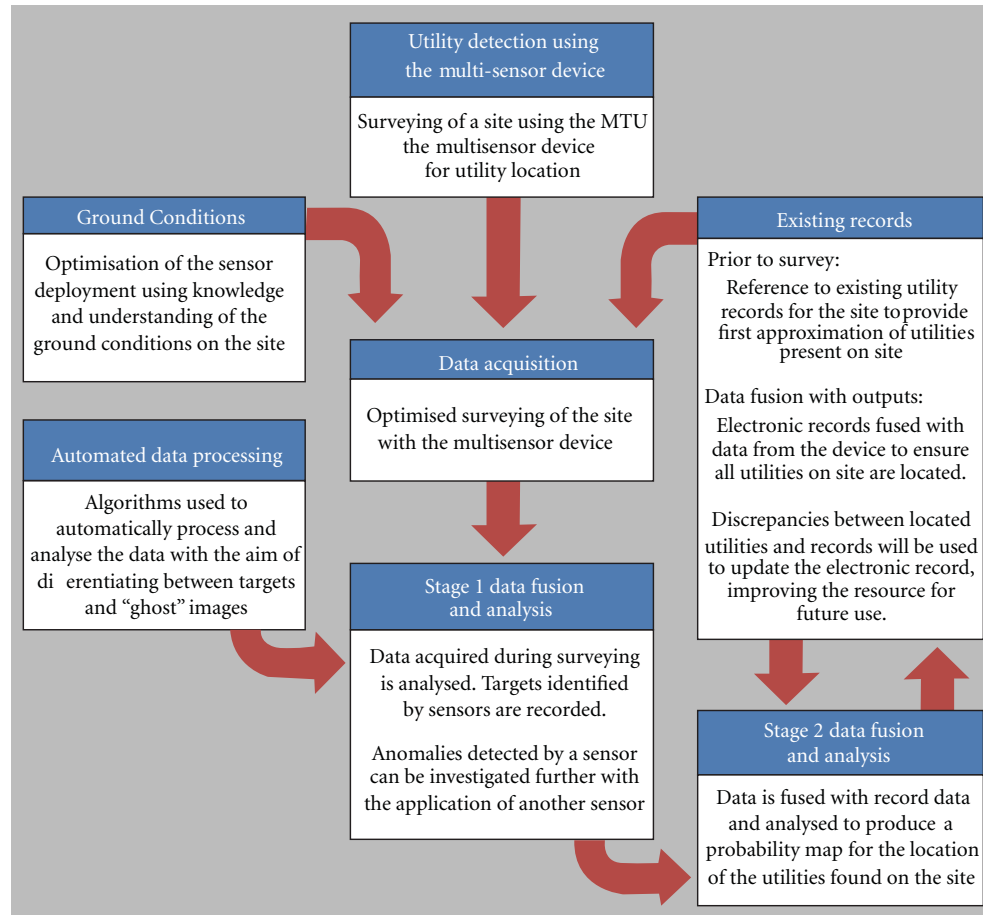


FIGURE 1: Flow diagram illustrating the principles behind the MTU multisensor device.

surface-mounted GPR sensor, that is, it is configured in “look-down” mode, while the second is an in-pipe GRP sensor that can be equipped with transmitter (Tx) and receiver (Rx) antennas to either “look-out” (by combining the Tx and Rx in the in-pipe device) or “look-through” with the Tx in pipe and the Rx mounted on the surface (Figure 2), or indeed vice versa. The GPR being developed for the project is configured to permit Orthogonal Frequency Division Multiplexing (OFDM; see Figure 3), as results of theoretical modelling suggest that swept frequency GPR (such as OFDM) could improve detection rates [6]. Unlike the other sensing technologies developed for the project, which are predominantly assembled in-house or from components purchased off the shelf, the bespoke components of the GPR have been outsourced for manufacture and its manufacture is only now being finalised. Initial proof testing has therefore been restricted to a commercially available dual frequency pulse-system GPR (250 MHz and 700 MHz) with the aim of determining whether conflicts between the sensing technologies arise when used in conjunction.

2.1.2. Vibro-Acoustics. The outcomes from a prior feasibility study [8] identified that a vibro-acoustic detection system would offer the opportunity to locate buried infrastructure,

in particular plastic pipes. Two basic deployment strategies were identified: direct excitation of the utility (via an access point, such as a man hole) and excitation of the ground. A modified system would also have significant potential for use in pipe, although this is not being researched at this stage.

Detection via pipe excitation arose from previous work on leak noise propagation and detection [9–11], indicating that when a leak is present, a significant amount of energy can propagate from the pipe to the surrounding medium at low frequencies. This energy then propagates to the ground surface. Whilst most leaks will not generate enough energy to significantly excite the necessary ground-borne waves, if the fluid in the pipe is excited intentionally, the energy propagation away from the pipe could be exploited to locate underground pipes. The technique is depicted in simplified form in Figure 4, with excitation of either the fluid directly or of the pipe structure. However, it is envisaged that it might be possible to locate buried pipe work by exciting the ground surface in the vicinity of the pipe and detecting the presence of waves scattered from it. When the ground is mechanically excited, waves will propagate away from the excitation point. Depending on the form of excitation, different wave types will be excited in the ground and these waves can be detected, depending of course on the frequency, at ranges of tens of metres. However they will be scattered

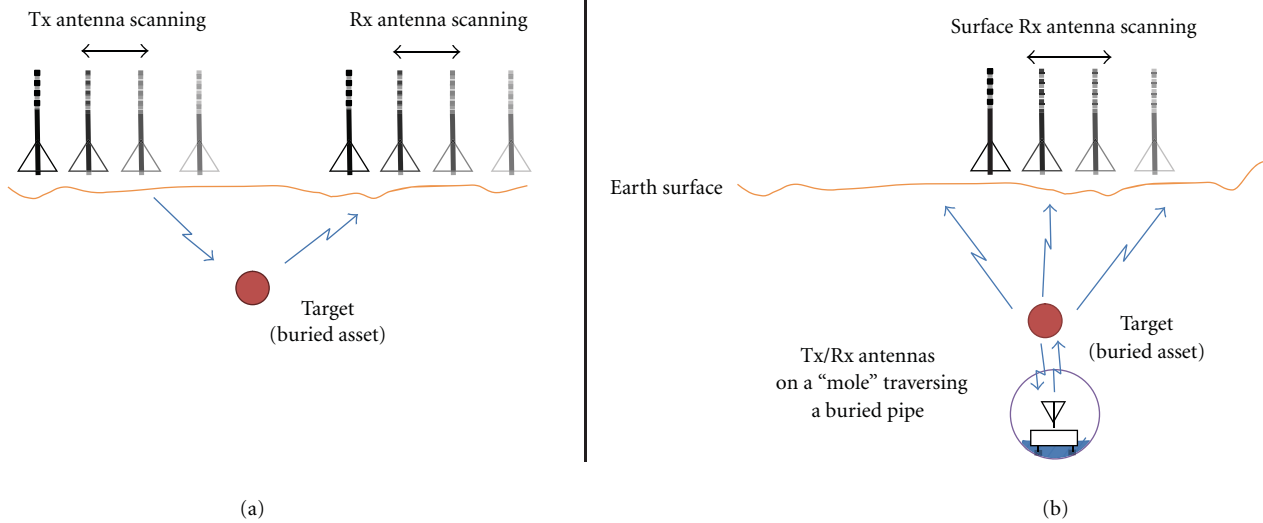


FIGURE 2: Two GPR applications: (a) traditional look-down mode and (b) look-out or look-through mode (where Tx is the transmitter and Rx the receiver antenna) (images previously published in Royal et al. [5]).

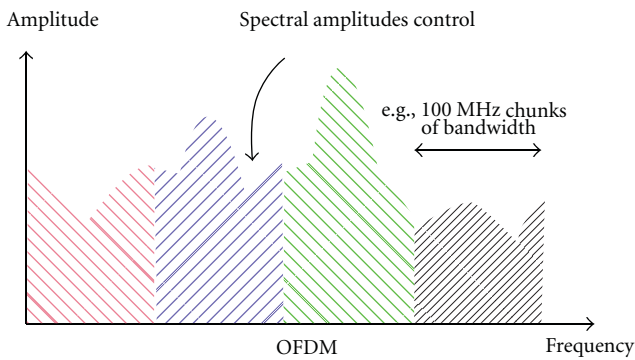


FIGURE 3: Illustration of Swept Frequency GPR: OFDM.

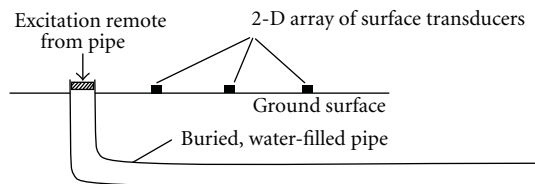


FIGURE 4: Illustration of pipe detection with vibro-acoustic sensing technology via excitation of water filled pipe (first published in [7]).

by objects, such as pipes, whose mechanical properties are different from the soil, even if the pipes are buried several metres deep. Detection and analysis of the scattered waves would, in principle, allow the pipes to be accurately located. Two possible basic configurations for this technique are shown in Figures 5(a) and 5(b), respectively.

Previous measurements on a dedicated experimental pipe rig [8] demonstrated that the pipe excitation method could be successful in locating the run of a pipe when the pipe was excited vertically at the surface with an inertial

shaker. Frequency response measurements relating vibrational velocity on the ground to the input excitation were acquired. Contour plots of spatially unwrapped phase revealed the location of the pipe to within 0.1 m-0.2 m. Magnitude contour plots revealed the excitation point and also the location of the pipe end. By examining the unwrapped phase gradients along a line above the pipe, it was possible to identify the wave type within the pipe responsible for the ground surface vibration. Furthermore, changes in the ground surface phase speed computed using this method enabled the location of the end of the pipe to be confirmed.

For the ground excitation, as for the pipe-excitation method, time-extended signals are used to generate an illuminating wave. A stacking method is then employed, which involves the measurement of velocities on the surface of the ground. Cross-correlation functions between the measured ground velocities and the excitation signal are then calculated and summed to generate a cross-sectional image of the ground. The wide cross-correlation peaks caused by high-ground attenuation are partially compensated for by using a generalised cross-correlation function called the smoothed coherence transform [12].

2.1.3. Low-Frequency Electromagnetic Fields. The LFEM sensor, implemented using frequency domain processing, has been developed from first principles for the project. It has been included within the multisensor device since it has the potential to complement GPR by locating utilities that GPR would have difficulty in detecting. Examples include small diameter plastic pipes and fibre optic cables, pipes that lie in the blind zone of GPR, and large deep buried infrastructure, such as deep sewers, that lie beyond the range of traditional methods. The LFEM sensor works by inducing a small current through the ground using capacitive coupling, in response to which a quasistatic electric field is

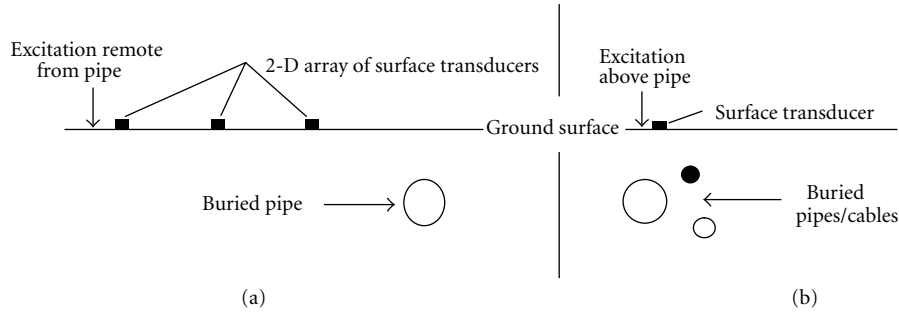


FIGURE 5: Illustration of pipe detection with vibro-acoustic sensing technology via ground excitation (a) offset from the utility and (b) directly above the utility. Note that the excitation can be normal or parallel to the ground surface, or a combination of both (first published in [7]).

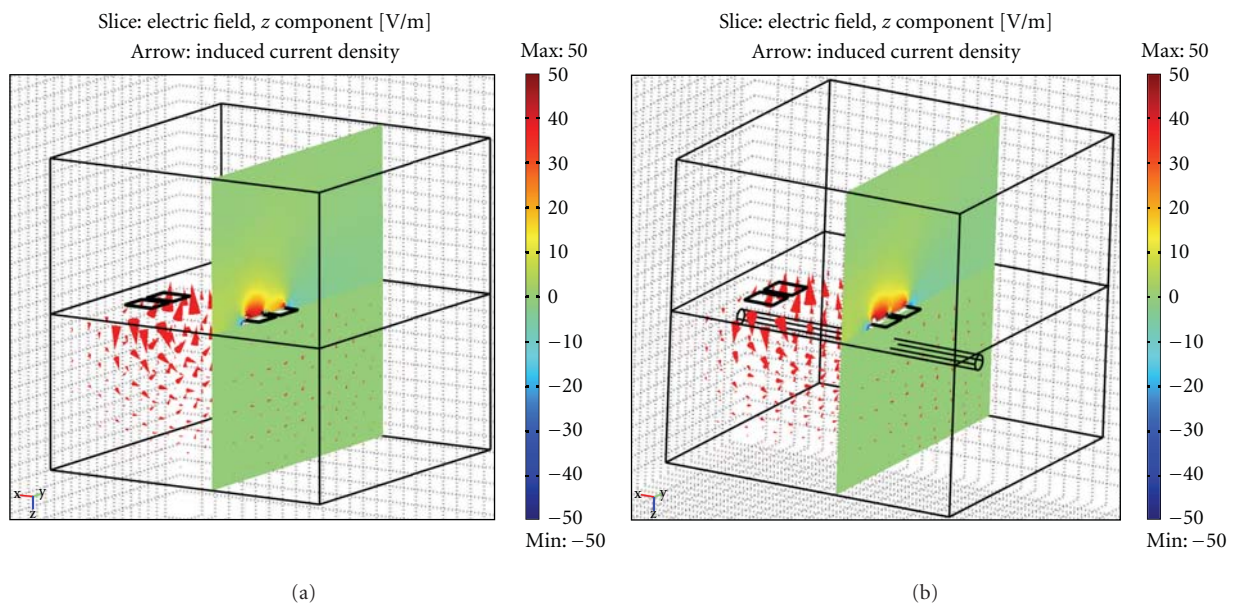


FIGURE 6: Finite element simulation of the near-surface electric field without pipes (a) and with pipe (b) (images previously published in Royal et al. [5]).

generated. Any materials that present a contrast in electrical properties to the soil will disturb the induced current flow [13–18]. By using precisely controlled digital-to-analogue signal converter generating voltages at two transmitting capacitive plates, anomalies in the electric field near the surface resulting from the disturbance of current density in the ground can be detected (Figure 6) by using an ultrahigh impedance amplifier connected to receiving capacitive plates. The synchronisation of the anomalies detected during the survey with the positional data for the multisensor device during the survey allows for the prediction of the position of the buried utilities. The depth can then be evaluated using inversion methods analogous to techniques in resistivity imaging [14].

The frequency selection strategy for this sensing technology is based upon avoiding strong ambient EM fields (e.g., 50 Hz and its harmonics) as well as interfering components from other sensors. This can be accomplished by first measuring the ambient field without active transmission across

the valid frequency range of 1 Hz to 25000 Hz and adaptively selecting the frequency component with the least energies. The transmission frequency must also be above the constraint imposed by the cut-off frequency associated with the physical dimension of the transmission plates. The transmission frequency was 1.735 kHz in this trial.

2.1.4. Passive Magnetic Fields. The flow of current within a buried AC power cable creates an associated oscillating magnetic field, which the PMF sensor can detect. Current flow within the power cable can also induce currents within neighbouring utility pipelines or ducts made from conducting materials, such as cast iron, and the PMF has the potential to detect these utilities also. Programs are being developed to use the detected signals to locate and identify various types of buried power cable or other conducting services. The PMF sensor comprises an array of passive search coils arranged in a 3D configuration to detect the magnetic field.

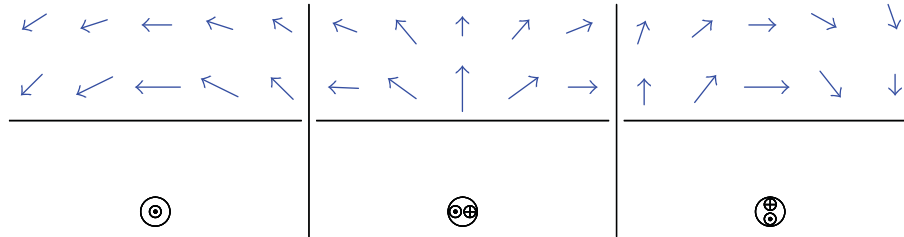


FIGURE 7: Illustration of the concept underpinning the detection of operational power cables using multiple passive search coils. The arrows show the flux density distribution due to three different current distributions in the power cable. The field plots shown are for a hypothetical untwisted cable, as the field of a more realistic twisted multi-core cable is difficult to represent in 2D.

Initially seven, though shortly to be increased to 27, passive search coils mean that the magnetic field can be measured at many positions simultaneously. Using simultaneous measurements of the flux in the various coils of the PMF sensor allows for the estimation of the cable position (Figure 7) by comparing the magnetic field recorded to theoretical responses for various types and configurations of power cables (three phase cables, single phase cables, cables with balanced or unbalanced loads, straight or twisted cables, etc.).

3. Outcomes from Preliminary Testing

To meet the aim of this MTU project, that is, to demonstrate the ability to detect *all* utilities buried below the carriageway, a comprehensive programme of proving trials is planned to assess the capability of the prototype device. However, as the sensing technologies and their deployment strategies are being developed it is important that initial phases of testing on sites containing simple utility layouts, with known positions, are carried out. The first phase of testing occurred at a site located near Blithfield reservoir in Staffordshire (Figure 8). The test site was specifically created to permit the investigation of leakage detection in water distribution pipes using acoustic technologies, and as such comprises a buried water pipe (over 100 m long) with several access points spaced along the pipe allowing for the simulation of leaks via a shaker or standpipe. The site also contains a buried electricity cable, thus allowing for the testing of all sensor types being developed for the project.

Initial site testing took place on three occasions in July, August, and November 2010: the PMF, dual-frequency pulsed GPR, and LFEM were deployed independently during the first visit; the GPR and LFEM were combined on the second occasion and the vibro-acoustics surveyed on the final occasion. Initially the section of the site selected for testing was surveyed with the commercial GPR using a coarse 1 m grid, and both utilities were readily detected. Having located the utilities' plan location and estimated the depths with the GPR, the prototype sensing technologies were deployed. The LFEM and vibro-acoustic sensing technologies were used to locate the water pipe and the PMF sensor the cable. The vibro-acoustic testing involved both pipe and ground excitation methods (Figure 9), with measurements of vibrational velocity on the ground (in three orthogonal directions, using

3-axis geophones). The geophones were deployed using both a grid pattern (for the pipe excitation method) and single lines traversing the pipe (for the ground excitation method). The grid used was 16 m long and extended 1.5 m on each side of the pipe, taking measurements every 0.5 m and using the centreline of the pipe as the baseline for the survey; the single lines each employed 7 geophones spaced at 1.0 m intervals. The LFEM survey was undertaken using GPS to provided positional information instead of following a grid pattern within the area of interest, taking the fence line as the baseline for the survey. The PMF sensor took readings at 16 points along a 4.5 m survey line that crosses the cable, again taking the fence line as the baseline for the survey.

3.1. Vibro-Acoustics. Two pipe excitation methods were used at the test site: an inertial shaker was attached at an access point (as used in previous work by the vibro-acoustics team), and "leak" noise was generated by opening a standpipe connected at the same access point (Figure 9). It was anticipated that, using either method, the wave predominantly excited in the pipe would be the axisymmetric, fluid-dominated wave [19], this being the preferred wave type. For both pipe excitation cases, frequency response measurements relating the vibrational velocity on the ground to the input excitation were acquired. In the case of the shaker excitation (a 2-minute swept sine input from 10 Hz to 400 Hz) the voltage input to the shaker was used as a reference, while for the "leak" noise excitation an accelerometer was located adjacent to the standpipe (visible in Figure 9(a)), the measured acceleration being used as the reference. It was found that the simulated leak excited the preferred wave in the pipe more effectively than the inertial shaker, with the straight-line frequency-unwrapped phase behaviour evident at frequencies between 30 Hz and 200 Hz at all grid locations in this case. For the shaker excitation, the upper cut-off for some grid locations was 100 Hz with the lower bound increasing in some cases to around 50 Hz. Data from both excitation types were found to be useful in inferring the pipe location, with the data from the "leak" excitation being superior. Contour plots of the spatially unwrapped phase for both the vertical velocity and horizontal (aligned parallel with the pipe) velocity measurements in the frequency range 40 Hz–80 Hz revealed the location of the pipe for this excitation type. Two sample frequencies (42 Hz and 72 Hz) are shown in Figure 10. At 42 Hz, the vertical geophone measurements

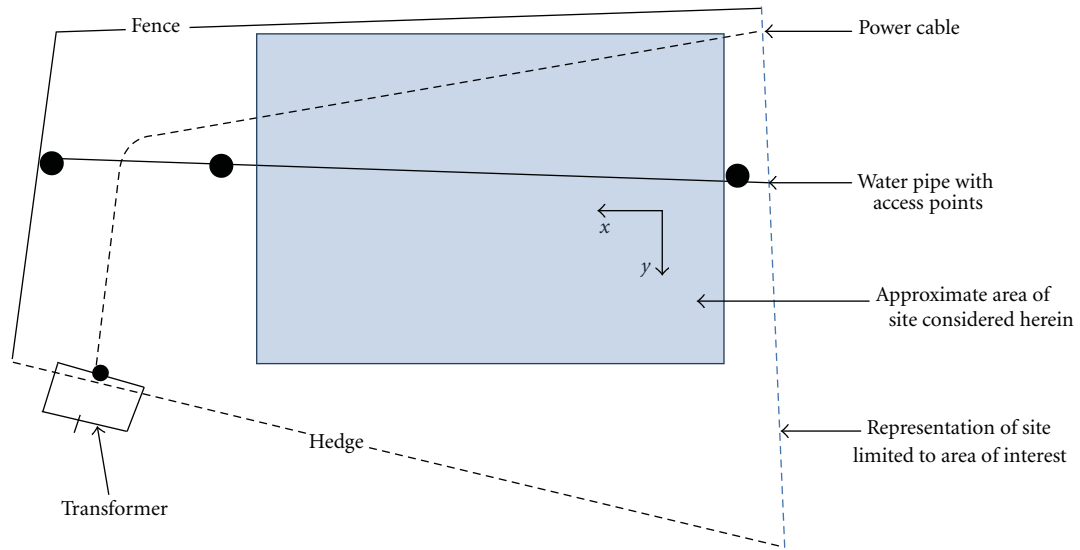


FIGURE 8: Layout of the Blithfield test site.

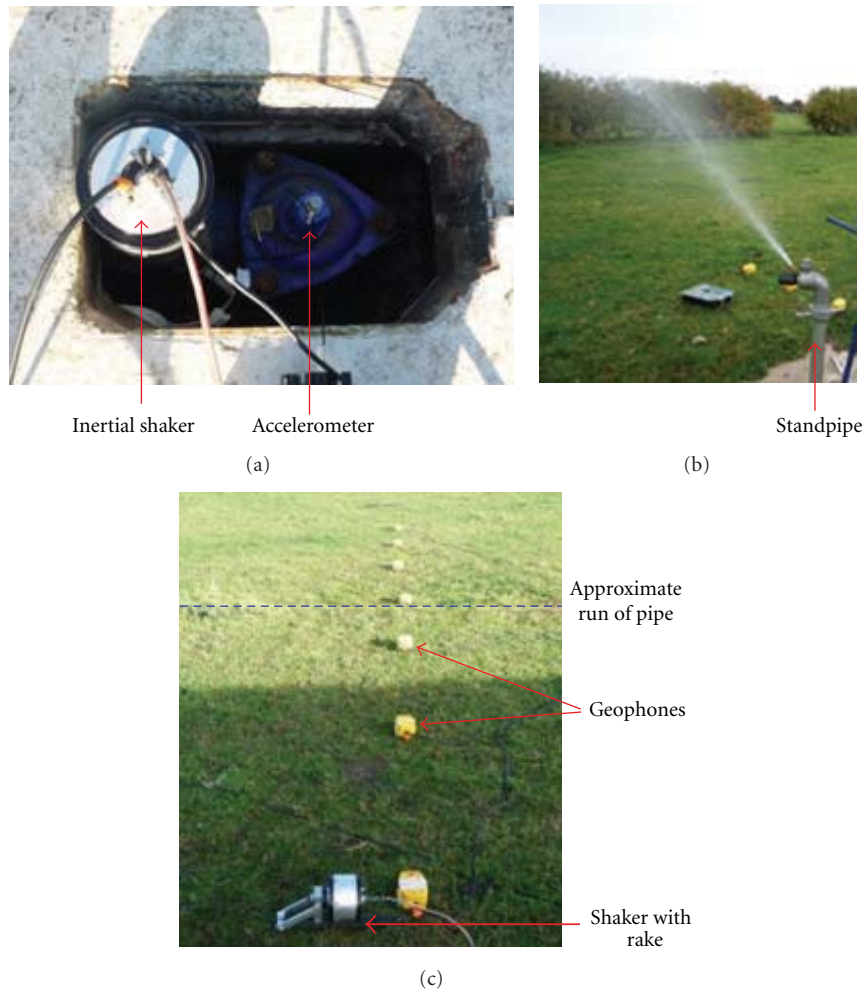


FIGURE 9: Excitation of (a) the pipe via inertial shaker, (b) the pipe via standpipe, and (c) excitation of the ground using an inertial shaker with rake attachment.

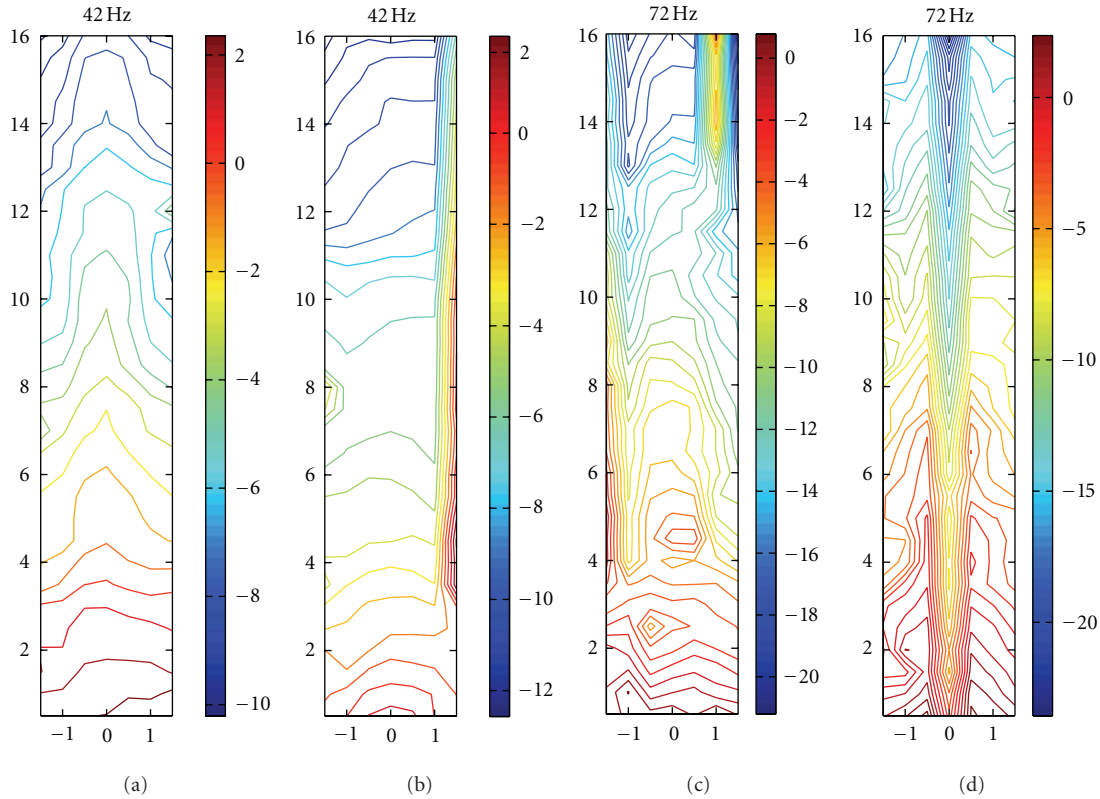


FIGURE 10: Contour plots of spatially unwrapped phase for simulated leak noise in each plot, the x - and y -axes correspond to the axes shown in Figure 8 rotated by 90 degrees; the unwrapped phase is shown in radians; the pipe runs up the centre line in each plot (a) vertical measurements: 42 Hz; (b) horizontal measurements: 42 Hz; (c) vertical measurements: 72 Hz; (d) horizontal measurements: 72 Hz.

clearly show the run of the pipe; at 72 Hz, the horizontal measurements show this more convincingly.

The ground excitation method employed at the test site was similar to that used by [20, 21], using a configuration similar to that shown in Figure 5(b); the pipe was thought to be buried too deeply for the point measurement method (Figure 5(a)) to be employed successfully. The ground was excited horizontally in order to preferentially excite horizontally polarized shear waves (these have been found to give more reliable results than using compressional waves). Directionality (a desirable feature) was achieved via extended contact with the ground, using a rake attached to the inertial shaker. Again a 2-minute swept sine input from 10 Hz to 400 Hz was employed. The surface vibration velocity was measured using a line of 7 geophones perpendicular to the run of the pipe, with a spacing of 1 m. The rake was placed in the ground so that the motion of the shaker was parallel with the pipe, thus producing shear waves travelling across it (the arrangement is shown in Figure 9(c)). The shaker and rake assembly was positioned at each geophone location in turn, thus enabling the stacking to be performed over 49 (7×7) source-receiver position combinations. Stacking requires that the shear wave velocity through the ground is known. This is calculated from the time delay associated with peaks in the correlation function at different source-receiver positions. Different pairs of positions will give slightly different results so there is always some uncertainty

in the final estimated wave speed (which, of course, may vary slightly from location to location). With this in mind, a range of speeds was used in performing the stacking and obtaining the final cross-sectional image. In this case, wave speeds of 65 m/s, 70 m/s, 75 m/s, 80 m/s, 85 m/s, and 90 m/s were used. Figure 11 shows the cross-sectional images obtained along with the geophone positions on the surface and the estimated location of the pipe (black circle—obtained from burial records). A dark red area can be seen in all the plots in the vicinity of the black circle (Figure 11), indicating the presence of a target. Examining the figures as a whole it can be seen that the perceived depth of the target increases with increases in the estimated wave speed, varying from approximately 0.8 m at 65 m/s to 1.7 m at 90 m/s. Laterally, the perceived position varies by around 0.3 m, slightly to the right of the expected location. The precise pipe burial location relative to the geophone positions was not confirmed by other means at the time of testing.

The results of the testing using vibro-acoustics corroborated the previous evidence of the ability to detect a buried utility using pipe excitation and the results from the initial ground excitation experimentation were encouraging. The vibration results from the ground excitation contain uncertainties and more work is needed to refine wave speed estimation, and so forth, as well as developing possible refinements to how the data are captured (e.g., geophone spacing) and processed. Excitation of the ground removes the

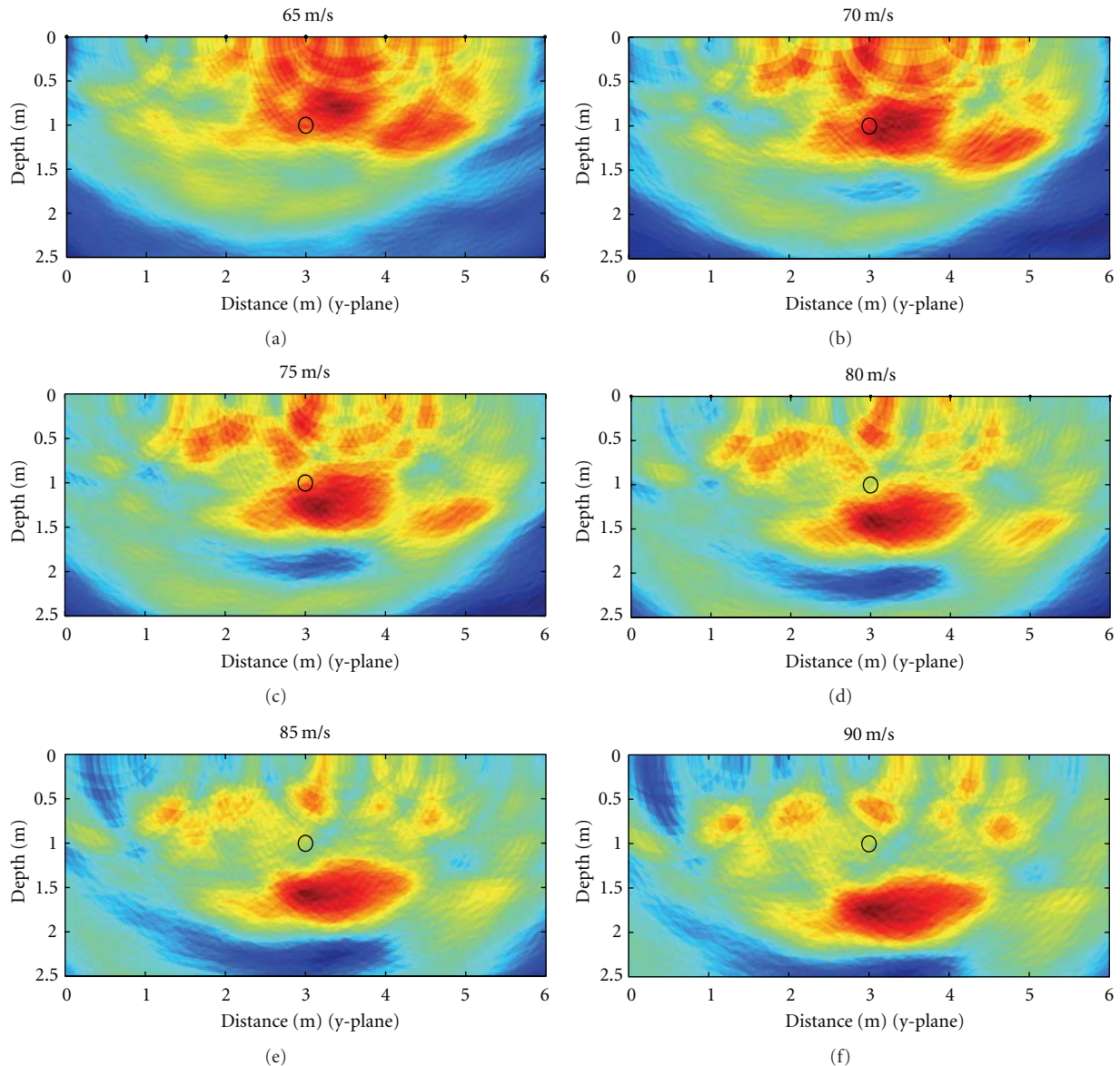


FIGURE 11: Cross-sectional stacking images using 6 different estimated wave speeds.

requirement for access to the utility, thereby greatly improving the potential flexibility of vibro-acoustics to detect utilities. Combining data from the different technologies could resolve the uncertainty attributed to this approach.

3.2. Passive Magnetic Fields. A seven-search-coil assembly was used on the test site (Figure 12). It was connected to an eight-channel data acquisition system and was manually moved along the heading chosen such that it crossed the power cable. The frame was aligned to the local coordinate system selected for the survey (the fence line in this case), and the new position measured and entered into the data acquisition program. These coordinates were added to the relative positions of the coils on the frame, which are loaded from a file. In the final prototype multisensor device it is envisaged that the positional information required to analyse the PMF data will be provided by common positional sensing

technologies (which will measure changes in inclination and azimuth with time) mounted on the platform.

Figure 13 illustrates the outcomes of the data analysis for a section of the survey undertaken with the PMF sensor. The image represents an error contour map, with the contours representing the proportion of the field that could not be explained by the magnetic field generated by any straight cable at the plotted position. This minimum error is generated for a cable position of $y = 3.5$ m, an apparent depth of 0.37 m, a heading of -12.4° , a twist rate of -4.65 rad/m; the returned error at this location is 3%. This positional information contradicts the utility records, which suggest that the cable position at this location is given by $y = 2.5$ m, with a depth between 0.4 m and 0.6 m and a heading of -13° (Figure 13). Based on the estimated currents for the best-fit parameter values, a 3-phase factor has been calculated. The value of this parameter can vary from zero



FIGURE 12: The prototype PMF sensing technology.

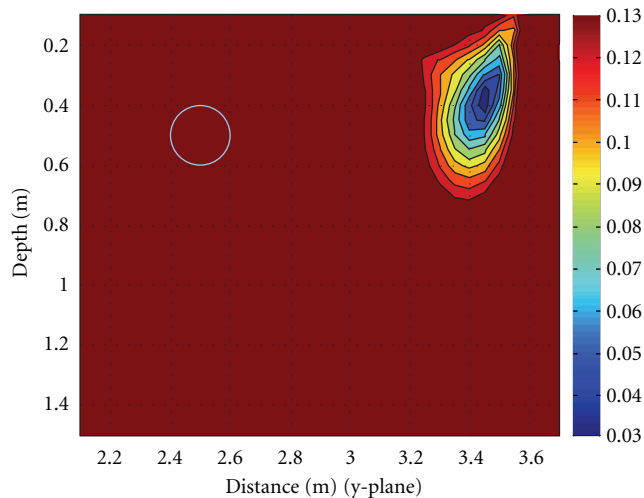


FIGURE 13: Error contour map generated from the recorded magnetic field, with the cable location most likely to occur where the errors are the least. The position of the cable according to the records is shown as a circle.

for a 2-core single-phase cable to 100% for a 3-core 3-phase cable with a balanced load. The calculated value of 62.1% could indicate a 3-phase cable with a very unbalanced load, a single-phase cable with substantial neutral-earth loop current, or a single phase cable that is not straight and has a net current. With reference to the transformer, it is visibly evident that there is only a single-phase supply, and hence it must be a single-phase cable. To distinguish between the two remaining interpretations would require measurements to be taken over a wider range of headings that cross the cable position, whereas all the measurements used to produce these results were taken with the support frame centred along one heading.



FIGURE 14: Prototype sensor platform deployed at the Blithfield test site (illustrating the LFEM sensor).

The outcomes of the PMF testing are encouraging and demonstrate the ability of the system to locate a power cable in an uncluttered environment. Further development is required for this detection technique to be effective in more cluttered urban environments. Ultimately, it should be possible to locate and identify different types of buried power cables and to locate other metal utilities that carry earth currents or currents induced by the magnetic field generated by operating power cables.

3.3. Ground Penetrating Radar and Low-Frequency Electromagnetic Fields. GPR and LFEM surveys were undertaken sequentially during the first visit to the site and were later followed by a combined GPR-LFEM survey with the sensing technologies mounted on a prototype platform (Figure 14). In each of these tests the sensing technologies were deployed using a dynamic test protocol, in which the GPR and the LFEM sensors are pushed across the site. The GPR was successful in detecting the two utilities of interest on the site during the first site visit in July, when the weather had been hot and dry for a reasonable period of time. As a result of the ground being relatively dry, the hyperbolae visible on the real-time display were very distinct (Figure 15(a)). Expressing the GPR as a plan view allows for the location of the pipe within the surveyed area to be determined (Figure 15(b)). Plotting the GPR data in such a format also allows for the comparison in performance of the LFEM sensor (Figure 15(c)). The LFEM sensor has identified anomalies within the site, as expected, and encouragement is taken from the accumulation of anomalies detected along the length of the pipe (highlighted by a red dotted ellipse on Figures 15(b) and 15(c)). The anomalies detected near the known location of the pipe (Figure 15(c)) exhibit variation in position when plotted in a plan view. This is partly due to the speed of survey (>0.5 m/s) which limited the signal-to-noise ratio of the collected data. This can be addressed with increased transmission voltage in order to maximise current flow in the ground. It also transpires that these variations can be attributed, in part, to the positioning system employed during the test. Two GPS systems were used with the LFEM sensing technology: a kinematic GPS for positioning and a secondary conventional GPS system for time synchronisation

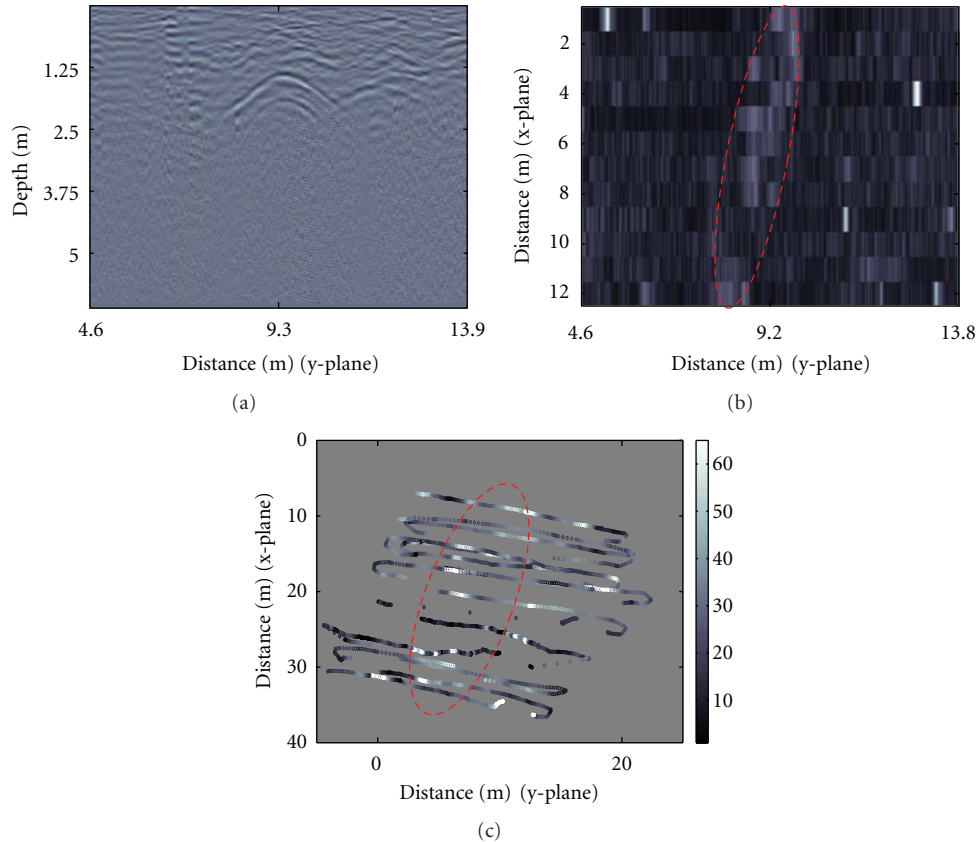


FIGURE 15: GPR results (250 MHz) from initial survey: (a) hyperbola returned when directly over the pipe, (b) plan view of the GPR survey (averaged at depth slices where the hyperbolae are prominent), and (c) the LFEM survey (overlaid onto the GPS positions within the predefined area), where a brighter region represents higher anomalous measurement.

(which was not suitable for precise positioning). Subsequent data analysis illustrated that the data from the kinematic GPS was corrupt, resulting in reliance on the conventional GPS system for positioning. Significant positional errors (of the order of one to two metres) were suspected as the brighter pixels indicating anomalies do not align linearly in the region where the target pipe is known to be buried. The outcome of this test thus highlighted the need to capture kinematic GPS data with short epochs to identify the position of the platform when on site. This amendment notwithstanding, the initial trial results were considered to be promising.

3.4. Potential Conflicts When Combining the Sensing Technologies. The four sensing technologies have not yet been mounted on a single platform, although the commercial GPR and prototype LFEM sensing technologies were successfully combined. However, the research team has identified a number of potential conflicts that are being addressed as the design of the prototype multisensor platform is advanced.

The combination of the GPR and LFEM sensors created no apparent conflicts when analysing the results. This was attributed to a difference in survey speeds, with GPR requiring milliseconds and the LFEM being developed to operate, at least initially, in the decisecond range. This has led to the proposal for a sequential protocol for sensor deployment, with the GPR sensor acquiring and storing data whilst the

other sensing technologies are “passive”; analysis of the GPR data can then take place whilst the other sensing technologies are triggered (Figure 16). The difference between the rates at which GPR and the other sensing technologies acquire data makes this a feasible strategy and in large part addresses the concerns arising from co-location of the GPR sensor. However, the survey speeds of the LFEM, PMF, and vibroacoustic sensing technologies are such that it is believed that these surveys must be undertaken concurrently to ensure the advance rate of the multisensor platform is not compromised.

Potential conflicts between the LFEM and PMF sensing technologies have been identified:

- (i) the magnetic fields associated with the current injection of the LFEM could be detected by the PMF,
- (ii) currents could be injected into the search coils via stray capacitance,
- (iii) the plates used in the LFEM could distort the magnetic field associated with the buried cables.

In order to minimise these potential conflicts, the frequency used by the LFEM has been raised to 16.67 kHz, thus minimising interference with the multiples of 50 Hz that are produced by AC power transmission. Moreover, the current injected by the LFEM technology is to be low

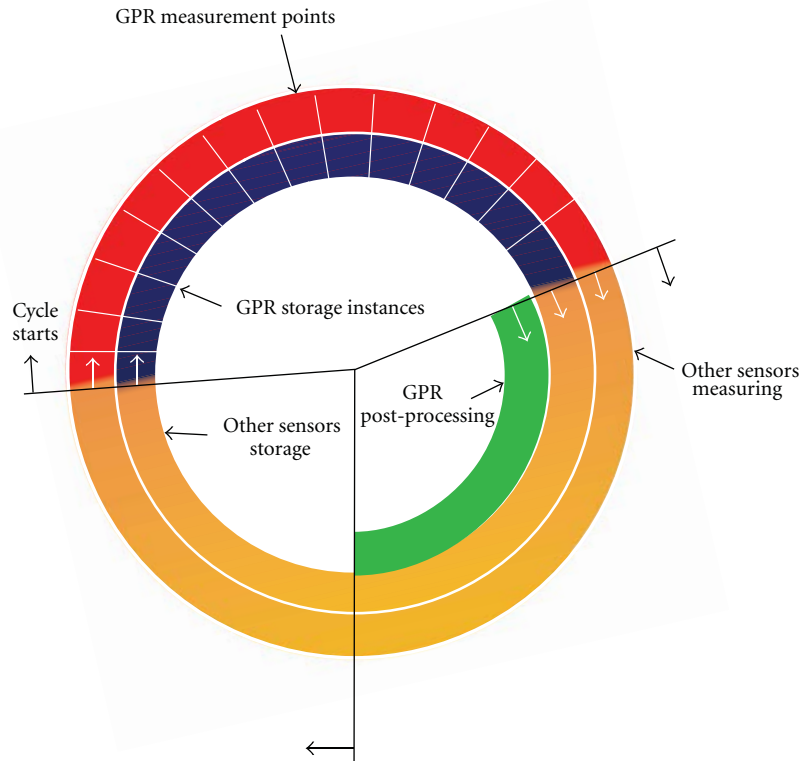


FIGURE 16: Schematic representation of data acquisition, storage, and processing.

(in the milliamp range), and the capacitance plates used in the LFEM are shielded with an aluminium cover. However, these precautions are not without limitations: whilst the shielding will greatly reduce the cross-coupling, it increases the distortion of the magnetic field caused by power-frequency eddy currents in the LFEM sensors, thereby reducing the benefit of using more coils. The current injected by the LFEM system will still induce voltages within the search coils, but the high frequency of the injected current makes it relatively easy to filter away the unwanted signal. For the chosen frequency and amplitude of the injected current, a minimum separation of 200 mm between the LFEM current leads and the PMF coils should ensure that these voltages are not significantly larger than those that the search coils are looking for; filtering can then be used to give adequate signal-to-noise ratios. Distortion of the field by the presence of the LFEM sensors is a bigger problem, as neither filtering nor time sharing will help. Simple modelling suggests that if the PMF coils are maintained at least 640 mm away from the LFEM plates, the distortion will be limited to about 1%. Until these conflicts can be quantified, the sensing technologies mounted on the multisensor platform are to be separated to minimise the potential effects of these conflicts. It is appreciated that a spacing of 640 mm between LFEM and PMF sensing technologies will make the platform relatively large, which would be undesirable for a commercial platform. However, as the platform is being developed as a prototype “proof of concept” device, its size is relatively unimportant at this stage. If, when the conflicts have been quantified, the required separation is considered too large,

alternative measures would have to be used to overcome the problem. Potential conflicts between the vibro-acoustics and other sensing technologies are currently being considered.

4. Intelligent Tuning of Sensing Technologies to the Ground

The MTU philosophy contends that in order to optimise the efficiency of the multisensor platform, the ground conditions in which the survey is to be undertaken should be known, as far as possible, and the implications of the ground conditions on the performance of the sensing technologies understood, prior to the deployment of the device on site. Such knowledge and understanding would allow the surveyor to identify the conditions where certain sensing technologies will perform significantly better or worse than the others, and thus potentially increase the probability for detection of the utilities on the site. For example, electrically conductive ground conditions cause significant attenuation losses of electromagnetic signals, resulting in shallow penetration depths for GPR. Knowing that such ground conditions are likely to be met on site might encourage a change in deployment of GPR from the traditional surface mounted “look-down” surveying to the adoption of the “look-out” or “look-through” modes of surveying with the use of the in-pipe GPR (Figure 2). Conversely, an alternative sensing technology, such as vibro-acoustics, might be selected as the primary sensor, with GPR being chosen to act as a back-up device in locations where it is deemed appropriate.

Therefore, one of the aims of the project is to develop a system that can be used to predict how the ground conditions will impact on the performance of the sensing technologies before deployment occurs.

The basis of the predictive tool being researched thus relies upon information on the ground conditions at any specific location, which in itself is not straightforward due to the type of information commonly available. The *geotechnical* properties of shallow ground conditions can be relatively well characterised within the UK. Databases such as the National Geotechnical Properties Database (NGPD) maintained by the British Geological Survey, BGS [22] and the soil properties map (maintained by the National Soil Resources Institute and geared towards agriculture science), along with data published in the literature, comprise a large collection of soil properties nationwide. However, whilst geographical variation in soil properties within the databases is apparent, there is little readily available information on the seasonal variation in soil moisture content, a factor that directly affects soil electromagnetic properties [23]. In addition, the *geophysical* properties of soil are often poorly characterised, with limited information within the public domain. The geotechnical (and limited geophysical) property data available within databases and the literature are predominately based upon drilling records and/or site/laboratory investigations. Whilst the information will act as an informative guide for the nature of the likely soil formation(s) to be encountered, the data only strictly relate to the specific site originally investigated. Moreover, the heterogeneous nature of soil, the natural variations in properties with depth, and the many anthropogenic alterations to the ground in urban areas suggest considerable potential variation and thus the information is indicative only.

While a simple prediction model for soil behaviour on a site would be desirable, it is believed that such an approach alone would struggle to predict the impact of the ground conditions on the performance of the sensing technologies. Instead it is proposed that a system with the ability to interpret a wide range of available information be adopted, drawing on a wide knowledge base that utilises *any* available input parameters in order to predict the electromagnetic properties of the ground. In turn, these need to be robustly related to the performance of the sensing technologies. This is the key motivation for implementing a knowledge-based system (KBS) approach for this work. The design of the KBS is illustrated in (Figure 17). The main output from the KBS is the prediction of the geophysical properties associated with individual sensing technologies. This data can be used to guide the survey by providing prior estimates of the suitability of individual sensing technologies to a survey site. The fine-tuning of the sensing technologies can then be carried out locally using estimates of ground properties obtained from the KBS together with those inferred from individual sensing technologies and (where possible) the results of in situ tests that directly measure geophysical ground properties.

There are three key inputs to the KBS to be used alongside expert, *a priori* knowledge: the link between available

geotechnical properties of the soil and its electromagnetic properties, the seasonal variation of the soil moisture content with depth, and the opportunistic approximation of soil properties based upon individual sensing technologies and in-situ tests. As stated previously, the availability of geophysical properties of a soil are typically limited, therefore additional research is being undertaken to develop test apparatus to readily measure the geophysical properties of various soils and further the understanding of the correlation between geotechnical and geophysical properties of soil technologies [24–28]. Research is also being undertaken to broaden the understanding of the relationships between changing seasons and recent weather, variations in soil water content profiles with depth [23], and the resulting geophysical properties for various soil types.

4.1. Linking Soil Geotechnical Properties to Its Electromagnetic Properties. The literature on soil electromagnetic properties presents a number of modelling and prediction methodologies. A review of these can be found in [29]. In the KBS, the model being adopted is the semiempirical mixing model that relies upon soil composition and moisture content, based upon the work of Peplinski et al. [30], Mironov et al. [31], and Dobson et al. [32]. The choice of this model is desirable given the availability of soil composition data from the NGPD, while soil classification tests are routinely performed on soil samples extracted in association with construction work being carried out in urban areas. The KBS should, and can, allow for the incorporation of additional modelling methodologies as well as the refinement of integrated models. Therefore, the choice of this semiempirical model presents a starting point for the implementation of the KBS and does not define its limitation.

Testing was undertaken at the Blithfield site using time domain reflectometry (TDR) and a coaxial sensor (developed for the project), in conjunction with the semiempirical model. A soil composition of 30% sand, 65% silt, and 5% clay was used in the model, based upon the particle size grading as specified in ISO 14688 for the identification and classification of soil. The bulk density was estimated to be 1.2 Mg/m^3 , while a volumetric water content of 8.2% was calculated by applying the model by Topp et al. [33] to the in-situ measurement carried out with the TDR. The complex permittivity predicted is shown in Figure 18, with the result demonstrating good agreement with the values obtained from the direct measurement of soil electromagnetic properties using coaxial probes, as described below.

The seasonal variation of soil moisture content can also be modelled and predicted. The work by Saxton et al. [34] and Saxton and Rawls [35] is being used as the basis for empirical modelling of soil water characteristics based upon soil composition. Assuming a noncovered surface, this model enables the prediction of water infiltration rate with respect to depth, and subsequently the variation of soil moisture content caused by weather events. A total of four long-term monitoring stations that measure the apparent permittivity and conductivity of the soil are being installed on sites with different soil composition [23]. Data collected from these monitoring stations are expected to provide experimental

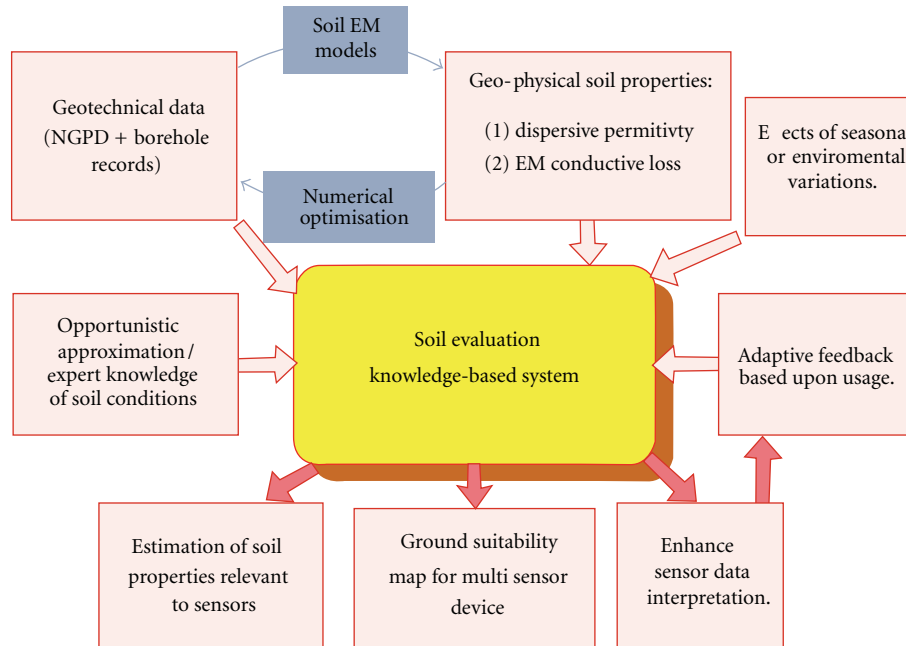


FIGURE 17: Illustration of the concept behind the soil evaluation knowledge-based system software.

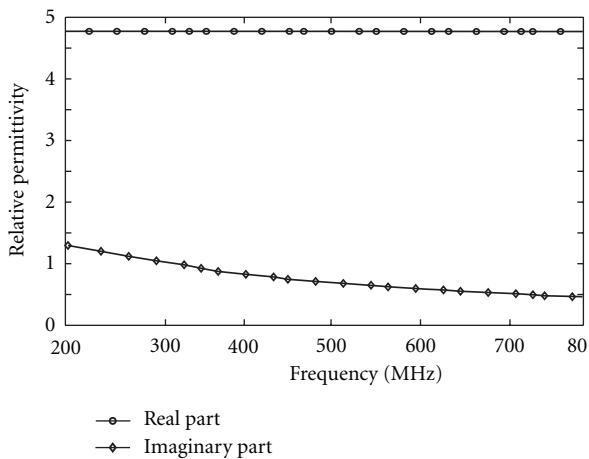


FIGURE 18: KBS modelled complex permittivity of the soil at the Blithfield test site at depth of 280 mm.

comparisons and validation of the model applied herein. This model was not necessary for the Blithfield test site as the moisture content was measured in-situ with a TDR. A simple test site has also been constructed at the University of Birmingham using TDR probes to measure changes with water content in a soil with depth and season.

While analytical models are useful in providing an estimation of soil conditions, they remain a generalised solution for a very wide set of unique input parameters. Therefore, as part of the KBS strategy (Figure 17), opportunistic approximation and input based upon expert knowledge and experience should be taken into account. As the LFEM sensor produces a measure of apparent resistivity, it may be possible to derive an estimate of electrical conductivity of the soil while a survey is being carried out, or very soon after. A

protocol is also being designed to extract information from the user based upon experience or visual observations, such as the conditions of road surface or pavement, whereby a positive visual observation of surface degradation may imply the possibility of water infiltration. As it was possible to dig on the test site, these methodologies were less significant because moisture content was measured with the TDR and deemed to be more reliable in this specific scenario.

4.2. Measurement of Soil Electromagnetic Properties. Analysis is being conducted, both *in situ* and in the laboratory, on the links between soil characteristics and its impact on the sensing technologies' performance, not only to provide an experimental means to validate and quantify the predictions of the KBS, but also to contribute to the body of knowledge that underpins the direct study of soil electromagnetic properties. This involves the design of sensing devices and techniques specifically for the direct measurement of soil electromagnetic properties *in situ*.

The dependence of utility location technologies such as GPR on the electromagnetic properties of the soil can be explained by (1) [36], where L represents the attenuation losses due to the soil, R is the distance from the GPR antennas to the target, f the frequency in Hz, c the speed of light in a vacuum, $\tan \delta$ the loss tangent of material, ϵ_r the relative permittivity of material, ϵ_0 the absolute permittivity of free space (8.854×10^{-12} farad/m), μ_r the relative permeability of material (for the underground applications considered herein the permeability is usually 1), and μ_0 the absolute permeability of free space ($4\pi \times 10^{-7}$ Henry/m). The research undertaken in this area for the project has concentrated on obtaining the relative permittivity ϵ_r of various soils. Several semiempirical models based on soil composition have been developed to predict the permittivity of soils [29, 30, 36]. Due

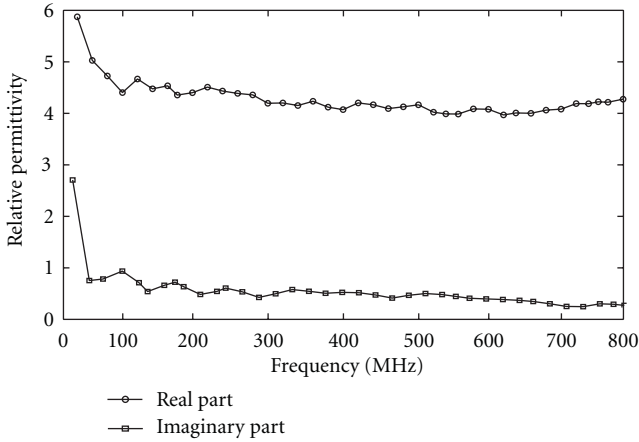


FIGURE 19: The measured permittivity at 280 mm depth at the Blithfield test site, using the open-ended coaxial probe (July 2010).

to the nature of the semiempirical approach, the accuracy of the models is highly dependent upon and restricted by the soil types used to develop the models, which means other soils with different compositions are predicted with less accuracy

$$L = 20 \log_{10} \left(2 \times R \times \frac{2\pi f}{c} \sqrt{\frac{\mu_0 \mu_r \epsilon_0 \epsilon_r}{2}} (\sqrt{1 + \tan^2 \delta} - 1) \right). \quad (1)$$

The TDR technique [37] is well developed and widely used in measuring the apparent permittivity of soils. It is noted that this approach gives a single permittivity value over a range of frequencies, which means the dispersive characteristics of lossy soils along the frequencies cannot be explained. More recent frequency domain techniques such as resonant cells and open-ended coaxial probes can measure this over a defined frequency range [38]. In particular, the resonant cell was used to measure the properties of fine-grained soils [26], while coaxial probes are used to carry out localized soil measurements. A large open-ended coaxial probe was built to measure various types of soils, including Leighton Buzzard sand, Oxford clay, and soil samples from the trial site. The analytical approach is used to calibrate the probe, and the results show good agreement between the coaxial probe and TDR, while the dispersive characteristics of soils are explained by the coaxial probe. As one example, the complex permittivity of soils at a depth of 280 mm at the Blithfield test site is shown in Figure 19. The TDR measured apparent permittivity was 4.74 at the same depth. The coaxial probe was also tested at another field site on the campus at University of Birmingham in July 2010 with similarly encouraging results, the comparison between the coaxial probe and TDR being shown in Table 1.

The design of flangeless open-ended coaxial probes with curved surfaces is also being investigated. The degree of the curvature (concave and convex) of the surface is selected to be about 16° , in which case the probes with these curved surfaces can still be modelled using the quasistatic approach that has been widely used for the probes with flat surfaces.

TABLE 1: Comparison between the measured real part of the permittivity and apparent permittivity by the coaxial probe and TDR at a test site at the University of Birmingham.

	Coaxial probe	TDR
At 10 cm depth	2-3	1.8
At 110 cm depth	5-8	6.8

The probes with curved surfaces are of potential value in applications where such probes must be assembled onto drilling devices widely used in fieldwork.

5. Fusion of Sensor Data with Buried Asset Records

5.1. Buried Utility Pipeline Mapping Based on Street Surveying and GPR. Utility maps are often produced from a combination of street surveys and geophysical scans. The surveyors will routinely investigate the on-site street furniture, such as manholes, as this is useful information regarding the utilities on site. Identification of street furniture positions provide information that can fit the utilities to a known surface location (assuming that the manholes are still in use and are connected to services) and provides information on the possible direction of these pipes as a starting point for a survey. However, this information is insufficient when producing utility pipeline maps as the underground environment is typically crowded and utilities do not necessarily transit directly between access points; bends, changes in direction, changes in depth, and tee-junctions could all conceivably occur between the known locations (assuming that the utility in question indeed runs between the these access points). Thus GPR and other geophysical surveying techniques will be usually employed to verify these hypotheses.

By combining the street survey and GPR data a utility map can be generated, employing techniques akin to those used in robotics [39]; in robotics new sensor measurements are associated with existing map landmarks before fusing data into the map. The problem can be viewed as a search problem in the space of observation-feature correspondences [40]. When mapping utilities, the data association is the connection of the observed manhole and GPR detection, that is, determining the pipes among the observed information from manholes and GPR data analysis. The map connecting problem is critical as a single incorrect association can induce divergence into the map estimate, often causing catastrophic failure of the algorithm. When developing the utility mapping algorithm for the project, two approaches were employed: Nearest Neighbour standard filter and Joint Compatibility Branch and Bound (JCBB) methods.

The Nearest Neighbour standard filter simply takes the nearest validated measurement to connect the map. The pipe will be regressed from the starting point to the possible ending point. The uncertainty of the starting point will be regressed to the ending point area. The two points are connected only when the Mahalanobis distance [42] (the distance measured based on correlations between variables

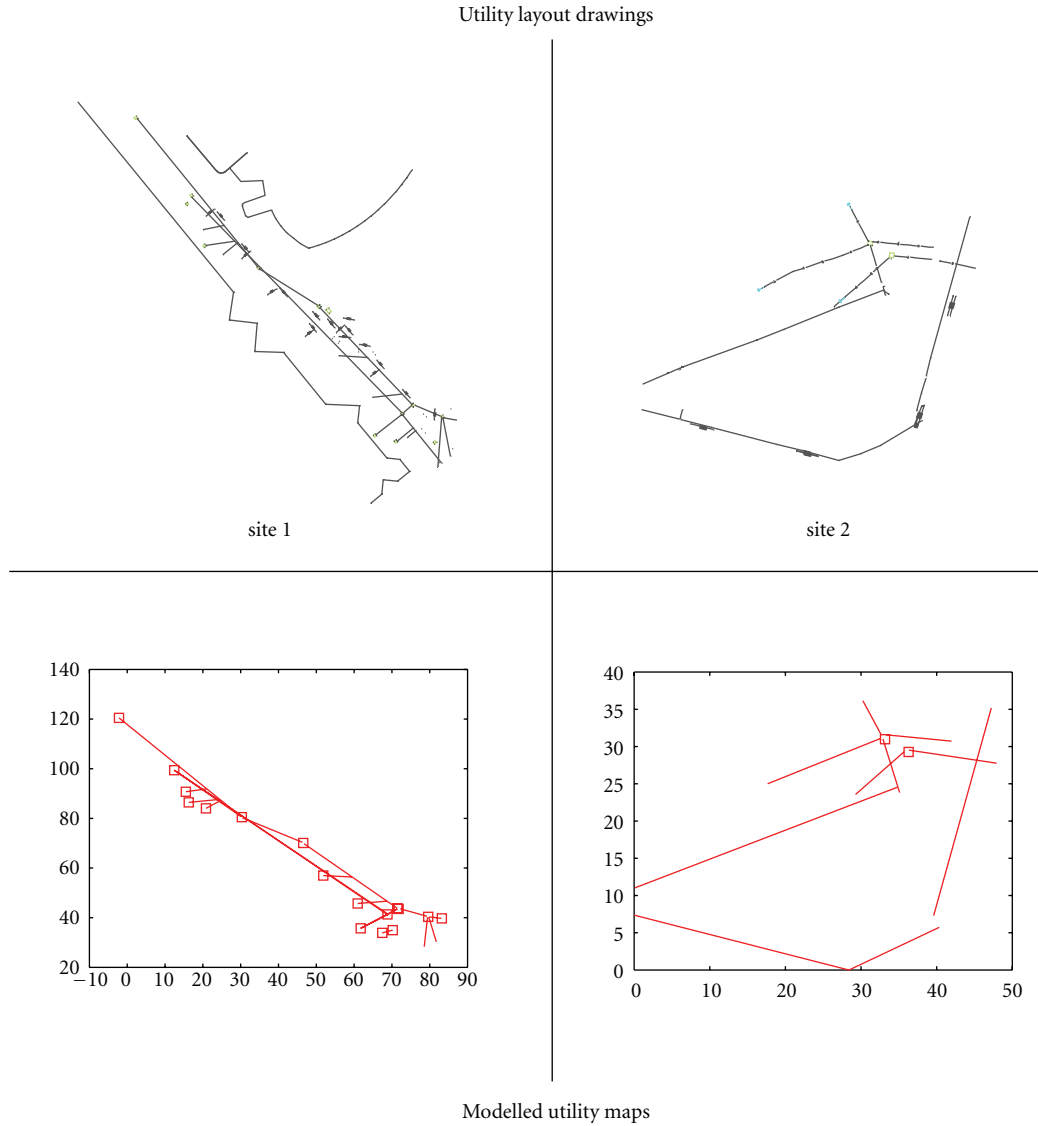


FIGURE 20: Utility maps for water utilities, (top) drawings from site survey, and (bottom) projections from modelling (created using JCBB) (images previously published in Chen and Cohn [41]).

by which different patterns can be identified and analysed) of two survey points (either manhole or GPR with pipe direction) is smaller than a threshold, that is, the validation gate. The validation gate is obtained from the inverse cumulative distribution at a significance level (typical values are 0.95 or 0.99; for this research 0.99 has been adopted as the significance level). The Nearest Neighbour algorithm uses individually compatible pairings to connect the maps, yet individually compatible pairings are not guaranteed to be jointly compatible to form a consistent hypothesis. Even if street observations and GPR analysis results are independent, correlations in the uncertainty of manhole locations might be present. *The JCBB method* addresses this issue by measuring the joint compatibility of a set of pairings and rejects spurious matching, thus is considered more robust in complex environments [43]. When dealing with the first manhole (where the GPR data and manhole location data are correlated), JCBB is preferable to Nearest

Neighbour because the utilities entering the manhole often follow roughly similar directions and thus the uncertainties of these estimations are not independent. However, although JCBB is considered to be more accurate than the Nearest Neighbour method, it is more time consuming as it undertakes a relatively “global” search of the joint compatibility, controlled by the “branch and bound” method.

An experimental study was undertaken to assess the performance of the Nearest Neighbour and JCBB methods using site-based data, comprising a street survey and GPR survey for two sites (Figure 20). In each case the GPR is moved forward 3 m ($d = 3$ m) for each scan and the uncertainty was selected as 0.2 m for manhole location and 0.4 m for GPR point scans. In terms of uncertainty for pipe directions, 8° and 15° were selected for manhole observation and GPR scans, respectively (providing that the pipe direction could be identified using the approach outlined above), although if the GPR scans prove that the uncertainty selected was

inconsistent for part of the model then this uncertainty can be increased. JCBB and Nearest Neighbour were used to create the utility maps for both sites (Figure 20) and it is apparent that JCBB made three errors on the first site and none on the second, compared to eight errors and two errors for the two sites, respectively, using Nearest Neighbour. JCBB required 4.3 s and 2.1 s to produce the model for site one and two, respectively, compared to 0.06 s and 0.05 s for Nearest Neighbour for the same sites.

The data fusion algorithm proposed herein aims to fuse data from several different sensors and to generate a consistent and complete map. The proposed algorithm contributes to an important practical application by largely automating the process of generating utility maps from surveys by combining sensor data and street observations. Given the extent of invasive street works in most countries, this has considerable potential for application.

Future work will initially focus on further trials with real data and using actual utility records. Research will also be undertaken on the incorporation of data from other sensors such as vibro-acoustic and LFEM. Finally, although at present the system operates off line as a research prototype, the eventual goal is on-board operation, giving real-time mapping, and also the possibility of directing the operator to take further readings in the area of most uncertainty.

6. Conclusions

The MTU multisensor device project focuses not only on the development of the multisensor platform, but also intelligent combination of the sensors' outputs with information on the properties of the ground, via the development of a KBS, as well as utility companies' record data. It is widely reported that the deployment of a single geophysical sensing technology, or a sequential use of sensor technologies, is unlikely to locate all utilities in all but the simplest of utilities layouts and/or most favourable ground conditions. By fusing the datasets from the various sensors; by incorporating information on ground conditions to be encountered into the deployment strategy and assessing the ground conditions during the survey (thus understanding how the ground will influence the various sensing technologies); and by fusing the resultant data with existing utility records, the probability of being able to detect all utilities on a site will markedly increase.

The development of the sensing technologies has reached the stage where initial testing was undertaken and the findings provide important leads for those seeking to optimise individual sensor technologies or seeking to combine sensors to improve detection rates. The results from the three prototype sensing technologies proved very encouraging. Excitation of the water-filled pipe resulted in the detection and accurate plan location of the pipe using the prototype vibro-acoustic sensing technology, and significant potential was shown when the ground away from the pipe was excited. The prototype LFEM sensing technology detected anomalies that appear to correlate with those detected by the commercially available GPR, while the prototype PMF

sensing technology located the position of the power cable crossing the site, that is, in the plane of cross-section, with a high degree of accuracy and confidence.

The KBS is under development, with research currently focused on developing correlations between geotechnical and geophysical properties of various soils and the changes in geophysical properties with the seasons and recent weather. The coaxial probe, developed to provide a means of direct measurement of the geophysical properties of the soil on site and thus inform the KBS of conditions on site, performed well and achieved values for the measured parameters that were close to the more traditional TDR approach. Research investigating the fusion of street survey and utility record data with GPR data to produce utility maps is producing encouraging results.

Acknowledgments

The authors wish to thank the UK Engineering and Physical Sciences Research Council for funding the project (EPSRC grants EP/F065965, EP/F06585X, EP/F065906, EP/F065973, EP/F06599X) and the project's many industrial partners who have contributed time, knowledge, and data to the project.

References

- [1] W. McMahon, M. H. Burtwell, and M. Evans, "Minimising street works disruption: the real costs of street works to the utility industry and society," Tech. Rep. 05/WM/12/8, UK Water Industry Research, London, UK, 2005.
- [2] T. Hao, H. J. Burd, D. J. Edwards, and C. J. Stevens, "Enhanced detection of buried assets," in *Proceedings of the Loughborough Antennas and Propagation Conference (LAPC '08)*, pp. 249–252, Loughborough, UK, March 2008.
- [3] A. R. Beck, G. Fu, A. G. Cohn, B. Bennett, and J. G. Stell, "A framework for utility data integration in the UK," in *Proceedings of the Urban Data Management Society Symposium*, V. Coors, M. Rumor, E. M. Fendel, and S. Zlatanova, Eds., Stuttgart, Germany, October 2007.
- [4] N. Metje, P. R. Atkins, M. J. Brennan et al., "Mapping the underworld: state of the art review," *Tunnelling and Underground Space Technology*, vol. 22, no. 5-6, pp. 568–586, 2007.
- [5] A. C. D. Royal, C. D. F. Rogers, P. R. Atkins et al., "Mapping the underworld: location phase II—latest developments," in *Proceedings of the 28th International No-Dig 2010 Conference and Exhibition*, Singapore, November 2010.
- [6] Q. Zhang, S. Pennock, M. Redfern, and A. Naji, "A novel OFDM based ground penetrating radar," in *Proceedings of the 13th International Conference on Ground Penetrating Radar (GPR '10)*, Lecce, Italy, June 2010.
- [7] J. M. Muggleton and M. J. Brennan, "The use of acoustic methods to detect & locate underground piping systems," in *Proceedings of the 9th International Conference on Recent Advances in Structural Dynamics (RASD '06)*, Southampton, UK, July 2006, paper no. WIP 3.
- [8] J. M. Muggleton and M. J. Brennan, "The design and instrumentation of an experimental rig to investigate acoustic methods for the detection and location of underground piping systems," *Applied Acoustics*, vol. 69, no. 11, pp. 1101–1107, 2008.

- [9] J. M. Muggleton, M. J. Brennan, and R. J. Pinnington, "Wavenumber prediction of waves in buried pipes for water leak detection," *Journal of Sound and Vibration*, vol. 249, no. 5, pp. 939–954, 2002.
- [10] J. M. Muggleton, M. J. Brennan, and P. W. Linford, "Axisymmetric wave propagation in fluid-filled pipes: wavenumber measurements in in vacuo and buried pipes," *Journal of Sound and Vibration*, vol. 270, no. 1-2, pp. 171–190, 2004.
- [11] J. M. Muggleton and M. J. Brennan, "Leak noise propagation and attenuation in submerged plastic water pipes," *Journal of Sound and Vibration*, vol. 278, no. 3, pp. 527–537, 2004.
- [12] Y. Gao, M. J. Brennan, and P. F. Joseph, "A comparison of time delay estimators for the detection of leak noise signals in plastic water distribution pipes," *Journal of Sound and Vibration*, vol. 292, no. 3–5, pp. 552–570, 2006.
- [13] O. Kuras, D. Beamish, P. I. Meldrum, and R. D. Ogilvy, "Fundamentals of the capacitive resistivity technique," *Geophysics*, vol. 71, no. 3, pp. G135–G152, 2006.
- [14] O. Kuras, P. I. Meldrum, D. Beamish, R. D. Ogilvy, and D. Lala, "Capacitive resistivity imaging with towed arrays," *Journal of Environmental and Engineering Geophysics*, vol. 12, no. 3, pp. 267–279, 2007.
- [15] A. Samouëlian, I. Cousin, A. Tabbagh, A. Bruand, and G. Richard, "Electrical resistivity survey in soil science: a review," *Soil and Tillage Research*, vol. 83, no. 2, pp. 173–193, 2005.
- [16] H. Shima, S. Sakashita, and T. Kobayashi, "Developments of non-contact data acquisition techniques in electrical and electromagnetic explorations," *Journal of Applied Geophysics*, vol. 35, no. 2-3, pp. 167–173, 1996.
- [17] V. M. Timofeev, *The employment of capacitively-coupled sensors in engineering and geological studies*, Ph.D. thesis, University of Moscow, Moscow, Russia, 1974.
- [18] K. Y. Foo, P. R. Atkins, A. M. Thomas, and C. D. F. Rogers, "Capacitive-coupled electric-field sensing for urban sub-surface mapping: motivations and practical challenges," in *Proceedings of the 1st International Conference on Frontiers in Shallow Subsurface Technology (FSST '10)*, pp. 157–160, The Netherlands, January 2010.
- [19] R. J. Pinnington and A. R. Briscoe, "Externally applied sensor for axisymmetric waves in a fluid filled pipe," *Journal of Sound and Vibration*, vol. 173, no. 4, pp. 503–516, 1994.
- [20] B. Papandreou, E. Rustighi, and M. J. Brennan, "On the detection of shallow buried objects using seismic wave reflections," in *Proceedings of the 16th International Congress on Sound and Vibration (ICSV '09)*, p. 8, Krakow, Poland, July 2009, paper no. 101.
- [21] B. Papandreou, M. J. Brennan, and E. Rustighi, "On the detection of objects buried at a shallow depth using seismic wave reflections," *Journal of the Acoustical Society of America*, vol. 129, no. 3, pp. 1366–1374, 2011.
- [22] S. Self and D. Entwisle, "The structure and operation of the BGS National Geotechnical Properties Database," Internal Report IR/06/092, British Geological Survey, 2006.
- [23] G. Curioni, D. N. Chapman, N. Metje et al., "Soil water content gradients with seasonal variations," in *Proceedings of the 3rd International Symposium on Soil Water Measurement Using Capacitance, Impedance and Time Domain Transmission*, Murcia, Spain, April 2010.
- [24] C. D. F. Rogers, D. N. Chapman, D. Entwisle et al., "Predictive mapping of soil geophysical properties for GPR utility location surveys," in *Proceedings of the 5th International Workshop on Advanced Ground Penetrating Radar (IWAGPR '09)*, pp. 60–67, Granada, Spain, May 2009.
- [25] A. M. Thomas, N. Metje, C. D. F. Rogers, and D. N. Chapman, "Ground Penetrating Radar interpretation as a function of soil response complexity in utility mapping," in *Proceedings of the 11th International Conference on Ground Penetrating Radar (GPR '06)*, Columbus, Ohio, USA, June 2006.
- [26] A. M. Thomas, D. N. Chapman, C. D. F. Rogers, N. Metje, P. R. Atkins, and H. M. Lim, "Broadband apparent permittivity measurement in dispersive soils using quarter-wavelength analysis," *Soil Science Society of America Journal*, vol. 72, no. 5, pp. 1401–1409, 2008.
- [27] A. M. Thomas, D. N. Chapman, C. D. F. Rogers, and N. Metje, "Electromagnetic properties of the ground: part I—fine-grained soils at the liquid limit," *Tunnelling and Underground Space Technology*, vol. 25, no. 6, pp. 714–722, 2010.
- [28] A. M. Thomas, D. N. Chapman, C. D. F. Rogers, and N. Metje, "Electromagnetic properties of the ground: part II—the properties of two selected fine-grained soils," *Tunnelling and Underground Space Technology*, vol. 25, no. 6, pp. 723–730, 2010.
- [29] R. L. van Dam, B. Borchers, and J. M. H. Hendrickx, "Methods for prediction of soil dielectric properties: a review," in *Detection and Remediation Technologies for Mines and Minelike Targets X*, vol. 5794 of *Proceedings of the SPIE*, pp. 188–197, Orlando, Fla, USA, 2005.
- [30] N. R. Peplinski, F. T. Ulaby, and M. C. Dobson, "Dielectric properties of soils in the 0.3-1.3 GHz range," *IEEE Transactions on Geoscience and Remote Sensing*, vol. 33, no. 3, pp. 803–807, 1995.
- [31] V. L. Mironov, L. G. Kosolapova, and S. V. Fomin, "Physically and mineralogically based spectroscopic dielectric model for moist soils," *IEEE Transactions on Geoscience and Remote Sensing*, vol. 47, no. 7, Article ID 4895263, pp. 2059–2070, 2009.
- [32] M. C. Dobson, F. T. Ulaby, M. T. Hallikainen, and M. A. El-Rayes, "Microwave dielectric behavior of wet soil-part II: dielectric mixing models," *IEEE Transactions on Geoscience and Remote Sensing*, vol. GE-23, no. 1, pp. 35–46, 1985.
- [33] G. C. Topp, J. L. Davis, and A. P. Annan, "Electromagnetic determination of soil water content: measurements in coaxial transmission lines," *Water Resources Research*, vol. 16, no. 3, pp. 574–582, 1980.
- [34] K. E. Saxton, W. J. Rawls, J. S. Romberger, and R. I. Papendick, "Estimating generalized soil-water characteristics from texture," *Transactions of the ASAE*, vol. 50, no. 4, pp. 1031–1036, 1986.
- [35] K. E. Saxton and W. J. Rawls, "Soil water characteristic estimates by texture and organic matter for hydrologic solutions," *Soil Science Society of America Journal*, vol. 70, no. 5, pp. 1569–1578, 2006.
- [36] D. J. Daniels, *Ground Penetrating Radar*, The Institution of Engineering and Technology, London, UK, 2nd edition, 2004.
- [37] D. A. Robinson, S. B. Jones, J. M. Wraith, D. Or, and S. P. Friedman, "A review of advances in dielectric and electrical conductivity measurement in soils using time domain reflectometry," *Vadose Zone Journal*, vol. 2, pp. 444–475, 2003.
- [38] U. Kaatz, "Techniques for measuring the microwave dielectric properties of materials," *Metrologia*, vol. 47, no. 2, pp. S91–S113, 2010.
- [39] H. Durrant-Whyte and T. Bailey, "Simultaneous localization and mapping: part I," *IEEE Robotics & Automation Magazine*, vol. 13, no. 2, pp. 99–110, 2006.
- [40] W. E. L. Grimson, *Object Recognition by Computer: The Role of Geometric Constraints*, MIT Press, Cambridge, UK, 1990.

- [41] H. Chen and A. G. Cohn, "Probabilistic robust hyperbola mixture model for interpreting ground penetrating radar data," in *Proceedings of the IEEE World Congress on Computational Intelligence (WCCI '10)*, Barcelona, Spain, 2010.
- [42] R. De Maesschalck, D. Jouan-Rimbaud, and D. L. Massart, "The mahalanobis distance," *Chemometrics and Intelligent Laboratory Systems*, vol. 50, no. 1, pp. 1–18, 2000.
- [43] J. Neira and J. D. Tardós, "Data association in stochastic mapping using the joint compatibility test," *IEEE Transactions on Robotics and Automation*, vol. 17, no. 6, pp. 890–897, 2001.

Research Article

Application of the Cylindrical Wave Approach to the Simulation of Buried Utilities

Fabrizio Frezza,¹ Lara Pajewski,² Cristina Ponti,² and Giuseppe Schettini²

¹ Department of Information Engineering, Electronics and Telecommunications, Sapienza, University of Rome, Via Eudossiana 18, 00184 Roma, Italy

² Department of Applied Electronics, Roma Tre University, Via della Vasca Navale 84, 00146 Roma, Italy

Correspondence should be addressed to Lara Pajewski, pajewski@uniroma3.it

Received 16 February 2011; Accepted 4 May 2011

Academic Editor: Francesco Soldovieri

Copyright © 2011 Fabrizio Frezza et al. This is an open access article distributed under the Creative Commons Attribution License, which permits unrestricted use, distribution, and reproduction in any medium, provided the original work is properly cited.

The cylindrical wave approach is resumed. It is a full-wave technique for the solution of the two-dimensional plane-wave scattering problem by a set of perfectly conducting and dielectric cylinders buried in a dielectric half-space, or in a finite-thickness slab. This method can be applied for simulating scenarios with cylindrical inhomogeneities buried in the earth. New numerical results are presented, concerning the simulation of buried utilities. In particular, metallic pipes and air cavities are simulated.

1. Introduction

The Ground Penetrating Radar (GPR) [1, 2] is an established and routine method for the inspection of civil engineering structures. It can provide high-resolution images of the subsurface, typically from 0 to 10 m depth, through wide-band nonsinusoidal electromagnetic waves. The employed frequencies range from 10 MHz to 4 GHz. This technique is effective, rapid, nondestructive and non-invasive. It is employed for surveying of roads and highway pavements [3], bridges [4], tunnels [5], and for detecting subsurface cavities and voids [6]. It can also be used for utility sensing [7], for example, to map all the buried structures in a region, enabling rapid installation of a new plant with the minimum disruption and damage to the existing one. Gas, water, sewage, electricity, telephone and cable utilities can be localized. Moreover, the GPR can be used to perform detailed quality controls of reinforced concrete [8, 9]. An analysis of geological structures can be performed, for the mapping of soil, rock or fill layers in geotechnical investigations and for foundation design [10].

An important factor, among those limiting the GPR surveying of buried pipes and cables, is the density of plant in urban areas: if a lot of underground infrastructures are present, it is difficult to interpret the measured data and to

clearly image the scenario, but this is just the situation where clarity is more needed.

The majority of buried plant is within 0.5 m to 2 m of the ground surface and it may have a wide variation in its size, may be metallic or nonmetallic, in close proximity to other plant. It may be buried in a wide range of soil types, involving large differences in electromagnetic propagation velocity and absorption. Therefore, obtaining adequate penetration of the emitted radiation together with good resolution is not straightforward, and some compromise has to be accepted.

The block diagram of a radar system is shown in Figure 1. A few nanosecond short impulse of electromagnetic energy is launched by a transmitting antenna. The antenna is mounted on a mobile trolley that is moved forward over the soil, at a very close distance from the ground surface. The energy scattered by the target is gathered by the receiving antenna, which is usually identical to the transmitting antenna and then processed by the receiver, to display the signal in a suitable form for the operator.

Radars solve inverse problems, to estimate the electromagnetic properties of a target, or of a complex scenario, from field measurements. At present, different algorithms are employed in the post-processing of collected GPR data; most of them need a fast and accurate forward-scattering solver, to perform repeated evaluations of the scattered

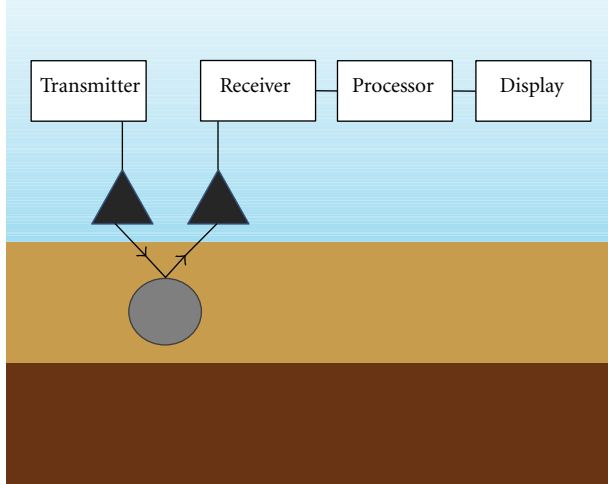


FIGURE 1: Block diagram of a GPR system.

electromagnetic field due to known targets and to be used in combination with some optimization techniques.

Almost all the objects sought in utility detection are long and thin, so in these applications two-dimensional scattering techniques are employed in the post-processing, being more effective and faster than three-dimensional ones.

The direct two-dimensional electromagnetic-scattering problem of buried objects is, therefore, a theme of great interest in GPR context, and it has been faced by several authors [1], both from a theoretical and a numerical point of view. Different methods have been developed for its solution, both in the frequency and time domains [11–13] (and references therein). Due to the complexity of the problem, many methods present limitations; for example, in [14] the obstacle size and the distance between buried scatterer and air-ground interface have to be much larger than the wavelength, the method proposed in [15] is valid only for small objects, no more than one cylinder is considered and only far-field results are calculated in [16]; some techniques can be applied only when the dielectric contrast between the obstacle and the hosting medium is low [17, 18]; some approaches suppose the ground to be lossless [11]. The finite-element method (FEM) [19], the finite-difference time-domain technique (FDTD) [20], and the method of moments (MoM) [21] can treat more general configurations and are often used.

The cylindrical-wave approach (CWA) [11–13, 22, 23] is an efficient spectral-domain technique, developed for the rigorous solution of the two-dimensional electromagnetic forward-scattering problem by a finite set of perfectly conducting or dielectric targets, buried in a dielectric half-space or in a finite-thickness slab. In this method, the field scattered by underground objects is represented in terms of a superposition of cylindrical waves. Use is made of the plane-wave spectrum [24] to take into account the interaction of such waves with the planar interfaces between air and soil and between different layers in the ground. Suitable reflected [25] and transmitted [11] cylindrical functions are defined. Adaptive integration procedures of Gaussian type, together

with acceleration algorithms, are employed for the numerical solution of the relevant spectral integrals [12, 26, 27]. All the multiple-reflection and -diffraction phenomena are taken into account.

The CWA may deal with both TM and TE polarization fields. It can be applied for arbitrary values of permittivity, size, and position of the targets. Obstacles of general shape can be simulated, by means of a suitable set of small circular-section cylinders. Since the CWA is implemented in the frequency domain, dispersive soils can be modelled. The technique has been extended to study the scattering of an incident pulsed wave, with a rather general time-domain shape, a sampling of the incident-field spectrum can be performed, and the scattering problem can be solved in the frequency domain by using the CWA [13, 28]. The method is accurate and fast; therefore, it may be exploited in iterative algorithms for the solution of inverse problems.

In Section 2, we briefly resume the theoretical basis of the CWA. In Section 3, new results are presented, showing the effectiveness of the method for the sensing of cylindrical inhomogeneities buried in the earth. In particular, an electromagnetic simulation is performed of suitable scenarios in the context of civil engineering applications.

2. Theoretical Basis of the CWA

2.1. Perfectly Conducting Cylinders in a Dielectric Half-Space. The application of the CWA to the solution of the monochromatic plane wave-scattering problem by a finite set of perfectly conducting cylinders buried in a dielectric half-space is described in detail in [11]. In this subsection, the method is briefly resumed.

Let us consider N perfectly conducting circular cylinders with possibly different radii, buried in a linear, isotropic, homogeneous, dielectric, lossless half-space, as schematized in Figure 2. Each cylinder is parallel to the y axis; the structure is assumed to be infinite along y direction. A monochromatic plane wave, with wavevector k^i lying in the xz plane, impinges at an angle φ_i from medium 0 (a vacuum) on the planar interface with medium 1. We introduce a normalized reference frame (O, ξ, ζ) , with coordinates $\xi = k_0 x$ and $\zeta = k_0 z$, $k_0 = 2\pi/\lambda_0$ being the vacuum wavenumber and λ_0 the vacuum wavelength. In such reference frame, the q th cylinder has axis located in (χ_q, η_q) , and its dimensionless radius is called $\alpha_q = k_0 a_q$. The time dependence of the field is assumed to be $e^{-i\omega t}$, where ω is the angular frequency. The solution to the scattering problem is carried out in terms of $V(\xi, \zeta)$, representing the y -component of the electric/magnetic field: $V = E_y(\xi, \zeta)$ for TM^(y) polarization, and $V = H_y(\xi, \zeta)$ for TE^(y) polarization.

In order to obtain a rigorous solution for $V(\xi, \zeta)$, the total field is expressed as the superposition of a set of terms, produced by the interaction between the incident field, the interface and the cylinders: the incident plane wave, the reflected field (due to the reflection in medium 0 of the incident plane wave by the interface), and the transmitted field (due to the transmission in medium 1 of the incident plane wave by the interface); the field scattered

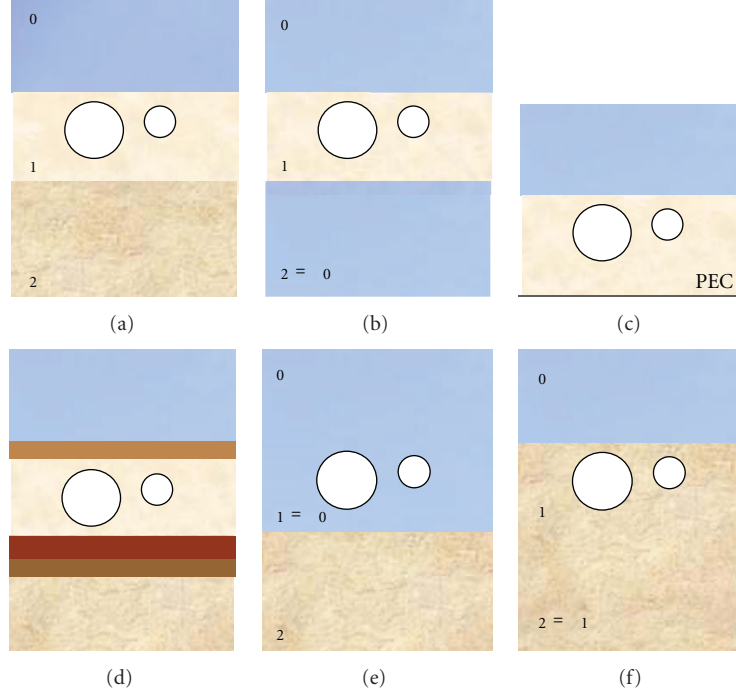


FIGURE 3: Cylinders in a finite-thickness slab, various scenarios.

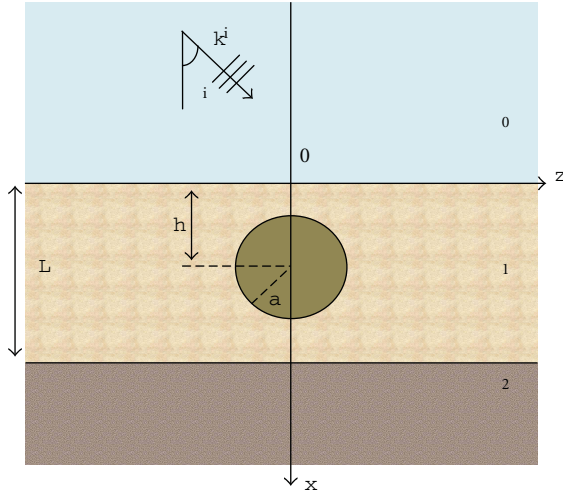


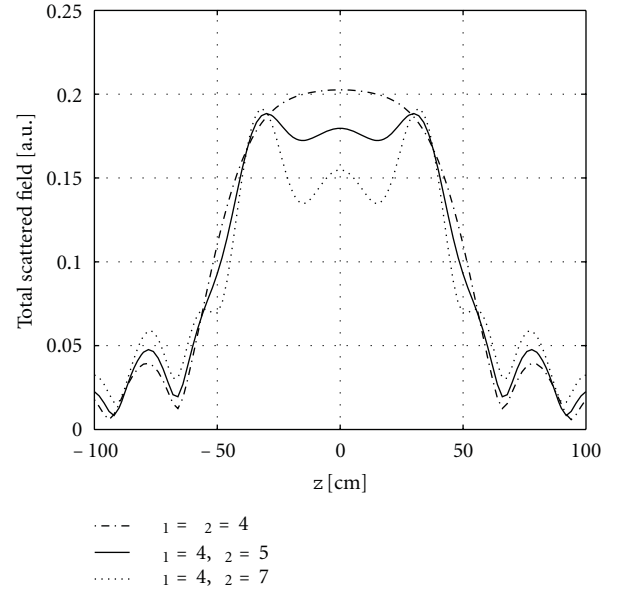
FIGURE 4: Geometrical layout of a buried utility.

by an expansion in terms of first-kind Bessel functions with unknown coefficients d_{qm} , as follows:

$$V_{cq} = V_0 \sum_{m=-\infty}^{+\infty} d_{qm} i^m e^{-im\varphi_i} J_m(n_{cq}\rho_q) e^{im\theta_q}, \quad (4)$$

where n_{cq} is the refractive index of the cylinder.

On the cylinder surfaces, the boundary conditions have to be imposed. A linear system is thus obtained, for the unknown coefficients of the cylindrical wave expansions and for the d_{qm} coefficients. Once the system has been solved, the total electromagnetic field is completely determined in any point of the space.

FIGURE 5: Total scattered field in air, along a line parallel to the interface, for the layout of Figure 4, with $L = 120$ cm.

2.3. Cylinders in a Finite-Thickness Slab. When the scatterers are inside a finite-thickness slab, among two different half-spaces, additional reflected-transmitted, multiple-reflected and multiple-reflected-transmitted cylindrical functions are introduced, to consider the complicated interaction between the cylinders and the planar interfaces delimiting the slab. The case of perfectly conducting cylinders is solved in [22]; the solution to the scattering problem by dielectric cylinders in a slab is described in [23].

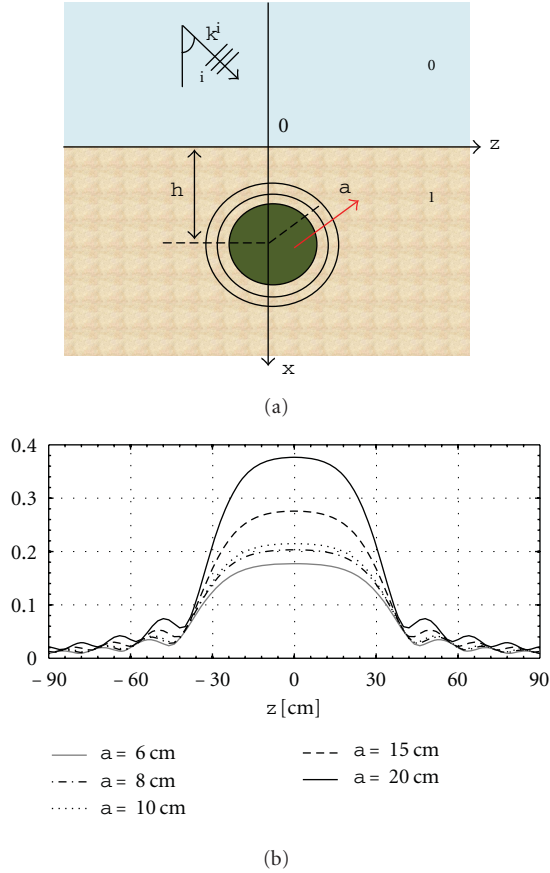


FIGURE 6: Total scattered field in air, along a line parallel to the interface, for different values of the radius of the metallic utility.

It is important to observe that this extension of the method allows to simulate several interesting scenarios, as sketched in Figure 3: objects in a soil layer, above a ground of different permittivity (a), objects inside a slab among two identical half-spaces, for example, cylinders in a wall (b), or else scatterers in a slab terminated on a perfectly conducting surface (c), in a layer of a stratified medium (d), or, finally, cylinders above (e) or in (f) a dielectric half-space.

2.4. Pulsed-Wave Analysis. By using the CWA technique, it is possible to solve the scattering problem by buried perfectly conducting or dielectric cylinders of an incident pulsed plane wave, with a rather general time-domain shape. We have to perform a sampling of the incident-field spectrum and of the spectra of the various field terms involved (reflected, transmitted, scattered, scattered-reflected, scattered-transmitted, etc.). The scattering problem can be solved in the frequency domain for any sample through the CWA. Finally, by means of an inverse transform, the solution in the time domain can be calculated. This procedure is described in detail in [13, 28].

3. Numerical Results

Let us consider an underground metallic utility at a standard burial depth of 50 cm: this suggests to operate in a frequency

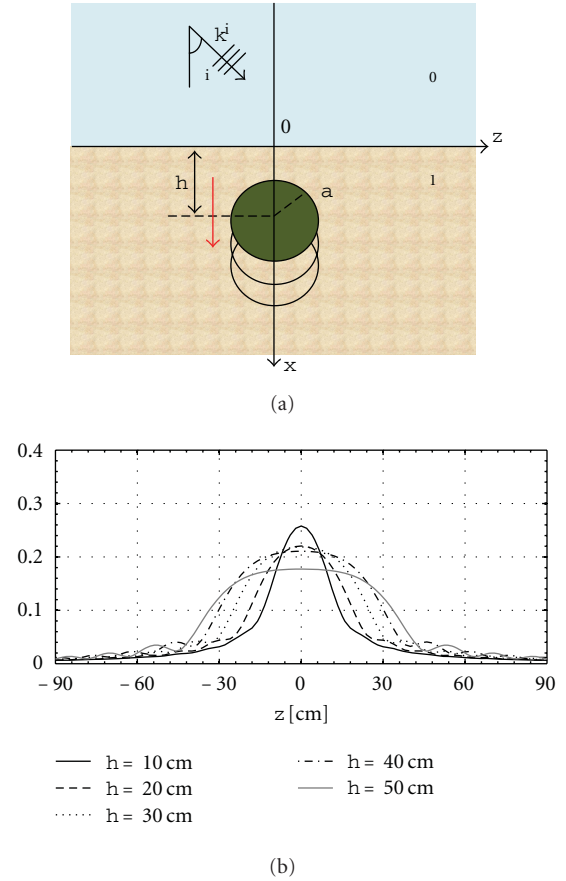


FIGURE 7: Total scattered field in air, along a line parallel to the interface, for different values of the burial depth.

range between 1 and 1.5 GHz. A circular section with a 6 cm diameter is assumed for a target, embedded in soil layer of relative permittivity $\epsilon_1 = 4$. In the CWA analysis with normalized quantities, these geometrical values correspond to a depth $\chi = 5\pi$ and a radius $\alpha = 0.6\pi$, at a frequency of 1.5 GHz. The layout is sketched in Figure 4. The total scattered field is evaluated in the upper medium, at the near-field distance of 5 cm, for a normally incident plane wave in TM polarization (electric field parallel to the cylinder axis).

In Figure 5, the scattered field is plotted for a layer of thickness $L = 120$ cm and for different permittivity values of the lower half-space. The relative permittivity of dry soil, such as dry sand, clay, and rock, is assumed as being comprised between 4 and 7. The hypothesis of dry materials is made to better meet the approximation of lossless materials of our analysis; moreover, in practical surveys the application of GPR to utility detection is limited by attenuation due to wet soil. When $\epsilon_1 = \epsilon_2 = 4$, the scatterer is buried in a semi-infinite medium. The scattered-field shows a behaviour, along a line parallel to the interface, that strongly depends on the presence of the second medium: when the object is in a finite-thickness slab, three peaks can be appreciated in the main lobe of the scattered field, while there are not oscillations in the main lobe when the cylinder is buried in a semi-infinite medium.

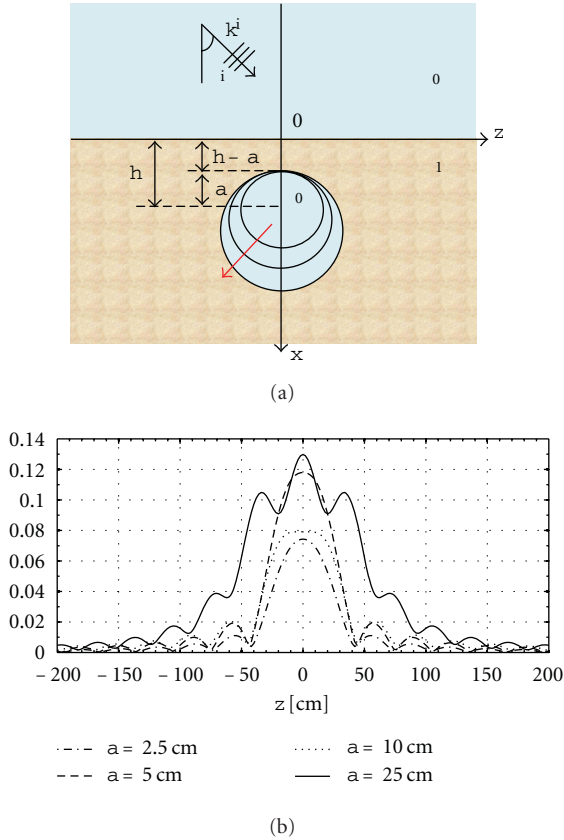


FIGURE 8: Total scattered field in air, along a line parallel to the interface, for air cavities of different size.

In Figures 6 and 7, the metallic utility is buried in a dielectric half-space with $\epsilon_1 = 4$. In particular, in Figure 6 different values of the cylinder radius are considered, and of course for a bigger utility, a stronger scattered field is observed. In Figure 7, an electric utility with radius $a = 6$ cm is buried at different depths; it can be observed that when it is deeper, the scattered field is less directive; since the soil is considered lossless, we do not obtain a significant reduction of the scattered field amplitude.

Let us now consider an underground air cavity in a dielectric half-space of permittivity $\epsilon_1 = 4$. As in previous simulations, the frequency is 1.5 GHz, and the total scattered field is evaluated in the air, at the near-field distance of 5 cm, for a normally incident plane wave in TM polarization. In Figure 8, different values of the cavity radius are considered, the distance between air-soil interface and the target is fixed and it is $h - a = 10$ cm; the electromagnetic effect of a bigger cavity is stronger and the main beam of the scattered field has a more jagged behaviour. In Figure 9 the radius is fixed, $a = 10$ cm, and different values of the burial depth are simulated; considerations similar to those of Figure 7 apply.

We finally present, in Figure 10, time-domain results for three buried metallic utilities. The geometry is sketched in the figure. The cylinder radii are $a_1 = a_3 = 2$ cm, $a_2 = 4$ cm, the burial depths are $h_1 = 30$ cm, $h_2 = 40$ cm, $h_3 = 35$ cm, and the distances along z axis are $z_1 = 0, z_2 = 21$ cm and

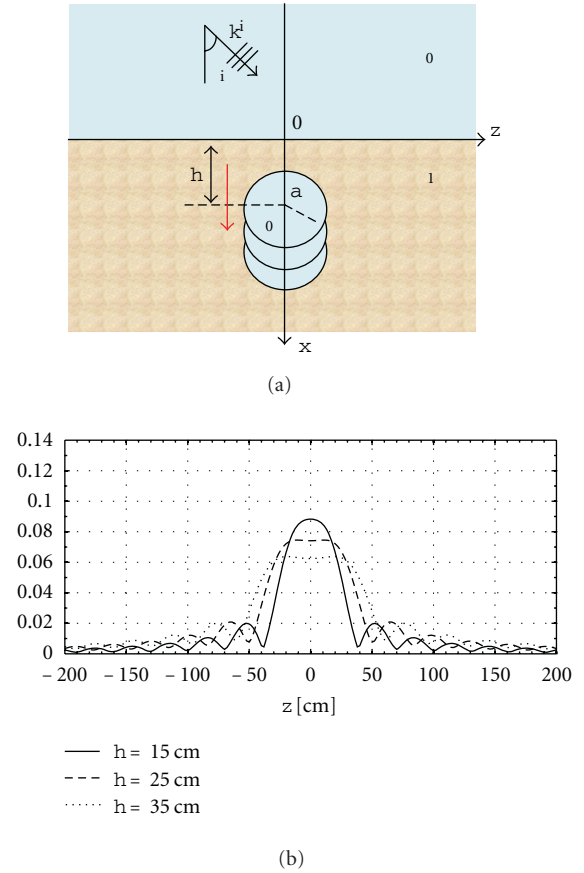


FIGURE 9: Total scattered field in air, along a line parallel to the interface, for air cavities located at various depths.

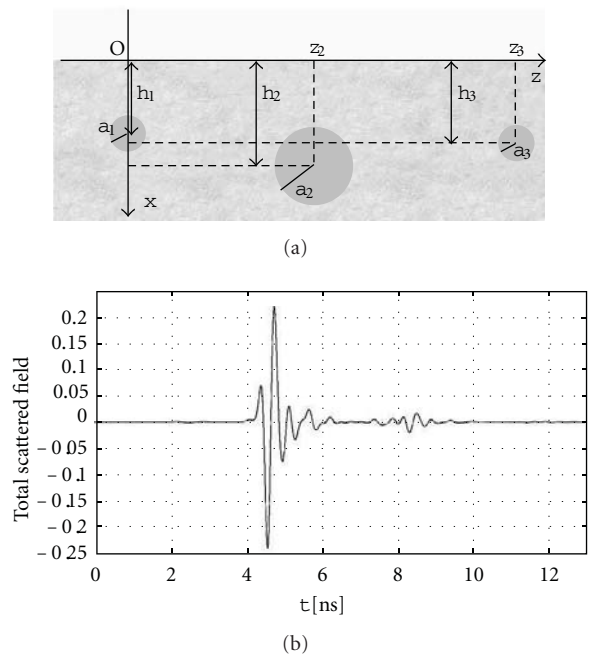


FIGURE 10: Time-domain results for three buried metallic utilities.

$z_3 = 42$ cm. The polarization of the incident field is TM, the frequency is 1.433 GHz, and the time-domain shape is the one proposed in [13]. The observation point is 15 cm above the ground, aligned with the bigger cylinder axis. We plotted the early-time response of the structure, that is, the total scattered field as a function of time, over a time interval that is of the order of the incident pulse duration and its propagation from the observation point to the targets. Several wavefronts can be identified due to combined effects of the diffraction from the cylinders, the reverberations between the cylinders and the air-ground interface, the creeping-wave circumnavigation of the cylinders.

4. Conclusions

In this paper, our work on the development of the cylindrical-wave approach for the solution of the two-dimensional plane wave scattering problem by a set of perfectly conducting and dielectric cylinders buried in a dielectric half-space or in a finite-thickness slab, is shortly reviewed. The proposed full-wave technique deals with both TM and TE polarization cases and yields results in both the near- and the far-field zones. Moreover, it may be applied for any value of the scatterers size and of the distance between the obstacles and the interface between air and soil.

The method can be used for the characterization of suitable scenarios in the context of ground-penetrating radar (GPR) applications, which usually employ purely-numerical finite-difference (FD) techniques. The CWA could be exploited in iterative algorithms for the solution of inverse problems, where fast, efficient, and accurate forward solvers are needed to perform repeated evaluations. The approach can be employed to study the scattering of an incident pulsed plane wave, with a rather general time-domain shape.

We have presented new numerical results concerning the simulation of buried utilities. In particular, metallic pipes and air cavities have been considered, and the effectiveness of the method for the sensing of cylindrical inhomogeneities buried in the earth has been shown.

References

- [1] D. J. Daniels, *Ground Penetrating Radar*, IEE, London, UK, 2nd edition, 2004.
- [2] H. Jol, *Ground Penetrating Radar: Theory and Applications*, Elsevier, Amsterdam, The Netherlands, 2009.
- [3] A. Benedetto and S. Pensa, "Indirect diagnosis of pavement structural damages using surface GPR reflection techniques," *Journal of Applied Geophysics*, vol. 62, no. 2, pp. 107–123, 2007.
- [4] J. Hugenschmidt, "Accuracy and reliability of radar results on bridge decks," in *Proceedings of the 10th International Conference on Ground Penetrating Radar*, pp. 371–374, Delft, The Netherlands, June 2004.
- [5] M. Kuloglu and C.-C. Chen, "Ground penetrating radar for tunnel detection," in *Proceedings of the International Geoscience and Remote Sensing Symposium (IGARSS '10)*, pp. 4314–4317, Honolulu, Hawaii, USA, July 2010.
- [6] T. Mochales, A. M. Casas, E. L. Pueyo et al., "Detection of underground cavities by combining gravity, magnetic and ground penetrating radar surveys: a case study from the Zaragoza area, NE Spain," *Environmental Geology*, vol. 53, no. 5, pp. 1067–1077, 2008.
- [7] A. Simi, G. Manacorda, M. Miniati, S. Bracciali, and A. Buonaccorsi, "Underground asset mapping with dual-frequency dual-polarized GPR massive array," in *Proceedings of the 13th International Conference on Ground Penetrating Radar*, p. 5, Lecce, Italy, June 2010.
- [8] W. L. Lai, T. Kind, and H. Wiggenhauser, "Detection of accelerated reinforcement corrosion in concrete by ground penetrating radar," in *Proceedings of the 13th International Conference on Ground Penetrating Radar*, p. 4, Lecce, Italy, June 2010.
- [9] B. Filali, F. Boone, J. Rhazi, and G. Ballivy, "Design and calibration of a large open-ended coaxial probe for the measurement of the dielectric properties of concrete," *IEEE Transactions on Microwave Theory and Techniques*, vol. 56, no. 10, pp. 2322–2328, 2008.
- [10] M. Tallini, A. Giamberardino, D. Ranalli, and M. Scozzafava, "GPR survey for investigation in building foundations," in *Proceedings of the 10th International Conference on Ground Penetrating Radar*, pp. 395–397, Delft, The Netherlands, June 2004.
- [11] M. Di Vico, F. Frezza, L. Pajewski, and G. Schettini, "Scattering by a finite set of perfectly conducting cylinders buried in a dielectric half-space: a spectral-domain solution," *IEEE Transactions on Antennas and Propagation*, vol. 53, no. 2, pp. 719–727, 2005.
- [12] M. Di Vico, F. Frezza, L. Pajewski, and G. Schettini, "Scattering by buried dielectric cylindrical structures," *Radio Science*, vol. 40, no. 6, Article ID RS6S18, 11 pages, 2005.
- [13] F. Frezza, P. Martinelli, L. Pajewski, and G. Schettini, "Short-pulse electromagnetic scattering by buried perfectly conducting cylinders," *IEEE Geoscience and Remote Sensing Letters*, vol. 4, no. 4, pp. 611–615, 2007.
- [14] K. Hongo and A. Hamamura, "Asymptotic solutions for the scattered field of plane wave by a cylindrical obstacle buried in a dielectric half-space," *IEEE Transactions on Antennas and Propagation*, vol. AP-34, no. 11, pp. 1306–1312, 1986.
- [15] J. D. Kanellopoulos and N. E. Buris, "Scattering from conducting cylinders embedded in a lossy medium," *International Journal of Electronics*, vol. 57, no. 3, pp. 391–401, 1984.
- [16] D. E. Lawrence and K. Sarabandi, "Electromagnetic scattering from a dielectric cylinder buried beneath a slightly rough surface," *IEEE Transactions on Antennas and Propagation*, vol. 50, no. 10, pp. 1368–1376, 2002.
- [17] D. A. Hill, "Electromagnetic scattering by buried objects of low contrast," *IEEE Transactions on Geoscience and Remote Sensing*, vol. 26, no. 2, pp. 195–203, 1988.
- [18] D. A. Hill, "Near-field detection of buried dielectric objects," *IEEE Transactions on Geoscience and Remote Sensing*, vol. 27, no. 4, pp. 364–368, 1989.
- [19] K. O'Neill, S. A. Haider, S. D. Geimer, and K. D. Paulsen, "Effects of the ground surface on polarimetric features of broadband radar scattering from subsurface metallic objects," *IEEE Transactions on Geoscience and Remote Sensing*, vol. 39, no. 7, pp. 1556–1565, 2001.
- [20] K. Demarest, R. Plumb, and Z. Huang, "FDTD modeling of scatterers in stratified media," *IEEE Transactions on Antennas and Propagation*, vol. 43, no. 10, pp. 1164–1168, 1995.
- [21] S. Vitebskij, K. Sturgess, and L. Carin, "Short-pulse plane-wave scattering from buried perfectly conducting bodies of revolution," *IEEE Transactions on Antennas and Propagation*, vol. 44, no. 2, pp. 143–151, 1996.

- [22] F. Frezza, L. Pajewski, C. Ponti, and G. Schettini, "Scattering by perfectly conducting circular cylinders buried in a dielectric slab through the cylindrical wave approach," *IEEE Transactions on Antennas and Propagation*, vol. 57, no. 4, pp. 1208–1217, 2009.
- [23] F. Frezza, L. Pajewski, C. Ponti, and G. Schettini, "Scattering by dielectric circular cylinders in a dielectric slab," *Journal of the Optical Society of America A*, vol. 27, no. 4, pp. 687–695, 2010.
- [24] G. Cincotti, F. Gori, M. Santarsiero, F. Frezza, F. Furnò, and G. Schettini, "Plane wave expansion of cylindrical functions," *Optics Communications*, vol. 95, no. 4–6, pp. 192–198, 1993.
- [25] R. Borghi, F. Gori, M. Santarsiero, F. Frezza, and G. Schettini, "Plane-wave scattering by a perfectly conducting circular cylinder near a plane surface: cylindrical-wave approach," *Journal of the Optical Society of America A*, vol. 13, no. 3, pp. 483–493, 1996.
- [26] R. Borghi, F. Frezza, C. Santini, M. Santarsiero, and G. Schettini, "Numerical study of the reflection of cylindrical waves of arbitrary order by a generic planar interface," *Journal of Electromagnetic Waves and Applications*, vol. 13, no. 1, pp. 27–50, 1999.
- [27] R. Borghi, F. Frezza, M. Santarsiero, C. Santini, and G. Schettini, "Quadrature algorithm for the evaluation of a 2D radiation integral with a highly oscillating kernel," *Journal of Electromagnetic Waves and Applications*, vol. 14, no. 10, pp. 1353–1370, 2000.
- [28] F. Frezza, P. Martinelli, L. Pajewski, and G. Schettini, "A CWA-based detection procedure of a perfectly-conducting cylinder buried in a dielectric half-space," *Progress In Electromagnetics Research B*, vol. 7, pp. 265–280, 2008.

Research Article

Multitemporal Satellite Images for Knowledge of the Assyrian Capital Cities and for Monitoring Landscape Transformations in the Upper Course of Tigris River

Giuseppe Scardozzi

CNR-IBAM, Consiglio Nazionale delle Ricerche—Istituto per i Beni Archeologici e Monumentali, Consiglio Nazionale delle Ricerche—Istituto per i Beni Archeologici e Monumentali, Strada per Monteroni c/o Campus Universitario, 73100 Lecce, Italy

Correspondence should be addressed to Giuseppe Scardozzi, g.scardozzi@ibam.cnr.it

Received 4 February 2011; Accepted 23 March 2011

Academic Editor: Nicola Masini

Copyright © 2011 Giuseppe Scardozzi. This is an open access article distributed under the Creative Commons Attribution License, which permits unrestricted use, distribution, and reproduction in any medium, provided the original work is properly cited.

The paper is concerned with the contribution that a rich documentation of multitemporal optical satellite images with high resolution provides for the knowledge of the five great Assyrian capital cities (Ashur, Kar-Tukulti-Ninurta, Kalhu, Dur-Sharrukin, and Nineveh, in northern Iraq). These images also allow monitoring changes of landscape in the higher course of the Tigris during the last half century and document damages in archaeological sites during the two Gulf Wars. The data set, available for each city, consists of panchromatic and multispectral images taken between 2001 and 2007 by modern commercial satellites (Ikonos-2, QuickBird-2, and WorldView-1) and of panchromatic photographs of U.S. spy satellites operating between 1965 and 1969 (Corona KH-4B and Gambit KH-7). These photos were taken before diffusion of mechanized agriculture and the expansion of urban areas, so they are very useful to document many archaeological features and the landscape that has been modified in the last decades, as shown by recent satellite images.

1. Introduction

The work concerns the contribution that multitemporal high-resolution images, taken by optical satellites, provide for the study of archaeological sites in ancient Mesopotamia. Over the last decade, using VHR satellite data in archaeology became common, particularly in study areas where large-scale maps or aerial photos are not available [1–3]. This paper regards the systematic use of these images for the knowledge of the five great Assyrian capital cities, sited in the modern northern Iraq. The data set, available for each city, consists of panchromatic and multispectral images taken between 2001 and 2007 by modern commercial satellites (Ikonos-2, QuickBird-2, and WorldView-1) and of panchromatic photographs taken between 1965 and 1969 by United States reconnaissance satellites (Corona KH-4B and Gambit KH-7) before diffusion of mechanized agriculture and the expansion of urban areas. So, these multitemporal images also allow monitoring changes of landscape in the higher course

of the Tigris during the last half century, and document damages in archaeological sites during the two Gulf Wars, especially the second.

1.1. The “Iraq Virtual Museum Project”. The rich remote-sensing data set used in this research was collected during the activities of the “Iraq Virtual Museum Project”, conducted between 2006 and 2010 by the Italian National Research Council. The project was designed to create a rich website (<http://www.virtualmuseumiraq.cnr.it/>) based on the archaeological collection of the National Museum of Baghdad, which has been looted in 2003 during the 2nd Gulf War. The project realizes an innovative virtual museum of the civilizations of ancient Mesopotamia, from the emergence of the Neolithic villages (7000 BC) until the Islamic period (IX-X century AD); in the website, new digital communication systems allow to access into an impressive archaeological collection, currently not available yet [4]. The virtual tour is

carried out across eight virtual exhibition “halls” organized according a chronological sequence.

In the “Iraq Virtual Museum Project”, the Institute for Archaeological and Monumental Heritage has dealt with the contextualization of the objects shown in the virtual museum; they were ideally linked not only to the sites of provenance, but also to the cultural sphere to which they belong, thanks the use of multitemporal high-resolution satellite images and thanks to 3D virtual reconstructions, very useful for the documentation and communication of the archaeological areas. More specifically, ancient sources and data from previous studies and research were integrated with satellite remote-sensing documentation; 3D image-based modelling techniques (photomodelling and digital photogrammetry) were used for the communication of the archaeological data [5]. In integration to the website, still in progress also is the realization of a webGIS that will allow a more detailed presentation of the archaeological sites, by means of multitemporal high-resolution satellite images, archaeological general maps and plans of the most important structures, and schedules of the historical and topographical development of the sites and their principal monuments; now, the sections concerning Dur-Sharrukin, Seleucia on the Tigris, and Hatra are completed [6].

The process of contextualization enables the museum “visitors” to view the original territorial contexts of finds, that is, the archaeological sites from which the materials came from. In the beginning stages, significant problems related to the documentation of the current state of these sites arose. Only a few terrestrial images and some oblique aerial photographs of limited sectors of the archaeological areas are generally available, together with some documents (graphic and photographic) of the excavations. An important contribution to solving this problem was provided by high-resolution multitemporal satellite images taken by recent commercial satellites during the 2000s. These images provided up-to-date and detailed documentation of the modern situation of the most important ancient cities and settlements of Mesopotamia; they are very useful in the presentation of archaeological sites (as a substitute for a real visit that is currently impossible) as well as for monitoring their transformation and preservation in recent years, particularly important in times of war. When it was possible, images of each archaeological site taken both before and after the Second Gulf War were used. For the documentation of the situation before the first Gulf War, numerous space photos of all the sites from the 1960s and 1970s, taken by United States reconnaissance satellites, and aerial photos from the 1920s, 1930s, and 1940s, taken by Royal Air Force pilots, were acquired and studied. The acquisition of these “historical” images was very important, as it allowed us to discover abundant data regarding territories that appear developed and have been partially modified and altered by the extension of urban areas or by realization of great infrastructures and the spread of mechanized agriculture devices.

So, the multitemporal remote-sensing data acquired during the project activities formed a fundamental documentation which made it possible to correctly “narrate” the main archaeological sites of Mesopotamia. They also made it

possible to expand upon what is already known and discover new data regarding the ancient topography, urban layout and paleoenvironmental contexts, which are critical for the reconstruction of historical landscape in which the ancient settlements were located. In fact, high-resolution satellite images provided a detailed view from above of the current state of the archaeological sites and their layouts; they allow to see even the smallest of details and elements that are not easily perceptible on the ground (like ancient roads and canals now buried, paleoriver beds, etc.) and to recognize traces of ancient structures that are still buried or that have been interred since their original excavation.

1.2. The Case Study Concerning the Assyrian Capital Cities.

The case of the Assyrian capital cities (Ashur, Kar-Tukulti-Ninurta, Kalhu, Dur-Sharrukin, and Nineveh), in northern Iraq (Figure 1), is exemplificative about the importance of the integrated use of “historical” space photos and recent satellite images. Ashur (modern Qal’al Sherqat) is located 390 km north of Baghdad, on the western bank of the Tigris River, about 27 km north-west of the confluence with its tributary Little Zab River. The city was occupied continuously starting from the early Dynastic period and was the main administrative capital of the Assyrian Empire during most of the Old and Middle Assyrian periods. Ashur was supplanted for some time during the Middle Assyrian period by Kar-Tukulti-Ninurta (modern Tulul al-’Aqr), the new capital city founded by king Tukulti-Ninurta I (1233–1197 BC); it is located about 4 km to the north of Ashur, on the east bank of the Tigris. The capital subsequently reverted to Ashur until king Ashurnasirpal II (883–859 BC) expanded the older city of Kalhu (modern Nimrud), located 70 km north, on the east bank of the Tigris valley, 11 km north of the confluence with its tributary Greater Zab River. Kalhu remained the royal capital during much of the 9th and 8th centuries BC, followed by Dur-Sharrukin (modern Khorsabad), the new city built by king Sargon II (721–705 BC) between the years 713 and 707 BC in the plain north-east of modern Mosul, about 13 km away. The final Assyrian capital was Nineveh, already an ancient and important royal city when Sennacherib (704–681 BC) designated it the imperial capital. The area of the ancient city, enlarged by Sannacherib, on the eastern bank of the Tigris, 28 km north-west of Kalhu, is today surrounded and partially overlaid by new suburbs of Mosul. Nineveh remained the capital of the Assyrian Empire until its destruction in 612 BC by the Medes, Babylonians, Scythians, and Elamites.

During the last decade, a systematic study of landscape and settlement in the Neo-Assyrian Empire was conducted using old aerial photos, Corona KH-4B and Gambit KH-7 photos, and low-resolution (15 m) modern ASTER (advanced spaceborne thermal emission and reflection radiometer) images [7–15]. The present research (of which this paper is a preliminary report) integrates the results of the previous studies, with the important contribution of the integrated use of recent high-resolution satellite images in the knowledge and monitoring archaeological evidence of the Assyrian capital cities and ancient roads and canals of the surrounding territories. Particularly, the knowledge of

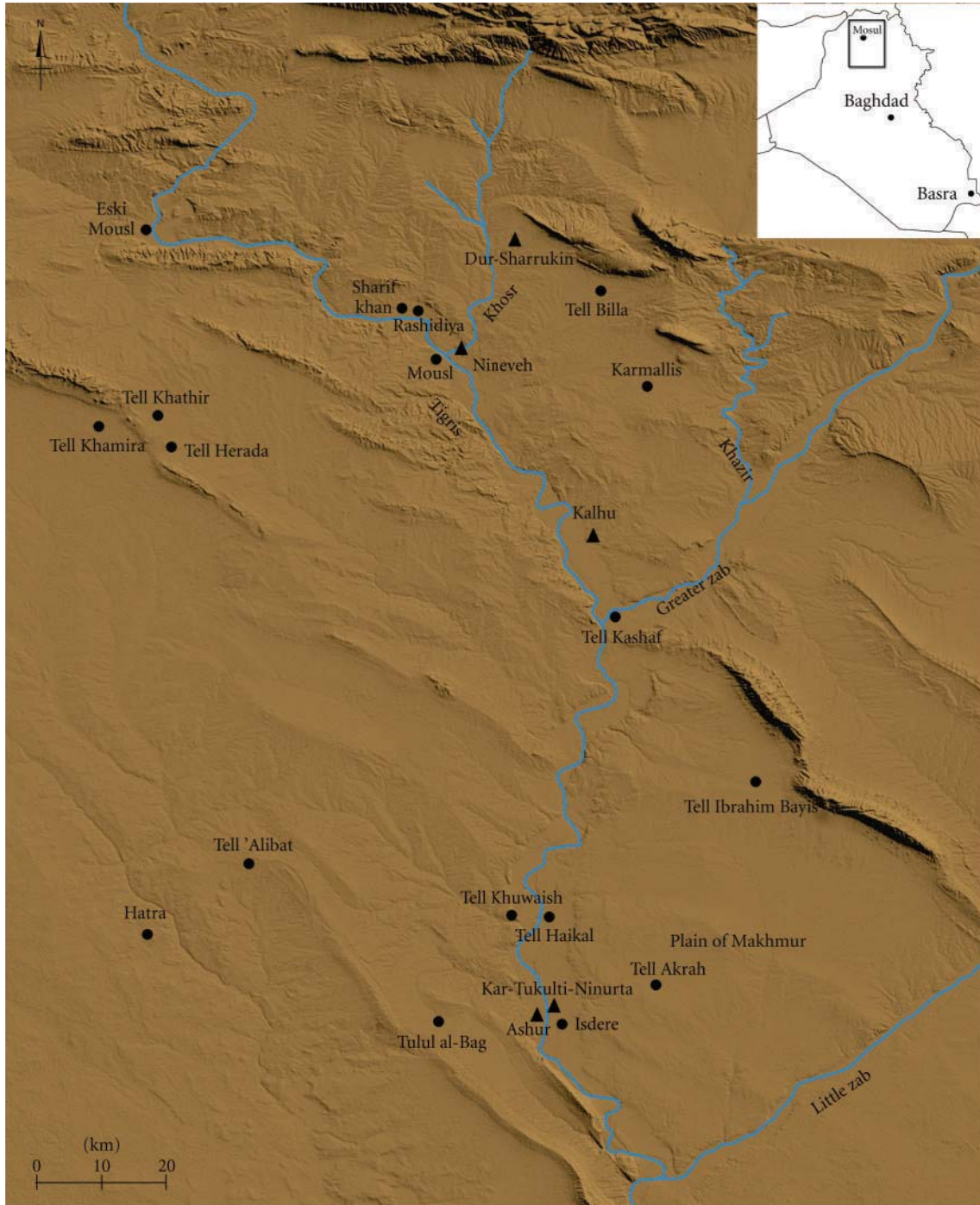


FIGURE 1: DEM (based on the shuttle radar topography mission) of the northern Iraq: the study area and the Assyrian capital cities along the Tigris valley are shown.

the ancient evidence scarcely visible on the surface and the monitoring of the archaeological remains are urgent needs in a landscape like the upper Tigris valley and the surrounding territories that during last decades are strongly changed. As example, it is important to highlight that in a report of October 2010 titled "Saving Our Vanishing Heritage", Global Heritage Fund named Nineveh one of the 12 sites most "On the Verge" of irreparable loss and destruction,

citing insufficient management, development pressures, and looting as primary causes.

2. Data Set and Methodology

In Iraq, remote sensing was a very important part of archaeology for a century, from the aerial photographs taken during the First World War by Royal Air Force pilots [16, 17].

However, today, easy access to aerial photography is often impossible to obtain. As a result, archaeologists have turned to optical satellite images, both declassified Corona and Gambit photos of the years 1960s and 1970s, and recent commercial high-resolution images (panchromatic and multispectral) that unfortunately are more expensive.

Corona was a United States Department of Defense intelligence program, operative from 1959 to 1972, which encompassed several “Keyhole” camera systems (KH-1 through KH-6). Corona photographs (about 860,000) were declassified by executive order in 1995 and have been publicly available since 1998; they can be acquired by the United States Geological Survey (<http://edc.usgs.gov/>). Archaeologists operating in the Near and Middle East were quick to recognize the potential of this new dataset, and these images were used during researches in several countries, such as Turkey, Syria, and Iraq [14, 18]. In the present study, only photos taken by Corona KH-4B satellites (operative from September 1967 to May 1972) are employed; they have the best ground resolution of the program (about 1.83 m), were taken in stereo utilizing forward and aft panoramic cameras, and covered all the study areas.

Gambit KH-7 Surveillance System was another reconnaissance satellite used by United States from July 1963 to June 1967, which produced high-resolution imagery that improved from 1.2 to 0.6 m over the course of the program. Its photos (about 19,000) were declassified in August 2002 and are available in USGS. The Gambit KH-7 coverage was much more limited than Corona satellites; most of its photos regarding Soviet and Chinese nuclear and missile installations, with smaller amounts of images concerning cities and harbors: Mosul was one of the urban centres targeted. As a result, several photographs of Nineveh and of the surrounding area from five KH-7 missions of the years 1965–1967 are available, and one of them covers also the area of Dur-Sharrukin; all these photos were used during the present study.

Corona and Gambit photos were used for direct visual analysis without any geometric preprocessing. The ground resolution of the photos acquired during the later Gambit KH-7 missions (in 1966 and 1967) can be compared favorably with the best commercial systems, such as Ikonos-2, Quickbird-2, and WorldView-1. Several images of the last satellites were acquired from the companies owning the platforms (<http://www.geoeye.com/>; <http://www.digitalglobe.com/>), and others are analyzed in Google Earth; these images, taken between 2001 and 2007, have a very high-resolution (between 0.50 and 1 m in panchromatic mode, and between 2.40 and 4 m in multispectral mode), and allow to investigate the visible and the near infrared; they don't have the typical geometrical distortion of Corona and Gambit photos, but are bought pre-processed (Ikonos Geo Ortho Kit level; QuickBird and WorldView Standard Ortho-ready levels) and with a radiometric resolution of 11 bits per pixel. Because of their high cost, only commercial images of the urban area (and its neighbors) of the Assyrian capital cities were purchased. These current high-resolution images were orthorectified by using a DEM

based on SRTM data and the Rational Polynomial resampling model; DEMs were also draped with spatial photos and satellite images for a 3D analysis of remote sensed documentation. In some cases (Dur-Sharrukin and Nineveh), even an automatic co-registration of recent satellite images was performed, and it was very useful for multitemporal analysis of pre- and post-Second Gulf War situations.

The data set concerning the Assyrian capital cities and their surrounding territory is the following:

- (i) Ashur and Kar-Tukulti-Ninurta: five Corona KH-4B photos (December 11, 1967; August 16, 1968; December 6, 1969; resp., missions 1102, 1104 and 1108); two QuickBird-2 images (September 10, 2002; August 2, 2005),
- (ii) Kalhu: two Corona KH-4B photos (August 16, 1968, and December 6, 1969, resp., missions 1104 and 1108); one QuickBird-2 image (August 10, 2002); one Ikonos-2 image (September 15, 2007),
- (iii) Dur-Sharrukin: one Gambit KH-7 photo (April 30, 1965, mission 4017); two Corona KH-4B photos (August 16, 1968, and December 6, 1969, resp., missions 1104 and 1108); one Ikonos-2 image (February 2, 2001); four QuickBird-2 images (June 4, 2002; June 30, 2003; August 20, 2004; August 2, 2005),
- (iv) Nineveh: six Gambit KH-7 photos (April 30, 1965; May 16, June 5 and September 20, 1966; June 8 and 9, 1967; resp., missions 4017, 4028, 4029, 4031 and 4038); two Corona KH-4B photos (August 16, 1968, and December 6, 1969, resp., missions 1104 and 1108); nine QuickBird-2 images (June 4, July 4 and October 2, 2002; June 25 and August 30, 2003; April 8, August 20 and December 29, 2004; February 16, 2005); one WorldView-1 image (December 22, 2007).

During the activities of the “Iraq Virtual Museum Project,” the study and the analysis of this multitemporal documentation represented an opportunity to acquire new data about the ancient topography of the archaeological sites examined. It is very important specifically for contexts that have been studied many years ago or that are characterized by a history of the research focus mainly on individual complexes, monuments, or wealth of finds and less interested in the general layout of settlements. The use and the analysis of the Corona KH-4B and Gambit KH-7 photos (and of the recent panchromatic satellite images) is the same of the traditional aerial photos, in which archaeological features are highlighted by microrelief and shadow and soil and crop marks [19]. These images predate the introduction of the large-scale irrigation schemes and industrial-scale agriculture schemes that have been so destructive to the cultural heritage of northern Iraq; moreover, they document Mosul and the villages along the Tigris course before the booming of their urban areas in the last decades, which have covered and destroyed a lot of archaeological features. In some cases, Corona and Gambit photos constitute a precious documentation of archaeological areas before any recent transformations and in some cases have shown ancient features that nowadays are not visible or have been destroyed.

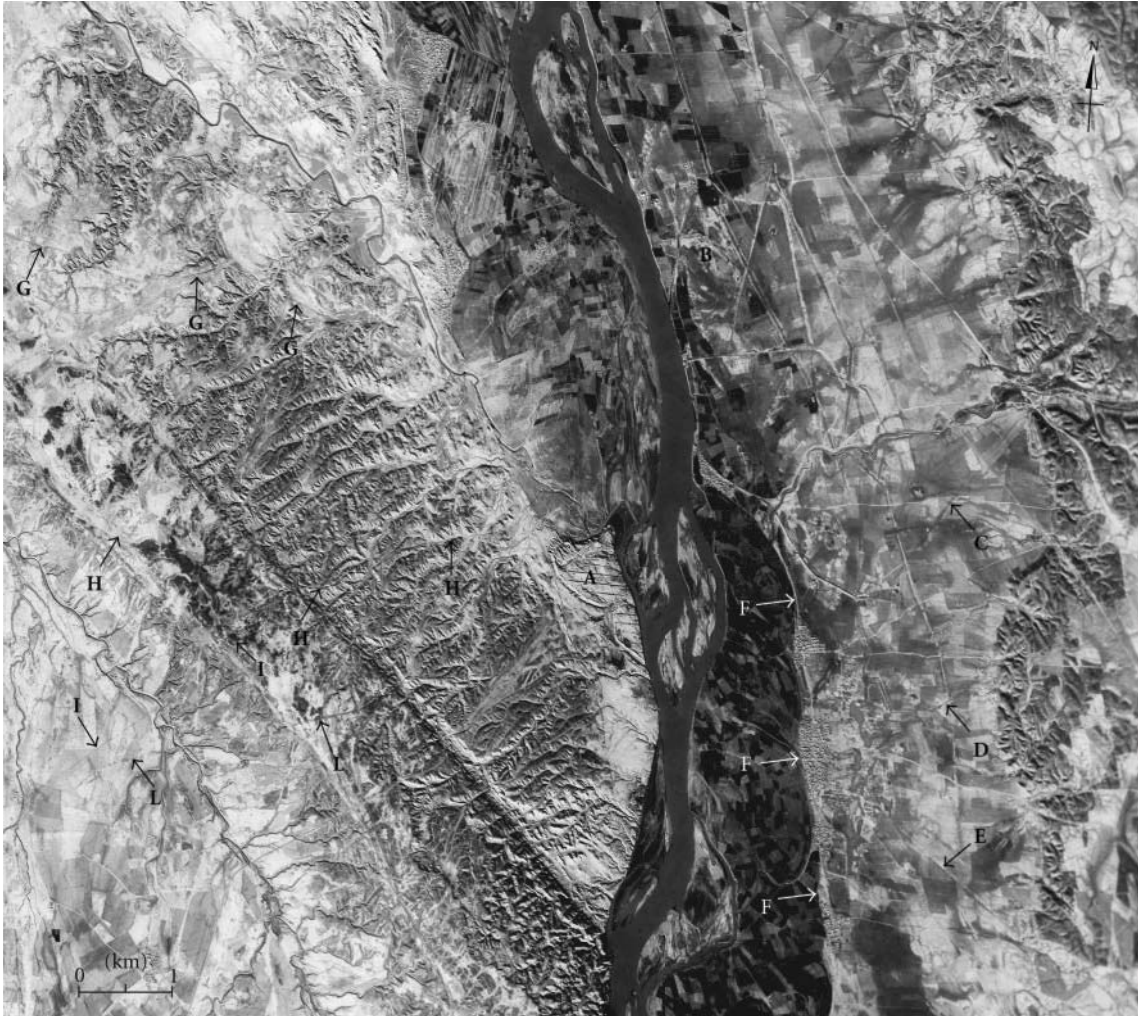


FIGURE 2: The area of Ashur (A) and Kar-Tukulti-Ninurta (B) in a Corona KH-4B image of 1967; traces and remains of ancient roads (C, D, E, G, H, and I) and a relict river meander of the Tigris (F) are also visible.

So, they are particularly useful for the reconstruction of ancient landscapes or aspects of the territories which are more similar to the ancient ones.

The Corona and Gambit space photos are the primary remote-sensing sources for locating archaeological and even paleoenvironmental features in the study areas; they show a lot of ancient remains and traces and anomalies linked to buried archaeological features, in particular sites, structures, walls, canals and roads, that is, the so-called “hollow ways” [15]. These linear hollows are remnants of ancient roads that can be commonly found in the Jazirah region (northern Iraq and Syria), caused by the continuous use of tracks by men and animals, and also by vehicles such as sleds, carts, or wagons [20, 21]; these features can be described as shallow linear depressions that have different soil, moisture and vegetation characteristics from the surrounding terrain. Since hollows have an elevation that is generally lower than the surrounding area, water is often captured at the bottom of the features; this enables more vigorous plant growth in the troughs. In the panchromatic images, these features are distinguishable from the soil by darker color than the sur-

rounding area. Even canals and remnants of canals have depressions that have similar properties to hollow ways, with moisture collecting and vigorous vegetation growing in the shadows, so cases of ambiguity between canals and linear hollows are present. In contrast to linear hollows, remnants of canals often have spoil banks that are composed of materials cast up from their excavation as well as silts cleaned out from the channels.

Recent commercial satellite images were used to document in detail the modern developed landscape in the ancient sites. They allowed monitoring of the archaeological areas and generally documented the destruction of a lot of ancient features; in certain areas, these images confirmed the existence of archaeological features and also showed them more clearly than the Corona and Gambit photos. Moreover, the Ikonos-2 and QuickBird-2 systems both integrate very high geometric resolution with multispectral characteristics that have a lot of potentialities in the archaeological research; for example, the near infrared band was very useful in highlighting buried features that produce a different vegetation growth on the surface. So, in some cases, the processing of

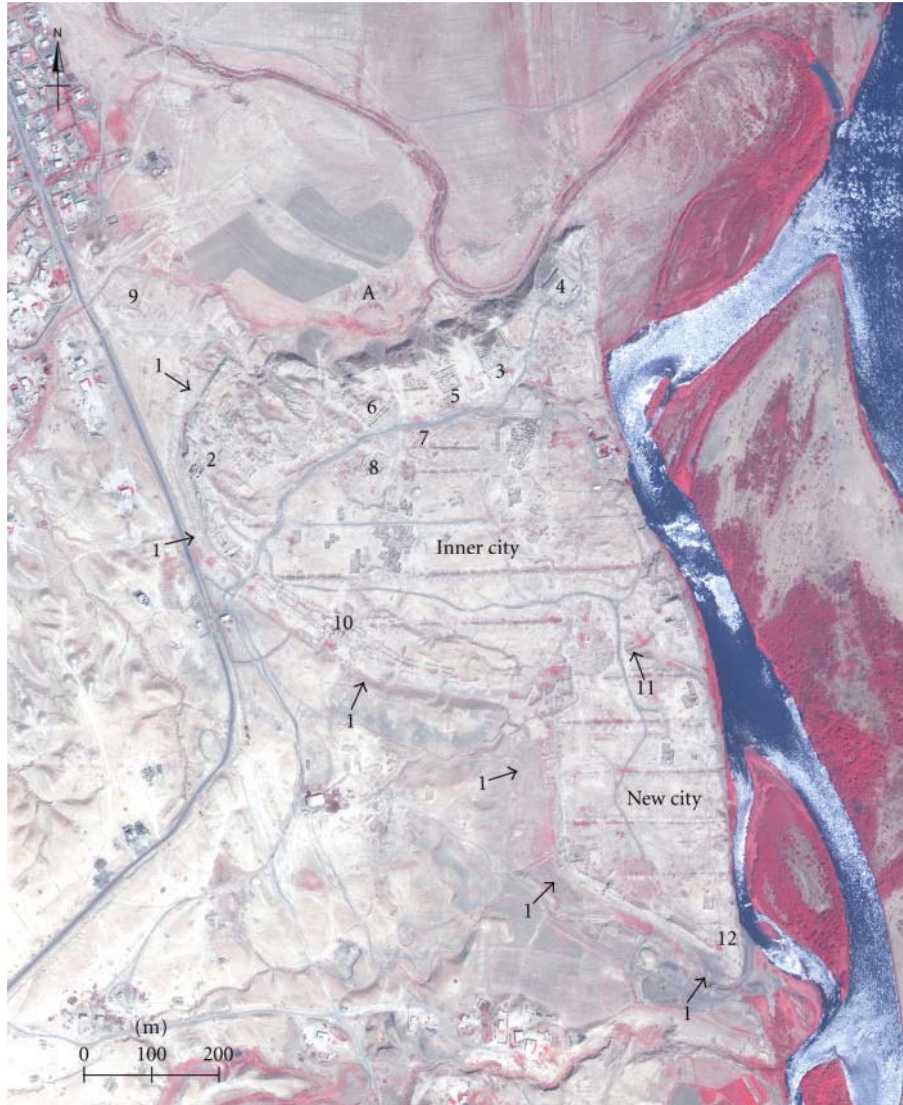


FIGURE 3: Ashur in a pan-sharpened (bands 4-3-2) QuickBird-2 image taken in 2005: (A) ancient river course of the Tigris; (1) moat outside the city walls; (2) Tabira Gate; (3) Ziggurat; (4) Temple of Ashur; (5) Old Palace and Palace of Adad-nirari I; (6) Temple of Anu and Adad; (7) Temple of Sin and Shamash; (8) Temples of Ishtar and of Nabu; (9) Akitu Temple; (10) West Gate; (11) South Gate of the inner walls; (12) South Gate of the outer walls.

multispectral images of Ikonos-2 and QuickBird-2, in which the measured radiation is divided in four bands including the visible spectrum and the near infrared, and the data fusion between panchromatic images and multispectral elaborations also made it possible to identify and highlight, in a better way, archaeological and paleoenvironmental traces and anomalies.

However, in the analysis of remote-sensing data, the verification on the ground of presences, traces and anomalies is very important, in order to clarify their real pertinence to archaeological elements, their interpretation, and, if possible, also their dating, avoiding misunderstandings, and mistakes; in fact, field work verification is the only way to fully certify any observation in the images. But in the study cases of the Assyrian capital cities (and also of the other archeological sites considered in the “Iraq Virtual Museum Project”), the

ground control with a survey of the sites was impossible, so often, we can formulate only hypotheses, and other verification methods of features observed must be used to certify the results as best as possible: for instance, by observing characteristics from known features, or using multiple images of the same areas, with the aim to verify that features visible on one image can be found in another image from a different time. So, all sites in this study were examined through analysis of multiple images taken in different years and seasons, because features identification is heavily dependent on ground conditions at the time of acquisition. By overlaying the different satellite images, it has been possible to extract information from them to arrive at a composite reconstruction that is in part visible in all of them but rarely completely visible in any single image.



FIGURE 4: (a) Corona KH-4B image of 1967 and (b) pan-sharpened (bands 3-2-1) QuickBird-2 image of 2002 showing the area of Kar-Tukulti-Ninurta. In the old space photo, the remains of the ancient capital city are well visible: (1) north Palace; (2) Ashur Temple and Ziggurat; (3) south Palace; (4) city walls; (5) Assyrian canals; (6) Islamic canals.

3. Some Results

About each Assyrian capital city, some of the principal results of the research are preliminary presented as examples. A more detailed atlas concerning the contribution of multitemporal remote-sensing data for the study and reconstruction of the ancient sites of Mesopotamia is in progress. It will be a hardcopy volume where all the documentation elaborated for the project and related to the archaeological sites will be collected: that is, processed satellite images and space photos, new archaeological plans and maps derived from the processing and analysis of remote-sensing data [22], virtual reconstructions, and reports concerning the historical and topographical development numerous ancient Iraqi sites from the Prehistory to the Islamic period (in addition to the Assyrian capital cities, also Ur, Uruk, Tell Es-Sawwan, Tell Asmar, Babylon, Sippar, Kish, Seleucia on the Tigris, Ctesiphon, Hatra, Samarra, and Ukhaydir).

3.1. Ashur and Kar-Tukulti-Ninurta. Ashur and Kar-Tukulti-Ninurta, respectively, on the west and the east banks of the Tigris, are well documented by a Corona KH-4B photo taken in 1967 (Figure 2 (A-B)). Traces of the ancient roads that connected Ashur to the important Middle Assyrian and Neo-Assyrian towns of Tell Akrah and Tell Ibrahim Bayis (Figure 2 (C-D)), located, respectively, east and north-east of the city,

in the plain of Makhmur (called in antiquity *mat Ashur*, i.e., “land of Ashur”) are visible [7, 8, 11, 13, 15]; also traces of roads leading toward south-east are clear in the space photo (Figure 2 (E)). Many of these hollow ways east of the Tigris seem to converge south-east of Ashur, near the modern village of Isdere and a relict river meander visible in the satellite image (Figure 2 (F)), in the eastern bank of the alluvial valley; it is possible that travellers to and from Ashur crossed the river at this juncture on a ferry or bridge. To the west of the city, other hollow ways are visible in the Corona space photo (Figure 2 (G-L)); they can be tied to specific gates mentioned by historical texts and revealed in excavations, such as Tabira Gates in the north-western sector of the city walls. In particular, these ancient roads connected Ashur to sites such as Tulul al-Bag and Tell’Alibat (resp., sited west and north-west of the city) occupied in Neo-Assyrian period and perhaps also in the Middle Assyrian period. It is, therefore, significant that at least one hollow way, leading toward north-west (Figure 2 (G)), connected Ashur to Hatra in the Parthian period, when the first city continued to have an important role.

The Corona KH-4B photo of 1967 contextualizes Ashur along the west bank of the Tigris; they also document the high escarpment and the trace of the arm of the river on the northern side of the city and the moat that was excavated outside the fortification system in the southern and western



FIGURE 5: Assyrian and Islamic canals in the Tigris valley north of Ashur (mosaic of Corona KH-4B photos of 1967): (1) *Pattu-mēšari*; (2) Nahr Qanausa; (3) off-takes or secondary branches of the Nahr Qanausa; (4) hollow way; (A) Ashur; (B) Kar-Tukulti-Ninurta; (C) Tell Haikal; (D) Tell Khuwaish.

sides. A QuickBird-2 image of 2005 (Figure 3) allows a more detailed view of Ashur, with the city walls (about 4 km long) that surround the urban area (about 65 ha), the “Inner City” and the “New City” on the south, separated by a wall, and the excavated buildings. A detail of the Corona photo of

1967 shows the remains of Kar-Tukulti-Ninurta excavated in 1913-1914, better preserved than today (Figure 4). The city was enormous (about 500 ha) and characterized by a walled area of about 800×800 meters that enclosed the royal-administrative quarter, divided into two halves by a canal



FIGURE 6: Remains of Assyrian and Islamic canals along the eastern bank of the Tigris, between Kar-Tukulti-Ninurta (A) and Tell Haikal (B), in a pan-sharpened (bands 3-2-1) QuickBird-2 image of 2002: 1, *Pattu-mēšari*; 2, Nahr Qanausa; 3, off-takes or secondary branches of the Nahr Qanausa. On the west bank of the river is Tell Khuwaish (C).

running roughly north-south almost the entire length of the city with a monumental gate at its southern end; this canal (Figure 4 (5)) was identified with a branch of the *Pattu-mēšari* (“Canal of Justice”), mentioned by historical texts and built by the same king Tukulti-Ninurta I (1233–1197 BC), who founded the city. The area of Kar-Tukulti-Ninurta is also crossed by branches or off-takes of an Islamic canal (Figure 4 (6)), the Nahr Qanausa, used about from the 7th to 16th century AD.

The area north of Ashur, along the eastern bank of the river, where is located Kar-Tukulti-Ninurta, as described, is, in fact, characterized by the presence of some ancient canals (dated in the Assyrian and the Islamic ages) [15], which are well visible in the satellite images and crossed an area partially transformed in recent years by agricultural works, expansion of villages, and building of infrastructures (Figures 5 and 6). The main remains of these canals, which have provided water to the alluvial plain along the east bank of the Tigris, are associated with the *Pattu-mēšari* and the

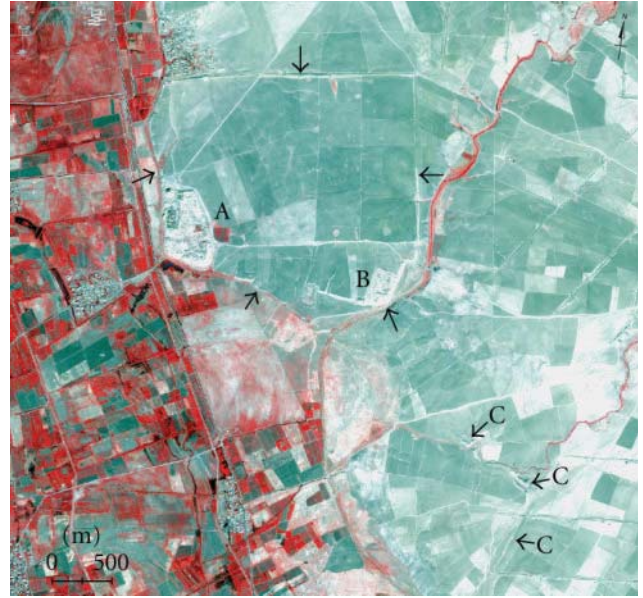


FIGURE 7: Kalhu in a pan-sharpened (bands 4-3-2) Ikonos-2 image of 2007: (A) Tell Nimrud; (B) Fort Shalmaneser; (C) traces and remains of the Assyrian canal identified with the *Pattu-nuši*; big arrows show traces and remains of the city walls.



FIGURE 8: Kalhu and the surrounding territory in a Corona KH-4B photo of 1969: (A) Tigris valley and traces of paleo-river beds; big arrows show traces of ancient roads, while small arrows point traces and remains of ancient canals (B, C, and D); 1–5, gates along the city walls.



FIGURE 9: The territory of Kalhu (A) in a Corona KH-4B photo of 1968; Tell Kashaf (B) and traces and remains of the Assyrian canal named *Pattu-nuši* (C, D, and E) and of another canal dated post the Neo-Assyrian period can be seen (F); an enlargement of the image shows the Assyrian settlement of Tell Kashaf, strategically located very near to the juncture of the Upper Zab and the Tigris.

Nahr Qanausa. Both canals tapped the Tigris in a location that is about 25 km north of Ashur and lied roughly north-south parallel the river; they have clear spoil heaps and are both relatively wide and long. The *Pattu-mēšari* defined the eastern boundary of Kar-Tukulti-Ninurta and extended well north of the city, crossing also the area of Tell Haikal (may be the ancient Ekallate), a site located 15 km north of Ashur and next to the Tigris on the east bank; it was occupied in the Middle Assyrian, Neo-Assyrian and post-Assyrian periods. On the other bank of the river, at the same distance from Ashur, is Tell Khuwaish (may be the ancient Ubase), also well documented by the satellite images (Figures 5 (D) and 6 (C)); it has a large defensive wall and was occupied in the Neo-Assyrian and post-Assyrian periods. An ancient road from this site toward north-west is also visible (Figure 5 (4)). The *Pattu-mēšari*, built in the Middle Assyrian period, may have continued to be used in the Neo-Assyrian period and irrigated the region near Ashur. The Nahr Qanausa is well visible in the satellite images and illustrates large-scale irrigation activity in this area during the Islamic period; the canal measured up to 100 m or more in width between its two banks and was 35 km long. Possible off-takes or secondary branches of this canal are also visible.

3.2. *Kalhu*. Satellite images clearly show the perimeter of the city walls (about 8 km long), which delimits the large urban area of Kalhu (roughly 380 hectares), and the two main areas of excavation, Tell Nimrud, in the south-western corner of the city, and Fort Shalmaneser in the south-eastern corner (Figure 7 (A-B)) [18, 23]. The city walls of Kalhu were built by king Ashurnasirpal II (883–859 BC), who considerably expanded the small Middle Assyrian settlement. The northern and eastern sides of the city walls are straight, while the other two were more irregular in shape, following the morphology of the territory; specifically, they followed the top of a short slope, leading down to the Shor Derreh stream, which flows along the south-east corner of the urban area and an ancient arm of the Tigris. In fact, Kalhu stood near the eastern bank of the Tigris, which ran along the western and south-western limit of the urban area and which today flows roughly 3 km further west.

A Corona KH-4B photo of 1969 is useful for documenting the ancient landscape around the city. Kalhu appears along the eastern bank of the Tigris valley, highlighted by residual humidity in the ground (Figure 8 (A)); in the valley, the traces of several paleo-river beds of the Tigris along

the western and south-western boundaries of the city are clearly visible. In the Corona photo, the perimeter of the city walls is more evident than today and less damaged by agricultural works (in particular, on the eastern side). In the same image, traces of ancient roads and canals are also well visible [15]. Ancient routes, shown in the space photo as grey linear features, can be seen to the south-east, east, and north-east of Kalhu; they probably started from the gates along the city walls, on the northern and eastern sides of the urban area (Figure 8 (1–5)). To the north-west of Kalhu, several canal excavations with developed spoil banks can be seen (Figure 8 (B-C)) although it is unclear when these features would have been created. The northernmost canal on the image appears to have been cut into the bedrock or at a depth that would have created relatively large spoil banks. These canals could have been used during high water levels to divert overflow from the Tigris into the terraces above the alluvial areas surrounding the river, so these canal may have been intended to transport water to the south-east [15]. South of the city, the evident remains of another ancient canal are visible (Figure 8 (D)); it reached the south-eastern corner of the urban area coming from the Greater (or Upper) Zab River. This canal, today less preserved due to agricultural activities (Figure 7 (C)), is identified with the *Patti-nuši* (“Canal of Abundance”) mentioned by historical texts and its remnants are well documented by a Corona KH-4B photo taken in 1968. In this image, the route of the canal until the Great Zab, 9 km away and where is the Negub tunnel, can be seen (Figure 9 (C)); here, along the southern bank of the river is Tell Kashaf, a large site which is dated to both the Middle Assyrian and Neo-Assyrian periods, and is associated to the ancient city of Kasappa, mentioned in the written sources.

Other remains of the *Patti-nuši* are visible south-east and east of the city (Figure 9 (D-E)), where the canal flowed parallel to the river. In fact, the *Patti-nuši* originates from the Khazir River (a tributary of the Great Zab which flowed north-east of Kalhu), then turning south toward the Zab and appears to have flowed parallel with this river until it reached directly south of Kalhu. From there, the channel runs north, with the canal likely having emptied its water into the area immediately around the city, where it irrigates meadows and gardens; it also provided the irrigation of the land just east its route, in the Tigris valley. The historical texts suggest at least two major construction phases for the canal and its conduit [15]. The initial canal built by Ashurnasirpal II may have been relatively small, leading from the Negub tunnel to Kalhu. It is possible that the segment of the *Patti-nuši* parallel to the Greater Zab and the course connecting to the Khazir River might have been a second phase constructed during Esarhaddon’s reign (681–669 BC).

Immediately to the south of the Greater Zab and parallel to this river, and lying near Tell Kashaf, remnants of another canal with clear spoil bank can be seen in the Corona KH-4B photo of 1968 (Figure 9 (F)). The date of this feature is unclear given the lack of field work; considering its characteristics, the canal is dated post the Neo-Assyrian period. Lastly, a QuickBird-2 image of 2002 (visible in Google Earth: consultation of March 2011) shows the modern situation of



FIGURE 10: Dur-Sharrukin in an Ikonos-2 panchromatic image of 2001: (A) Palace of Sargon II; (B) Palace F; 1–7, gates along the city walls.

the territory of Kalhu, where agricultural activities of last decades have damaged some ancient features.

3.3. Dur-Sharrukin. An Ikonos-2 image of 2001 (Figure 10) shows the quadrangular plan of Dur-Sharrukin (“Fortress of Sargon”) as established by Sargon II (721–705 BC), who founded the city between 713 and 707 BC [24]. Its characteristic regular shape appears still preserved in the fields to the east of the modern village of Khorsabad; in fact, the boundaries of the urban area (about 330 ha) can be clearly distinguished, with the remains and traces of the city walls (about 7 km long) and of the seven monumental gates (Figure 10 (1–7)). Of paramount importance in the layout of Dur-Sharrukin is the wish of symmetry, which implies to set two gates in each side of the square, except in the north-west, where one passage is replaced by a monumental bastion built out on both faces of the city wall. The function of this high platform is to support the Royal Palace of Sargon II (Figure 10 (A)), dominating the lower town on the north-west side. At the south-western end of the city, a similar platform, on which is built the so-called Palace F (Figure 10 (B)), protected the entrance through Gate 5, which was connected to the main traffic road to Nineveh.

The regular plan of the city apparently contrasts with some asymmetries which are documented within the Citadel, where are the Palace of Sargon and the Ziggurat, for instance, in the case of Building M, Residence K, and Nabu Temple. Two details of Gambit KH-7 photo taken in 1965 and of a QuickBird-2 image taken in 2003 document the decay of a lot of ancient structures excavated in the XIX-XX centuries, which today are characterised by a very poor state of conservation and damages due to agricultural works [18]. In the Gambit photo are clearly visible the remains

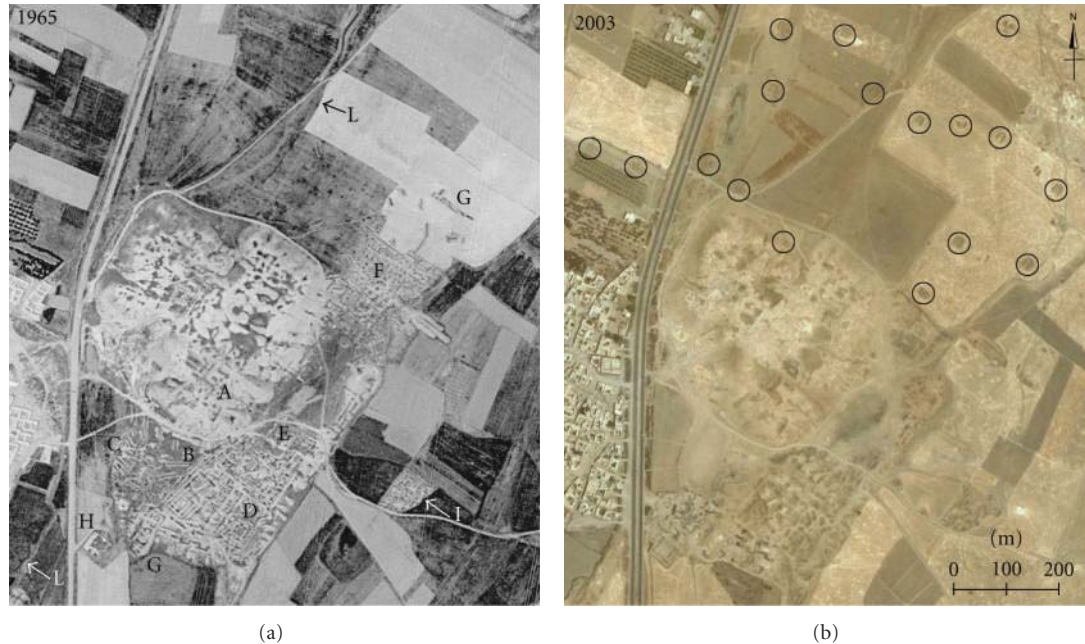


FIGURE 11: The Citadel of Dur-Sharrukin in a Gambit KH-7 photo of 1965 and in a pan-sharpened (bands 3-2-1) QuickBird-2 image of 2003: (A) Palace of Sargon; (B) Nabu Temple; (C–F) Residences (M, J, K, and L; G) remains of the walls defending the Citadel; (H) Sibitti Temple; (I) Residence Z; (L) city walls; small circles highlight some military installations.

and the plans of numerous buildings: the Sin, Adad and Shamash temples located on the same platform as the Palace of Sargon (Figure 11 (A)), the Nabu Temple (Figure 11 (B)), and the Residences M, J, K, and L (Figure 11 (C–F)), with the rooms arranged around courtyards; of the circuit of walls defending the Citadel, a few remains can be distinguished in the western side, near Gate B, and in the eastern side (Figure 11 (G)). Outside the Citadel, the remains of Sibitti Temple and Residence Z (Figure 11 (H–I)), and the traces of the city walls (Figure 11 (L)) can also be seen. In the eastern sector of the Citadel, the image of 2003 also shows some artillery positions of the Iraqi Republican Force; they are arranged in a “U” formation and are even present in the south-eastern corner of Dur-Sharrukin, where a few trenches can be seen. These military installations are visible in the 2002 and 2003 QuickBird-2 images (the last was taken about two months after the end of the Second Gulf War) and are progressively less numerous in the images acquired by the same satellite in 2004 and 2005, in which they appear to have been largely replaced by agricultural activities.

A poor state of conservation characterized also the Palace F (Figure 12 (A)), intended as private residence for the crown prince Sennacherib and located on a terrace in the south-eastern side of the city walls, near Gate 5 (Figure 12 (B)); the remains of the building have been progressively damaged by weathering and agricultural activities. In a Gambit KH-7 photo of 1965, it is possible to distinguish the general plan of the excavated sectors of the palace, containing some rooms and today scarcely preserved; indeed, a Corona KH photo of 1969 also shows the traces of the palace’s internal sector, with a quadrangular general shape, while today this sector is largely used for agriculture.

The Corona KH photo of 1969 provides a general view of the territory of Dur-Sharrukin (Figure 13 (A)) in the fruitful plain of Jebel Bashiqa (ancient Mount Musri) crossed by Khosr River (Figure 13 (B–C)). The area of Dur-Sharrukin, mentioned in the Assyrian inscriptions to have water projects related to its construction, is endowed with a good number of springs that could have been exploited to provide for the city and its surrounding territory [9, 15]. Furthermore, the Khosr River is not far from Dur-Sharrukin and may have been an important water source. Inscriptions also describe how king Sennacherib, who moved the capital to Nineveh after the death of his father Sargon II in 705 BC (see below), enlarged the openings of several springs at the base of Mount Musri, created reservoirs, and diverted their flow via canals into the Khosr. These works were intended for the new capital water supply; in fact, the plain below Dur-Sharrukin and Tell Billa (ancient Shibaniba: Figure 13 (H)) was certainly a major breadbasket region for Nineveh, located to its south-eastern end, at the juncture between the Tigris and the Khosr. The four major springs at the base of the Jebel Bashiqa (from the north: Barima, Fadhiliya, ’Ain Bahr and Bashiqa) are visible in the space photo of 1969 (Figure 13 (D–G)); the springs are recognizable by associated irrigated fields. The two springs above Dur-Sharrukin (at Barima and Fadhiliya) flow through natural channels into the Khosr River, lying in or very close to the ancient urban area.

3.4. *Nineveh*. Comparing a Gambit KH-7 photo of 1967 (Figure 14) and a WorldView-1 image of 2007 (Figure 15), the considerable expansion of the suburbs of Mosul around the ancient urban area of Nineveh and on its southern sector is evident; for this reason, only the use of old space photos

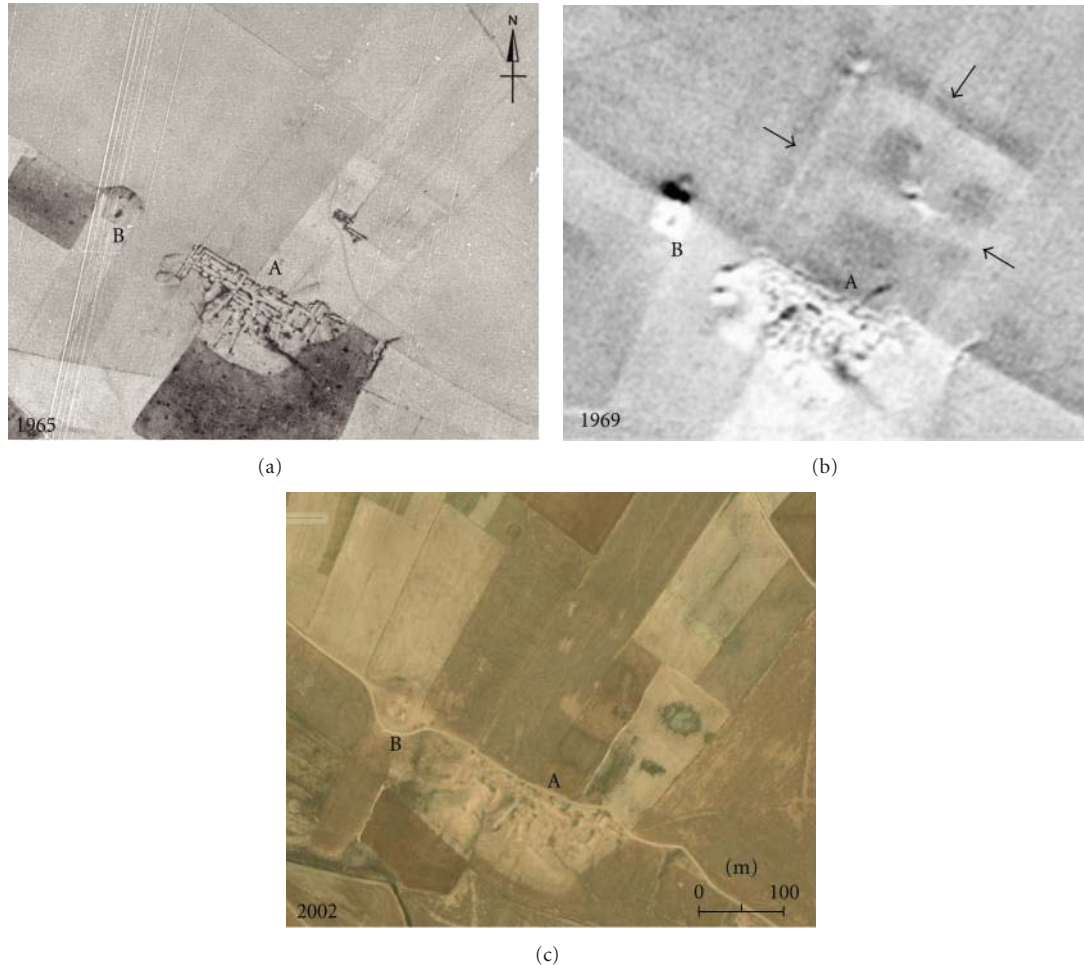


FIGURE 12: Dur-Sharrukin: the area of Palace F (A) and Gate 5 (B) in a Gambit KH-7 photo (1965), in a Corona KH-4B photo (1969), and in a pan-sharpened (bands 3-2-1) QuickBird-2 image (2002).

provides a fundamental documentation for the reconstruction of the settlement, of the ancient road and canal networks that surrounded it, and of the ancient landscape that characterized the site. The shape and the dimension of the city visible in the images were established by king Sennacherib (704–681 BC), who designed Nineveh, already a royal residence of some Middle Assyrian and Neo-Assyrian kings, as new capital of the Empire. The long city walls (about 12 km), which are fitted with fifteen monumental gateways and circumscribe the very large urban area (about 750 ha), can be seen. The wall system consisted of an ashlar stone retaining wall about 6 m high, surmounted by a mudbrick wall about 10 m high and 15 m thick; in the 2007 image it is more evident due to its restoration and reconstruction.

The available space photos of 1960s show very well the ancient landscape in which Nineveh was located, near the eastern bank of the Tigris and its junction with the Khosr River, which flowed through the urban area; the city occupied a strategic position at a Tigris River crossing. Nineveh was built in a flat terrain characterized by two mounds, which rise about 20 m above the surrounding plain: Kuyunjik (Figure 14 (A)), occupied just during Middle Assyrian

period, on which the Temples of Nabu and Ishtar, and the Palaces of Ashurbanipal and Sennacherib were built as well as Nebi Yunus (Figure 14 (B)), which was the ancient arsenal of the city. Around Nineveh, along its northern, eastern and southern sides, traces of ancient moats can be seen as well as the remains of a large canal (Figure 14 (F)): from the Khosr, it flowed about 3.5 km north-south and then turned to the west reaching the Tigris. It is possible that there was another moat or, better, an ancient arm of the Tigris along the western side of the city; in fact, in this area some traces of paleo-river beds, also running near the city walls, are visible (Figure 14 (C-D)). In the same area, today almost fully urbanized (Figure 15), immediately to the south-west of Kuyunjik mound, the land extends westward (Figure 14 (E)), at a bend in the Tigris and at the confluence of this river with the Khosr; in this point, where the bridges between the two sides of the Tigris were always built and, on the western bank of the river, the ancient Mosul was founded, there was an ancient river crossing to which converged important commercial routes.

At the end of the 8th century BC, Sennacherib excavated an elaborate set of canals to bring water from the mountains to the north of Nineveh down onto the plain behind the city,

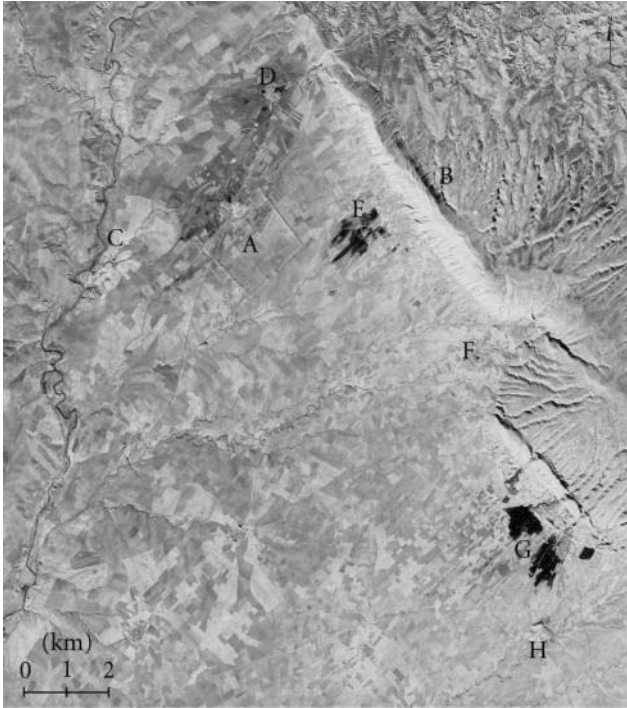


FIGURE 13: The territory of Dur-Sharrukin in a Corona KH-4B photo of 1969: the urban area of the capital city (A), Jebel Bashiqa (B), Khosr River (C), springs at Barima (D), Fadhiliya (E), 'Ain Bahr (F) and Bashiqa (G), and the ancient settlement of Tell Billa (H) are shown.

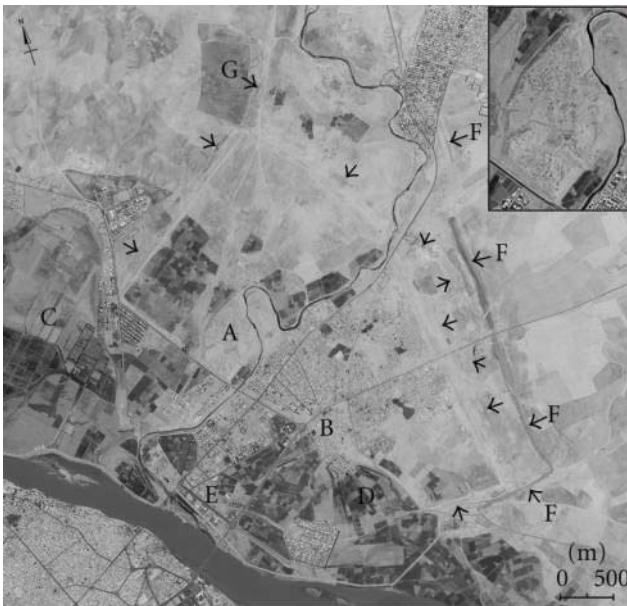


FIGURE 14: Nineveh in a Gambit KH-7 photo of June 9, 1967: (A) Kuyunjik; B, Nebi Yunus; (C-D) area with traces of paleo-river beds; (E) area at the confluence between the Tigris and the Khosr; big arrows show traces and remains of the ancient moats around the city walls, while small arrows point traces and remains of ancient canals (F-G). An enlargement of the image shows the mound of Kuyunjik.



FIGURE 15: Nineveh in a panchromatic WorldView-1 image of 2007; an enlargement of the image shows the mound of Kuyunjik.

with the aim to intensify agricultural activities [9–11, 14, 15]. The remains and traces of the canal systems planned by the king are visible in the Corona KH-4B and Gambit KH-7 space photos of the 1960s (Figure 16). These images show a landscape that in the last forty years was much transformed by the expansion of Mosul, new irrigation schemes and diffusion of mechanized agriculture (Figure 17). One of the Sennacherib's waterworks visible in the space photos is the Kisiri canal, built in 705–703 BC, that flowed along or near the present course of the Khosr River. It was connected to the later Khinnis canal (688 BC) to make a larger system that provided more distant waters to Nineveh; this later system cut into the mountains north-east of Nineveh, and water was transported roughly 40 km from the highlands to the fields north-east and east of the capital. A Corona KH-4B photo of 1967 shows the remains (4 km long) of the Kisiri canal north of Nineveh (Figures 14 (G) and 16 (A)), near the west bank of the Khosr's present course.

A second ancient canal visible in the satellite images is the Tarbisu, mentioned in one inscription from Sennacherib's reign; this text indicates that it was used for irrigating fruits, grain, and sesame fields in the region of Nineveh. The remains (about 12 km long) of this canal are visible north of Mosul, lying parallel to the northern bank of the Tigris (Figures 16 (B) and 18 (A)). It originated at the point where the Wadi al-Milh joins the Tigris and ran along the edge of the left river terrace; it transported water to the area of ancient Tarbisu (now the modern village of Sharif Khan, 8 km north-west of Nineveh), but the remains seem to document its flowing also in the direction of the capital city. So, the Tarbisu canal would have irrigated the fields on the Tigris floodplain upstream from Nineveh. This canal had been probably reused after the Neo-Assyrian period: in fact, it is much more linear than the other canals and its spoil banks are much more defined than those of the other ones.



FIGURE 16: The territory of Nineveh in a Corona KH-4B photo of 1967: black arrows show traces and remains of ancient canals ((A) Kisiri canal; (B) Tarbisu canal) and modern waterworks (C), while white arrows point traces and remains of ancient roads.



FIGURE 17: Nineveh (A) and the surrounding territory in a pan-sharpened (bands 3-2-1) QuickBird-2 image of 2004.

A Gambit KH-7 photo of 1967 clearly shows its remains on the northern bank of the Tigris, in the area of the village of Rashidiya; the image was taken before the building of the Eski Mosul dam, upstream from this area, so the river bed appears larger than today. In a QuickBird-2 image of 2004, the partial destruction of the Tarbisu canal's remains can be seen; it was deleted by agricultural works and expansion of modern villages. In both space photo and satellite image, another canal can be observed in the southern bank of the

Tigris (Figures 16 (C) and 18 (B)); it appears to be carved or hewn into the bedrock or soil. This feature may have derived its waters from a nearby wadi or the Tigris itself, providing water to the fields just to the west of Mosul; this canal is dated to the 20th century.

Satellite images also provide interesting data concerning the ancient road system around Nineveh [7, 15]. Many traces of ancient routes (also followed by modern roads) can be seen in the area east and south-east of the city (Figure 16); they seem to lead to the Ashur, Shamash, Kar-Mullissi, and Shibaniba Gates, opened along the eastern side of Nineveh's city walls, and connected the new capital to regional cities such as Shibaniba (today Tell Billa) and Kar-Mullissi (today Karmallis), or to the old capital Kalhu. Other traces of ancient roads are also visible to the north and north-east of Nineveh, respectively, in direction of the land between the capital and the mountains and toward Dur-Sharrukin.

Lastly, other linear hollow ways can also be seen in the area west of the Tigris (Figure 16). They connected Nineveh to Neo-Assyrian sites located north-west of Mosul, such as Khirbet Khan, along the ancient route coming from Eski Mosul, still used in Roman times and also documented by the *Tabula Peutingeriana* [25]. The ancient roads coming from the west also connected Nineveh to the Neo-Assyrian sites located in the area south and south-east of Jebel Sheikh Ibrahim, such as Tell Khathir, Tell Khamira, and Tell Herada.

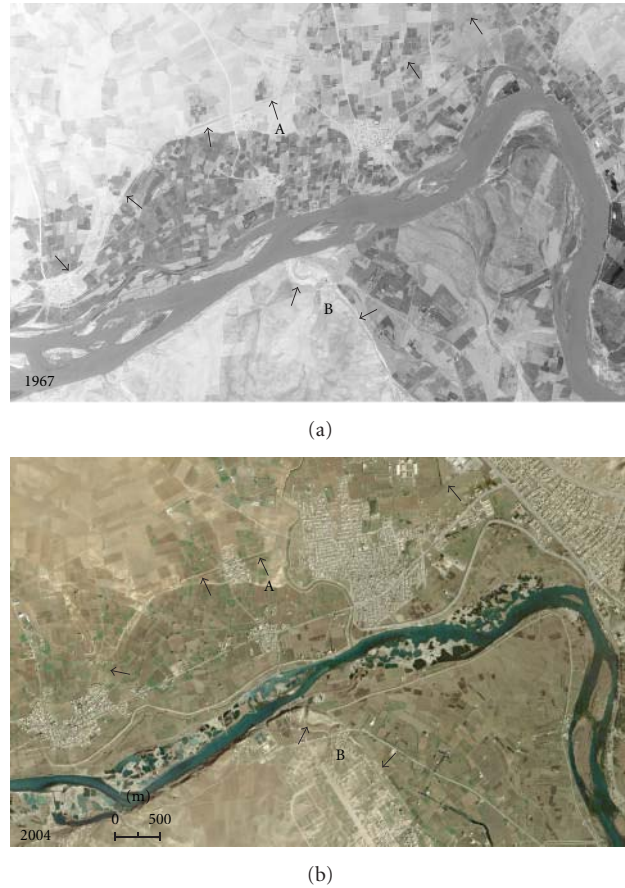


FIGURE 18: The remains of the Tarbisu canal (A) in the area of Rashidiya, north-west of Nineveh, visible in a Gambit KH-7 photo of June 9, 1967, and in a pan-sharpened (bands 3-2-1) QuickBird-2 image of 2004; a canal dated to the 20th century is visible south of the river (B).

4. Conclusions

The presented experience shows the importance of the integration of old space photos and modern satellite images, both with very high ground resolution, in the study of archaeological sites and in the reconstruction of historical landscape in ancient Mesopotamia. In fact, the high historical value of the first documentation must be integrated with the high geometric and spectral characteristics of recent images, which have clear benefits for archaeological research. The integration of these two remote-sensing sources is also necessary for monitoring transformations of the landscape and conservation of ancient features. In particular about the Assyrian capital cities, very interesting data emerged during the research using multitemporal satellite images concern the identification of the paleo-river beds of the Tigris, the documentation of ancient urban areas and their layouts, the reconstruction of canals systems and roads networks in the surrounding territories. Remote-sensed data with high geometric resolution allowed the main archaeological elements to be mapped accurately, also with reference to their topographic context. Multitemporality of remote sensed documentation was fundamental in the study of changing in the landscape, while seasonality of data and the use of a multisensor approach were very important in the identification of archaeological features and paleoenvironmental evidence

with different characteristics and a good visibility only in some periods of the year.

Lastly, the main causes of damage of the ancient remains during the last half century are weathering (without a preservation policy), mechanized agricultural works, new irrigation schemes, extension of urban areas and the two Gulf Wars (in particular the second). Weathering and damages due to military installations especially concerned Dur-Sharrukin and Nineveh, while land-use modifications have altered the ancient landscape in the surroundings of all Assyrian capital cities and in some cases (Kar-Tukulti-Ninurta, Kalhu and Dur-Sharrukin) also the areas inside them; moreover, the extension of the modern Mosul on the eastern bank of the Tigris have deleted the ancient topography of the territory around Nineveh and partially covered also the area inside the city.

Acknowledgments

For his constant support during the research activities, I thank Dr. Massimo Cultraro, scientific coordinator of the "Iraq Virtual Museum Project". Special thanks also go to Doctors Laura Castrianni, Giacomo Di Giacomo, Imma Ditaranto, Fabrizio Ghio, and Giuseppe Pellino belonging to the CNR-IBAM team that worked on the study of Iraqi archaeological sites and the processing of satellite images.

References

- [1] “From space to place,” in *Proceedings of the 2nd International Conference on Remote Sensing in Archaeology*, S. Campana and M. Forte, Eds., CNR, Rome, Italy, December 2006.
- [2] “Remote sensing for archaeology and cultural heritage management,” in *Proceedings of the 1st International Workshop*, R. Lasaponara and N. Masini, Eds., Rome, Italy, October 2008.
- [3] G. Scardozzi, “Multitemporal satellite high resolution images for the knowledge and the monitoring of the Iraqi archaeological sites: the case of Seleucia on the Tigris,” *European Journal of applied Remote Sensing*, vol. 45, no. 4, pp. 143–160, 2009.
- [4] M. Cultraro, F. Gabellone, and G. Scardozzi, “The virtual musealization of archaeological sites: between documentation and communication,” in *Proceedings of the 14th International Congress on Cultural Heritage and New Technologies*, pp. 294–308, Vienna City Hall, Austria, November 2009.
- [5] F. Gabellone and G. Scardozzi, “From the object to the territory: image-based technologies and remote sensing for the reconstruction of ancient contexts,” *Archeologia e Calcolatori*, supplement 1, pp. 123–142, 2007.
- [6] G. Di Giacomo and G. Scardozzi, “Un webGIS per la conoscenza delle antiche città della Mesopotamia,” in *Proceedings of the 2nd Congreso Internacional de Arqueología e Informática Gráfica, Patrimonio e Innovación*, 2010.
- [7] M. R. Altaweel, “The roads of Ashur and Niniveh,” *Akkadica*, vol. 124, pp. 221–228, 2003.
- [8] M. Altaweel, “The use of ASTER satellite imagery in archaeological contexts,” *Archaeological Prospection*, vol. 12, no. 3, pp. 151–166, 2005.
- [9] J. A. Ur, “Sennacherib’s northern Assyrian canals: new insights from satellite imagery and aerial photography,” *Iraq*, vol. 67, pp. 317–345, 2005.
- [10] J. A. Ur, “Les imatges per satèl·lit i l’estructura dels paisatges antics: exemples del Pròxim Orient,” *Cota Zero*, vol. 20, pp. 129–138, 2005.
- [11] T. J. Wilkinson, E. Wilkinson, J. A. Ur, and M. R. Altaweel, “Landscape and settlement in the Neo-Assyrian empire,” *Bulletin of the American Schools of Oriental Research*, vol. 340, pp. 23–56, 2005.
- [12] B. H. Menze, S. Mühl, and A. G. Sherratt, “Virtual survey on north Mesopotamian tell sites by means of satellite remote sensing,” in *Broadening Horizons. Multidisciplinary Approaches to the Study of Past Landscapes*, pp. 5–29, Cambridge, UK, 2007.
- [13] S. Mühl, “Mat Ashur—Land of Ashur. The Plain of Makhmur, Iraq,” *ArchAtlas*, 2007, <http://www.archatlas.dept.shef.ac.uk/workshop/Muehl07.php>.
- [14] J. A. Ur, “Agricultural and pastoral landscapes in the Near East: case studies using Corona satellite photography,” *ArchAtlas*, 2007, <http://www.archatlas.org/workshop/Ur07.php>.
- [15] M. R. Altaweel, *The Imperial Landscape of Ashur: Settlement and Land Use in the Assyrian Heartland*, Heidelberg, 2008.
- [16] G. A. Beazeley, “Air photography in archaeology,” *The Geographical Journal*, vol. 53, no. 5, pp. 330–335, 1919.
- [17] G. A. Beazeley, “Surveys in Mesopotamia during the war,” *The Geographical Journal*, vol. 55, no. 2, pp. 109–127, 1920.
- [18] G. Scardozzi, “Old high resolution satellite images for landscape archaeology: case studies from Turkey and Iraq,” in *Remote Sensing for Environmental Monitoring, GIS Applications, and Geology*, vol. 7110 of *Proceedings of SPIE*, pp. 1–14, 2008.
- [19] F. Piccarreta and G. Ceraudo, *Manuale di Aerofotografia Archeologica. Metodologia, Tecniche e Applicazioni*, Bari, Italy, 2000.
- [20] T. J. Wilkinson, “Linear hollows in the Jazira, upper Mesopotamia,” *Antiquity*, vol. 67, no. 256, pp. 548–562, 1993.
- [21] T. J. Wilkinson and D. J. Tucker, *Settlement Development in the North Jazira, Iraq. A Study of the Archaeological Landscape*, Warminster, UK, 1995.
- [22] G. Scardozzi, “The contribution of high resolution satellite images to the production of base-maps and cartographies for archaeological research in Turkey and Iraq,” in *Remote Sensing for Environmental Monitoring, GIS Applications, and Geology*, vol. 7478 of *Proceedings of SPIE*, pp. 1–12, 2009.
- [23] F. Gabellone and G. Scardozzi, “Integrated technologies for the reconstructive study of Mesopotamian cultural heritage: the cases of Ur, Uruk and Nimrud,” in *Proceedings of the International Congress on Cultural Heritage and New Technologies*, Vienna, Austria, 2006.
- [24] M. Cultraro, F. Gabellone, and G. Scardozzi, “Integrated methodologies and technologies for the reconstructive study of Dur-Sharrukin (Iraq),” in *Proceedings of the 21st International Symposium on AntiCIPAting the Future of the Cultural Past (CIPA’07)*, vol. 1, pp. 253–258, Athens, Greece, 2007.
- [25] H. Hauser, “Die mesopotamischen Handelswege nach der Tabula Peutingeriana,” in *Beiträge zur Kulturgeschichte Vorderasiens. Festschrift für R. M. Boehmer, U. Finkbeiner, R. Dittmann, and H. Hauptmann*, Eds., pp. 225–235, 1995.

Research Article

Integrated Methodologies for the 3D Survey and the Structural Monitoring of Industrial Archaeology: The Case of the Casalecchio di Reno Sluice, Italy

Gabriele Bitelli, Giorgia Gatta, Valentina Alena Girelli, Luca Vittuari, and Antonio Zanutta

Department of Civil, Environmental, and Materials Engineering (DICAM), University of Bologna, Viale del Risorgimento 2, 40136 Bologna, Italy

Correspondence should be addressed to Gabriele Bitelli, gabriele.bitelli@unibo.it

Received 24 March 2011; Accepted 17 April 2011

Academic Editor: Francesco Soldovieri

Copyright © 2011 Gabriele Bitelli et al. This is an open access article distributed under the Creative Commons Attribution License, which permits unrestricted use, distribution, and reproduction in any medium, provided the original work is properly cited.

The paper presents an example of integrated surveying and monitoring activities for the control of an ancient structure, the Casalecchio di Reno sluice, located near Bologna, Italy. Several geomatic techniques were applied (classical topography, high-precision spirit levelling, terrestrial laser scanning, digital close-range photogrammetry, and thermal imagery). All these measurements were put together in a unique reference system and used in order to study the stability and the movements of the structure over the period of time observed. Moreover, the metrical investigations allowed the creation of a 3D model of the structure, and the comparison between two situations, before and after the serious damages suffered by the sluice during the winter season 2008–2009. Along with the detailed investigations performed on individual portions of the structure, an analysis of the whole sluice, carried out at a regional scale, was done via the use of aerial photogrammetry, using both recently acquired images and historical photogrammetric coverage. The measurements were carried out as part of a major consolidation and restoration activity, carried out by the “Consorzio della Chiusa di Casalecchio e del Canale di Reno”.

1. Introduction

The concept of “industrial archaeology” was introduced in 1950 in England to consider the branch of archaeology that, in synergy to engineering, architecture, and economy, studies the industrial past with the aim of documenting, protecting, and exploring the cultural heritage of industrial heritage [1]. The systematic study of this type of structures requires an integrated approach, which starts from the investigation of the historical aspects of the subject, and arrives to its complete qualitative and 3D quantitative description, even considering the characteristics of the surrounding area. From an engineering point of view, often the investigations should lead to an assessment about the danger of cracks and deformations in structures, from the viewpoint of static conditions and thus to ensure the stability, security, and the possibility of preservation over time.

In this context, the first objective of this work is to discuss—on an interesting case study—some of the possibilities provided today by engineering geomatics through the integration of different surveying techniques and methods. The case study is related to the description of high-precision surveys and metrical investigations on the main elements of the ancient sluice located in Casalecchio di Reno on the Reno river, close to Bologna, Italy (Figure 1 and Figure 2). The sluice is considered the most ancient hydraulic system still in activity in Europe and was recently included in the UNESCO list of Monuments and Sites as Messengers of Peace.

As for the geometry of the structure, it must be noted that the upper edge is not horizontal, but it shows a depressed area in order to redirect water to the hydraulic right edge of the dam, where a water deviation is performed. The length of the sluice is 160.4 meters. The highest point is located at the left edge and it rises to 0.54 m with respect to the most

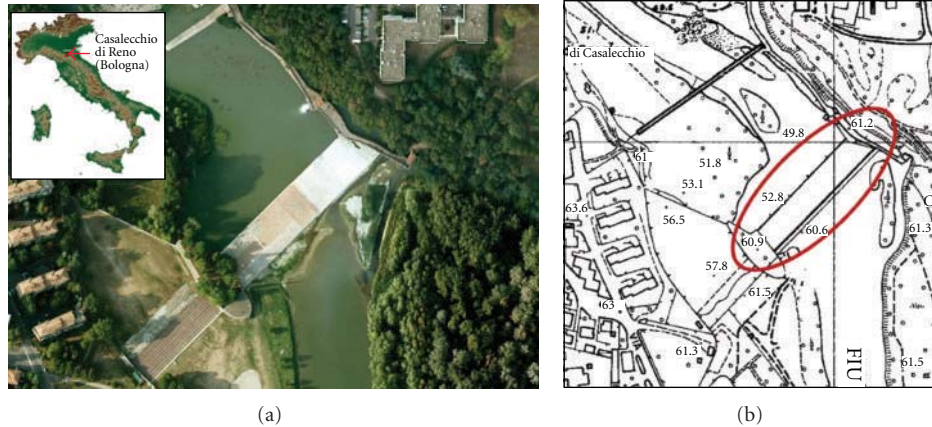


FIGURE 1: The Casalecchio di Reno sluice on high-resolution satellite image and 1 : 5000 technical map.

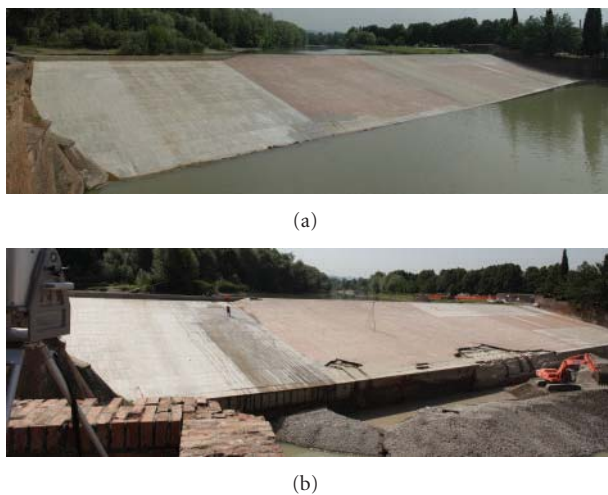


FIGURE 2: Images of the sluice, taken in 2005 (a) and 2009 (b); the second shows the damages suffered after the winter season 2008-2009.

depressed portion of the barrier, located at a distance of 71 meters from the right edge. The height difference between the upper and lower margins is 8.03 m.

An integrated approach to the surveying problem was required to obtain a complete level of knowledge on the conditions of the structure, to be complemented by historical studies and geophysical surveys to improve the understanding of both visible and underground parts of the sluice. In a preliminary phase of the work, a contextualisation of the structure was performed, assessing its geometry and the relationship with the surrounding environment, in order to get in tune with the history of the building and to better understand its characteristics and transformations over the centuries. Subsequently, a rigorous metrical description was performed aiming at monitoring the structure and supporting the recent restoration works.

2. Historical Notes and Geological Setting

Water is one of the sources of civilisation, and along the history of human civilisation several solutions have

been implemented to overcome water lack and increase guaranteed supply of water. Since ancient times, the idea to stop a river was developed in the arduous construction of containment barriers. These works were inspired by different needs. For example, the rudimentary wooden barriers were intended to create small reservoirs and encourage fishing. People were ingenious in the design of locks, bars, and dams with the primary intent of creating water stocks to support human life, livestock, production activities, and agriculture. Usually, actions undertaken to stop a river are technically complex and require detailed studies under the structural, hydraulic, and hydrogeological points of view. Therefore the techniques of construction of the locks were refined over time through various more or less positive experiences.

The Casalecchio di Reno sluice played in the past and still plays today a very important role for water management in the Bologna territory [2, 3]. The first historical notes on the Casalecchio di Reno sluice are very old; they date back to the I millennium A. D. and report the news of a wooden barrage of Italy's Reno river. In this area, the Reno river shows the transition zone between the end of the mountain basin and the beginning of the valley basin [4]. The boundary between the two districts is represented by the sluice of Casalecchio and by its side spillway. In this section the Reno is of particular importance, having to fulfil the role of hydraulic connection between the Apennines and the torrential regime of a river dammed to the course of the plains. The river flows through recent wetlands and very old alluvial deposits. From a morphological point of view the area is developed between the large alluvial Apennines fans, generated by the Reno and Savena rivers, which are part of the transition zone between the northern edge of the Apennines and the alluvial plain. The entire plain near Casalecchio, extended by the river's bed to the base of the hill slopes, is identified with the southern portion of the large alluvial fan of the Reno. The structure of this fan is complex, and, proceeding northbound, the fan is expanded considerably, embracing the western suburban area of Bologna. Pulling back to the south towards the village of Sasso Marconi, it shrinks in its apical part, to progressively assume the characteristics of a typical Apennine valley. From the geological point of view, in

the lower part of the watercourse there are alluvial soils, with extensive gravel mattresses whereas, climbing to the ridge, variously alternated limestone, sandstone, and clay can be observed; in the area characterised by gullies the presence of scaly clays prevails, while slightly further North, chalky outcrops can be observed within the Messinian evaporite rocks.

The first historic notes on the sluice date back to the I millennium A. D., then a text dated 1191 cites people called “Ramisani” as the builders of a wooden sluice for supplying mechanical energy to the mills.

In 1208 the municipality of Bologna, with a contract, acquired by the “Ramisani” the right to use excess water and made a commitment to the reconstruction and maintenance of the water lock “de lapidibus” that started in 1250 and was completed in 1278. Some operations were carried out at the beginning of the fourteenth century under the care of the Dominican and Franciscan friars. The most important ones date back to 1317 and 1324 when Cardinal Bertrando del Poggetto entrusted the Hermit Friars with the construction of a new sluice. This property was ruined after a few years for technical reasons or maybe because of the war. Ruins located downstream of the present structures can be observed today and from the remains we can assess that the artefact was made up of a conglomerate of rocks and stones tied to the bottom, with the presence of support joists which acted as the matrix. The current construction of the lock, that is in its final form, dates back to the years between 1360 and 1367 thanks to the initiative of the Papal Legate Cardinal Egidio Albornoz. In 1567, after serious damage caused by floods, the sluice was almost completely rebuilt thanks to Pope Pius V, who intervened in support of the City into financial difficulties. It was ordered that from that moment, the maintenance costs would have been supplied by all those who would have taken profit from the water. The construction of walls that held the channel from the sluice should instead go back to 1547. The work was executed by Jacopo Barozzi, known as “Vignola” (1507–1573). During the flood of 1617 much of the oak tables that covered the surface of the sluice were destroyed, causing even more serious damage to the walls. The restoration was undertaken under the direction of Vincenzo Sassi, and the works continued until 1627. In 1691, Domenico Guglielmi was appointed superintendent of the sluice of Casalecchio and, thanks to his experience in regulating the hydraulic systems, he performed surveys with the drawings of graphical hydraulic profiles. The extraordinary restoration of the sluice ended in the eighteenth century, and underwent routine maintenance (Figure 3).

In the next century the Reno recorded more flood events. Three of these exceeded the height of three meters to the section of Casalecchio. On the 1st of October 1893, a violent storm hit the night of the Tuscan-Emilian Apennines [5]. The Reno Valley was upset by the force of water that caused landslides and overflowing rivers. The wave of flood, with its overwhelming force, arrived in Casalecchio at ten o'clock in the morning. At eleven o'clock the hydrometer recorded the height of 4.70 meters above the lower edge of the sluice, a value never before achieved and never surpassed. During the

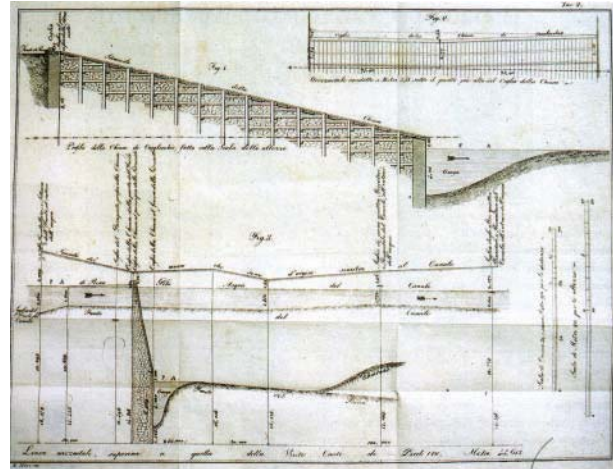


FIGURE 3: Sections of the Casalecchio di Reno by Antonio Lecchi, 1776.

“great flood” the structure itself did not show any structure failure or serious injury, it was bypassed by the water on the left side. The energy of the flood then poured on the wall that was already weakened by earlier events, it did not resist the pressure and collapsed. The result was a profound change of the river bed that dug a new course on the left. This caused the block of the industries in Bologna as well as its sewage and irrigation systems. Thanks to 660 workers that carried out the major works, in 1895 the complex was rebuilt in its final structure. In the new structure the slide was entirely covered with sheets of white granite with a thickness of 10–12 cm instead of the old coating made with planks of oak attached to the wall structure. In 1915 the central plank of wood was replaced with slabs of red granite. In the years 1926-27 and later in the year 1939-40 other white granite slabs on the left side structure were incorporated. The sluice was then repaired after an air force raid during the war in 1945 before replacing the last parts of the wooden table with sheets of trachyte. The complex hydraulics of the sluice is now owned by the “Consorzio della Chiusa di Casalecchio.”

This institution is responsible for the management, maintenance, and enhancement of this magnificent work: the reported activities have been requested by the Consortium in the framework of this task.

3. Materials and Methods

The surveying activities on the sluice structure were carried out in 2005, 2006, and 2009 and involved different surveying techniques: classical topography, high-precision spirit levelling, range-based terrestrial laser scanning, digital photogrammetry, and thermal imagery.

The last measurement campaign in 2009 was mainly devoted to support the restoration activities, carried out after the severe damages suffered by the lowest part of the sluice structure during the 2008-2009 winter (Figure 2).

The whole set of activities, methods, and measures were planned in order to allow an effective integration

between the various techniques chosen on the basis of their respective potential. Regarding the horizontal and vertical reference systems, the main work was carried out on a local system, but the availability in the same area of a GPS point already established by the University of Bologna for regional subsidence monitoring, and of a benchmark from an important district levelling network, permits to move all the results in absolute system when necessary.

4. High-Precision Three-Dimensional Topographic Surveys

In 2005, a three-dimensional network has been installed on the sluice to achieve high-precision three-dimensional measurements using highly accurate engineering total stations (Figure 4). The network was surveyed in 2005, 2006, and 2009; in the last campaign, five points in the lower border of the slide were lost due to the damages occurred in the 2008–2009 winter.

The control network consisted of 11 self-centering devices on the slide, anchored to the structure below the slabs, and used for the positioning of the retroreflective prisms and also of the reference targets used in the laser scans. Moreover, 22 additional points were identified, already present in the structure, that were used also as reference benchmarks for the high-precision geometric levelling.

From two positions located outside the structure of the dam, the measurements were carried out using high-precision Leica total stations (TCA2003 and TC2003 in 2005–2006, two TCA2003 in 2009), characterised by an angular accuracy of 0.5'' and a nominal precision of 1 mm + 1 ppm for the distances. The total stations were equipped with dual-axis compensators, which compensate the horizontal and vertical readings for small deviations of the principal axes with respect to the vertical line; the robotic station Leica TCA2003 is able to automatically recognize the centre of the targets.

The atmospheric refraction was modelled from the measurements of air temperatures, barometric pressure levels, and relative humidity recorded during the measurements on both sides of the structure. In fact, knowledge of the refractive index (n) of the prevailing atmosphere is necessary in order to apply a correction for velocity to the measured distance; the classical approach described by [6], subsequently adapted considering wavelengths between 560 and 900 nm, was adopted.

A rigorous least squares adjustment of the dataset was carried out adopting a redundant number of measurements, but using minimum constraints to define the reference system; in this way the coordinates of all control points were computed. Regarding the precision of the surveys, for the 11 points along the chute the major semiaxis of the associated error ellipses at 95% probability level reached maximum values on the order of 2.5 mm whilst worse results were obtained for the other points not characterised by self-centring devices. The comparison between subsequent campaigns (2005 versus 2006, 2009 versus 2006), taking into account the confidence intervals associated to the

coordinates, has generally shown nonsignificant planimetric movements for the structure.

5. Differential Levelling

Aiming at detecting high-precision estimates of elevation changes, annual spirit levelling surveys have been performed by means of high-accuracy digital levels.

Due to the impossibility, for logistics problems, to realize specific benchmarks along the superior and inferior borders of the sluice, a network of 25 benchmarks, mainly defined by small holes along the borders (on steel joints or on stones), was established in 2005. The height origin was benchmark 21 located on the top boundary of the sluice (Figure 4(b)).

The levelling measurements have been carried out with a classical scheme using two invar staffs and by interconnected closed rings to achieve redundant data. The benchmark heights coming from the statistical analysis of the observations (adjustment computation), have been characterised by a precision to a tenth of a millimetre. The difference in elevation between surveys were in the order of the standard deviation associated to the adjusted heights, proving that the main structure did not suffer significant movements, with the exception of the points located in the inferior border near the damaged zone, where uplift movements in the order of 1 mm were detected (Figure 5(b)).

6. Terrestrial Laser Scanning Surveys, Digital Photogrammetry, and Thermal Surveys

High-density three-dimensional point clouds have been surveyed by means of terrestrial laser scanner (TLS) and integration with digital photogrammetry [7].

The first laser scanner survey of the sluice and the surrounding area has been generated in 2006 by using a Riegl LMSZ-420i instrument whilst a second survey was carried out in 2009 using a Riegl LMS-Z390; the declared precision of the two TLS instruments is, respectively, 4 mm (averaged) and 2 mm. It must be noticed that in the last survey, the lower part of the structure was visible, since the water supply was interrupted by a detour. The laser scanners were coupled with calibrated Nikon D70 and Nikon D200 digital cameras [8]. The average density of point clouds was in the order of 5 cm on the slide, and it was increased in particular in the damaged area, located on the bottom right side of the structure (Figure 6).

To cover up the entire surface, point clouds have been acquired from four different standing points around the structure, for a total number of more than 10 millions of points.

The presence of water at the bottom of the sluice and the particular flat shape of the structure needed an accurate procedure of data processing. As a matter of fact the water surface has been the source of disturbance that locally affected the quality of the laser measurements. The relative incidence angle of the laser ray, in respect to the air-water separation surface, led in some parts to the achievement of Brewster angle limit with completely wrong points, acquired by the laser through a specular reflection of the sluice

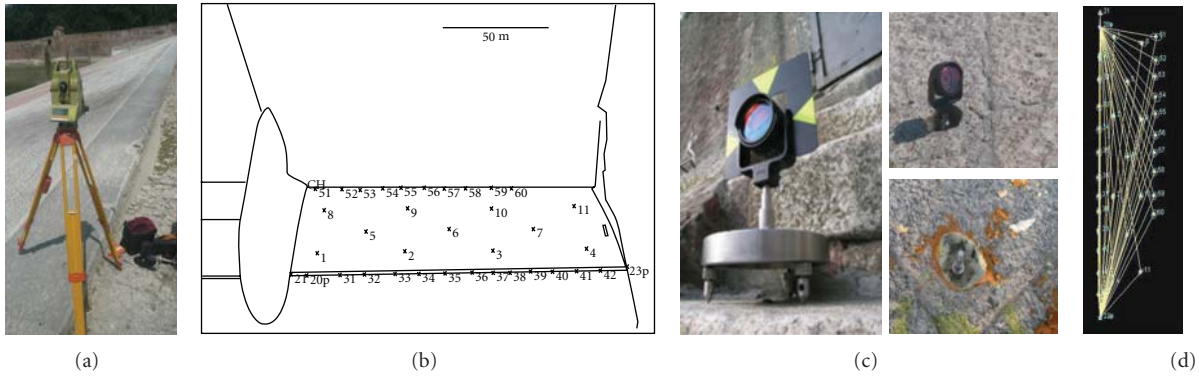


FIGURE 4: Classical topographic surveying : (a) total station; (b) scheme of control points distribution; (c) examples of GCPs characterised by forced centering devices (outside the structure and on the slide, resp.) measured using prisms; (d) map of the 3D adjusted network.

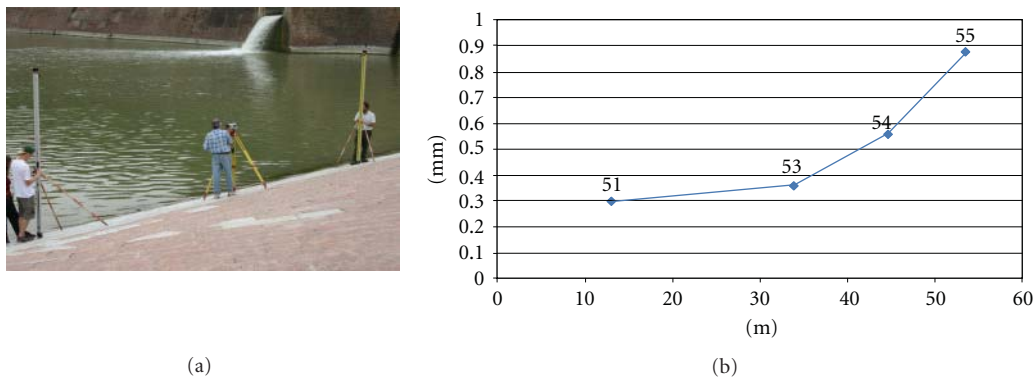


FIGURE 5: Field operations of high-precision spirit leveling (a); vertical displacements concerning the 2006–2009 time span for four benchmarks located on the bottom of the slide near the damaged zone (b).

structures (Figure 7); in this case the mirror was accidentally realised by the water surface itself. These points have been eliminated by appropriate filtering.

The flat and gently sloping surface of the chute, together with really small incidence angles, from the stations on the bottom, produced a surface affected by an unreal roughness and unexpected outliers which have been reduced by means of smoothing and filtering procedure. In this situation it must be considered that the laser footprint is very elongated, affecting the precision of the measured point.

After the postprocessing phases of laser data (filtering, merging, decimation, etc.) the point clouds have been triangulated, forming a continuous digital surface model (DSM) by means of interpolation algorithms.

The images collected with the calibrated digital camera supplied—through a postprocess—a textured representation of the three-dimensional surface models and the true orthophoto mosaics.

The resulting products of the laser surveys have been clouds of three-dimensional points referred to the same local reference system. The registration of the multiple scans has been performed using dedicated cylindrical retroreflectors placed inside the chute plan, using the same self-centring devices adopted for the planimetric survey. By so doing also the laser scanner data were referred to the same system of the other data.

During 2009, the sluice has been furthermore surveyed by means of a thermal camera, in order to investigate the capability of metrical use of thermal images.

The test has been performed by means of an NEC Thermo Tracer 9100 Pro, characterised by a single spectral band in the 8–14 μm interval, a sensitivity of 0.08 K and a field of view ranging from 16° to 21°. The camera is characterised by an uncooled focal plane array detector, 320 × 240 pixels.

The thermographic camera detects radiation in the thermal infrared range of the electromagnetic spectrum and produces images of that radiation which could be used in the same way as conventional photogrammetric images. The main problem for integrating these data with the other is the geometric calibration of the camera, and the stability of the geometry along the images sequences. Once these problems are solved, these low-resolution thermal images can be used also for a variety of metrical-based applications [9].

Three coverage strips of the sluice have been collected trying to cover the entire structure from different points of view.

In order to dispose of a large set of visible ground control points either for exterior and interior orientation, a dense three-dimensional model of the sluice coming from the terrestrial laser scanning survey was used, recognising on the model the control points needed; a field calibration

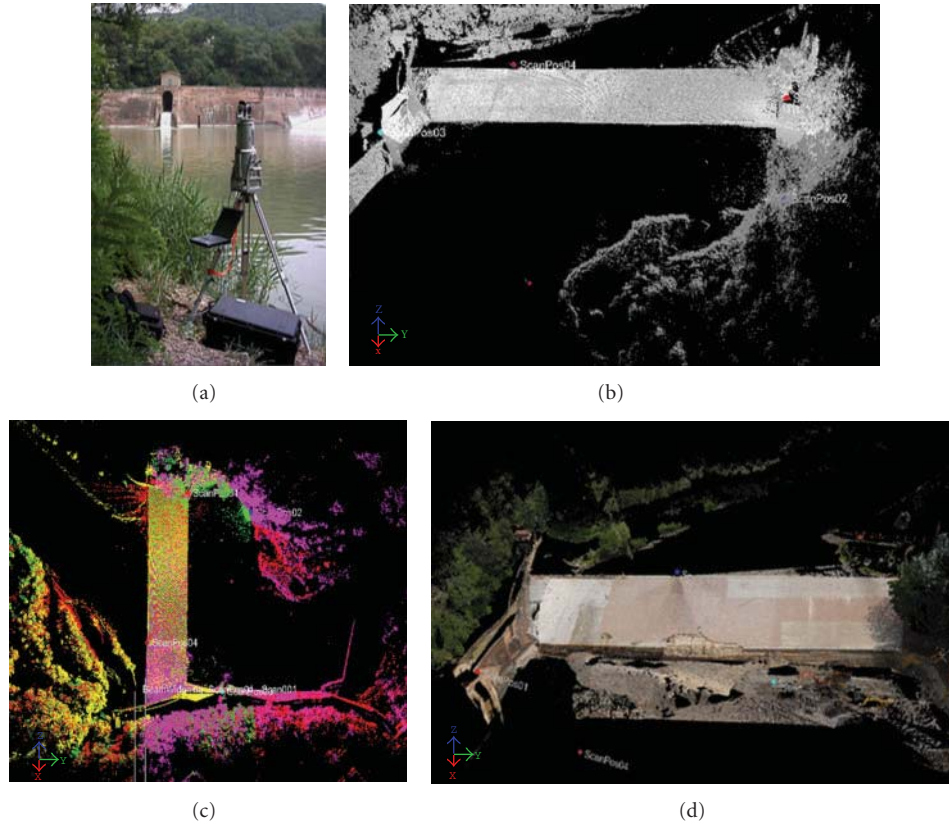


FIGURE 6: Terrestrial laser scanning surveys and digital photogrammetry: (a) Riegl LMSZ420i coupled with Nikon D200 digital camera; (b, c) laser scanning points clouds of the sluice and the surrounding area (2006); (d) the 3D raster model of the chute after the great damages suffered by the structure during the 2008-2009 winter.

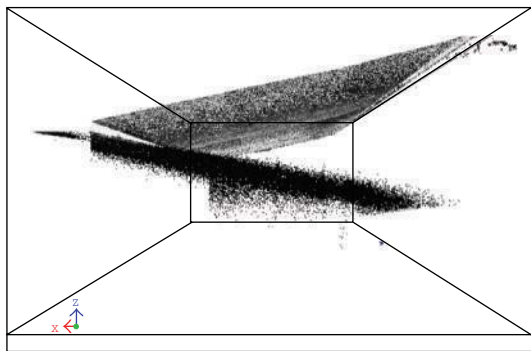


FIGURE 7: Vertical section, showing in the lower part of the points cloud the wrong points generated by a specular effect due to the achievement of Brewster angle by the incident laser ray in respect to the water surface.

procedure was experimented to estimate the intrinsic internal parameters of the camera and the external parameters of the images.

The results of camera calibration showed high distortion values, and large shifts of the principal point, but allowed to create three-dimensional raster models and thermal orthophotos of the sluice. These documents (after considering emissivity of the materials) provide temperature

distribution on the structure and this information could be used to better assess the lack of homogeneity in the surface of the slide (Figure 8).

7. Aerial Photogrammetric Processing

In an effort to provide a geographic database covering the whole area and referring also to the changes that occurred in the recent past, a photogrammetric analysis was performed by means of the processing of aerial images acquired in different periods, starting from 1971. These data can be inserted in a dedicated GIS developed to store all the geographical data collected in the past and in the recent surveys concerning the sluice.

The example considered refers to a stereocouple at photographic scale 1:13000 from 1976 that has been scanned at 1200 dpi resolution and calibrated using an analytical procedure.

To solve the orientation problem and reconstruct the absolute geometric relationships among the images, 12 GCPs have been adopted coming from 1:5000 cartographic representations of the area (CTR 220120), after a careful analysis in order to retrieve points available also in the historical images.

A 2×2 m grid DTM of the area has been generated automatically, by Leica Photogrammetric Suite software,

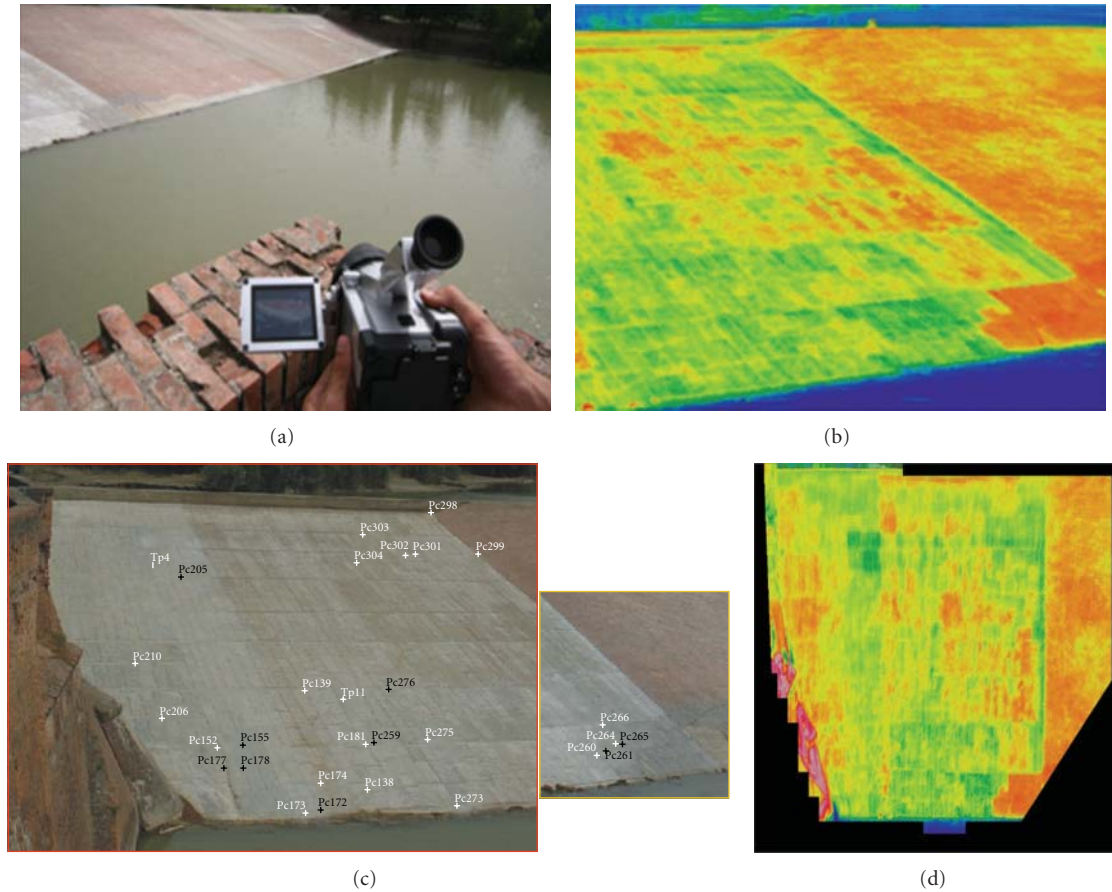


FIGURE 8: Thermal imagery: (a) NEC TH9100 PRO 320×240 thermal camera; (b) an example of thermal image characterised by 5 cm pixel on the object; (c) each thermal image has been calibrated by photogrammetric procedures and oriented in the space by means of the dense clouds of laser points; (d) the thermal orthophoto of a portion of the slide showing the blocks of different material related to different restoration activities carried out in the past.

with manual postediting to correct errors deriving from the image matching technique. The editing procedure consisted of manual insertion of breaklines into incorrect zones, with consequent local recalculation of the surface area.

Starting from the DSM, an orthophoto of the area characterized by a ground pixel size of 0.5 m has been produced and finally superimposed on the existing vector map (Figure 9).

8. Results and Discussion

This methodological work was initiated as part of an interdisciplinary project, created to better understand the functions of ancient structures, and as support for restoration activities. The purpose of metric investigations was twofold: to have a detailed geometric description of the structure in order to highlight the required actions and to get evidence about movements within the structures. The comparison between the results obtained in 2005-2006 and those reached in 2009 from all the activities undertaken (three-dimensional topographic surveys, analysis of geometric surface patterns produced by repeated series of laser scanner data) has allowed us to have information about the extent of the damaged sectors and the description of movements in

progress. The study of the movements undertaken within the chute of the sluice showed no significant changes between the positions of control points. The absence of differential movements is an indicator of good health in the structure of the dam itself.

Nevertheless spirit levelling surveys have pointed out some significant changes at the border.

The main differences concerned the damaged area of the sluice destroyed after an exceptional atmospheric event registered during the 2009 winter. The strong rains and floods have caused the destruction of some benchmarks and the removal of large stone blocks located at the bottom of the sluice.

The high-density multitemporal DSMs generated by means of TLS have been registered in one reference system thanks to the presence of GCPs available on the sluice. From the comparison of the surfaces some significant differences have been evaluated (Figure 10).

9. Conclusions

The city of Bologna, with an advance of more than three centuries, prefigures the production model known as the “First Industrial Revolution” thanks to the Sluice of Casalecchio

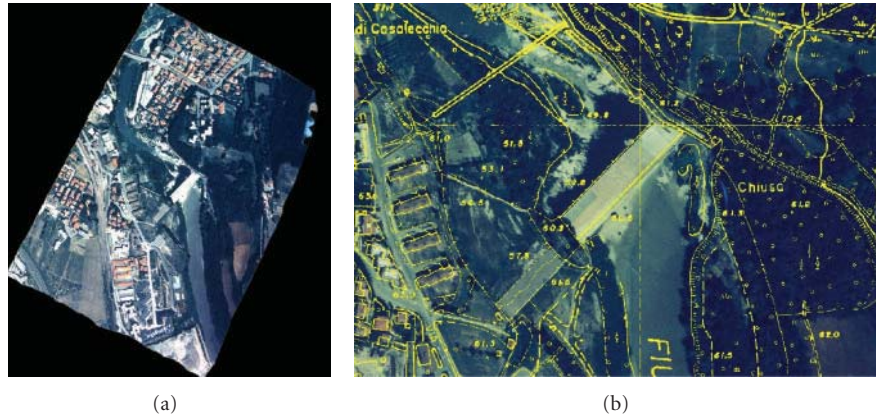


FIGURE 9: The orthophoto (a) and the superimposition of vector map on a detail related to the sluice area (b).

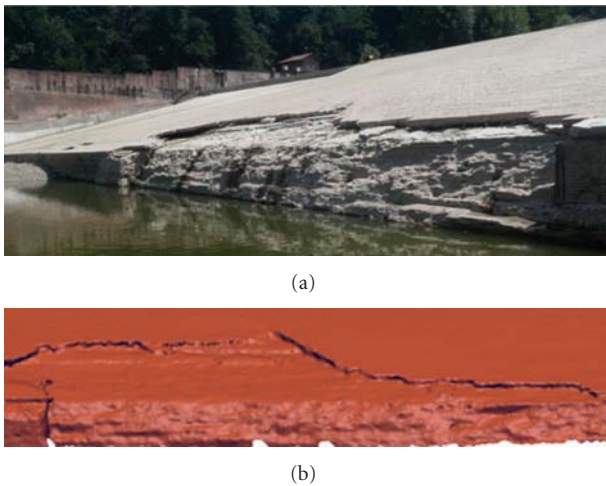


FIGURE 10: Detail of the damaged area at the bottom of the sluice (2009) before restoration: (a) RGB image; (b) TLS 3D raster model.

which can be considered as a symbol of this new economic model.

Due the importance of this hydraulic structure, the public owners always demonstrated care and periodical restoration works have been performed.

Starting from 2005 a multidisciplinary project concerning the full study of the sluice took place. As a result of the geomatic surveys performed, a 3D model of the structure has been generated. Concerning the monitoring of the stability of the sluice by means of topographic methods, no significant displacements have been detected (exceptions are represented by a few benchmarks located on the bottom of the structure, close to the damaged zone). These results confirm the good health of the old structure.

Acknowledgments

The authors want to acknowledge the “Consorzio della Chiusa di Casalecchio e del Canale di Reno,” in particular F. Marchi, for allowing the possibility to realize this work,

and A. Raffagli, responsible for the structural works. Thanks also to C. Bonini, G. Capone, D. Garbellini, F. Girardi, E. Mandanici, M. Mannina, B. Roffarè, and M. A. Tini, for the collaboration in different phases of the surveys.

References

- [1] N. Cossons, Ed., *Perspectives on Industrial Archaeology*, London Science Museum, 2000.
- [2] F. Maranesi, F. Marchi, M. Poli, and G. Tabarroni, *Le Acque a Bologna*, Editrice Compositori, Bologna, Italy, 2005.
- [3] A. Zanotti, *Il Sistema delle Acque a Bologna dal XIII al XIX Secolo*, Editrice Compositori, Bologna, Italy, 2000.
- [4] A. Papetti, *Casalecchio di Reno, Aspetti Idrogeologici del Territorio*, Telesio Editrice, Milano, Italy, 2003.
- [5] U. Brunelli and F. Canonici, *La Chiusa di Casalecchio e i Lavori Eseguiti dalla Provincia di Bologna per la Chiusura della Rotta di Reno in Sinistra Avvenuta il 1° Ottobre 1893 e per la Sistemazione del Fiume a monte della Chiusa*, Regia Tipografia, Bologna, Italy, 1896.
- [6] H. Barrell and J. E. Sears, “The Refraction and dispersion of air for visible spectrum,” *Philosophical Transactions of the Royal Society of London. Series A*, vol. 238, pp. 1–64, 1939.
- [7] K. Kraus, *Photogrammetry—Geometry from Images and Laser Scans*, De Gruyter, Berlin, Germany, 2007.
- [8] T. Luhmann, S. Robson, S. Kyle, and I. Harley, *Close Range Photogrammetry*, Whittles, 2006.
- [9] H. Kaplan, *Practical Applications of Infrared Thermal Sensing and Image Equipment*, SPIE, 2007.

Research Article

Data Fusion for Electromagnetic and Electrical Resistive Tomography Based on Maximum Likelihood

Sven Nordebo,^{1,2} Mats Gustafsson,² Therese Sjöden,¹ and Francesco Soldovieri³

¹ School of Computer Science, Physics, and Mathematics, Linnaeus University, 35195 Växjö, Sweden

² Department of Electrical and Information Technology, Lund University, P.O. Box 118, 22100 Lund, Sweden

³ Institute for Electromagnetic Sensing of the Environment, National Research Council, Street Diocleziano 328, 80124 Naples, Italy

Correspondence should be addressed to Sven Nordebo, sven.nordebo@lnu.se

Received 15 February 2011; Revised 13 April 2011; Accepted 3 May 2011

Academic Editor: Nicola Masini

Copyright © 2011 Sven Nordebo et al. This is an open access article distributed under the Creative Commons Attribution License, which permits unrestricted use, distribution, and reproduction in any medium, provided the original work is properly cited.

This paper presents a maximum likelihood based approach to data fusion for electromagnetic (EM) and electrical resistive (ER) tomography. The statistical maximum likelihood criterion is closely linked to the additive Fisher information measure, and it facilitates an appropriate weighting of the measurement data which can be useful with multiphysics inverse problems. The Fisher information is particularly useful for inverse problems which can be linearized similar to the Born approximation. In this paper, a proper scalar product is defined for the measurements and a truncated Singular Value Decomposition (SVD) based algorithm is devised which combines the measurement data of the two imaging modalities in a way that is optimal in the sense of maximum likelihood. As a multiphysics problem formulation with applications in geophysics, the problem of tunnel detection based on EM and ER tomography is studied in this paper. To illustrate the connection between the Green's functions, the gradients and the Fisher information, two simple and generic forward models are described in detail regarding two-dimensional EM and ER tomography, respectively.

1. Introduction

Nondestructive monitoring systems based on information, communication, and sensor technologies will be used to provide future emergency and disasters stakeholders with high situation awareness by means of realtime and detailed information and images of the infrastructure status [1]. Important technologies include electrical resistive tomography (ERT) as well as ground penetrating radar (GPR), which have become widely applied to obtain images of the subsurface in areas of complex geology [2–4]. The development and implementation of complex ICT-based monitoring systems will also rely on new technologies, techniques, and algorithms including the integration and correlation of the electromagnetic properties corresponding to imaging modalities such as ERT and GPR [1].

Statistical maximum likelihood (ML) or Bayesian approaches towards multisensor data fusion have been considered previously in, for example, [5–8]. In this paper,

the general approach to information fusion is to perform a multiphysics data fusion based on the maximum likelihood principle, and to exploit the elements of Fisher information analysis that has been developed in [9–11]. In particular, an infinite-dimensional Fisher information formulation is employed which is suitable for analytical Green's function and gradient-based approaches [11], as well as with adjoint field formulations [10].

The Fisher information is a local measure of information with respect to the state space of parameter values, and it is therefore particularly useful for inverse problems which can be linearized, such as with the Born approximation [3], and so forth. In this paper, it is shown how the principle of maximum likelihood (under the assumption of Gaussian noise) can be used to derive a proper scalar product for the measurement data. By using this scalar product, it is shown that the truncated pseudoinverse based on the singular value decomposition (SVD) of the multiphysics forward model is equivalent to a one-step Newton method based on the

principle of maximum likelihood together with a truncated SVD of the Fisher information. Hence, a linearized and regularized inversion based on the proposed scalar product yields a weighting of the measurement data which is statistically optimal and which is able to deal with a diversity of multiphysics forward problems, a combination of complex valued and real valued data, and a diversity of measurement sensors and qualities, and so forth.

As a generic example concerning a multiphysics inverse problem based on geophysical sensing, this paper addresses the problem of tunnel detection [4] based on data fusion with electromagnetic (EM) and electrical resistive (ER) tomography. A two-dimensional problem is considered with radio frequency as well as electrical sensors placed horizontally above a tunnel in the ground. A Green's function approach is used to obtain the gradients for the Fisher information analysis [11] as well as for the related SVD-based inversion algorithm. The numerical examples demonstrate the potential impact of an imbalance between the singular values and the variance of the measurement noise when different imaging modalities are incorporated in the inversion. The examples furthermore illustrate the significance of taking a statistically based weighting of the measurement data into proper account.

2. Multiphysics Data Fusion Based on Maximum Likelihood

In this section multiphysics data fusion is discussed. Section 2.1 settle the statistical model and the gradients. This is then used in Section 2.2 to describe data fusion with SVD and ML approach.

2.1. Statistical Model and Gradients for the Multiphysics Problem. Consider the multiphysics inverse problem of combining electromagnetic (EM) and electrical resistive (ER) tomography based on the following physical/statistical measurement model

$$\begin{aligned} \xi_{mnq}^{(1)} &= \psi_{mnq}^{(1)}(\theta) + w_{mnq}^{(1)}, & m &= 1, \dots, M_1, \\ n &= 1, \dots, N_1, & q &= 1, \dots, Q, \\ \xi_{mn}^{(2)} &= \psi_{mn}^{(2)}(\theta) + w_{mn}^{(2)}, & m &= 1, \dots, M_2, \\ n &= 1, \dots, N_2. \end{aligned} \quad (1)$$

Here, $\xi_{mnq}^{(1)}$ are complex valued data (dynamic electrical fields) obtained in the frequency domain and $\xi_{mn}^{(2)}$ are real valued data (static electrical potentials), which are obtained from simultaneous EM and ER tomographic measurements, respectively. It is assumed that there are N_i excitations with $n = 1, \dots, N_i$, and M_i measurements for each excitation with $m = 1, \dots, M_i$, where $i = 1, 2$ corresponds to the two EM and ER imaging modalities, respectively. Hence, for each imaging modality, the measurements are uniquely identified by the double index (mn). For the EM modality there are also Q frequency domain measurements with $q = 1, \dots, Q$.

The unknown, real parameter function (distributed parameter) of interest is $\theta(\mathbf{r}) = [\epsilon_r(\mathbf{r}) \ \sigma(\mathbf{r})]^T$ where $\epsilon_r(\mathbf{r})$ is the relative permittivity and $\sigma(\mathbf{r})$ the conductivity, and where both parameter functions are defined over some spatial domain Ω with $\mathbf{r} \in \Omega$. Here, $(\cdot)^T$ denotes the transpose operation.

The physical forward models are denoted $\psi^{(1)}(\theta) = \{\psi_{mnq}^{(1)}(\theta)\}$ and $\psi^{(2)}(\theta) = \{\psi_{mn}^{(2)}(\theta)\}$ in the two EM and ER tomography problems, respectively. The Fréchet derivative [12], or the Jacobian [13] of the forward operator $\psi^{(i)}$, is the bounded linear operator $\mathcal{J}^{(i)}$ that yields the first order variation of $\psi^{(i)}$, denoted as

$$\delta\psi^{(i)} = \mathcal{J}^{(i)}\delta\theta, \quad (2)$$

where $i = 1, 2$, and which are defined for each modality and measurement by

$$\begin{aligned} \delta\psi_{mnq}^{(1)}(\theta) &= \int_{\Omega} \delta_{\theta^T(\mathbf{r})} \psi_{mnq}^{(1)}(\theta) \delta\theta(\mathbf{r}) d\mathbf{v} \\ &= \int_{\Omega} \delta_{\epsilon_r(\mathbf{r})} \psi_{mnq}^{(1)}(\theta) \delta\epsilon_r(\mathbf{r}) d\mathbf{v} \\ &\quad + \int_{\Omega} \delta_{\sigma(\mathbf{r})} \psi_{mnq}^{(1)}(\theta) \delta\sigma(\mathbf{r}) d\mathbf{v}, \\ \delta\psi_{mn}^{(2)}(\theta) &= \int_{\Omega} \delta_{\theta^T(\mathbf{r})} \psi_{mn}^{(2)}(\theta) \delta\theta(\mathbf{r}) d\mathbf{v} \\ &= \int_{\Omega} \delta_{\epsilon_r(\mathbf{r})} \psi_{mn}^{(2)}(\theta) \delta\epsilon_r(\mathbf{r}) d\mathbf{v} \\ &\quad + \int_{\Omega} \delta_{\sigma(\mathbf{r})} \psi_{mn}^{(2)}(\theta) \delta\sigma(\mathbf{r}) d\mathbf{v}, \end{aligned} \quad (3)$$

where $\delta\theta(\mathbf{r}) = [\delta\epsilon_r(\mathbf{r}) \ \delta\sigma(\mathbf{r})]^T$ denotes a perturbation of $\theta(\mathbf{r})$ and $\delta_{\theta^T(\mathbf{r})} \psi_{mnq}^{(1)}(\theta)$ and $\delta_{\theta^T(\mathbf{r})} \psi_{mn}^{(2)}(\theta)$ the corresponding gradients [12]. The following notation is employed for the Jacobian \mathcal{J} of the combined multiphysics problem

$$\delta\psi = \begin{pmatrix} \delta\psi^{(1)} \\ \delta\psi^{(2)} \end{pmatrix} = \begin{pmatrix} \mathcal{J}^{(1)} \\ \mathcal{J}^{(2)} \end{pmatrix} \delta\theta = \begin{pmatrix} \mathcal{J}_{\epsilon_r}^{(1)} & \mathcal{J}_{\sigma}^{(1)} \\ 0 & \mathcal{J}_{\sigma}^{(2)} \end{pmatrix} \begin{pmatrix} \delta\epsilon_r \\ \delta\sigma \end{pmatrix} = \mathcal{J} \delta\theta, \quad (4)$$

where $\psi(\theta) = [\psi^{(1)}(\theta) \ \psi^{(2)}(\theta)]^T$, and where it has been emphasized that the electric resistive (ER) tomography measurements depend only on the conductivity parameter $\sigma(\mathbf{r})$.

The measurement noise in the statistical model (1) is denoted $w_{mnq}^{(1)}$ and $w_{mn}^{(2)}$, and is assumed to be the samples of a zero mean and uncorrelated multivariate Gaussian random variable [14] with variance

$$\begin{aligned} R_{mnq}^{(1)} &= \mathcal{E} \left\{ \left| w_{mnq}^{(1)} \right|^2 \right\}, \\ R_{mn}^{(2)} &= \mathcal{E} \left\{ \left| w_{mn}^{(2)} \right|^2 \right\}, \end{aligned} \quad (5)$$

corresponding to the EM and ER imaging modalities, respectively. Here, $\mathcal{E} \{ \cdot \}$ denotes the statistical expectation operator.

For the EM-modality, the random variable is complex Gaussian with $\mathcal{E}\{(w_{mnq}^{(1)})^2\} = 0$, and for the ER-modality, the random variable is real Gaussian, see, for example, [14, 15].

2.2. *Maximum Likelihood and the Truncated SVD.* Let $\ln p(\xi | \theta)$ denote the loglikelihood function of the measurement statistics [14]. The Fisher information integral operator is then defined by the outer product

$$\mathcal{I}(\mathbf{r}', \mathbf{r}'') = \mathcal{E}\{\delta_{\theta(\mathbf{r}')} \ln p(\xi | \theta) \delta_{\theta(\mathbf{r}'')} \ln p(\xi | \theta)\}, \quad (6)$$

$$\mathbf{r}', \mathbf{r}'' \in \Omega,$$

where $\mathcal{E}\{\cdot\}$ denotes the expectation and $\delta_{\theta(\mathbf{r})}$ the gradient operator, cf. [10, 11, 14].

The multiphysics inverse problem (1) relates to a combination of a complex valued Gaussian and a real valued Gaussian measurement statistics. The negative loglikelihood function (or cost function) and the Fisher information (FI) for this situation is given by

$$F(\theta) = -\ln p(\xi | \theta)$$

$$= \sum_{m,n,q=1,1,1}^{M_1, N_1, Q} \frac{1}{R_{mnq}^{(1)}} \left| \psi_{mnq}^{(1)}(\theta) - \xi_{mnq}^{(1)} \right|^2$$

$$+ \sum_{m,n=1,1}^{M_2, N_2} \frac{1}{2R_{mn}^{(2)}} \left| \psi_{mn}^{(2)}(\theta) - \xi_{mn}^{(2)} \right|^2, \quad (7)$$

$$\mathcal{I}(\mathbf{r}', \mathbf{r}'') = 2 \operatorname{Re} \left\{ \sum_{m,n,q=1,1,1}^{M_1, N_1, Q} \frac{1}{R_{mnq}^{(1)}} \delta_{\theta(\mathbf{r}')} \psi_{mnq}^{(1)*}(\theta) \delta_{\theta(\mathbf{r}'')} \psi_{mnq}^{(1)}(\theta) \right\}$$

$$+ \sum_{m,n=1,1}^{M_2, N_2} \frac{1}{R_{mn}^{(2)}} \delta_{\theta(\mathbf{r}')} \psi_{mn}^{(2)}(\theta) \delta_{\theta(\mathbf{r}'')} \psi_{mn}^{(2)}(\theta), \quad (8)$$

where $(\cdot)^*$ denotes the complex conjugate, and $\mathbf{r}', \mathbf{r}'' \in \Omega$, cf. [10, 11, 14].

To obtain a useful relationship between the maximum likelihood method and the singular value decomposition (SVD) of the forward operator, the adequate scalar products must be defined, cf. [10, 11]. For the real valued parameter functions $\theta_1 = [\epsilon_{r1} \ \sigma_1]^T$ and $\theta_2 = [\epsilon_{r2} \ \sigma_2]^T$, the following scalar product is employed

$$\langle \theta_1, \theta_2 \rangle = \int_{\Omega} \theta_1^T(\mathbf{r}) \theta_2(\mathbf{r}) d\mathbf{v}$$

$$= \int_{\Omega} \epsilon_{r1}(\mathbf{r}) \epsilon_{r2}(\mathbf{r}) d\mathbf{v} + \int_{\Omega} \sigma_1(\mathbf{r}) \sigma_2(\mathbf{r}) d\mathbf{v}. \quad (9)$$

For the mixed complex and real valued measurement data $\xi = [\xi^{(1)} \ \xi^{(2)}]^T$ and $\eta = [\eta^{(1)} \ \eta^{(2)}]^T$, the following real scalar product is defined

$$\langle \xi, \eta \rangle_{\text{d}} = \operatorname{Re} \left\{ \sum_{m,n,q=1}^{M_1, N_1, Q} \frac{1}{R_{mnq}^{(1)}} \xi_{mnq}^{(1)*} \eta_{mnq}^{(1)} \right\} + \sum_{m,n=1}^{M_2, N_2} \frac{1}{2R_{mn}^{(2)}} \xi_{mn}^{(2)} \eta_{mn}^{(2)}, \quad (10)$$

where $R_{mnq}^{(1)}$ and $R_{mn}^{(2)}$ are the variance of the noise as defined in (5), and which are also employed in (7) and (8). It can be readily verified that (10) is a scalar product. Note, for example, that the n -dimensional vector space \mathbb{C}^n over the complex scalar field and with scalar product $\mathbf{x}^H \mathbf{y}$ is isomorphic with the $2n$ -dimensional vector space consisting of complex vectors over the real scalar field and with real scalar product $\operatorname{Re} \mathbf{x}^H \mathbf{y}$. Note that \mathbf{x} and $i\mathbf{x}$ are orthogonal in the latter space.

For later use, the adjoint forward operator \mathcal{J}^* is now given by

$$\mathcal{J}^* \xi = \langle \delta_{\theta(\mathbf{r})} \psi(\theta), \xi \rangle_{\text{d}}$$

$$= \operatorname{Re} \left\{ \sum_{m,n,q=1,1,1}^{M_1, N_1, Q} \frac{1}{R_{mnq}^{(1)}} \delta_{\theta(\mathbf{r})} \psi_{mnq}^{(1)*}(\theta) \xi_{mnq}^{(1)} \right\}$$

$$+ \sum_{m,n=1,1}^{M_2, N_2} \frac{1}{2R_{mn}^{(2)}} \delta_{\theta(\mathbf{r})} \psi_{mn}^{(2)}(\theta) \xi_{mn}^{(2)}$$

$$= \mathcal{J}^{(1)*} \xi^{(1)} + \mathcal{J}^{(2)*} \xi^{(2)}, \quad (11)$$

where $\langle \mathcal{J} \delta \theta, \xi \rangle_{\text{d}} = \langle \delta \theta, \mathcal{J}^* \xi \rangle$, see also [10–12, 16].

Based on the scalar product (10), the negative loglikelihood function (7) can now be written

$$F(\theta) = \langle \psi(\theta) - \xi, \psi(\theta) - \xi \rangle_{\text{d}}. \quad (12)$$

By using the adjoint operator defined in (11), the first and second order variations of $F(\theta)$ are obtained as

$$\delta F = \langle \delta \theta, 2\mathcal{J}^* (\psi - \xi) \rangle,$$

$$\delta^2 F = \langle \delta \theta, 2\mathcal{J}^* \mathcal{J} \delta \theta \rangle + 2 \langle \delta^2 \psi, \psi - \xi \rangle_{\text{d}}, \quad (13)$$

where $\delta \theta$ is the perturbation, $\psi = \psi(\theta)$ the forward operator evaluated at some known background parameter value θ and $\delta^2 \psi$ the second order variation of the forward operator. It is observed that the Fisher information operator defined in (8) is given by

$$\mathcal{I} = 2\mathcal{J}^* \mathcal{J} = 2\mathcal{J}^{(1)*} \mathcal{J}^{(1)} + 2\mathcal{J}^{(2)*} \mathcal{J}^{(2)} = \mathcal{I}^{(1)} + \mathcal{I}^{(2)}, \quad (14)$$

where $\mathcal{I}^{(1)} = 2\mathcal{J}^{(1)*} \mathcal{J}^{(1)}$ and $\mathcal{I}^{(2)} = 2\mathcal{J}^{(2)*} \mathcal{J}^{(2)}$ are the Fisher information operators for each modality. The gradient $\delta_{\theta(\mathbf{r})} F(\theta)$ of the cost function $F(\theta)$ is furthermore given by

$$\delta_{\theta(\mathbf{r})} F(\theta) = 2\mathcal{J}^* (\psi - \xi)$$

$$= 2\mathcal{J}^{(1)*} (\psi^{(1)} - \xi^{(1)}) + 2\mathcal{J}^{(2)*} (\psi^{(2)} - \xi^{(2)}), \quad (15)$$

where

$$\begin{aligned}
& 2\mathcal{J}^{(1)*}(\psi^{(1)} - \xi^{(1)}) \\
&= 2 \operatorname{Re} \sum_{m,n,q=1,1,1}^{M_1, N_1, Q} \frac{1}{R_{mnq}^{(1)}} \delta_{\theta(r)} \psi_{mnq}^{(1)*}(\theta) \left(\psi_{mnq}^{(1)}(\theta) - \xi_{mnq}^{(1)} \right), \\
& 2\mathcal{J}^{(2)*}(\psi^{(2)} - \xi^{(2)}) \\
&= \sum_{m,n=1,1}^{M_2, N_2} \frac{1}{R_{mn}^{(2)}} \delta_{\theta(r)} \psi_{mn}^{(2)}(\theta) \left(\psi_{mn}^{(2)}(\theta) - \xi_{mn}^{(2)} \right).
\end{aligned} \tag{16}$$

A linearization is now considered where it is assumed that the second order variation of the forward operator $\delta^2\psi$ can be neglected. Consider hence the quadratic functional

$$\begin{aligned}
\Delta F(\delta\theta) &= \delta F(\delta\theta) + \frac{1}{2} \delta^2 F(\delta\theta) \\
&= \langle \delta\theta, \delta_{\theta(r)} F(\theta) \rangle + \frac{1}{2} \langle \delta\theta, \mathcal{L} \delta\theta \rangle,
\end{aligned} \tag{17}$$

where the linear and quadratic terms in (13) have been used with $\delta^2\psi = 0$. Note that the Hessian of F is given here by the Fisher information $\mathcal{L} = 2\mathcal{J}^* \mathcal{J}$. A regularized one-step Newton algorithm for this functional is hence given by

$$\delta\theta^+ = -\mathcal{L}^+ \delta_{\theta(r)} F(\theta), \tag{18}$$

where \mathcal{L}^+ denotes a truncated pseudoinverse of the Fisher information \mathcal{L} , which is based on the singular value decomposition (SVD), see also [10, 11, 17].

It can be readily shown that the regularized maximum likelihood solution (18) is equivalent to a regularized pseudoinverse based directly on the linearized operator problem

$$\mathcal{J} \delta\theta = \xi - \psi, \tag{19}$$

provided that the scalar products are properly chosen as in (9) and (10). To this end, it is assumed that the operator \mathcal{J} is compact and hence that the following singular system exists

$$\begin{aligned}
\sqrt{2} \mathcal{J} v_l &= \sigma_l u_l, \\
\sqrt{2} \mathcal{J}^* u_l &= \sigma_l v_l,
\end{aligned} \tag{20}$$

where $\{u_l\}$ and $\{v_l\}$ are orthonormal systems and σ_l the singular values. (Note that σ is used here to denote singular values as well as conductivity. The correct interpretation should be evident from the context without confusion [12].) The Fisher information is the self-adjoint operator $\mathcal{L} = 2\mathcal{J}^* \mathcal{J}$ with eigenvalues $\mu_l = \sigma_l^2$ and eigenfunctions v_l , that is,

$$\mathcal{L} v_l = \mu_l v_l. \tag{21}$$

The operator \mathcal{J} can now be represented by the singular value decomposition (SVD)

$$\mathcal{J} \delta\theta = \frac{1}{\sqrt{2}} \sum_l \sigma_l u_l \langle v_l, \delta\theta \rangle, \tag{22}$$

and the pseudoinverse (if it exists) is given by

$$\begin{aligned}
\mathcal{J}^+ (\xi - \psi) &= \sqrt{2} \sum_l \frac{1}{\sigma_l} v_l \langle u_l, \xi - \psi \rangle_d \\
&= \sqrt{2} \sum_l \frac{1}{\sigma_l} v_l \left\langle \frac{\sqrt{2}}{\sigma_l} \mathcal{J} v_l, \xi - \psi \right\rangle_d \\
&= \sum_l \frac{1}{\sigma_l^2} v_l \langle v_l, 2\mathcal{J}^* (\xi - \psi) \rangle \\
&= - \sum_l \frac{1}{\sigma_l^2} v_l \langle v_l, \delta_{\theta(r)} F(\theta) \rangle \\
&= -\mathcal{L}^+ \delta_{\theta(r)} F(\theta),
\end{aligned} \tag{23}$$

which is the same as (18).

The relationship between ML, SVD, and FI has been described. This will be used in Section 4 to calculate the pseudoinverse and find the parameters.

3. Green's Functions and Gradients

Below is given a description of green's functions and the gradients used with the EM and ER tomographic problems in this paper.

3.1. The Electromagnetic (EM) Tomography Problem. A two-dimensional electromagnetic tomography problem is considered where the harmonic electric field is polarized as $\mathbf{E} = \psi(\rho, \phi) \hat{\mathbf{z}}$ where the scalar field $\psi(\rho, \phi)$ is independent of the z -coordinate. Here, ρ and ϕ denote the radial and angular circular coordinates, respectively, and $\boldsymbol{\rho} = \rho \hat{\boldsymbol{\rho}}$ the two-dimensional radius vector. Let $k = \omega \sqrt{\mu_0 \epsilon_0}$, $\eta_0 = \sqrt{\mu_0 / \epsilon_0}$, μ_0 and ϵ_0 denote the wave number, the wave impedance, the permeability, and the permittivity of free space, respectively, and where ω is the angular frequency. The time convention employed here is given by $e^{i\omega t}$.

The EM-field $\psi_n^{(1)}(\rho, \phi)$ resulting from excitation index n is obtained as the solution to the wave equation

$$(\nabla^2 + k^2 \epsilon) \psi_n^{(1)} = ik \eta_0 \delta(\boldsymbol{\rho} - \boldsymbol{\rho}_n), \quad n = 1, \dots, N_1, \tag{24}$$

where $\epsilon = \epsilon_r - i\sigma \eta_0 / k$ is the complex valued relative permittivity, ϵ_r the relative permittivity, and σ the conductivity. Here, $\delta(\cdot)$ denotes the Dirac-delta function indicating that the excitation is modeled here as a point source at position $\boldsymbol{\rho}_n$.

Let $\epsilon = \epsilon_D + \delta\epsilon$ where $\epsilon_D = \epsilon_{rD} - i\sigma_D \eta_0 / k$ and $\delta\epsilon = \delta\epsilon_r - i\delta\sigma \eta_0 / k$ denote the corresponding background parameter values and a perturbation $\delta\theta = [\delta\epsilon_r, \delta\sigma]^T$, respectively. For the homogeneous background ϵ_D , the solution to (24) is given by

$$\psi_n^{(1)}(\boldsymbol{\rho}) = -ik \eta_0 G_D^{(1)}(\boldsymbol{\rho}, \boldsymbol{\rho}_n), \tag{25}$$

where $G_D^{(1)}(\boldsymbol{\rho}, \boldsymbol{\rho}')$ is green's function for the homogeneous background satisfying $(\nabla^2 + k^2 \epsilon_D)G_D^{(1)}(\boldsymbol{\rho}, \boldsymbol{\rho}') = -\delta(\boldsymbol{\rho} - \boldsymbol{\rho}')$, and which is given by

$$G_D^{(1)}(\boldsymbol{\rho}, \boldsymbol{\rho}') = \frac{1}{4i} \sum_m J_m(k\sqrt{\epsilon_D}\rho_{<}) H_m^{(2)}(k\sqrt{\epsilon_D}\rho_{>}) e^{im(\phi - \phi')}, \quad (26)$$

where $J_m(\cdot)$ and $H_m^{(2)}(\cdot)$ denote the Bessel function and the Hankel function of the second kind, respectively, both of order m [18]. Here, $\rho_{<} = \min\{\rho, \rho'\}$ and $\rho_{>} = \max\{\rho, \rho'\}$.

A first order perturbation analysis of (24) yields the following wave equation for the perturbed field $\delta\psi_n^{(1)}$

$$(\nabla^2 + k^2 \epsilon) \delta\psi_n^{(1)} = -k^2 \delta\epsilon \psi_n^{(1)}, \quad (27)$$

where $\psi_n^{(1)}$ is the solution to (24) and $\delta\epsilon$ the perturbation in parameter values. For the homogeneous background with $\epsilon = \epsilon_D$, the solution to (27) is hence given by

$$\begin{aligned} \delta\psi_n^{(1)}(\boldsymbol{\rho}) &= k^2 \int_{\Omega} G_D^{(1)}(\boldsymbol{\rho}, \boldsymbol{\rho}') \psi_n^{(1)}(\boldsymbol{\rho}') \delta\epsilon(\boldsymbol{\rho}') d\mathbf{v}' \\ &= -ik^3 \eta_0 \int_{\Omega} G_D^{(1)}(\boldsymbol{\rho}, \boldsymbol{\rho}') G_D^{(1)}(\boldsymbol{\rho}', \boldsymbol{\rho}_n) \delta\epsilon(\boldsymbol{\rho}') d\mathbf{v}'. \end{aligned} \quad (28)$$

It should be noted that this is the same result, that is, obtained by employing a Born approximation [4], in which case $\psi_n^{(1)}(\boldsymbol{\rho})$ represents the *incident field* and $\delta\psi_n^{(1)}(\boldsymbol{\rho})$ the *scattered field*.

Let $\psi_{mn}^{(1)}$ denote the measured quantity $\psi_{mn}^{(1)} = \psi_n^{(1)}(\boldsymbol{\rho}_{mn})$ where $\boldsymbol{\rho}_{mn}$ is the measurement position at measurement m with excitation n . The corresponding gradients are then given by

$$\begin{aligned} \delta_{\epsilon(\boldsymbol{\rho})} \psi_{mn}^{(1)} &= -ik^3 \eta_0 G_D^{(1)}(\boldsymbol{\rho}_{mn}, \boldsymbol{\rho}) G_D^{(1)}(\boldsymbol{\rho}_n, \boldsymbol{\rho}), \\ \delta_{\sigma(\boldsymbol{\rho})} \psi_{mn}^{(1)} &= -k^2 \eta_0^2 G_D^{(1)}(\boldsymbol{\rho}_{mn}, \boldsymbol{\rho}) G_D^{(1)}(\boldsymbol{\rho}_n, \boldsymbol{\rho}), \end{aligned} \quad (29)$$

where the symmetry of green's function has been employed.

In the simulation examples given below, a homogenous cylinder is used to model a tunnel buried in the ground. Green's function for the cylinder is denoted $G_c^{(1)}(\boldsymbol{\rho}, \boldsymbol{\rho}')$, and the measured quantity is hence modeled by

$$\psi_{mn}^{(1)} = \psi_n^{(1)}(\boldsymbol{\rho}_{mn}) = -ik\eta_0 G_c^{(1)}(\boldsymbol{\rho}_{mn}, \boldsymbol{\rho}_n). \quad (30)$$

Green's function $G_c^{(1)}(\boldsymbol{\rho}, \boldsymbol{\rho}')$ for a homogeneous cylinder of radius a placed in a homogeneous background space is given in Appendix A, and is used to generate the synthetic data in the numerical example.

3.2. The Electrical Resistive (ER) Tomography Problem. A two-dimensional electrical resistive tomography problem is considered where the electric potential field $\Phi^{(2)}(\rho, \phi)$ is independent of the z -coordinate, and where ρ and ϕ are used to denote the radial and angular circular coordinates,

as above. The potential field resulting from excitation index n is obtained here as the solution to the following differential equation

$$\begin{aligned} \nabla \cdot (\sigma \nabla \Phi_n^{(2)}) &= \delta(\boldsymbol{\rho} - \boldsymbol{\rho}_n) - \delta(\boldsymbol{\rho} - \boldsymbol{\rho}_{N_2+1}), \\ n &= 1, \dots, N_2, \end{aligned} \quad (31)$$

where σ is the conductivity and the excitation is defined by current point sources at positions $\boldsymbol{\rho}_n$ with a common ground connection at $\boldsymbol{\rho}_{N_2+1}$, see also [17].

Let $\sigma = \sigma_D + \delta\sigma$ where σ_D and $\delta\sigma$ denote the corresponding background parameter value and a perturbation, respectively. For the homogeneous background σ_D , the solution to (31) is given by

$$\Phi_n^{(2)}(\boldsymbol{\rho}) = G_D^{(2)}(\boldsymbol{\rho}, \boldsymbol{\rho}_n) - G_D^{(2)}(\boldsymbol{\rho}, \boldsymbol{\rho}_{N_2+1}), \quad (32)$$

where $G_D^{(2)}(\boldsymbol{\rho}, \boldsymbol{\rho}')$ is green's function for the homogeneous background satisfying $\nabla \cdot (\sigma_D \nabla G_D^{(2)}(\boldsymbol{\rho}, \boldsymbol{\rho}')) = \delta(\boldsymbol{\rho} - \boldsymbol{\rho}')$, and which is given by

$$G_D^{(2)}(\boldsymbol{\rho}, \boldsymbol{\rho}') = \frac{1}{2\pi\sigma_D} \ln \rho_{>} - \frac{1}{4\pi\sigma_D} \sum_{m \neq 0} \frac{1}{|m|} \left(\frac{\rho_{<}}{\rho_{>}} \right)^{|m|} e^{im(\phi - \phi')}, \quad (33)$$

where $\rho_{<} = \min\{\rho, \rho'\}$ and $\rho_{>} = \max\{\rho, \rho'\}$, see also [18].

The observed voltage quantity $\psi_{mn}^{(2)}$ corresponding to the homogeneous background is given by

$$\begin{aligned} \psi_{mn}^{(2)} &= \Phi_n^{(2)}(\boldsymbol{\rho}_{mn}) - \Phi_n^{(2)}(\boldsymbol{\rho}_0) \\ &= G_D^{(2)}(\boldsymbol{\rho}_{mn}, \boldsymbol{\rho}_n) - G_D^{(2)}(\boldsymbol{\rho}_{mn}, \boldsymbol{\rho}_{N_2+1}) \\ &\quad - G_D^{(2)}(\boldsymbol{\rho}_0, \boldsymbol{\rho}_n) + G_D^{(2)}(\boldsymbol{\rho}_0, \boldsymbol{\rho}_{N_2+1}), \end{aligned} \quad (34)$$

where $\boldsymbol{\rho}_{mn}$ is the measurement position at measurement m and excitation n , and $\boldsymbol{\rho}_0$ is a position used as a voltage reference.

Note that green's function $G_D^{(2)}(\boldsymbol{\rho}, \boldsymbol{\rho}_n)$ satisfies the differential equation

$$\nabla \cdot (\sigma_D \nabla G_D^{(2)}(\boldsymbol{\rho}, \boldsymbol{\rho}_n)) = \delta(\boldsymbol{\rho} - \boldsymbol{\rho}_n). \quad (35)$$

A first order perturbation analysis of (35) yields the following differential equation for the perturbed field $\delta G_D^{(2)}(\boldsymbol{\rho}, \boldsymbol{\rho}_n)$

$$\nabla \cdot (\sigma_D \nabla \delta G_D^{(2)}(\boldsymbol{\rho}, \boldsymbol{\rho}_n)) = -\nabla \cdot (\delta\sigma \nabla G_D^{(2)}(\boldsymbol{\rho}, \boldsymbol{\rho}_n)). \quad (36)$$

The solution to (36) is given by

$$\begin{aligned} \delta G_D^{(2)}(\boldsymbol{\rho}, \boldsymbol{\rho}_n) &= - \int_{\Omega} G_D^{(2)}(\boldsymbol{\rho}, \boldsymbol{\rho}') \nabla' \cdot (\delta\sigma \nabla' G_D^{(2)}(\boldsymbol{\rho}', \boldsymbol{\rho}_n)) d\mathbf{v}' \\ &= \int_{\Omega} \nabla' G_D^{(2)}(\boldsymbol{\rho}, \boldsymbol{\rho}') \cdot \nabla' G_D^{(2)}(\boldsymbol{\rho}_n, \boldsymbol{\rho}') \delta\sigma(\boldsymbol{\rho}') d\mathbf{v}', \end{aligned} \quad (37)$$

where Green's theorem [18] has been used together with the assumption that $\delta\sigma = 0$ on the boundary of Ω . The gradient of green's function $G_D^{(2)}(\boldsymbol{\rho}_l, \boldsymbol{\rho}_n)$ is hence given by

$$\delta_{\sigma(\rho)} G_D^{(2)}(\boldsymbol{\rho}_l, \boldsymbol{\rho}_n) = \nabla G_D^{(2)}(\boldsymbol{\rho}_l, \boldsymbol{\rho}) \cdot \nabla G_D^{(2)}(\boldsymbol{\rho}_n, \boldsymbol{\rho}), \quad (38)$$

where $\nabla G_D^{(2)}(\boldsymbol{\rho}_n, \boldsymbol{\rho})$ can be obtained from (33) as

$$\begin{aligned} \nabla G_D^{(2)}(\boldsymbol{\rho}_n, \boldsymbol{\rho}) = & \hat{\boldsymbol{\rho}} \left\{ \frac{-1}{4\pi\sigma_D\rho_n} \sum_{m \neq 0} \left(\frac{\rho}{\rho_n} \right)^{|m|-1} e^{im(\phi_n - \phi)} \right\} \\ & + \hat{\boldsymbol{\phi}} \left\{ \frac{i}{4\pi\sigma_D\rho} \sum_{m \neq 0} \left(\frac{m}{|m|} \right) \left(\frac{\rho}{\rho_n} \right)^{|m|} e^{im(\phi_n - \phi)} \right\}, \end{aligned} \quad (39)$$

where (ρ_n, ϕ_n) are the circular coordinates of $\boldsymbol{\rho}_n$, and $\rho < \rho_n$. The gradient of the observed voltage quantity $\psi_{mn}^{(2)}$ defined in (34) can finally be obtained as

$$\begin{aligned} \delta_{\sigma(\rho)} \psi_{mn}^{(2)} = & \delta_{\sigma(\rho)} G_D^{(2)}(\boldsymbol{\rho}_{mn}, \boldsymbol{\rho}_n) - \delta_{\sigma(\rho)} G_D^{(2)}(\boldsymbol{\rho}_{mn}, \boldsymbol{\rho}_{N_2+1}) \\ & - \delta_{\sigma(\rho)} G_D^{(2)}(\boldsymbol{\rho}_0, \boldsymbol{\rho}_n) + \delta_{\sigma(\rho)} G_D^{(2)}(\boldsymbol{\rho}_0, \boldsymbol{\rho}_{N_2+1}), \end{aligned} \quad (40)$$

which can be computed with the aid of (38) and (39).

In the simulation examples given below, a homogenous cylinder is used to model a tunnel buried in the ground. Green's function for the cylinder is denoted $G_c^{(2)}(\boldsymbol{\rho}, \boldsymbol{\rho}')$, and the measured quantity is hence modeled by

$$\begin{aligned} \psi_{mn}^{(2)} = & G_c^{(2)}(\boldsymbol{\rho}_{mn}, \boldsymbol{\rho}_n) - G_c^{(2)}(\boldsymbol{\rho}_{mn}, \boldsymbol{\rho}_{N_2+1}) \\ & - G_c^{(2)}(\boldsymbol{\rho}_0, \boldsymbol{\rho}_n) + G_c^{(2)}(\boldsymbol{\rho}_0, \boldsymbol{\rho}_{N_2+1}), \end{aligned} \quad (41)$$

similar to (34). Green's function $G_c^{(2)}(\boldsymbol{\rho}, \boldsymbol{\rho}')$ for a homogeneous cylinder of radius a placed in a homogeneous background space is given in Appendix B, and is used to generate the synthetic data in the numerical example.

4. Numerical Example

As a numerical example, we consider the problem of tunnel detection based on electromagnetic (EM) and electrical resistive (ER) tomography in geophysical sensing. A two-dimensional problem is studied where the tunnel is represented by a circular structure embedded in a homogeneous background. The measurement setup is illustrated in Figure 1, which also shows green's functions $G_c^{(1)}(\boldsymbol{\rho}, \boldsymbol{\rho}')$ and $G_c^{(2)}(\boldsymbol{\rho}, \boldsymbol{\rho}')$ of the circular object which have been used to generate the synthetic data. The superscripts (1) and (2) refer to the EM and ER imaging modalities, respectively. One single frequency with $\omega = 2\pi \cdot 200 \cdot 10^6$ (200 MHz) is employed with the EM modality. The large circle in the center indicates the simulated tunnel of radius $a = 0.5$ m, and the 21 small circles the horizontal sensors which are modeled here as point sources. The measurement line is

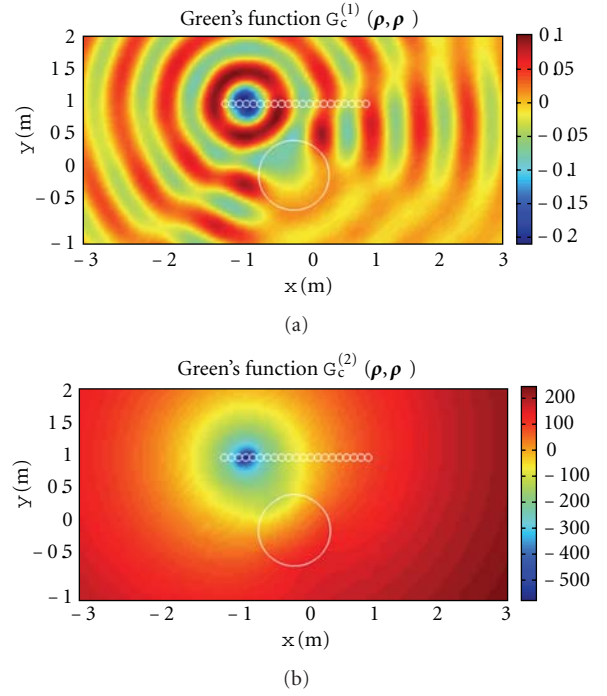


FIGURE 1: Illustration of measurement setup and Green's functions $G_c^{(1)}(\boldsymbol{\rho}, \boldsymbol{\rho}')$ and $G_c^{(2)}(\boldsymbol{\rho}, \boldsymbol{\rho}')$ in electromagnetic and electrical resistive tomography, respectively. The large circle in the center indicates the tunnel of radius $a = 0.5$ m, and the 21 small circles the horizontal sensors (point sources). In both plots shown above, the source is at $\boldsymbol{\rho}'$ corresponding to the fourth sensor from the left.

2 m long. The surrounding medium has relative permittivity $\epsilon_{rD} = 5$ and conductivity $\sigma_D = 1$ mS/m ($\sigma_D = 0.001$ S/m). The tunnel is modeled with relative permittivity $\epsilon_{ra} = 1$ and conductivity $\sigma_a = 0$. This formulation has been chosen to illustrate the data fusion, as it represents a simple and generic multiphysics inverse problem which is severely ill-posed due to the narrow measurement aperture (narrow spatial window) and the narrow measurement bandwidth.

The signal-to-noise-ratio (SNR) in the measurement model (1) is defined as

$$\begin{aligned} \text{SNR}^{(1)} = & \frac{\max_{mnq} |\psi_{mnq}^{(1)}|^2}{R^{(1)}}, \\ \text{SNR}^{(2)} = & \frac{\max_{mn} |\psi_{mn}^{(2)}|^2}{R^{(2)}}, \end{aligned} \quad (42)$$

where $\psi_{mnq}^{(1)}$ and $\psi_{mn}^{(2)}$ represent the (noiseless) measured quantities, and $R^{(1)}$ and $R^{(2)}$ the corresponding measurement noise variances defined in (5) corresponding to the EM and ER imaging modalities, respectively. Here, the measurement noise variance is assumed to be independent of the measurement index (m, n, q) , and hence $R_{mnq}^{(1)} = R^{(1)}$ and $R_{mn}^{(2)} = R^{(2)}$. In the simulation examples described below, the measurement noise was chosen such that $\text{SNR}^{(1)} = 80$ dB, $\text{SNR}^{(2)} = 70$ dB and $R^{(2)}/R^{(1)} = 92$. It should be noted that

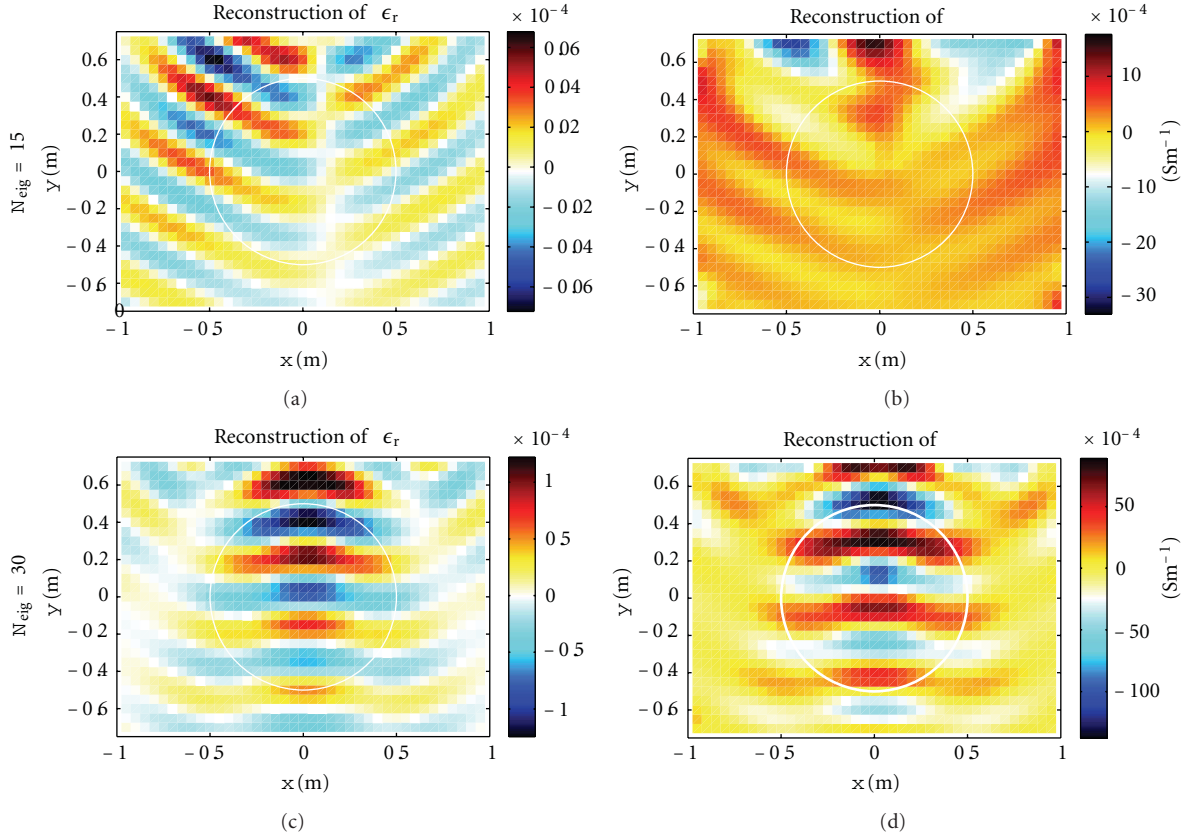


FIGURE 2: Reconstruction of $\delta\epsilon_r$ and $\delta\sigma$ in a straightforward data fusion without statistically based weighting (the weighting is assumed to be uniform with $R^{(2)}/R^{(1)} = 1$). The upper and lower rows are obtained by using $N_{\text{eig}} = 15$ and $N_{\text{eig}} = 30$ eigenvalues, respectively.

the values of the signal-to-noise-ratios are rather high for a practical implementation, but are required here due to the absence of directivity of the point sources used in this model. However, the main point here is to illustrate the significance of the ratio $R^{(2)}/R^{(1)}$ which is independent of the absolute value of the SNR.

In Figures 2 and 3 are shown reconstruction results for $\delta\epsilon_r$ and $\delta\sigma$ using the truncated SVD inversion technique for data fusion that has been outlined in Section 2.2. Here, the upper and lower rows show reconstruction results obtained by using $N_{\text{eig}} = 15$ and $N_{\text{eig}} = 30$ eigenvalues, respectively.

In Figure 2 is shown the reconstructions in a straightforward data fusion without statistically-based weighting. In these reconstructions, the weighting is assumed to be uniform with $R^{(2)}/R^{(1)} = 1$ even though the simulation data has been generated with $R^{(2)}/R^{(1)} = 92$. Hence, the correct multiphysics model has been employed, but the sensor noise statistics has not been taken into consideration.

In Figure 3 is shown the reconstructions in a maximum likelihood-based data fusion where the statistically-based weighting with $R^{(2)}/R^{(1)} = 92$ has been exploited. Hence, the correct multiphysics model has been employed, and the sensor noise statistics has been taken into proper

consideration based on the principle of maximum likelihood.

A comparison of Figures 2 and 3 in this example illustrates the expected behavior of the data fusion for an ill-posed multiphysics inverse problem, that is, the sensitivity of the inversion with respect to the discrepancies in the statistical assumptions. In this example, $\max_{mn} |\psi_{mn}^{(2)}|^2 = 9.2$, $\max_{mn} |\psi_{mn}^{(1)}|^2$ and $\text{SNR}^{(2)} = \text{SNR}^{(1)}/10$, yielding an imbalance in the weighting of data corresponding to the ratio $R^{(2)}/R^{(1)} = 92$. As can be seen in the Figures 2 and 3, the consequence of neglecting this imbalance can be significant, especially for $N_{\text{eig}} = 15$.

In Figure 4 is shown the singular values $\mu_n(\mathcal{J})$ for the three different measurement scenarios with electromagnetic (EM), electrical resistive (ER), and combined electromagnetic and electrical resistive (EM+ER) tomography. The figure illustrates that ER tomography contributes mainly at the lower eigenvalue indices whereas EM tomography contributes at higher indices in this particular problem. It can be anticipated that this behavior is typical since the eigenvalue distribution of ER tomography usually drops off rapidly already from the first indices whereas with EM tomography there is typically a threshold in the distribution of eigenvalues after which the eigenvalues drop off in rapid descent, see, for example, [10, 11, 13, 19, 20].

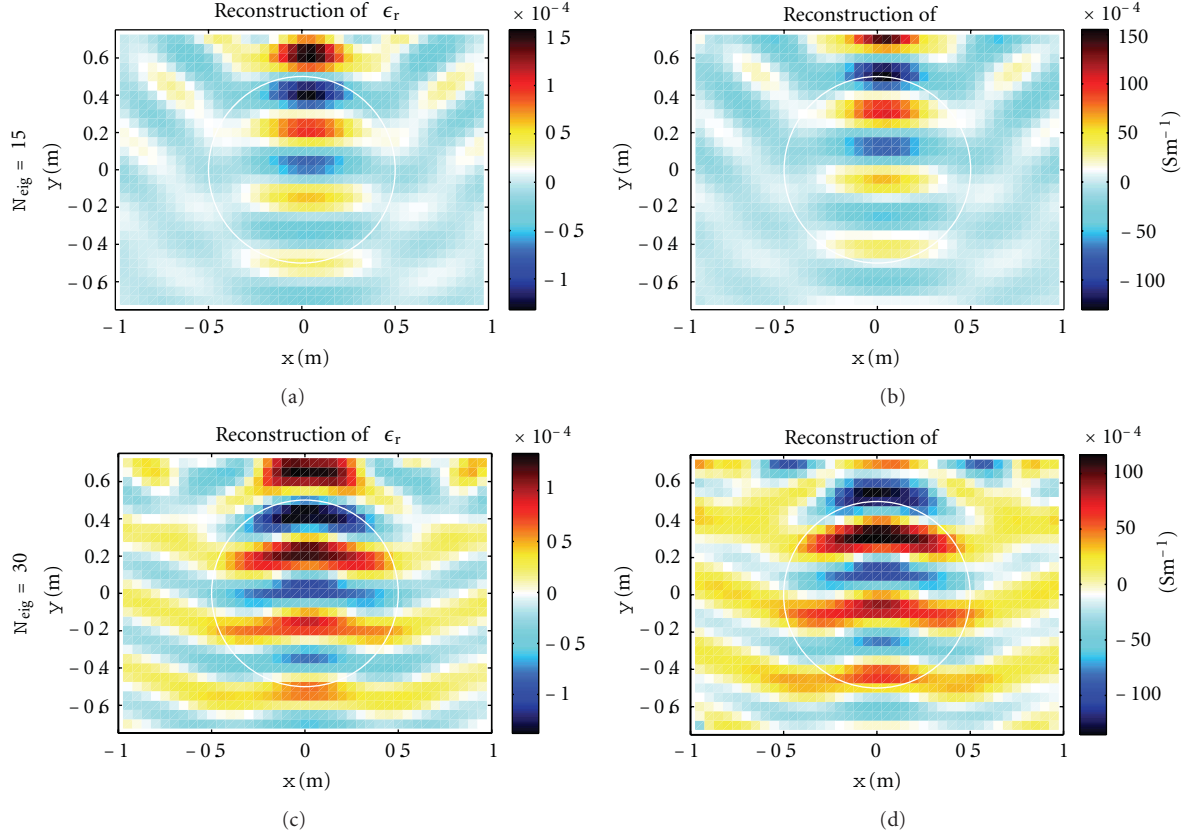


FIGURE 3: Reconstruction of $\delta\epsilon_r$ and $\delta\sigma$ in a maximum likelihood-based data fusion where the statistically-based weighting is $R^{(2)}/R^{(1)} = 92$. The upper and lower rows are obtained by using $N_{\text{eig}} = 15$ and $N_{\text{eig}} = 30$ eigenvalues, respectively.

5. Summary

A maximum likelihood-based approach to data fusion for electromagnetic (EM) and electrical resistive (ER) tomography has been presented. The Fisher information is an additive measure of information which is closely linked to the principle of maximum likelihood, and which can be useful in the study of inverse problems. The Fisher information is particularly useful for inverse problems which can be linearized similar to the Born approximation. In this paper, a proper scalar product has been defined for the measurements and a truncated singular value decomposition- (SVD-) based algorithm has been devised which combines the measurement data of the two imaging modalities in a way that is optimal in the sense of maximum likelihood.

As a multiphysics problem formulation with applications in geophysics, the problem of tunnel detection based on EM and ER tomography has been studied in this paper. The connection between green's functions, the gradients, and the Fisher information has been illustrated by a detailed description of two simple and generic forward models regarding two-dimensional EM and ER tomography, respectively. Numerical examples have been included to illustrate the potential impact of an imbalance between the singular values and the variance of the measurement noise when different imaging modalities are incorporated in the inversion, and the

significance of taking a statistically-based weighting of the measurement data into proper account.

Appendices

A. EM Green's Function for a Homogeneous Cylinder

Green's function $G_c^{(1)}(\rho, \rho')$ for a homogenous cylinder of radius a is derived below. The complex valued permittivity of the background and the cylinder are given by $\epsilon_D = \epsilon_{rD} - i\sigma_D\eta_0/k$ and $\epsilon_c = \epsilon_{rc} - i\sigma_c\eta_0/k$, respectively.

Green's function $G_c^{(1)}(\rho, \rho')$ satisfies the scalar wave equation

$$\left\{ \frac{1}{\rho} \frac{\partial}{\partial \rho} \rho \frac{\partial}{\partial \rho} + \frac{1}{\rho^2} \frac{\partial^2}{\partial \phi^2} + k^2 \epsilon \right\} G_c^{(1)}(\rho, \phi, \rho', \phi') = -\frac{\delta(\rho - \rho')}{\rho} \delta(\phi - \phi'), \quad (\text{A.1})$$

together with appropriate boundary conditions. By introducing the Fourier series expansion

$$G_c^{(1)}(\rho, \phi, \rho', \phi') = \sum_{m=-\infty}^{\infty} \tilde{G}_m(\rho, \rho', \phi') e^{im\phi}, \quad (\text{A.2})$$

the wave equation (A.1) transforms to

$$\left\{ \frac{\partial^2}{\partial \rho^2} + \frac{1}{\rho} \frac{\partial}{\partial \rho} + k^2 \epsilon - \frac{m^2}{\rho^2} \right\} \tilde{G}_m(\rho, \rho', \phi') = -\frac{\delta(\rho - \rho') e^{-im\phi'}}{\rho 2\pi}. \quad (\text{A.3})$$

Assume that the source is outside the cylinder, that is, $\rho' > a$. The solution to (A.3) is then given by

$$\tilde{G}_m(\rho, \rho', \phi') = \begin{cases} A_m J_m(k\sqrt{\epsilon_c}\rho) & 0 < \rho < a, \\ B_m H_m^{(1)}(k\sqrt{\epsilon_D}\rho) + C_m H_m^{(2)}(k\sqrt{\epsilon_D}\rho) & a < \rho < \rho', \\ D_m H_m^{(2)}(k\sqrt{\epsilon_D}\rho) & \rho > \rho'. \end{cases} \quad (\text{A.4})$$

The appropriate boundary conditions are given by

$$\begin{aligned} -\tilde{G}_m(a_-, \rho', \phi') + \tilde{G}_m(a_+, \rho', \phi') &= 0, \\ -\frac{\partial}{\partial \rho} \tilde{G}_m(a_-, \rho', \phi') + \frac{\partial}{\partial \rho} \tilde{G}_m(a_+, \rho', \phi') &= 0, \\ -\tilde{G}_m(\rho'_-, \rho', \phi') + \tilde{G}_m(\rho'_+, \rho', \phi') &= 0, \\ -\frac{\partial}{\partial \rho} \tilde{G}_m(\rho'_-, \rho', \phi') + \frac{\partial}{\partial \rho} \tilde{G}_m(\rho'_+, \rho', \phi') &= -\frac{1}{\rho'} \frac{e^{-im\phi'}}{2\pi}. \end{aligned} \quad (\text{A.5})$$

The boundary conditions (A.5) yield the linear system of equations

$$\begin{pmatrix} -J_m(k\sqrt{\epsilon_c}a) & H_m^{(1)}(k\sqrt{\epsilon_D}a) & H_m^{(2)}(k\sqrt{\epsilon_D}a) & 0 \\ -k\sqrt{\epsilon_c}J'_m(k\sqrt{\epsilon_c}a) & k\sqrt{\epsilon_D}H_m^{(1)'}(k\sqrt{\epsilon_D}a) & k\sqrt{\epsilon_D}H_m^{(2)'}(k\sqrt{\epsilon_D}a) & 0 \\ 0 & -H_m^{(1)}(k\sqrt{\epsilon_D}\rho') & -H_m^{(2)}(k\sqrt{\epsilon_D}\rho') & H_m^{(2)}(k\sqrt{\epsilon_D}\rho') \\ 0 & -k\sqrt{\epsilon_D}H_m^{(1)'}(k\sqrt{\epsilon_D}\rho') & -k\sqrt{\epsilon_D}H_m^{(2)'}(k\sqrt{\epsilon_D}\rho') & k\sqrt{\epsilon_D}H_m^{(2)'}(k\sqrt{\epsilon_D}\rho') \end{pmatrix} \times \begin{pmatrix} A_m \\ B_m \\ C_m \\ D_m \end{pmatrix} = \begin{pmatrix} 0 \\ 0 \\ -\frac{1}{\rho'} \frac{e^{-im\phi'}}{2\pi} \\ 0 \end{pmatrix}, \quad (\text{A.6})$$

which is solved for the constants A_m , B_m , C_m , and D_m defined in (A.4).

B. ER Green's Function for a Homogeneous Cylinder

Green's function $G_c^{(2)}(\rho, \rho')$ for a homogenous cylinder of radius a is derived below. The conductivity of the background and the cylinder are denoted by σ_D and σ_c , respectively.

Green's function $G_c^{(2)}(\rho, \rho')$ satisfies the partial differential equation

$$\begin{aligned} \nabla \cdot (\sigma \nabla G_c^{(2)}(\rho, \rho')) &= \sigma \nabla^2 G_c^{(2)}(\rho, \rho') \\ &+ \nabla \sigma \cdot \nabla G_c^{(2)}(\rho, \rho') \\ &= \delta(\rho - \rho'), \end{aligned} \quad (\text{B.1})$$

or

$$\begin{aligned} \left\{ \sigma \left[\frac{1}{\rho} \frac{\partial}{\partial \rho} \rho \frac{\partial}{\partial \rho} + \frac{1}{\rho^2} \frac{\partial^2}{\partial \phi^2} \right] + \frac{\partial \sigma}{\partial \rho} \frac{\partial}{\partial \rho} \right\} G_c^{(2)}(\rho, \phi, \rho', \phi') \\ = \frac{\delta(\rho - \rho')}{\rho} \delta(\phi - \phi'), \end{aligned} \quad (\text{B.2})$$

where $\partial \sigma / \partial \rho = (\sigma_D - \sigma_c) \delta(\rho - a)$. By introducing the Fourier series expansion

$$G_c^{(2)}(\rho, \phi, \rho', \phi') = \sum_{m=-\infty}^{\infty} \tilde{G}_m(\rho, \rho', \phi') e^{im\phi}, \quad (\text{B.3})$$

the differential equation (B.2) transforms to

$$\begin{aligned} \left\{ \sigma \left[\frac{\partial^2}{\partial \rho^2} + \frac{1}{\rho} \frac{\partial}{\partial \rho} - \frac{m^2}{\rho^2} \right] + (\sigma_D - \sigma_c) \delta(\rho - a) \frac{\partial}{\partial \rho} \right\} \\ \times \tilde{G}_m(\rho, \rho', \phi') \\ = \frac{\delta(\rho - \rho')}{\rho} \frac{e^{-im\phi'}}{2\pi}. \end{aligned} \quad (\text{B.4})$$

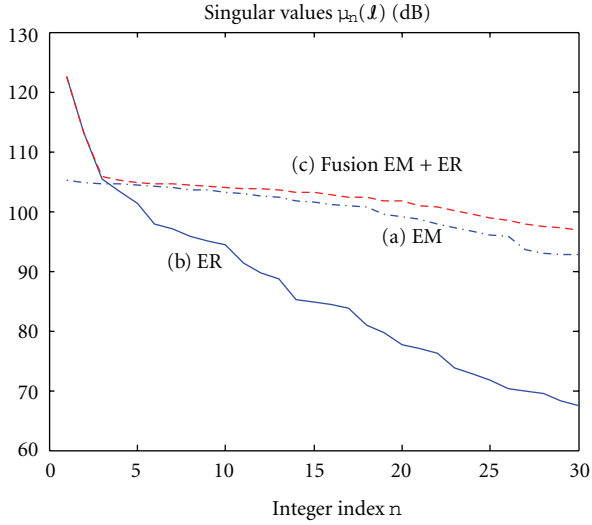


FIGURE 4: Singular values $\mu_n(L)$ for the three different measurement scenarios. (a) Electromagnetic tomography with $\text{SNR}^{(1)} = 80$ dB. (b) Electrical resistive tomography with $\text{SNR}^{(2)} = 70$ dB. (c) Maximum likelihood-based data fusion with electromagnetic and electrical resistive tomography combined.

Assume that the source is outside the cylinder, that is, $\rho' > a$. The solution to (B.4) for $m \neq 0$ is then given by

$$\tilde{G}_m(\rho, \rho', \phi') = \begin{cases} A_m \rho^{|m|}, & 0 < \rho < a, \\ B_m \rho^{|m|} + C_m \rho^{-|m|}, & a < \rho < \rho', \\ D_m \rho^{-|m|}, & \rho > \rho', \end{cases} \quad (\text{B.5})$$

$$\begin{pmatrix} -a^{|m|} & a^{|m|} & a^{-|m|} & 0 & 0 & 0 \\ -|m|a^{|m|-1}\sigma_c & |m|a^{|m|-1}\sigma_D & -|m|a^{-|m|-1}\sigma_D & 0 & 0 & 0 \\ 0 & -(\rho')^{|m|} & -(\rho')^{-|m|} & (\rho')^{-|m|} & 0 & 0 \\ 0 & -|m|(\rho')^{|m|-1} & |m|(\rho')^{-|m|-1} & -|m|(\rho')^{-|m|-1} & 0 & 0 \end{pmatrix} \times \begin{pmatrix} A_m \\ B_m \\ C_m \\ D_m \end{pmatrix} = \begin{pmatrix} 0 \\ 0 \\ 0 \\ -\frac{1}{\sigma_D \rho'} \frac{e^{-im\phi'}}{2\pi} \end{pmatrix}, \quad (\text{B.8})$$

which is solved for the constants $A_m, B_m, C_m,$ and D_m defined in (B.5). For $m = 0$, the boundary conditions (B.7) yield the following linear system of equations

$$\begin{pmatrix} -1 & 1 & \ln a & 0 \\ 0 & 0 & \frac{1}{a}\sigma_D & 0 \\ 0 & -1 & -\ln \rho' & \ln \rho' \\ 0 & 0 & -\frac{1}{\rho'} & \frac{1}{\rho'} \end{pmatrix} \times \begin{pmatrix} A_0 \\ B_0 \\ C_0 \\ D_0 \end{pmatrix} = \begin{pmatrix} 0 \\ 0 \\ 0 \\ \frac{1}{\sigma_D \rho'} \frac{1}{2\pi} \end{pmatrix}, \quad (\text{B.9})$$

which is solved for the constants $A_0, B_0, C_0,$ and D_0 defined in (B.6). The solution is readily obtained as $A_0 = B_0 = (1/\sigma_D)(1/2\pi) \ln \rho', C_0 = 0$ and $D_0 = (1/\sigma_D)(1/2\pi)$.

and for $m = 0$

$$\tilde{G}_0(\rho, \rho', \phi') = \begin{cases} A_0 & 0 < \rho < a, \\ B_0 + C_0 \ln \rho & a < \rho < \rho', \\ D_0 \ln \rho & \rho > \rho'. \end{cases} \quad (\text{B.6})$$

The appropriate boundary conditions are obtained from the continuity of $\tilde{G}_m(\rho, \rho', \phi')$ and the discontinuity of $(\partial/\partial\rho)\tilde{G}_m(\rho, \rho', \phi')$ at $\rho = a$ and $\rho = \rho'$. Hence,

$$\begin{aligned} -\tilde{G}_m(a_-, \rho', \phi') + \tilde{G}_m(a_+, \rho', \phi') &= 0, \\ -\frac{\partial}{\partial\rho}\tilde{G}_m(a_-, \rho', \phi')\sigma_c + \frac{\partial}{\partial\rho}\tilde{G}_m(a_+, \rho', \phi')\sigma_D &= 0, \\ -\tilde{G}_m(\rho'_-, \rho', \phi') + \tilde{G}_m(\rho'_+, \rho', \phi') &= 0, \\ -\frac{\partial}{\partial\rho}\tilde{G}_m(\rho'_-, \rho', \phi') + \frac{\partial}{\partial\rho}\tilde{G}_m(\rho'_+, \rho', \phi') &= \frac{1}{\sigma_D \rho'} \frac{e^{-im\phi'}}{2\pi}. \end{aligned} \quad (\text{B.7})$$

The boundary conditions (B.7) yield the following linear system of equations for $m \neq 0$

Acknowledgment

The research leading to these results has received funding from the European Community's Seventh Framework Programme (FP7/2007–2013) under Grant Agreement no. 225663.

References

- [1] M. Proto, M. Bavusi, R. Bernini et al., "Transport infrastructure surveillance and monitoring by electromagnetic sensing: the ISTIMES project," *Sensors*, vol. 10, no. 12, pp. 10620–10639, 2010.
- [2] A. Perrone, A. Iannuzzi, V. Lapenna et al., "High-resolution electrical imaging of the varco d'Izzo earthflow (southern

- Italy),” *Journal of Applied Geophysics*, vol. 56, no. 1, pp. 17–29, 2004.
- [3] G. Leone and F. Soldovieri, “Analysis of the distorted born approximation for subsurface reconstruction: truncation and uncertainties effects,” *IEEE Transactions on Geoscience and Remote Sensing*, vol. 41, no. 1, pp. 66–74, 2003.
- [4] L. L. Monte, D. Erricolo, F. Soldovieri, and M. C. Wicks, “Radio frequency tomography for tunnel detection,” *IEEE Transactions on Geoscience and Remote Sensing*, vol. 48, no. 3, pp. 1128–1137, 2010.
- [5] A. Tarantola, *Inverse Problem Theory and Methods for Model Parameter Estimation*, Society for Industrial and Applied Mathematics, Philadelphia, Pa, USA, 2005.
- [6] J. Kaipio and E. Somersalo, *Statistical and Computational Inverse Problems*, Springer, New York, NY, USA, 2005.
- [7] H. B. Mitchell, *Multi-Sensor Data Fusion: An Introduction*, Springer, Berlin, Germany, 2007.
- [8] J. F. Claerbout, *Fundamentals of Geophysical Data Processing*, Pennwell Books, Tulsa, Okla, USA, 1985.
- [9] S. Nordebo, M. Gustafsson, and F. Soldovieri, “Data fusion for reconstruction algorithms via different sensors in geophysical sensing,” in *Proceedings of the European Geosciences Union General Assembly*, European Geosciences Union General Assembly, Vienna, Austria, May 2010.
- [10] S. Nordebo, R. Bayford, B. Bengtsson et al., “An adjoint field approach to fisher information-based sensitivity analysis in electrical impedance tomography,” *Inverse Problems*, vol. 26, no. 12, Article ID 125008, 2010.
- [11] S. Nordebo, A. Fhager, M. Gustafsson, and B. Nilsson, “A green’s function approach to fisher information analysis and preconditioning in microwave tomography,” *Inverse Problems in Science and Engineering*, vol. 18, no. 8, pp. 1043–1063, 2010.
- [12] A. Kirsch, *An Introduction to the Mathematical Theory of Inverse Problems*, Springer, New York, NY, USA, 1996.
- [13] Q. Fang, P. M. Meaney, and K. D. Paulsen, “Singular value analysis of the Jacobian matrix in microwave image reconstruction,” *IEEE Transactions on Antennas and Propagation*, vol. 54, no. 8, pp. 2371–2380, 2006.
- [14] S. M. Kay, *Fundamentals of Statistical Signal Processing, Estimation Theory*, Prentice-Hall, Englewood Cliffs, NJ, USA, 1993.
- [15] K. S. Miller, *Complex Stochastic Processes*, Addison-Wesley, Boston, Mass, USA, 1974.
- [16] R. Kress, *Linear Integral Equations*, Springer, Berlin, Germany, 2nd edition, 1999.
- [17] M. Cheney, D. Isaacson, and J. C. Newell, “Electrical impedance tomography,” *SIAM Review*, vol. 41, no. 1, pp. 85–101, 1999.
- [18] J. D. Jackson, *Classical Electrodynamics*, John Wiley & Sons, New York, NY, USA, 3rd edition, 1999.
- [19] R. Pierri and F. Soldovieri, “On the information content of the radiated fields in the near zone over bounded domains,” *Inverse Problem*, vol. 14, no. 2, pp. 321–337, 1998.
- [20] R. Pierri, A. Liseno, and F. Soldovieri, “Shape reconstruction from PO multifrequency scattered fields via the singular value decomposition approach,” *IEEE Transactions on Antennas and Propagation*, vol. 49, no. 9, pp. 1333–1343, 2001.

Review Article

Review of Environmental and Geological Microgravity Applications and Feasibility of Its Employment at Archaeological Sites in Israel

Lev V. Eppelbaum

Department of Geophysics and Planetary Science, Raymond and Beverly Sackler Faculty of Exact Sciences, Tel Aviv University, Ramat Aviv, Tel Aviv 69978, Israel

Correspondence should be addressed to Lev V. Eppelbaum, levap@post.tau.ac.il

Received 17 January 2011; Accepted 17 April 2011

Academic Editor: Jean Dumoulin

Copyright © 2011 Lev V. Eppelbaum. This is an open access article distributed under the Creative Commons Attribution License, which permits unrestricted use, distribution, and reproduction in any medium, provided the original work is properly cited.

Microgravity investigations are widely applied at present for solving various environmental and geological problems. Unfortunately, microgravity survey is comparatively rarely used for searching for hidden ancient targets. It is caused mainly by small geometric size of the desired archaeological objects and various types of noise complicating the observed useful signal. At the same time, development of modern generation of field gravimetric equipment allows to register promptly and digitally microGal (10^{-8} m/s²) anomalies that offer a new challenge in this direction. An advanced methodology of gravity anomalies analysis and modern 3D modeling, intended for ancient targets delineation, is briefly presented. It is supposed to apply in archaeological microgravity the developed original methods for the surrounding terrain relief computing. Calculating second and third derivatives of gravity potential are useful for revealing some closed peculiarities of the different Physical-Archaeological Models (PAMs). It is underlined that physical measurement of vertical gravity derivatives in archaeological studying has a significant importance and cannot be replaced by any transformation methods. Archaeological targets in Israel have been ranged by their density/geometrical characteristics in several groups. The performed model computations indicate that microgravity investigations might be successfully applied at least in 20–25% of archaeological sites in Israel.

1. Introduction

Development of a new modern gravimetric and variometric (gradientometric) equipment (permitting registering earlier inaccessible small anomalies and improving the observation methodology) and creation of new methodologies for gravity data processing and interpretation have triggered an arising of microgravity methodology application in environmental and economic minerals geophysics.

Microgravity is recognized now as a effective tool for analysis of various geological inhomogeneities in subsurface, monitoring of volcanic activity, and prospecting of useful minerals (e.g., [1–30]). Butler [6, 7] carried out a careful investigation of the gravity and gravity-gradient determination concepts and corresponding interpretative procedures of microgravity. The types of noise (disturbances) arising in the microgravity investigations are studied in detail in Debeglia and Dupont [31]. Styles et al. [17] discussed a few actual

problems suggested to removing of noise components arising in microgravity under complicated environments.

2. A Brief Review of Employment of Microgravity Investigations at Archaeological Sites: A World Experience

Obviously, the history of gravity (microgravity) application at archaeological sites is beginning from the work of Linnington [32]. The Linnington's attempt to examine the Etruscan chambered tombs at Cerveteri (Italy) was not very successful, but next microgravity applications in archaeology have shown the prospectiveness of this method.

Fajkiewicz [3] investigation was suggested to examination of the gravity vertical gradient (W_{zz}) over underground galleries. Apparently, he was first indicating the significant difference between the physically measured W_{zz} and this

value obtained by the way of any transformation. Interesting examples of microgravity anomalies examination from some archaeological targets are presented in Blížkovský [4].

Kerisel [33] has been used microgravity method for estimation of the Cheops pyramid (Egypt) weight and peculiarities of its structure. Lakshmanan [34] microgravity investigations inside, above, and around the Cheops pyramid led to an evaluation of the structure's overall density and of density changes in the structure.

Slepek [35] obtained gravity anomalies of 30–80 microGals reflecting the remains of ancient buildings in the territory of Kazan Kremlin (Russia). A careful examination of microgravity anomaly at the Boden Veau (Cornwall, UK) allowed to suggest existence of new archaeological remains [36].

Pasteka and Zahorec [37] examined a complex microgravity anomaly in the area of a former church of St. Catherine (Dechtice, Slovakia) by the use of stripping technology. Microgravity anomalies of 15–20 microGals were registered over the remains of the Late Byzantine church walls in Umm er-Rasad (Jordan) [38].

A small number of microgravity measurements were performed in the Bedem archaeological locality in Yugoslavia [39]. Abad et al. [23] have carried out an assessment of a buried rainwater cistern in the Carthusian Monastery (Valencia, Spain) on the basis of 2D microgravity modeling. Microgravity survey has been successfully employed at the Roman Amphitheatre of Durres, Albania [40]. Microgravity examination performed by Sarris et al. [41] allowed identifying negative gravity anomalies above the ancient tombs in the Roman Cemetery at Kenchreai (Korinthia), Greece.

Castiello et al. [42] have been delineated underground ancient cavity in the complex urban environment of Naples. Detailed gravity examination has been effectively performed in the Red Square (Moscow) several years ago with the aim to delineate ancient underground galleries (personal communications).

3. Analysis of Microgravity Anomalies

It is known that the trivial formulas of quantitative analysis (based on simple relationships between the gravity field semiamplitude and center of the disturbing body) are widely presented in the geophysical literature (e.g., [43, 44]). However, absence of reliable information about the normal gravity field in the studied areas strongly limits practical application of these methods.

3.1. Some Common Aspects between the Magnetic and Gravity Fields. Gravity field intensity \mathbf{F} is expressed as

$$\mathbf{F} = -\text{grad}W, \quad (1)$$

where W is the gravity potential.

For anomalous magnetic field \mathbf{U}_a we can write (when magnetic susceptibility ≤ 0.1 SI unit) [45]

$$\mathbf{U}_a = -\text{grad}V, \quad (2)$$

where V represents the magnetic potential.

Let us consider analytical expressions of some typical models employed in magnetic and gravity fields (Table 1).

Here Z_v is the vertical magnetic field component at vertical magnetization, I is the magnetization, b is the horizontal semithickness of thin bed (TB), m is the elementary magnetic mass, z is the depth to a center of body (for HCC and sphere) and depth to the upper edge of TB and rod (point source), and M is the mass of sphere.

It is clear that expressions (1) and (2) are analogical ones and $(*)$ and $(**)$, (\dagger) , and $(\dagger\dagger)$, respectively, are proportional ones.

Taking into account all above mentioned, we can apply for the gravity field analysis the advanced interpreting methodologies developed in magnetic prospecting for complicated environments [45]. For instance, we can interpret anomaly from the gravity HCC by the use of formulas applied in the magnetic TB (see Table 1).

We can also calculate the “gravity moment,” which could be used for classification and ranging gravity anomalies from various types of targets. The “gravity moment” of HCC may be calculated by the use of corresponding formula for the magnetic TB [45]:

$$M_{\Delta g} = \frac{1}{2} \Delta g_a h, \quad (3)$$

where $M_{\Delta g}$ is the gravity moment, Δg_a is the amplitude of gravity anomaly (in mGal), and h is depth of HCC occurrence (in meters).

3.2. Calculation of Inclined Terrain Relief Influence. A significant number of archaeological sites occur under conditions of rugged terrain relief. Uneven observation lines are responsible for variations in the distance from the point of measurements to the source that can strongly complicate quantitative analysis of gravity anomalies [46]. If anomalies are observed on an inclined profile, then the obtained parameters characterize a certain fictitious body. The transition from fictitious body parameters to those of the real body is performed using the following expressions (the subscript “ r ” stands for a parameter of the real body) [45]:

$$\begin{cases} h_r = h + x_0 \cdot \tan \omega_0 \\ x_r = -h \cdot \tan \omega_0 + x_0 \end{cases}, \quad (4)$$

where h is the depth of the upper edge occurrence, x_0 is the location of the source's projection to plan relative to the extremum having the greatest magnitude, and ω_0 is the angle of the terrain relief inclination ($\omega_0 > 0$ when the inclination is toward the positive direction of the x -axis).

A simple example of interpreting gravity anomaly from a buried cavity on inclined profile is presented in Figure 1. It should be noted that if the well will be drilled on the projection of gravity anomaly minimum to the earth's surface could not meet this target (due to disturbing effect of inclined relief). Application of the improved tangent's method (developed in the magnetic prospecting for complex environments [45]) together with (4) permits to obtain the position of the cavity center (bold red point in Figure 1)

TABLE 1: Comparison of some analytical expressions for magnetic and gravity fields.

Field	Analytical expression	
Magnetic	Thin bed (TB)	Point source (rod)
	$Z_v = 2I2b \frac{z}{x^2 + z^2}$ (*)	$Z_v = \frac{mz}{(x^2 + z^2)^{3/2}}$ (†)
Gravity	Horizontal Circular Cylinder (HCC)	Sphere
	$\Delta g = 2G\sigma \frac{z}{x^2 + z^2}$ (**)	$\Delta g = GM \frac{z}{(x^2 + z^2)^{3/2}}$ (††)

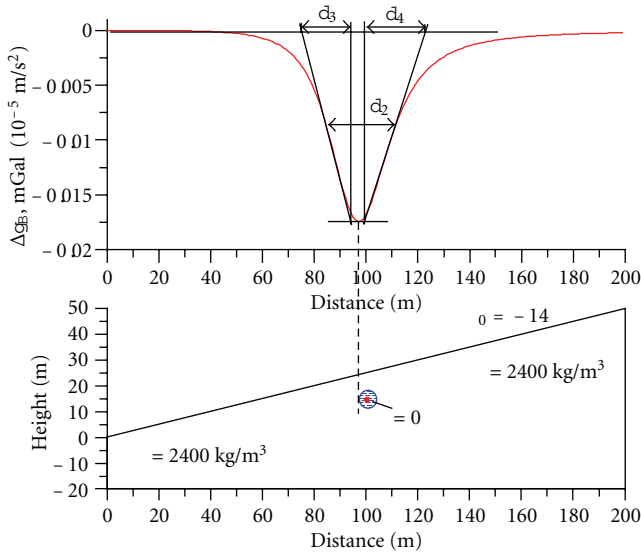


FIGURE 1: Quantitative analysis of gravity anomaly on inclined profile from a buried sphere.

with the sufficient accuracy. $M_{\Delta g}$ in this example consists of $1/2 \cdot 10.5 \text{ m} \cdot 0.0175 \text{ mGal} \cong 0.092 \text{ mGal} \cdot \text{m}$.

3.3. Calculation of Second and Third Derivatives of Gravitational Potential. Second and third derivatives of gravity potential could be very useful for defining some important peculiarities of archaeological targets location in different physical-archaeological models (PAMs). It is well known that gravity field is a function of mass and derivatives of gravity field is a function of density. Taking into account small depth of archaeological targets and their not large geometrical size, observation of both vertical and horizontal derivatives of gravity field undoubtedly will permit to obtain new important information about the desired targets. Obviously, integrated analysis of gravity field and vertical and horizontal derivatives will significantly extend the possibilities of geophysical investigations at archaeological sites. It is necessary to underline that physical measurement of vertical gravity derivatives cannot be replaced by computing of this parameter obtained by any transformation procedures: the W_{zz} values computed from the field Δg_B , as rule, show decreasing values compared with the W_{zz} obtained from physical measurements (or computation at two levels).

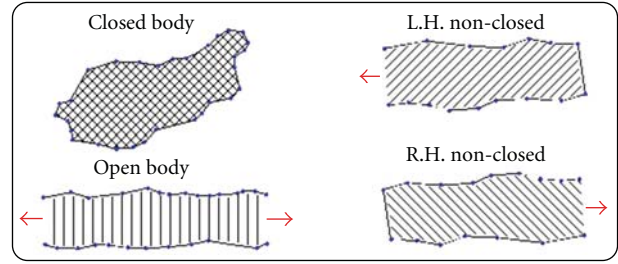


FIGURE 2: Types of geological bodies used in modeling.

4. The Developed Algorithm for 3D Modeling of Gravity Field

The GSF (Geological Space Field Calculation) program was developed for solving a direct 3D gravity and magnetic prospecting problem under complex geological conditions [16, 45]. This program has been designed for computing the field of Δg (Bouguer, free-air, or observed value anomalies), ΔZ , ΔX , ΔY , ΔT , as well as second derivatives of the gravitational potential under conditions of rugged relief and inclined magnetization. The geological space can be approximated by (1) three-dimensional, (2) semi-infinite bodies and (3) those infinite along the strike closed, left-hand non-closed, right-hand non-closed and open (Figure 2). Geological bodies, are approximated by horizontal polygonal prisms (Figure 3).

The program has the following main advantages (besides abovementioned ones): (1) simultaneous computing of gravity and magnetic fields; (2) description of the terrain relief by irregularly placed characteristic points; (3) computation of the effect of the earth-air boundary by the method of selection directly in the process of interpretation; (4) modeling of the selected profiles flowing over rugged relief or at various arbitrary levels (using characteristic points); (5) simultaneous modeling of several profiles; (6) description of a large number of geological bodies and fragments. The basic algorithm realized in the GSF program is the solution of the direct 3D problem of gravity and magnetic prospecting for horizontal polygonal prism limited in the strike direction (Figure 3). In the developed algorithm integration over a volume is realized on the surface limiting the anomalous body.

Analytical expression for the first vertical derivative of gravity potential of $(m-1)$ angle horizontal prism (Figure 3) has been obtained by integrating a common analytical

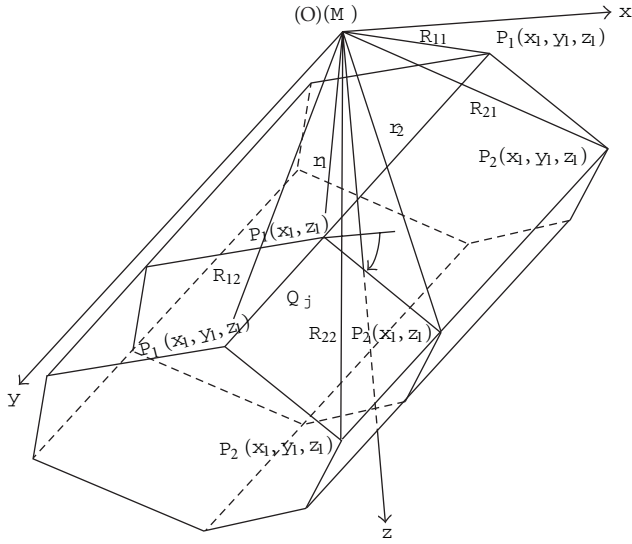


FIGURE 3: Computing derivatives of gravity potential for a horizontal polygonal prism.

expression:

$$W_{z'} = - \int_s \frac{z}{(R+y)R} dx dz \Big|_{y_1}^{y_2}, \quad (5)$$

where $R = \sqrt{x^2 + y^2 + z^2}$, S is the area of normal section of the prism by the plane of xOz

$$W_{z'T} = \left\{ -G\sigma \sum_{j=1}^{m-1} \left[V_j \sin \alpha_j \left(\ln \frac{R_{12j} + y_2}{R_{22j} + y_2} - \ln \frac{R_{11j} + y_1}{R_{21j} + y_1} \right) + V_j \cos \alpha_j \left(\operatorname{sgn}(y_2 V_j) \arccos \frac{V_j^2 R_{12j} R_{22j} + U_{1j} U_{2j} y_2^2}{r_{1j} r_{2j} (y_2^2 + V_j^2)} \right) - \left(\operatorname{sgn}(y_1 V_j) \arccos \frac{V_j^2 R_{11j} R_{21j} + U_{1j} U_{2j} y_1^2}{r_{1j} r_{2j} (y_1^2 + V_j^2)} \right) + \cos \alpha_j \left(y_2 \ln \frac{R_{12j} + U_{1j}}{R_{22j} + U_{2j}} - y_1 \ln \frac{R_{11j} + U_{1j}}{R_{21j} + U_{2j}} \right) \right] \right\}, \quad (6)$$

where G is the gravitational constant, σ is the density of the body, and α_j is the angle of the prism's side inclination.

Detailed description of analytical expressions for the first and second derivatives of gravity potential of the approximation model of the horizontal polygonal prism and their connection with magnetic field is presented in Khesin et al. [45].

5. Terrain Correction Applied for High-Accuracy Gravity Investigations: Two Nonconventional Approaches

It is well known that accuracy of microgravity investigations substantially depend on the accuracy of terrain correction

(TC) computing. Two approaches presented below were applied for exact TC calculation for the detailed Bouguer gravity observed at ore deposits occurring in the Lesser and Greater Caucasus.

5.1. First Approach. A first method was applied in the Kyzylbulakh gold-pyrite deposit situated in the Mekhmana ore region of the Nagorny Karabakh (Lesser Caucasus) under condition of rugged relief. This deposit is well investigated by mining and drilling operations and therefore was used as a reference field polygon for testing this approach. A special scheme for obtaining the Bouguer anomalies has been employed to suppress the terrain relief effects dampening the anomaly effects from the objects of prospecting. The scheme is based on calculating the difference between the free-air anomaly and the gravity field determined from a 3D model of a uniform medium with a real topography. 3D terrain relief model with an interval of its description of 80 km (the investigated 6 profiles of 800 m length are in the center of this interval) was employed to compute (by the use of *GSFC* software) the gravitational effect of the medium ($\sigma = 2670 \text{ kg/m}^3$). With applying such a scheme the Bouguer anomalies were obtained with accuracy in two times higher than that of TC received by the conventional methods. As a result, on the basis of the improved Bouguer gravity with the precise TC data, the geological structure of the deposit was defined [9].

5.2. Second Approach. Second approach was employed at the complex Katekh pyrite-polymetallic deposit, which is located at the southern slope of the Greater Caucasus (northern Azerbaijan). The main peculiarities of this area are very rugged topography of SW-NE trend, complex geology and severe tectonics. Despite the availability of conventional Δg_B (TC far zones were computed up to 200 km), for the enhanced calculation of surrounding terrain topography, a digital terrain relief model was created [16]. The SW-NE regional topography trend in the area of the Katekh deposit occurrence was computed as a rectangular digital terrain relief model (DTRM) of 20 km long and 600 m wide (our interpretation profile with a length of 800 m was located in the geometrical center of the DTRM). As a whole, about 1000 characteristic points were used to describe the DTRM (most frequently points were focused in the center of the DTRM and more rarely—on the margins). Thus, in the interactive 3D Δg_B modeling (by the use of *GSFC* software) was computed effect not only from geological bodies occurring in this area, but also from surrounding DTRM. In the issue of this scheme application, two new ore bodies were discovered [16].

6. Feasibility of Microgravity Application on archaeological Sites in Israel

Analysis of the numerous archaeological and geological publications as well as the author's investigation (e.g., [29, 47]) indicates that the ancient objects supposed for examination by the use of microgravity survey may be classified (in the

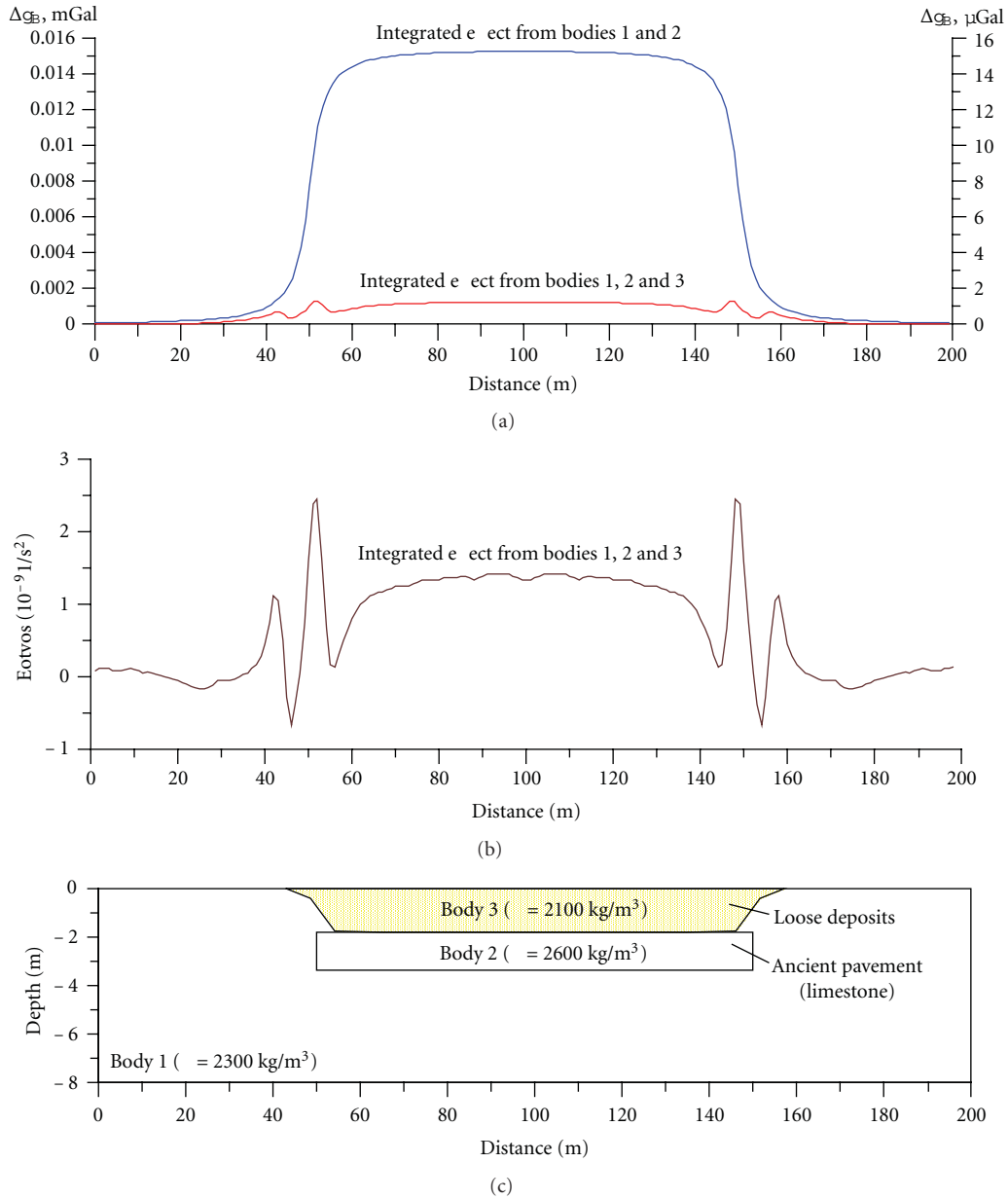


FIGURE 4: Comparison of Bouguer gravity and vertical gradient anomalies. (a) Bouguer gravity, (b) vertical gradient g_z (W_{zz}) computed for the base of 1.2 m, and (c) archaeological sequence.

order of decreasing) by the following way:

- (1) underground ancient cavities and galleries,
- (2) walls, remains of temples, churches, and various massive constructions,
- (3) pavements and tombs,
- (4) roman aqueducts (under favorable physical-geological environments),
- (5) areas of ancient primitive metallurgical activity, including furnaces, (under favorable physical-geological environments).

Examining the different archaeological targets in Israel, it was supposed that microgravity method might be effectively applied at least on 20–25% of ancient sites [29, 47].

A simplified model example of buried pavement delineation is presented in Figure 4. A buried pavement having the positive density contrast of 400 kg/m^3 and occurring at a depth of 1.8 m in uniform medium (*PAM* of one of the Megiddo sites was selected as a basis) could be easily recognized by a microgravity survey (Figure 4(a), anomalous effect from two bodies). Let us assume a low-density layer (2100 kg/m^3) over the pavement. It makes the delineation of the pavement practically impossible in

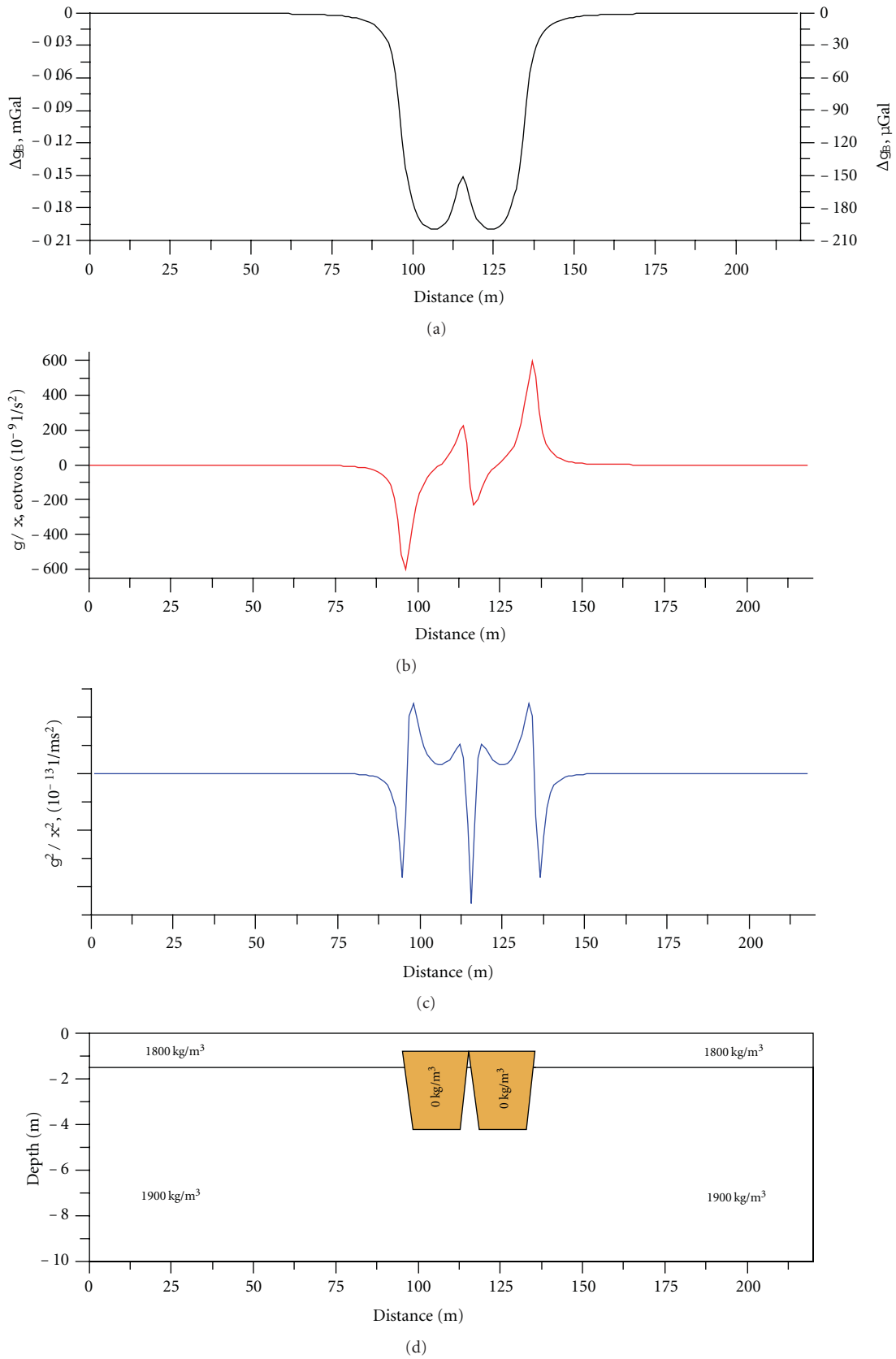


FIGURE 5: Computing of horizontal derivatives from models of two closely disposed caves. (a) computed gravity curve, (b) calculated first horizontal derivative of gravity field Δg_x , (c) calculated second horizontal derivative of gravity field Δg_{xx} , and (d) physical-geological model.

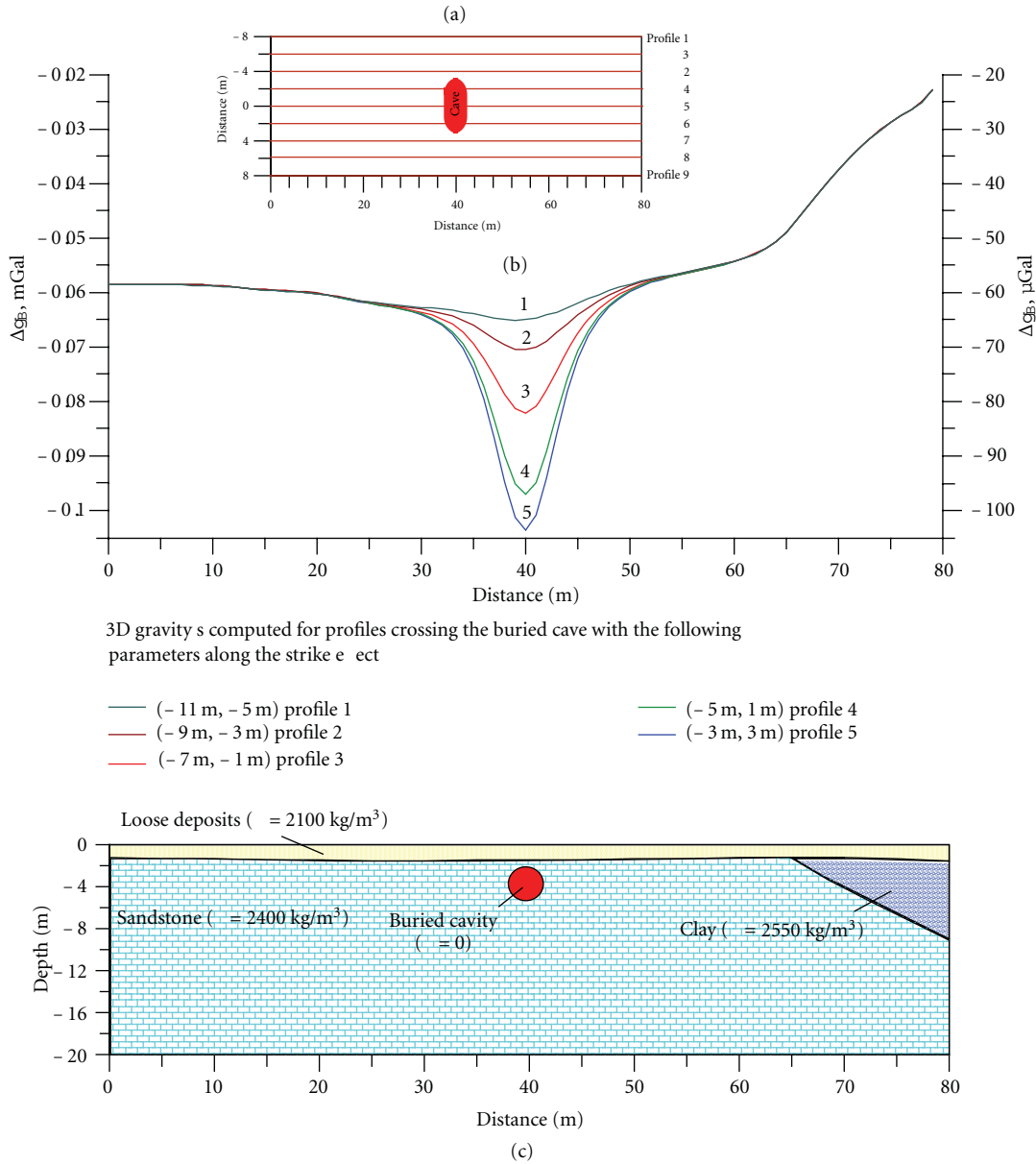


FIGURE 6: Physical-geological model of buried prehistoric cave and computed 3D gravity anomalies. (a) location of projected profiles and disposition of buried cave (view over), (b) 3D computed gravity effects along profiles 1–5, (c) geological-archaeological sequence.

field conditions (registered anomaly is oscillating about 1 microGal) (Figure 4(a), anomalous effect from three bodies). At the same time values of the second vertical derivative of gravity potential W_{zz} (computed for the levels of 0.3 and 1.5 m) with a measurable accuracy testify to a presence of disturbing body (Figure 4(b)). The similar graphs were developed for the models of buried ancient caves of various radius, ancient iron furnaces, Roman aqueducts, and so forth.

Calculations of W_{xxz} and W_{zzz} might be also useful for delineation of anomalies from closely disposed objects and removing of regional background, respectively. Taking into account that many archaeological sites in Israel are located in the vicinity of natural (sea and lake basins, mountains,

water channels, forests, etc.) and industrial (plants, buried pipelines, tunnels, railways, etc.) disturbing objects, this fact might have an essential significance. For instance, Figure 5 shows that computing of W_{xxz} (g_{xx}) makes it possible to recognize reliably gravity effects from two closely located underground caves. Ancient Prehistoric caves corresponding to this PAM are investigated in several archaeological sites disposed closely to the Golan Heights.

The planning microgravity investigations must be accompanied by development of preliminary physical archaeological models (PAM) [47, 48]. The PAM presented in Figure 6 reflects a real archaeological site located in the vicinity of Beit-Shemesh town (central Israel). The developed PAM was used for the estimation of expected gravity

anomalies amplitudes, calculation of the most optimal step of observations along profiles, and distances between profiles.

7. Conclusions

Archaeological remains in the Israeli territory are classified by the degree of microgravity method applicability. The described characteristics of the developed software for combined 3D gravity-magnetic modeling under complicated environments indicate that it is a powerful tool for microgravity examination at archaeological sites. Two earlier applied nonconventional schemes for computing of surrounding terrain relief in ore deposits may be successfully adopted for obtaining Δg_{B+TC} in archaeological sites situated in the mountainous (submountainous) regions of Israel. A proposed scheme of gravity anomalies quantitative interpretation is briefly discussed and explained on a model example. It is shown the necessity of gravity field derivatives employment in some specific situations. The developed PAM of the typical prehistoric cave (central Israel) testifies to the usefulness of such models utilization.

Acknowledgments

The author would like to thank two anonymous reviewers, who thoroughly reviewed the paper, and their critical comments were helpful in preparing this paper. The author thank the U.S. Agency for International Development and the European Community's FP7 Program under Grant Agreement no 225663 Joint Call FP7-ICT-SEC-2007-1 for supporting this investigation.

References

- [1] G. C. Colley, "The detection of caves by gravity measurements," *Geophysical Prospecting*, vol. 11, no. 1, pp. 1–9, 1963.
- [2] A. A. Arzi, "Microgravimetry for engineering applications," *Geophysical Prospecting*, vol. 23, no. 3, pp. 408–425, 1975.
- [3] Z. J. Fajkiewicz, "Gravity vertical gradient measurements for the detection of small geologic and anthropogenic forms," *Geophysics*, vol. 41, no. 5, pp. 1016–1030, 1976.
- [4] M. Blížkovský, "Processing and applications in micro gravity surveys," *Geophysical Prospecting*, vol. 27, no. 4, pp. 848–861, 1979.
- [5] M. Bichara, J. C. Erling, and J. Lakshmanan, "Technique de mesure et d'interprétation minimisant les erreurs de mesures en microgravimétrie," *Geophysical Prospecting*, vol. 29, no. 5, pp. 782–789, 1981.
- [6] D. K. Butler, "Interval gravity-gradient determination concepts," *Geophysics*, vol. 49, no. 6, pp. 828–832, 1984.
- [7] D. K. Butler, "Microgravimetric and gravity-gradient techniques for detection of subsurface cavities," *Geophysics*, vol. 49, no. 7, pp. 1084–1096, 1984.
- [8] J. F. Thimus and M. van Ruymbeke, "Improvements in field technique for use of the Lacoste and Romberg gravimeter in microgravity surveys," *First Break*, vol. 6, no. 4, pp. 109–112, 1988.
- [9] B. E. Khesin, V. V. Alexeyev, and L. V. Eppelbaum, "Investigation of geophysical fields in pyrite deposits under mountainous conditions," *Journal of Applied Geophysics*, vol. 31, pp. 187–205, 1993.
- [10] D. Patterson, J. C. Davey, A. H. Cooper, and J. K. Ferris, "The application of microgravity geophysics in a phased investigation of dissolution subsidence at Ripon, Yorkshire," *Quarterly Journal of Engineering Geology and Hydrogeology*, vol. 28, pp. 83–94, 1995.
- [11] D. E. Yule, M. K. Sharp, and D. K. Butler, "Microgravity investigations of foundation conditions," *Geophysics*, vol. 63, no. 1, pp. 95–103, 1998.
- [12] M. Beres, M. Luetscher, and R. Olivier, "Integration of ground-penetrating radar and microgravimetric methods to map shallow caves," *Journal of Applied Geophysics*, vol. 46, no. 4, pp. 249–262, 2001.
- [13] D. K. Butler, "Potential fields methods for location of unexploded ordnance," *The Leading Edge*, vol. 20, no. 8, pp. 890–895, 2001.
- [14] M. Rybakov, V. Goldshmidt, L. Fleischer, and Y. Rotstein, "Cave detection and 4-D monitoring: a microgravity case history near the Dead Sea," *The Leading Edge*, vol. 20, no. 8, pp. 896–900, 2001.
- [15] T. Hunt, M. Sugihara, T. Sato, and T. Takemura, "Measurement and use of the vertical gravity gradient in correcting repeat microgravity measurements for the effects of ground subsidence in geothermal systems," *Geothermics*, vol. 31, no. 5, pp. 525–543, 2002.
- [16] L. V. Eppelbaum and B. E. Khesin, "Advanced 3-D modelling of gravity field unmasks reserves of a pyrite-polymetallic deposit: a case study from the Greater Caucasus," *First Break*, vol. 22, no. 11, pp. 53–56, 2004.
- [17] P. Styles, S. Toon, E. Thomas, and M. Skittrall, "Microgravity as a tool for the detection, characterization and prediction of geohazard posed by abandoned mining cavities," *First Break*, vol. 24, no. 5, pp. 51–60, 2006.
- [18] D. K. Butler, *Near-Surface Geophysics (Investigations in Geophysics, No. 13)*, Society of Exploration Geophysicists, 2005.
- [19] J. S. da Silva Jr. and F. J. F. Ferreira, "Gravimetry applied to water resources and risk management in karst areas: a case study in Parana state, Brazil," in *Proceedings of the 23rd FIG Congress*, Munich, Germany, 2006.
- [20] M. W. Branston and P. Styles, "Site characterization and assessment using the microgravity technique: a case history," *Near Surface Geophysics*, vol. 4, no. 6, pp. 377–385, 2006.
- [21] N. Debeglia, A. Bitri, and P. Thierry, "Karst investigations using microgravity and MASW: application to Orleans, France," *Near Surface Geophysics*, vol. 4, pp. 215–225, 2006.
- [22] M. Ezersky, I. Bruner, S. Keydar, P. Trachtman, and M. Rybakov, "Integrated study of the sinkhole development site on the Western shores of the Dead Sea using geophysical methods," *Near Surface Geophysics*, vol. 4, no. 5, pp. 335–343, 2006.
- [23] I. R. Abad, F. G. García, I. R. Abad et al., "Non-destructive assessment of a buried rainwater cistern at the Carthusian Monastery 'Vall de Crist' (Spain, 14th century) derived by microgravimetric 2D modelling," *Journal of Cultural Heritage*, vol. 8, no. 2, pp. 197–201, 2007.
- [24] C. C. Bradley, M. Y. Ali, I. Shawkly, A. Levannier, and M. A. Dawoud, "Microgravity investigation of an aquifer storage and recovery site in Abu Dhabi," *First Break*, vol. 25, no. 11, pp. 63–69, 2007.
- [25] L. V. Eppelbaum, "Revealing of subterranean karst using modern analysis of potential and quasi-potential fields," in

- Proceedings of the 2007 SAGEEP Conference*, vol. 20, pp. 797–810, Denver, Colo, USA, 2007.
- [26] T. Mochales, A. M. Casas, E. L. Pueyo et al., “Detection of underground cavities by combining gravity, magnetic and ground penetrating radar surveys: a case study from the Zaragoza area, NE Spain,” *Environmental Geology*, vol. 53, pp. 1067–1077, 2007.
- [27] L. V. Eppelbaum, M. Ezersky, A. Al-Zoubi, V. Goldshmidt, and A. Legchenko, “Study of the factors affecting the karst volume assessment in the Dead Sea sinkhole problem using microgravity field analysis and 3D modeling,” *Advances in Geosciences*, vol. 19, pp. 97–115, 2008.
- [28] S. Deroussi, M. Diament, J. B. Feret, T. Nebut, and T. Staudacher, “Localization of cavities in a thick lava flow by microgravimetry,” *Journal of Volcanology and Geothermal Research*, vol. 184, no. 1–2, pp. 193–198, 2009.
- [29] L. V. Eppelbaum, “Application of microgravity at archaeological sites in Israel: some estimation derived from 3D modeling and quantitative analysis of gravity field,” in *Proceedings of the 2009 SAGEEP Conference*, vol. 22, no. 1, pp. 434–446, Texas, USA, 2009.
- [30] F. Greco, G. Currenti, C. Del Negro et al., “Spatiotemporal gravity variations to look deep into the southern flank of Etna volcano,” *Journal of Geophysical Research*, vol. 115, Article ID B11411, 2010.
- [31] N. Debeglia and F. Dupont, “Some critical factors for engineering and environmental microgravity investigations,” *Journal of Applied Geophysics*, vol. 50, no. 4, pp. 435–454, 2002.
- [32] R. E. Linnington, “The test use of a gravimeter on Etruscan chambered tombs at Cerveteri,” *Prospezioni Archaeology*, vol. 1, pp. 37–41, 1966.
- [33] J. Kerisel, “Le Dossier scientifique sur la pyramide de Kheops,” *Archeologia*, vol. 232, pp. 46–54, 1988.
- [34] J. Lakshmanan, “The generalized gravity anomaly: endoscopic microgravity,” *Geophysics*, vol. 56, no. 5, pp. 712–723, 1991.
- [35] Z. Slepak, “Electromagnetic sounding and high precision gravimeter survey define ancient stone building remains in the territory of Kazan Kremlin (Kazan, Republic of Tatarstan, Russia),” *Archaeological Prospection*, vol. 6, pp. 1147–160, 1999.
- [36] N. T. Linford, “Geophysical survey at Boden Vean, Cornwall, including an assessment of the microgravity technique for the location of suspected archaeological void features,” *Archaeometry*, vol. 40, no. 1, pp. 187–216, 1998.
- [37] R. Pašteka and P. Zahorec, “Interpretation of microgravimetric anomalies in the region of the former church of St. Catherine, Dechtice,” *Contributions to Geophysics and Geodesy*, vol. 30, no. 4, pp. 373–387, 2000.
- [38] A. Batayneh, J. Khataibeh, H. Alrshdan, U. Tobasi, and N. Al-Jahed, “The use of microgravity, magnetometry and resistivity surveys for the characterization and preservation of an archaeological site at Ummer-Rasas, Jordan,” *Archaeological Prospection*, vol. 14, no. 1, pp. 60–70, 2007.
- [39] S. Komatina and Z. Timotijevic, “Some case studies of geophysical exploration of archaeological sites in Yugoslavia,” *Journal of Applied Geophysics*, vol. 41, no. 2–3, pp. 205–213, 1999.
- [40] M. Di Filippo, S. Santoro, and B. Toro, “Microgravity survey of Roman Amphitheatre of Durres (Albania),” in *Proceedings of the 6th Archaeological Prospection*, Rome, Italy, 2005.
- [41] A. Sarris, R. K. Dunn, J. L. Rife, N. Papadopoulos, E. Kokkinou, and C. Mundigler, “Geological and geophysical investigations in the Roman Cemetery at Kenchreai (Korinthia), Greece,” *Archaeological Prospection*, vol. 14, no. 1, pp. 1–23, 2007.
- [42] G. Castiello, G. Florio, M. Grimaldi, and M. Fedi, “Enhanced methods for interpreting microgravity anomalies in urban areas,” *First Break*, vol. 28, no. 8, pp. 93–98, 2010.
- [43] W. M. Telford, L. P. Geldart, and R. E. Sheriff, *Applied Geophysics*, Cambridge University Press, 1993.
- [44] D. S. Parasnis, *Principles of Applied Geophysics*, Prentice and Hall, 1997.
- [45] B. E. Khesin, V. V. Alexeyev, and L. V. Eppelbaum, *Interpretation of Geophysical Fields in Complicated Environments*, Advanced Approaches in Geophysics, Kluwer Academic Publisher, Dordrecht, The Netherlands, 1996.
- [46] V. V. Alexeyev, B. E. Khesin, and L. V. Eppelbaum, “Geophysical fields observed at different heights: a common interpretation technique,” in *Proceedings of the Meeting of Society of Exploration Geophys.*, pp. 104–108, Jakarta, 1996.
- [47] L. V. Eppelbaum, “Archaeological geophysics in Israel: past, present and future,” *Advances in Geosciences*, vol. 24, pp. 45–68, 2010.
- [48] L. V. Eppelbaum, “Applicability of geophysical methods for localization of archaeological targets: an introduction,” *Geoinformatics*, vol. 11, no. 1, pp. 19–28, 2000.

Research Article

Postprocessing of Infrared Reflectography to Support the Study of a Painting: The Case of Vivarini's Polyptych

Laura Fragasso and Nicola Masini

IBAM-CNR (Istituto per i Beni Archeologici e Monumentali), C. da S. Loja, Tito Scalo, 85050 Potenza, Italy

Correspondence should be addressed to L. Fragasso, l.fragasso@ibam.cnr.it

Received 12 February 2011; Revised 27 March 2011; Accepted 2 May 2011

Academic Editor: Francesco Soldovieri

Copyright © 2011 L. Fragasso and N. Masini. This is an open access article distributed under the Creative Commons Attribution License, which permits unrestricted use, distribution, and reproduction in any medium, provided the original work is properly cited.

Infrared (IR) reflectography is an imaging diagnostic technique widely used to study and evaluate the assessment of paintings' conservation state. The study case analyzed in this paper is related to a polyptych panel attributed to Vivarini's workshop conserved in the "Sigismondo Castromediano" Museum in Lecce. The painting's IR reflectography has been acquired through a CCD camera with spectral sensitivity ranging 400–1150 nm and manual positioning system. In order to offset the technological limits of the CCD camera, reflectograms have been processed through Principal Component Analysis and spectral indices. Postprocessing provided information related to the different pictorial drafting and restoration works, as well as emphasized graphic details and shadings, useful to improve the knowledge of the painting techniques.

1. Introduction

As the photoreceptors of the human eye can "see" only in the "visible" spectrum, that is between 380 nm (blue) and 750 nm (red), they are able to detect only the reflected and diffused radiations coming from the most superficial pictorial layers of a painting. If the same photoreceptors were able to detect radiation at greater wave length ($>1\ \mu\text{m}$), they could "see" below the pictorial surface. In fact, the near infrared radiations (with wavelengths ranging from 1 to $3\ \mu\text{m}$) are able to greatly penetrate the pictorial layer. Part of the radiation is diffused, while the rest is reflected, making it possible to put in evidence what is underdrawings.

Exploiting such a physical characteristic, an imaging diagnostic technique based on near infrared reflectography has been widely employed to study works of art since the sixties [1].

This technique is based on lighting a work of art, in particular a painting, by a source of near infrared radiations. An infrared camera captures the light which reflects off the painting surface. The image captured, that is the infrared reflectogram, is digitized and processed by means of suitable imaging softwares.

The transparency (and reflectance) of a pictorial layer depends on: (i) the optic properties of materials and, therefore, the chemical nature of the pigments, (ii) the thickness of the paint, and the infrared radiation wavelength.

- (i) Many paintings are partially or completely transparent while others (i.e., frescoes) absorb the infrared radiations and appear dark. The transparency of the paint layers to the near infrared radiations (with wavelengths ranging from 1 to $2\ \mu\text{m}$) makes it possible to identify hidden details not visible to the naked eye, such as the underdrawings, changes in the paint layers, and other features behind the pictorial layers [2].
- (ii) The longer the infrared wavelength and the thinner the paint layers are, the easier it is to penetrate to the layers beneath.

Since the first studies and applications, lead by Van Asperen De Boer in the sixties [3], NIR reflectography technologies have been strongly increased and improved, especially after the epochal shift from photographic techniques to digital imaging.

The most frequently used technological devices are: (i) camera with Vidicon tube and lead sulfide detector (Pbs), (ii) solid state CCD (Charged Couple Device) camera with silicon detector (CCD-Si), (iii) solid state camera with indium gallium-antimonide (InGaAs) and platinum silicide (PtSi) detectors, and (iv) Infrared scanners [4, 5].

Vidicon cameras acquire images at wavelengths ranging from 0.7 to 2.2 μm , depending on models. Their disadvantages in comparison to more advanced devices are: lower spatial resolution, thermal instability, geometrical distortion.

CCD cameras acquire reflectograms at higher spatial resolution, with better contrast in comparison to Vidicon cameras. However, they have a smaller spectral sensitivity (sp.se.), thus covering the visible spectrum and the near infrared (up to 1 μm). This prevents the sensor from exploring deeper pictorial layers.

Vice versa, solid state cameras with Indium Gallium-Antimonide (InGaAs) and platinum silicide (PtSi) detectors are able to reach deeper layers due to their larger spectral sensitivity, ranging, respectively, from 0.9 to 1.7 μm and from 1.2 to 5 μm . Unfortunately, such cameras are very expensive and so their use is restricted to the study of paintings.

In the last twenty years, new devices based on scanning technology have been developed [6]. For example, the INOA IR scanner is a modular device based on an optical head provided with InGaAs photodiode with spectral sensitivity up to 1700 nm and a lighting system which move together on a x - y precision translation stage, which makes it possible to take images at very high resolution (16 pixel points for mm^2) without any geometrical distortion [7].

This kind of device has been employed in Italy to map what lays underdrawings and study the painting technique of Pietro Vannucci called "Il Perugino" [8, 9].

Recently, Ambrosini et al. [10] compared such device with a camera provided with an array CCD colour filtered sensor, nominally 350–1100 nm sensitive range, to study "the Virgin with Child" attributed to Cimabue. The underdrawing visibility is improved in the IR Scanner reflectograms thanks to the more extended and uniform spectra sensitivity. However, they are complementary in terms of spectral response to identify several information about the conservation [10].

Gargano et al. [11] compared the performance of different IR reflectographic systems (Vidicon camera, sp.se. up to 2000 nm; solid state Si CCD photcamera, sp.se. up to 1050 nm, 1920×2500 pixel; FPA InGaAs camera, sp.se. up to 1700 nm, 320×240 pixel; FPA MCT (HgCdTe) camera, sp.se. up to 2500 nm, 320×256 pixel; InSb thermocamera, spectr. range 3000–5000 nm, argon cooled) to detect and visualize the underdrawings of paintings.

The comparative study confirmed that the majority pigment's transparency is greater in the 1330–2200 nm range. However, as some pigments are nontransparent in the 0.8–1 μm range, the analyses performed with CCD detector (sp.se. up to 1050 nm) gave immediately preliminary information about these pigments.

For this reason a CCD detector is more effective in detecting restorations and pictorial integrations than wider IR band systems which tend to give very similar responses



FIGURE 1: St. Antonio Abbot attributed to Bartolomeo Vivarini, section of a polyptych dating back to the 15th century, Lecce, Museum "Sigismondo Castromediano": image acquired in the visible spectrum (Panchromatic).

(reflectance and transparency) for different pigments, unless they use band-pass filters with a 0.8–1 μm range [11].

This paper deals with the use of a CCD detector to map hidden features and alterations in a painting on a wooden board by Vivarini, an important Renaissance painter. The instrument limits have been overcome by means of post-processing methods, such as the Principal Component Analysis (PCA) and spectra indices. The choice to adopt such an approach has also been made to enhance possible details in underdrawings and "repentances" not evident observing the non post processed data set.

This paper is organized as follows. Section 2 deals with the potentials of PCA and spectral indices to process IR reflectograms. In Section 3, the study case is described. Section 4 focuses on the experimental section: from acquisition to postprocessing of IR reflectograms. In Section 5, the postprocessing results are described. Conclusions follow in Section 6.

2. Postprocessing of IR Reflectograms by PCA and Spectral Indices: Rational Basis and Study Cases

PCA is a linear transformation which decorrelates multivariate data by translating and/or rotating the axes of the original feature space [12]. In this way, the data can be represented without correlation in a new component space. In order to do this, the process firstly computes the covariance matrix (S) among all input spectral channels, then eigenvalues and eigenvectors of S are calculated in order to obtain the new feature components

$$\text{cov } k_1, k_2 = \frac{1}{m-1} \sum_{i=1}^m (SB_{i,k_1} - \mu_{k_1})(SB_{i,k_2} - \mu_{k_2}), \quad (1)$$



FIGURE 2: Visible RGB of Figure 1.



FIGURE 3: Image acquired with IR2 band with additional information and features (indicated with red and purple color) provided respect to the visible spectrum (RGB and Panchromatic).

where k_1, k_2 are two input spectral channels, SB i, j , spectral value of the given channel in row i and column j , n number of row, m number of columns, and μ mean of all pixel SB values in the subscripted input channels.

The percent of total dataset variance explained by each component is obtained by (2)

$$\%i = 100 * \frac{\lambda_i}{\sum_{i=1} \lambda_i}, \quad (2)$$

where λ_i are eigenvalues of S .

Finally, a series of new image layers (called eigenchannels or components) are computed (3) by multiplying, for each

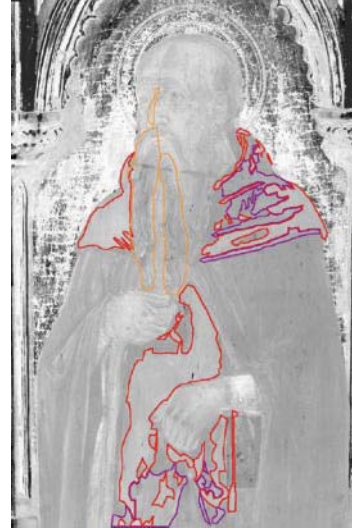


FIGURE 4: PC2 result with additional information and features provided with respect to the visible spectrum indicated with red and purple colour and to IR2 band, with orange colour, as well.



FIGURE 5: PC3 result with additional information and features provided with respect to the visible spectrum indicated with red and purple colour and to IR2 band, with green colour, as well.

pixel, the eigenvector of S for the original value of a given pixel in the input bands

$$P_i = \sum_{k=1} P_k u_{k,i}, \quad (3)$$

where P_i indicates a spectral channel in component i , $u_{k,i}$ eigenvector element for component i in input band k , P_k spectral value for channel k , number of input band.

A loading, or correlation R , of each component i with each input date k can be calculated by using(4)

$$R_{k,i} = u_{k,i}(\lambda_i)^{1/2}(\text{var}_k)^{1/2}, \quad (4)$$

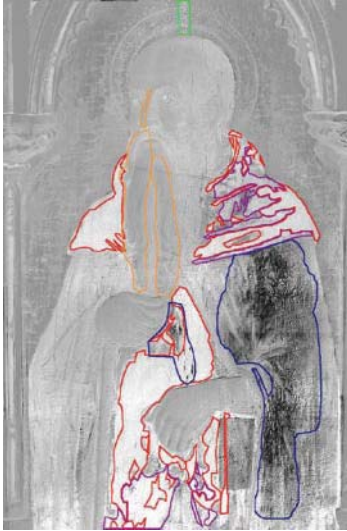


FIGURE 6: NDI result with additional information and features provided with respect to the visible spectrum (all colours) and to IR2 band, as well (indicated with green, orange and blue colour).

where $\text{var } k$ is the variance of input data k (obtained by reading the k th diagonal of the covariance matrix)

So, the PCA transforms the input multispectral bands in new components whose number is equal to (or less than) the input channels.

The PC components are hierarchically ordered, that is, PC1 contains the major variance portion and provides a sort of average of all the input channels, PC2 represents the second maximum variance, and so on.

The major portion of the variance in a multispectral data set is associated with homogeneous areas, whereas localised surface anomalies will be enhanced in later components, which contain less of the total dataset variance. This is the reason why they may represent information variance for a small area or essentially noise, and, in this case, it must be disregarded.

The spectral indices are generally computed by a linear combination of different spectral bands in order to obtain quantitative measures of the surface properties. For environmental studies, spectral indices are used to quantify surface properties such as brightness, moisture, biomass cover, and vegetative vigour. The widest used index is the Normalized Difference Vegetation Index (NDVI) obtained by using the following formula:

$$\text{NDVI} = \frac{(\text{NIR} - \text{RED})}{(\text{NIR} + \text{RED})}. \quad (5)$$

The NDVI operates by contrasting intense chlorophyll pigment absorption in the RED against the high reflectance of leaf mesophyll in the NIR.

PCA and NDVI have been experienced on multispectral satellite images for archaeological purposes [13, 14].

Such methods have been applied for the multispectral imaging of works of art, in particular paintings. By means of PCA, from n -spectral band n -principal components

(noncorrelated images) are extrapolated, thus reducing redundancy of the multispectral dataset.

PCA has been applied on images acquired by near-infrared spectroscopic imaging instrumentation, in particular a CCD camera with spectral sensitivity ranging from 650–1040 nm. The images were related to a drawing made by ink and charcoal attributed to Veit Hirschvogel the Elder (1461–1525). A multivariate image analysis produced a set of principal component (PC) images providing a direct visualization of the compositional characteristics of the work of art [15].

A similar PCA case on imaging spectroscopy has been performed by Bacci et al. [16] to investigate the details of drawings by Parmigianino (1503–1540).

PCA has been used by Baronti et al. [17, 18] to analyze different pigments in a painting by Luca Signorelli (well known as “Predella della Trinità”). Different images have been acquired by a Vidicon camera in the visible spectrum (420–750 nm) in the near infrared (750–1550 nm). The visual inspection of PC2 and PC3 in NIR images made it possible to distinguish some areas which, observing the input NIR channel, seemed to be painted with the same pigment.

As for the use of spectral indices, it is possible to mention the application of NDVI to study the fresco “Vergine con Bambino” (Virgin with Child) in the Basilica of St. Peter in Vincoli in Rome [19]. NDVI made it possible to discriminate red pigments in the Virgin’s dress from those in the rest of the painting.

For our study case, a normalized difference index of IR1 and IR2 ($\text{NDI} = (\text{IR2} - \text{IR1})/(\text{IR2} + \text{IR1})$), along with a ratio of the two spectral band ($\text{IR1}/\text{IR2}$), have been applied.

3. Study Case

IR reflectography has been experienced on a painting on a wooden board which depicts St. Antonio Abbot (Figure 1). It is part of a polyptych which is considered very important by historical criticism because it witnesses Venetian painting in Apulia (Southern Italy).

The polyptych dates back to the 15th century (post-1463), and it comes from the Church of S. Caterina from Alessandria in Galatina (Lecce, Southern Italy). At present time, it is conserved in the Gallery of Lecce Province Museum “Sigismondo Catromediano.”

It is composed of fourteen distempered panels (total dimensions cm. 215×265) depicting on the upper part, from left to right, respectively: St. Caterina from Alessandria, St. Antonio Abbot, St. Nicola from Bari, the Holy Trinity between St. Francesco from Assisi and St. Domenico, St. Ambrogio, St. Girolamo, and St. Agnese.

The panels on the lowest part of the polyptych portray, from left to right, respectively: St. Giovanni Battista, St. Vescovo, St. Paolo, the Virgin in Throne with Child, St. Pietro, St. Benedetto, and St. Michael Archangel.

The polyptych has been restored mainly in the lowest part in 1876 and 1934. It is attributed to the venetian workshop of Vivarini’s family. In particular, the panel which portrays St. Antonio Abbot is attributed to Bartolomeo Vivarini [20, 21].

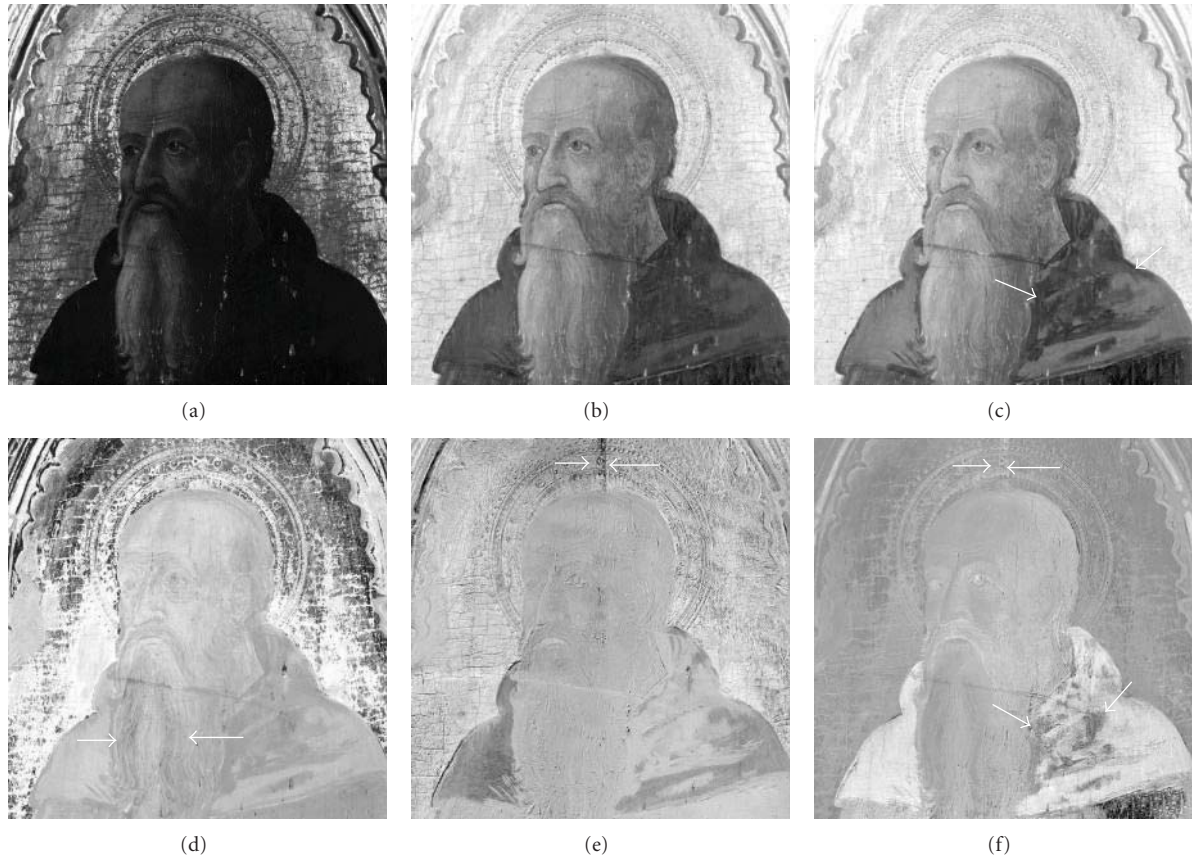


FIGURE 7: Detail of the upper part of the Saint from PAN (a), IR1 (b), IR2 (c), PC2 (d), PC3 (e), and NDI (f).



FIGURE 8: RGB image with additional information provided by postprocessing with respect to the data input (see Table 1).

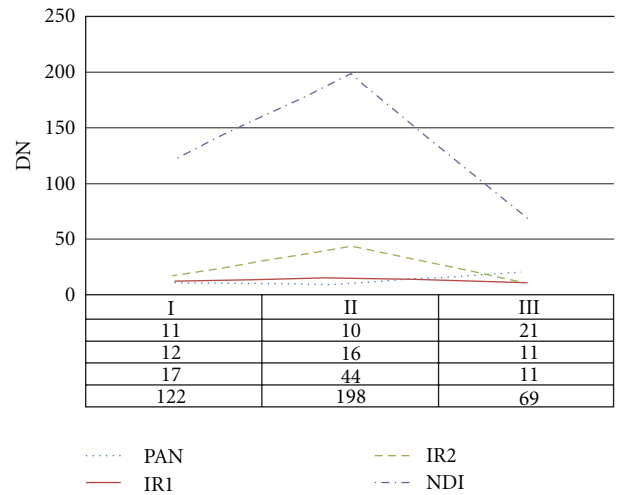


FIGURE 9: DN average of patterns I, II, and III measured from PAN, IR1, IR2, and NDI.

4. Experimental Section

4.1. *Equipment.* The IR reflectography of the painting has been acquired by a multispectral imaging system ARTIST,

belonging to the Lecce Province Museum “Sigismondo Catromediano.” It consists in a CCD photcamera with spectral sensitivity ranging from 400–1150 nm and manual positioning system.

TABLE 1: Additional features provided by IR2 with respect to visible, and by PCA and NDI with respect to visible and IR2.

Color	Additional features provided by	With respect to
Red	IR2, PC2, PC3, and NDI	Visible (RGB and PAN)
Purple	IR2, PC2, PC3, and NDI	Visible
Blue	NDI	Visible and IR2
Orange	PC2 and NDI	Visible and IR2
Green	PC3 and NDI	Visible and IR2

The photocamera acquires images in the visible spectrum (panchromatic and RGB, sp.se. 400–700 nm), in the near infrared spectral bands IR1 (sp.se. 700–950 nm), and IR2 (sp.se. 950–1150 nm), at the spatial resolution of 1360×1036 pixel/inch.

The optical head is provided with two lens: one is wide-angle (23 mm focal length) working in F/1.4 configuration, and the other is a zoom (10–108 mm focal length) working in F/2.5 configuration. The lighting system (in the visible and infrared) consists of two 60 W halogen lamps illuminating the painting surface at 45° at the distance of 120 cm.

4.2. *Image Acquisition and Processing.* The image acquisition and processing consisted in the following steps.

- (1) Image acquisition by using the ARTIST software. The picture has been subdivided into a grid of “ n ” rows and “ n ” columns, in order that each acquisition in each band, such as visible panchromatic (PAN), IR1 and IR2, covers an area of 297×214 mm.
- (2) Mosaic of the single shots in order to obtain the entire painting image, by using the Panavue Image Assembler 2.06 software, with 20% overlapping.
- (3) Georegistration and ortho-rectification of all data set (visible PAN and RGB, IR1, and IR2) by using Global Mapper. This is a crucial step which makes it possible to obtain a precise and orth-rectified overlay of the mosaics over different bands.
- (4) First comparative visual inspection of the georegistered and ortho-rectified scenes and first interpretation hypotheses.
- (5) Postprocessing of images consisting in filtering, convolution, the application of PCA, and spectral indices using ENVI software.

As for the spectral indices, a Normalized Difference Index (derived from the NDVI)

$$\text{NDI} = \frac{(\text{IR2} - \text{IR1})}{(\text{IR2} + \text{IR1})} \quad (6)$$

has been applied.

The expected results of the above-said postprocessing approach are the enhancement of features and information useful to discriminate pigments.

5. Results

The comparative analysis of the input dataset (PAN, RGB, IR1, and IR2) (see Figures 1–3) have pointed out as follows:

- (i) Visible PAN and RGB images highlight the painting conservation state, with a spread phenomenon of crackle and superficial deposits. The painting has undergone different restorations (under the left hand of the Saint there is a protective coat coming from the most recent interventions; see Figures 1 and 2).
- (ii) The infrared data, in particular IR2 channel, add further information (see Figure 3) with respect to the scenes acquired in the visible (for such reason and for sake of brevity only IR2 image is showed). As showed in Figure 3, IR2 image reveals on the Saint’s tunic and mantle some areas (darker grey) referable to later painting layers, with the classical effect of “leopard spots.”

Valuable results have been obtained through PCA and NDI. In detail, the computed principals component have been three, with percentage variance from P1 to P3 of 73%, 21%, and 5%, respectively.

- (i) The PC1 image summarizes the first maximum variance of the data-set and provides a sort of average of all the input channels. The result is similar to PAN and IR1. This could be due to the fact that the illumination source used has a maximum value of irradiance in the infrared.
- (ii) The PC2 (Figure 4) image with respect to PAN puts in evidence the same further information provided by IR2 referable to later intervention of restoration on Saint’s tunic and mantle.
- (iii) In addition to IR2, PC2 points out brush-strokes to outline the beard and moustaches, as well as to mark some details in the Saint’s face (contour of the nose, eyes, expression lines in cheekbones, and forehead, see also Figure 7(d))
- (iv) The PC3 image (Figure 5) conserves the additional information of PC2 with respect to PAN related to the mantle and the tunic, but not to the beard of the Saint. Some information of the face disappear. However PC3 put in evidence some more information on decay pathologies and on a discontinuity line in the wooden board on top of the saint halo (contoured by green line in Figure 5; see also Figure 7(e)).

The application of the Normalized index NDI confirms the features observed in PC3 image and provides further data, as well (Figure 6). In particular, the most relevant information provided by NDI is related to the right part of the mantle, contoured by blue line in Figure 6. It is characterized by a nonhomogeneous darker tone which suggests the presence of a restoration work.

As for the filtering, good results have been obtained by directional and high pass, to emphasize the microcracks and fissures which affect the pictorial layer.

Figure 8 shows the RGB image with the features extracted IR2, PCA, and NDI.

As a whole, the comparative observation of data input and the postprocessing results put in evidence that the dark brown mantle and tunic of the Saint has been painted during three phases (I, II, and III, in Figure 8). Figure 9 put in evidence the different discrimination of the patterns I, II, and III in terms of reflectance values (DN values) of IR2 and NDI with respect to the PAN. In particular from PAN and IR1, DN values of the mentioned patterns are similar; whereas from NDI image, DNI values of patterns I, II, and III are very dissimilar.

6. Conclusions

An IR reflectographic system has been used to investigate, in noninvasive way, a spectral region of the visible and near infrared. This is crucial but not exhaustive to characterize the surface and pictorial layers below, due to the limits of the employed sensor (CCD). In order to offset such limits, reflectograms have been processed by PCA and spectral indices (such as NDI).

The analysis has been aimed at focusing some issues of the study case, a polyptych dating back to the 15th century, composed of fourteen panels, among which, for the sake of brevity, only the panel of St. Antonio Abbot has been examined in this paper.

The investigation has been carried on with two aims:

- (i) the first is to analyze the stylistic features, since the polyptych is attributed to Vivarini workshop and, in particular, the panel portraying St. Antonio Abbot is thought to be painted by Bartolomeo Vivarini;
- (ii) the second aim is to map the restorations which followed each other between the second half of the 19th century and the first half of the 20th century.

The postprocessing methods applied to reflectograms provided additional information with respect to the image input (PAN, IR1 and IR2). A comparative analysis of data input and postprocessing results has been performed by visual observation. Such analysis put in evidence the effectiveness of later principal components (in particular PC3) and the index NDI in discriminating pictorial patterns with the same color (i.e., the dark brown of the mantle and the tunic), thus suggesting different painting phases or restoration works.

Acknowledgments

Thanks are due to the staff working at Lecce Province Museum "Sigismondo Catromediano", in particular to the Museum Director Antonio Cassiano, the Restoration Laboratory Director Brizia Minerva, the Restorer Nicola Ancona, and the Researcher Maria D. Pilolli.

References

- [1] J. R. J. Van Asperen de Boer, "Infrared reflectograms of panel painting," *Studies in Conservation*, vol. 11, pp. 45–46, 1966.
- [2] R. Tilley, *Colour and the Optical Properties of Materials*, Wiley, Chichester, UK, 2000.
- [3] J. R. J. Van Asperen De Boer, "Infrared Reflectography of paintings using an infra-red vidicon television system," *Studies in Conservation*, vol. 14, pp. 96–118, 1969.
- [4] A. Aldovrandi and M. Picollo, *Metodi di documentazione e di indagini non invasive sui dipinti*, Saonara, Padova, Italy, 2001.
- [5] G. Poldi and G. Villa, *Dalla conservazione alla storia dell'arte. Riflettografia e analisi non invasive per lo studio dei dipinti*, Edizioni della Normale, Pisa, Italy, 2006.
- [6] D. Bertani, M. Cetica, P. Poggi et al., "A scanning device for infrared reflectography," *Studies in Conservation*, vol. 35, pp. 113–116, 1990.
- [7] R. Fontana, D. Bencini, P. Carcagni et al., "Multi-spectral IR reflectography," in *O3A: Optics for Arts, Architecture, and Archaeology*, C. Fotakis, L. Pezzati, and R. Salimbeni, Eds., vol. 6618 of *Proceedings of SPIE*, Munich, Germany, June 2007.
- [8] M. Materazzi, L. Pezzati, and P. Poggi, "IR-colour scanning reflectography. The Painting technique of Pietro Vannucci called Il Perugino," in *Proceedings of the Labs Tech Workshop*, vol. 53, pp. 65–70, 2004.
- [9] R. Bellucci and C. Frosinini, "The myth of cartoon reuse in Perugino's underdrawing: technical investigation. The Painting technique of Pietro Vannucci called Il Perugino," in *Proceedings of the Labs Tech Workshop*, vol. 53, pp. 71–80, 2004.
- [10] D. Ambrosini, C. Daffara, R. Di Biase et al., "Integrated reflectography and thermography for wooden paintings diagnostics," *Journal of Cultural Heritage*, vol. 11, no. 2, pp. 196–204, 2010.
- [11] M. Gargano, N. Ludwig, and G. Poldi, "A new methodology for comparing IR reflectographic systems," *Infrared Physics and Technology*, vol. 49, no. 3, pp. 249–253, 2007.
- [12] J. A. Richards, *Remote Sensing Digital Image Analysis*, Springer, Berlin, Germany, 1986.
- [13] R. Lasaponara and N. Masini, "Improving satellite Quickbird-based identification of landscape archaeological features through Tasseled Cap Transformation and PCA," in *Proceedings of 21st CIPA Symposium*, pp. 812–816, Atene, Greece, June 2007.
- [14] R. Lasaponara and N. Masini, "Identification of archaeological buried remains based on the normalized difference vegetation index (NDVI) from quickbird satellite data," *IEEE Geoscience and Remote Sensing Letters*, vol. 3, no. 3, pp. 325–328, 2006.
- [15] M. Attas, E. Cloutis, C. Collins et al., "Near-infrared spectroscopic imaging in art conservation: investigation of drawing constituents," *Journal of Cultural Heritage*, vol. 4, no. 2, pp. 127–136, 2003.
- [16] M. Bacci, A. Casini, C. Cucci, A. Muzzi, and S. Porcinai, "A study on a set of drawings by Parmigianino: integration of art-historical analysis with imaging spectroscopy," *Journal of Cultural Heritage*, vol. 6, no. 4, pp. 329–336, 2005.
- [17] S. Baronti, A. Casini, F. Lotti, and S. Porcinai, "Principal component analysis of visible and near-infrared multispectral images of works of art," *Chemometrics and Intelligent Laboratory Systems*, vol. 39, no. 1, pp. 103–114, 1997.
- [18] S. Baronti, A. Casini, F. Lotti, and S. Porcinai, "Multispectral imaging system for the mapping of pigments in works of art by use of principal-component analysis," *Applied Optics*, vol. 37, no. 8, pp. 1299–1309, 1998.

- [19] I. Roselli and P. Testa, "High resolution vis and nir reflectography by digital ccd telescope and imaging techniques: application to the fresco "Vergine con Bambino" in S.Pietro in Vincoli, Rome," in *Proceedings of the 8th International Conference on Non destructive Investigations and Microanalysis for the Diagnostics and Conservation of the Cultural and Henvironmental Heritage (Art '05)*, Lecce, Italy, May 2005.
- [20] M. D'Elia, *Mostra dell'arte in Puglia dal tardo antico al Rococò*, Roma, Bari, Italy, 1964.
- [21] A. Cassiano, *Momenti di arte gotica nel Salento*, Lecce, 1987.

Research Article

Ground Penetrating Radar in Dam Monitoring: The Test Case of Acerenza (Southern Italy)

A. Loperte,¹ M. Bavusi,¹ G. Cerverizzo,² V. Lapenna,¹ and F. Soldovieri³

¹*Institute of Methodologies for Environmental Analysis (IMAA), CNR Tito Scalco, 85050 Potenza, Italy*

²*National Irrigation Development and Agrarian Transformation in Puglia, Basilicata and Irpinia (EIPLI), 85100 Potenza, Italy*

³*Institute for Electromagnetic Sensing of the Environment (IREA), CNR 80124 Napoli, Italy*

Correspondence should be addressed to M. Bavusi, bavusi@imaa.cnr.it

Received 15 February 2011; Accepted 20 April 2011

Academic Editor: Erica Utsi

Copyright © 2011 A. Loperte et al. This is an open access article distributed under the Creative Commons Attribution License, which permits unrestricted use, distribution, and reproduction in any medium, provided the original work is properly cited.

Nowadays, dam safety management is gaining great importance since it affects in a crucial way the monitoring and improvement of risky reservoirs, but this topic is very challenging since the dam safety requires long-term and time-continuous monitoring. In this framework, the exploitation of conventional geotechnical investigation methods often requires invasive actions in the inner of the structure to be investigated (destructiveness) and only provides punctual information for small volumes. On the contrary, the application of noninvasive sensing techniques makes it possible to investigate higher volumes without affecting the structure. In this paper we describe the application of GPR for the monitoring and diagnostics of one of the largest dams in the Basilicata region (Southern Italy). The investigation aims at detecting and localizing underground sandstone banks that are potential ways of flow of water below the dam. The manageability and the noninvasiveness of GPR have resulted in particularly suitable for this kind of application because the versatility of this geophysical method allows to investigate large areas with a good spatial resolution giving the possibility to detect the presence of inhomogeneities in the subsoil below the dam.

1. Introduction

Maintenance and monitoring of the critical infrastructures play an important role for public safety and prevention and thus it is important to routinely monitor and control them [3]. In particular, the exploitation of noninvasive diagnostic techniques is crucial for the monitoring of the critical infrastructures since they do not affect the normal operating behaviour of the structure, which is one of the main requirements during the control inspections.

Here, we focus on the problem of the detection, characterization, and evaluation of the potential losses of water through a dam, which is an important aspect of civil, hydrology, and environmental engineering. In particular, this contribution deals with the exploitation of Ground Penetrating Radar (GPR) technique for monitoring and diagnostics of a dam.

In fact, among the possible issues that may affect dams, the presence of voids or fractured zones embedded in the structure or in its foundation soil represents one of the

most significant problems to be tackled. Voids, lithological discontinuities, or induced discontinuities, for instance by reparation, are sometimes hard to be identified by visual inspection and can dangerously damage the structure itself by jeopardizing its stability.

Traditional inspection methods have, in particular, drawbacks; in fact, conventional geotechnical investigation methods applied on the structure often require invasive actions in the inner of the structure to be investigated (destructiveness) and only provide punctual information for small volumes.

In recent years, nondestructive investigations on building and civil infrastructures are increasingly improving [4–7], but, the literature on the applicability of GPR techniques to the problem of levees and dams is still very limited [3, 8]. Determining their state of health in a nondestructive and, possibly, fast way is a critical issue for a number of public bodies and institutions (e.g., civil protection agencies, river basin authorities, etc.).

GPR techniques offer the possibility of quickly investigating large portions of dam interior without the need

of destructive actions. In particular, the paper deals with the surveys, which have been carried out at Acerenza dam, through its longitudinal tunnel inspection, in order to locate underground sandstone layers and banks, potential routes of flow of water below the dam.

These basins create a “complex water system” designed to provide drinking water, irrigation, and industrial use, not only for the Basilicata region, but also neighbouring regions, in particular Puglia and Calabria.

Therefore, the paper is organised as follows: Section 2 presents the hydrological scheme of the Basilicata region; Section 3 deals with the geological background at regional and local scales; Section 4 deals with the diagnostic requirements of the Acerenza dam in the framework of local geology and the GPR survey design. Then, GPR results are presented and discussed in Section 5; finally, in Section 6, conclusions are discussed.

2. Hydrological Setup

Basilicata is one of the few regions of Southern Italy that has a large number of water resources due to the presence of a close hydrographic network [9].

Its water system is based on five main rivers: the Bradano, the Basento, the Cavone, the Agri, and the Sinni. They develop from northwest to southeast, all flowing into the Jonian Sea (Figure 1), and their basins extend over 70% of the regional land. The rest of the region is concerned, to the north, with the basin of the river Ofanto, which flows into the Adriatic Sea, and, to the south and southeast, with the basins of the rivers Sele and Noce, both flowing into the Tyrrhenian Sea. Besides the rivers, there is an extensive network of small waterways and numerous springs.

Described hydrogeographic network is regulated and exploited by great hydraulic works such as dams, crosses, spring and groundwater collectors, supply networks and distribution systems, lifting and water drinkability plants. This infrastructure system was designed and implemented largely in the 50s and 60s, with the main objective to develop and enhance agriculture, then considered as the determining factor for the socioeconomic emancipation of regions Basilicata and Puglia.

In the 70s, the system was expanded and integrated through the construction of new works in order to satisfy the civil needs as well as to potentiate the industrial plants.

The system of dams, built on main rivers of Basilicata region and on their main tributaries, consists of 16 large- and medium-sized river basins, including:

the basins of San Giuliano, Acerenza, Genzano and Basentello on the Bradano;

Pertusillo and Marsico Nuovo basins on the Agri;

Monte Cutugno basin on the Sinni;

Rendina basin on the Ofanto;

Camastra basin on the Basento.

TABLE 1: Primary system of water infrastructure in Basilicata region (modified from [9]).

Basilicata	257 MCM per year (million meters cubes per years)	40%
Puglia	373 MCM per year (million meters cubes per years)	58%
Calabria	10 MCM per year (million meters cubes per years)	2%

These basins create a complex water system that is intended to supply drinking water, irrigation, and industrial and hydroelectric power not only to Basilicata itself, but also to the neighbouring regions, especially to Puglia and Calabria (Table 1).

The system can supply about 5 million inhabitants, 100,000 hectares of cultivated land, and hundreds of industrial companies including one of the most important Italian steelworks such as the Ilva in Taranto, which has 14,000 employees.

In particular, the reservoir of Acerenza, with a capacity of 47 million cubic meters, is part of the water scheme Basento-Bradano, consisting of works of storage (reservoirs and cross) and works of adduction. It is intended for the irrigation of the land underlying the dam of commons Acerenza Oppido and Tolve.

3. Geological Background

The investigated area is located in the northern part of the Bradanic trough, which is a narrow Pliocene-Pleistocene sedimentary basin, with a NW-SE direction, placed between the southern Apennines and the Apulian foreland. This trough is filled by a thick Pliocene-to-Pleistocene sedimentary succession (up to 2-3 km) whose upper part of Late Pliocene(?)-Late Pleistocene in age, widely outcrops in Southern Italy because of the intense quaternary uplift occurred in the area [10].

The neotectonic uplift was driven by the arrival at the subduction hinge of the thick buoyant south adriatic continental lithosphere, which caused a lower penetration rate of the slab and a consequent buckling of the lithosphere [11]. It occurred first in the northern sectors of the trough and after in the southern most ones. Moreover, it was higher in the western edge than in the eastern one, producing then a regional tilting of the geological formations deposited in the Bradanic trough [12, 13] towards the Adriatic Sea.

The progressive uplift is testified by the regressive trend of the sediments deposited in this trough from early Pleistocene, which are represented by the geological formation shown in Figure 2. In particular, Figure 2 depicts, from top to bottom, *Marine-Terraced Deposits* (regressive deposits consisting of sands, conglomerates, and silts of Middle-Upper Pleistocene in age, outcropping in the southern parts), formations of *Sabbie di Monte Marano* and *Conglomerato di Irsina* (sands and conglomerates of Early-Middle Pleistocene in age outcropping in the northernmost and central sectors),



FIGURE 1: Primary system of water infrastructure in Basilicata region (modified from [9]).

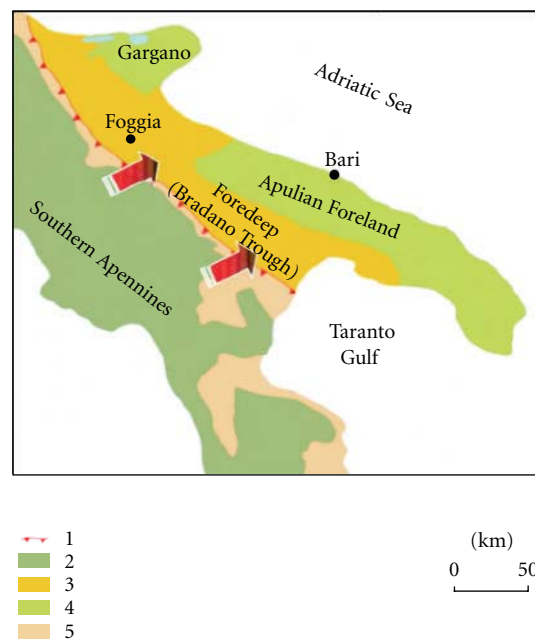


FIGURE 2: Schematic representation of the Southern Italy structural domains. Legend: (1) outcropping buried thrusts front; (2) chain domain; (3) foredeep deposits; (4) calcareous foreland domain; (5) outer thrust-belt front and piggy-back basins (modified from [1]).

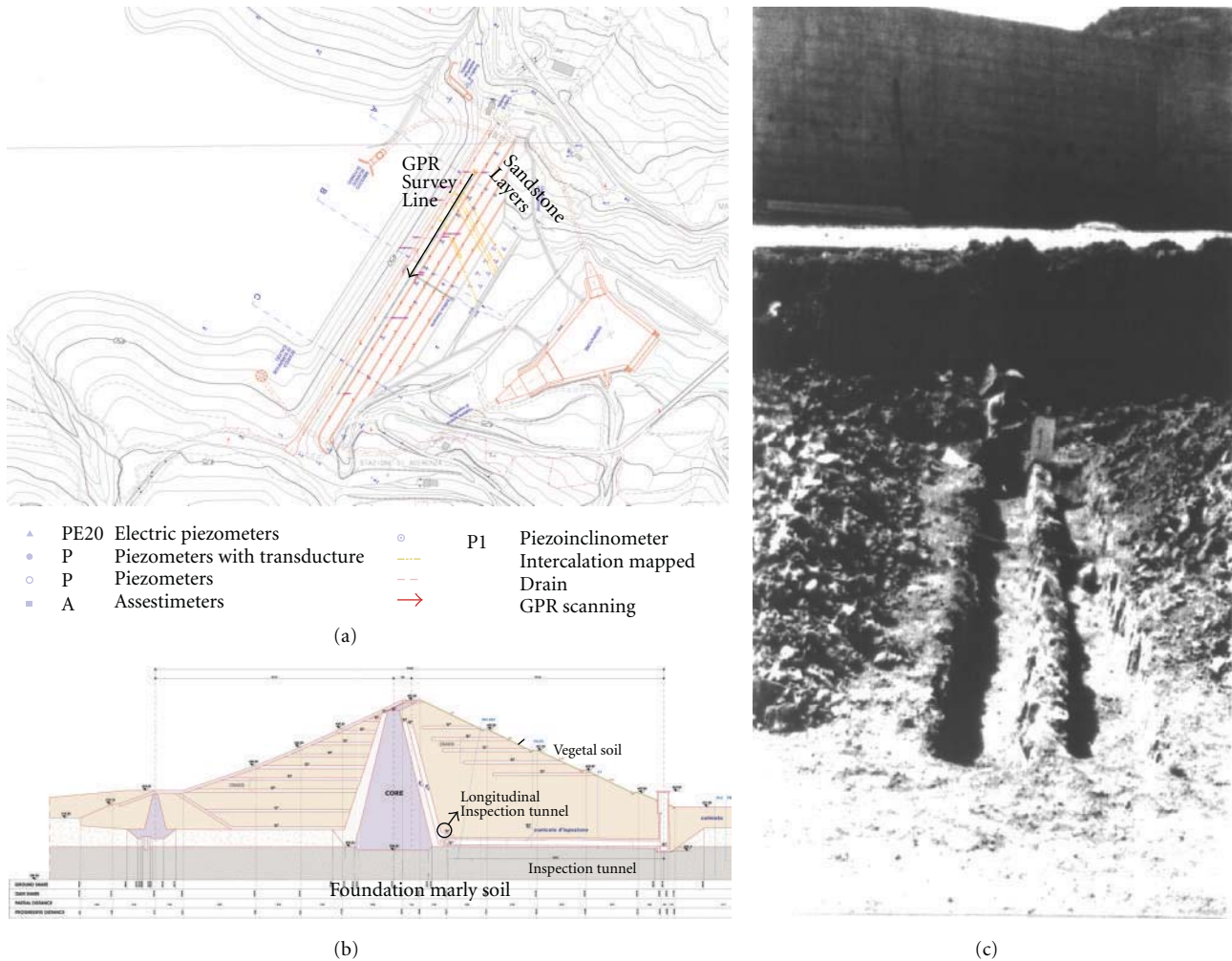


FIGURE 4: Map (a) and cross-section (b) of the zoned-earth Acerenza dam; (c) sandstone layers outcropping after the dam building excavations.

4. Diagnostic Requirements and Survey Design

The Acerenza dam is a zoned-earth embankment dam built on the Bradano river (Figures 1(a) and 1(b)). During its building works (1973–1986), several subvertical sandstone banks and layers belonging to the Serra Palazzo formation directed 60°–70° N in the north-eastern sector of the foundation soil were detected (Figure 1(c)).

Such layers were suspected to be permeable and possible cause of erosion of the dam foundation soil and core. In fact, they were described by the technicians involved in excavation work as strongly fractured and saturated.

Therefore, specific works were designed and carried out in order to waterproof the head of discovered layers, while a series of coring was performed in order to detect other possible arenaceous intercalations. Finally, a piezometric network was installed downstream of the dam in order to detect possible losses.

Such works revealed some inaccuracies in the localization of the permeable layers. Despite of the above said difficulties, the building of the dam continued, but the Italian Dams

Office has imposed a strong limitation on the amount of water that the dam can hold, by limiting the fill quote to 432 m above the level sea from the initial level established at 454.50 m. In order to restore the capacity of the dam to its initial volume, an hydraulic monitoring of the foundation soil was required. In the subsequent years, some piezometers were installed in the foundation soil through the inspection tunnel both in the marly and in the sandstone layers, but without the certainty of placing a piezometer in each permeable layer.

This strong limitation persists until now, since the presence and the exact position of all possible permeable layers in the dam foundation soil are not perfectly known.

Therefore, GPR investigation was requested with the aim of achieving a detailed mapping of permeable layers. In particular, a GPR profile 180 m long has been carried out in the northeastern part of the inspection tunnel by using a 400 MHz central frequency antenna in combination with a GSSI SIR 3000 control unit (Figures 4(a) and 5(a)).

The narrow catwalk allowed to perform just a 2D profile without odometer (Figure 5(b)). Then, the survey line has

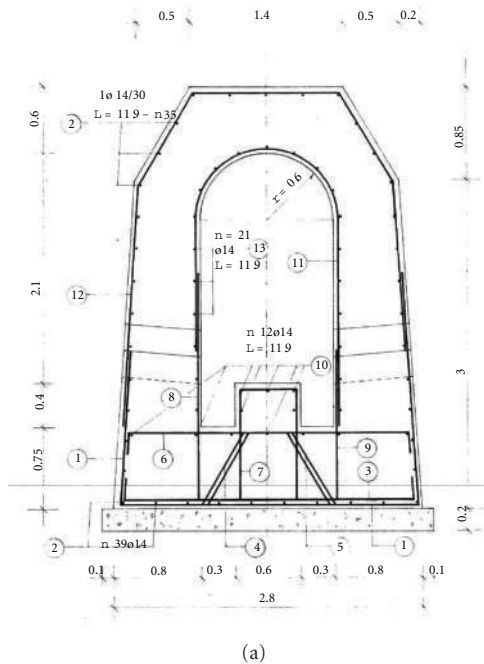


FIGURE 5: Detail of the longitudinal inspection tunnel: (a) cross-section and (b) picture.

been split in several adjoining profiles 20 m long, in order to limit possible marker mispositioning.

During the survey, the position of the existing piezometer along the GPR profile, revealing the position of yet identified sandstone layers, has been annotated in order to check their radar response.

5. Data Processing and Discussion

All radargrams, having a range of 65 ns, have been processed according to the following steps:

- (i) trace removal for removing initial and final traces of the radargram gathered when the antenna is standing,
- (ii) marker interpolation for equalizing the number of traces between markers imputed each meter during the acquisition,
- (iii) dewow, necessary to remove low frequency system-dependent noise,
- (iv) fk-filter, an advanced bandpass filter acting in a frequency-wavenumber domain,
- (v) migration, for improving section resolution and provide more realistic images.

The velocity analysis, carried out by using the hyperbola method, provided an average velocity of 0.1 m/ns.

Figure 6 shows all processed radargrams with the projection of sandstone layers detected during the dam building works (grey arrows and lowercase letters), novel sandstone layer detected on the basis of the GPR interpretation

(black arrows with capital letters), and the positions of the piezometers (bold grey arrows and “Pn” symbol).

Reflectors related to the reinforced concrete structure of the catwalk and inspection tunnel are present in all radargrams. They are highlighted just in the radargram no. 1 of Figure 5. In particular, between 0.0 m and 0.4 m of depth, several reflectors can be related to the structure of the catwalk. Between 0.4 m and 0.8 m, other reflectors can be related to the reinforced concrete structure of the tunnel. Finally, between 0.8 m and 1.0 m reflectors can be related to a thin reinforced concrete plate. Then, geological structures are visible below 1 m depth.

By comparing the sandstone layer positions projected below the inspection tunnel with those derived from the radargram interpretation, it is possible to note that not always they coincide. Moreover, piezometers encountered on the antenna path are perfectly recognizable in the radargrams, and their positions, previously annotated, are perfectly overlapping with their anomaly. Table 2 reports the comparison between the positions of the sandstone layer derived from the projection of direct data with those derived from the radargram interpretation. The table reports the piezometer positions too.

At first glance, GPR allows to detect more sandstone layers than the previous studies detecting just seven zones interested by arenaceous inclusions, mainly concentrated between 20 m and 40 m. Instead, the GPR survey allowed to detect around twenty sandstone layers present along all the antenna path. In particular, between 0 m 20 m three layers have been detected by the GPR against no layers previously known. No piezometers have been installed in this area.

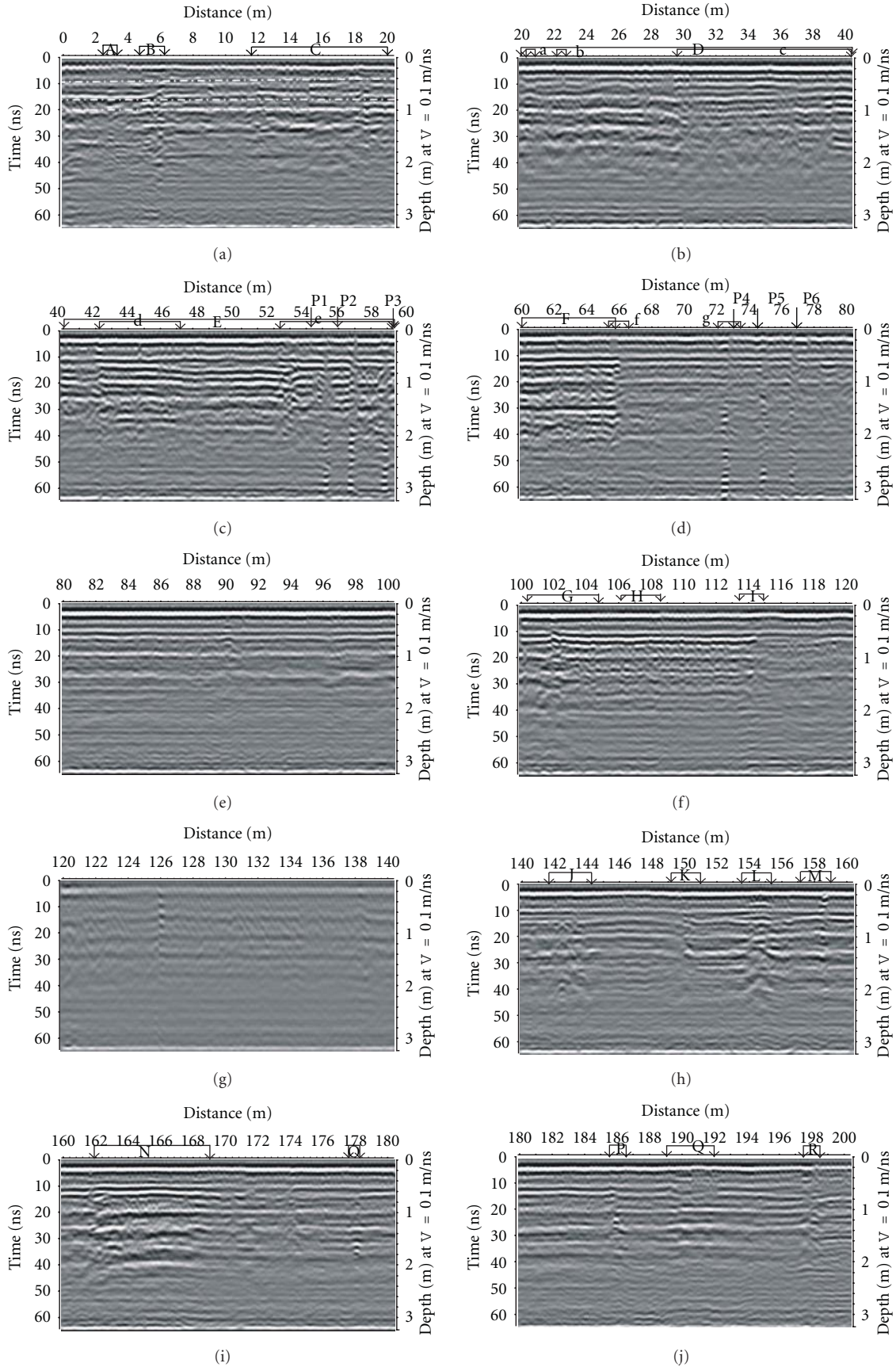


FIGURE 6: Continued.

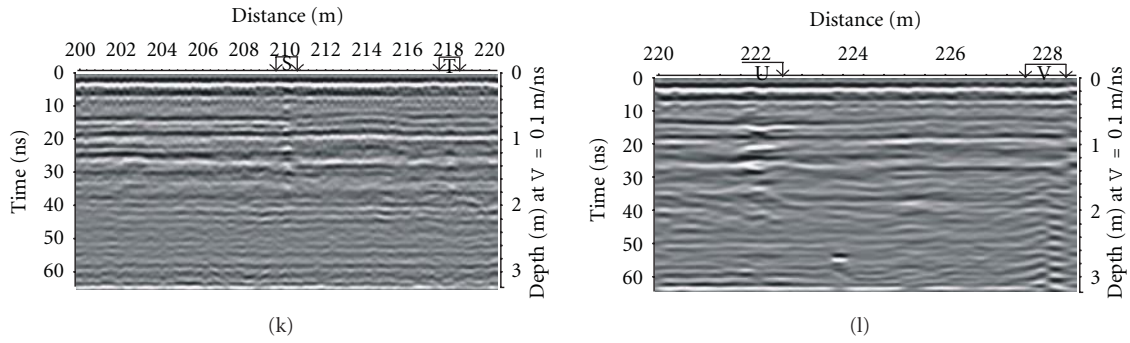


FIGURE 6: Processed radargrams covering the northeastern part of the inspection tunnel.

TABLE 2: Positions of the sandstone layers derived from the dam building excavations and from the GPR survey compared with position of the piezometers.

Sandstone layers projected positions	Start (m)	End (m)	Sandstone layer positions derived from GPR	Start (m)	End (m)	Piezometer	Position (m)
			A	2.4	2.6		
			B	4.4	6.1		
			C	11.5	20.0		
a	20.3	20.8					
b	22.1	22.3	D	20.0	40.0		
c	29.5	40.0					
d	42.1	47.0				P1	55.90
			E	40.0	60.0	P2	57.80
e	53.0	60.0				P3	59.65
f	65.2	66.4	F	60	65.6		
g	72.0	73.6				P4	72.35
						P5	74.55
						P6	76.30
			G	100.4	104.7		
			H	106.0	108.4		
			I	113.2	114.7		
			J	141.7	144.3		
			K	149.1	160.8		
			L	153.3	155.2		
			M	156.5	158.7		
			N	161.9	168.9		
			O	177.3	178.0		
			P	185.5	186.5		
			Q	189.0	191.8		
			R	197.2	198.2		
			S	209.5	210.4		
			T	217.2	218.3		
			U	221.7	222.5		
			V	227.5	228.3		

The zone between 20 m and 65 m has been interpreted as potentially rich in sandstone layer in agreement with previous studies. However, spatial resolution available in the band frequency used does not allow to distinguish each layer. However, piezometers P1, P2, and P3 installed in this area certainly indicate sandstone layers.

In the following part of the radargram some differences can be noted. In fact, previous studies report just the layer (g) where the piezometer P4 has been installed. Moreover, GPR survey confirmed that piezometers P5 and P6 have been installed outside any sandstone layer, in the marly soil. Finally, GPR survey gives its main contribution further on 100 m to the end of the antenna path where twelve zones hosting sandstone layers can be inferred by the radargram interpretation.

6. Conclusions

In this paper, we described a 2D GPR survey carried out at Acerenza dam in attempt to detect all possible fractured sandstone layers under the embankment, potential way of water loss, and consequent damage for the structure.

The GPR techniques, carried out in the northerneast part of the inspection tunnel, revealed very useful in the handled case, since it allowed to confirm the presence of previously known sandstone layers and to detect further ones. In fact, along a big section of the surveyed inspection tunnel several unknown sandstone layers have been detected. Moreover, by comparing sandstone layer positions with piezometers ones, it is possible to select more suitable holes for hydraulic tests and plan further corings. This experience demonstrates that the GPR can be a useful tool for dams' nonintrusive diagnostic encouraging its use for other typologies of defects affecting the dams such as: waterproof layer fractures and detachment and concentrated water infiltration zones. Main encountered limitation is that not always the spatial resolution has been adequate to resolve each sandstone layer, so that just large sections potentially hosting searched layer have been detected. A possible solution in order to overcome this limitation could be the use of novel data processing approach such as tomographic approaches.

Acknowledgment

The research leading to these results has received funding from the European Community's Seventh Framework Programme (FP7/2007-2013) under Grant Agreement n° 225663 Joint Call FP7-ICT-SEC-2007-1.

References

- [1] M. Lazzari, "Tectonic and sedimentary behaviour of the Bradanic Foredeep basin during Early Pleistocene," *Memorie descrizione Carta Geologica d'Italia*, vol. 77, pp. 61–76, 2008.
- [2] M. Labriola, V. Onofrio, S. Gallicchio, and M. Tropeano, "Stratigraphic and structural features of the frontal sector of the Lucanian Apennines between Acerenza and Oppido Lucano (Potenza, Basilicata)," *Memorie descrizione Carta Geologica d'Italia*, vol. 77, pp. 111–118, 2008.
- [3] M. Di Prinzio, M. Bittelli, A. Castellarin, and P. R. Pisa, "Application of GPR to the monitoring of river embankments," *Journal of Applied Geophysics*, vol. 71, no. 2-3, pp. 53–61, 2010.
- [4] J. Hugenschmidt and R. Mastrangelo, "GPR inspection of concrete bridges," *Cement and Concrete Composites*, vol. 28, no. 4, pp. 384–392, 2006.
- [5] V. Lapenna, M. Bavusi, A. Loperte, F. Soldovieri, and C. Moroni, "Ground Penetrating Radar and Microwave Tomography for high resolution post-earthquake damage assessment of a public building in L'Aquila City (Abruzzo Region, Italy)," in *Proceedings of the AGU Fall Meeting*, San Francisco, Calif, USA, December 2009.
- [6] M. Bavusi, F. Soldovieri, S. Piscitelli, A. Loperte, F. Vallianatos, and P. Soupios, "Ground-penetrating radar and microwave tomography to evaluate the crack and joint geometry in historical buildings: some examples from Chania, Crete, Greece," *Near Surface Geophysics*, vol. 8, pp. 377–387, 2010.
- [7] J. Hugenschmidt, A. Kalogeropoulos, F. Soldovieri, and G. Prisco, "Processing strategies for high-resolution GPR concrete inspections," *NDT and E International*, vol. 43, no. 4, pp. 334–342, 2010.
- [8] X. Xu, Q. Zeng, D. Li, J. Wu, X. Wu, and J. Shen, "GPR detection of several common subsurface Cooids inside dikes and dams," *Engineering Geology*, vol. 111, no. 1–4, pp. 31–42, 2010.
- [9] M. Vita, M. Gerardi, and G. Lo Vecchio, "La gestione della risorsa idrica in Basilicata," *Geologia Territorio e Ambiente*, vol. 16, pp. 10–16, 2010.
- [10] N. Ciaranfi, M. Maggiore, P. Pieri, L. Rapisardi, G. Ricchetti, and N. Walsh, "Considerazioni sulla neotettonica della Fossa Bradanica," *Progetto Finalizzato Geodinamica del CNR*, vol. 251, pp. 73–95, 1979.
- [11] C. Doglioni, M. Tropeano, F. Mongelli, and P. Pieri, "Middle-Late Pleistocene uplift of Puglia: an "anomaly" in the Apenninic foreland," *Memorie Società Geologica Italiana*, vol. 52, pp. 457–468, 1996.
- [12] N. Ciaranfi, F. Ghisetti, M. Guida et al., "Carta Neotettonica dell'Italia meridionale," *Progetto Finalizzato Geodinamica del CNR*, no. 515, 1983.
- [13] M. Tropeano, L. Sabato, and P. Pieri, "Filling and cannibalization of a foredeep: the Bradanic Trough, southern Italy," in *Sediment Flux to Basins: Causes, Controls and Consequences*, S. J. Jones and L. E. Frostick, Eds., vol. 191, pp. 55–79, Geological Society of London, Special Publications, London, UK, 2002.

Research Article

From Geophysics to Microgeophysics for Engineering and Cultural Heritage

P. L. Cosentino, P. Capizzi, R. Martorana, P. Messina, and S. Schiavone

Dipartimento delle Scienze della Terra e del Mare, University of Palermo, 90123 Palermo, Italy

Correspondence should be addressed to P. L. Cosentino, pietro.cosentino@unipa.it

Received 16 February 2011; Accepted 25 March 2011

Academic Editor: Francesco Soldovieri

Copyright © 2011 P. L. Cosentino et al. This is an open access article distributed under the Creative Commons Attribution License, which permits unrestricted use, distribution, and reproduction in any medium, provided the original work is properly cited.

The methodologies of microgeophysics have been derived from the geophysical ones, for the sake of solving specific diagnostic and/or monitoring problems regarding civil engineering and cultural heritage studies. Generally, the investigations are carried out using different 2D and 3D tomographic approaches as well as different energy sources: sonic and ultrasonic waves, electromagnetic (inductive and impulsive) sources, electric potential fields, and infrared emission. Many efforts have been made to modify instruments and procedures in order to improve the resolution of the surveys as well as to significantly reduce the time of the measurements without any loss of information. This last point has been achieved by using multichannel systems. Finally, some applications are presented, and the results seem to be very promising and promote this new branch of geophysics. Therefore, these methodologies can be used even more to diagnose, monitor, and safeguard not only engineering buildings and/or large structures, but also ancient monuments and cultural artifacts, such as pottery, statues, and so forth.

1. Introduction

Microgeophysics is one of most recent branches of geophysics. It includes a lot of methodologies derived from geophysics and it is applied, with more or less miniaturized instrumentations, to small volumes of soil or masonry, as well as to simple artifacts such as statues, pottery, corbels, and so forth.

At the beginnings of the 90s, little by little microgeophysics was born following the miniaturization of geophysical instrumentation, in particular transducers both transmitter and receivers, so that they could be adapted to small-scale and very small-scale applications.

Indeed, the very first attempts of miniaturization were carried out in the 1950s, when many researchers were used to build physical models on a small scale (e.g., [1–3]) to evaluate the possibilities offered by some new geophysical methods or to test the results obtained by the standard methodologies on particular not simple soil models [4]. In fact, at that time personal computers had still not been developed, so a lot of the problems encountered in the field of applied geophysics were simply solved by using physical

models on a small scale rather than mathematical models. Such physical models were often built in appropriate tanks using various kind of materials (see, for instance, [5]), either natural or not. In some rare cases, the models were made in small pieces of subsoil suitably prepared. But, these kinds of studies did not allow researchers to obtain models with high-resolution details, thereby necessitating a great deal of additional investigation over the years. However, this in turn contributed to the advancement of the investigation and physical tests on small structures and objects, certainly promoting the birth of this new branch of geophysics.

Furthermore, the advent of digitalization and the development of effective a/d converters stimulated both the simultaneous sampling of a large number of channels (i.e., the manufacture of multichannel instruments) and speeding up processing and interpretation of the acquired data by means of computers driven by appropriate software programs.

However, microgeophysics is an expanding branch: major demands come from conservation and restoration in the fields of civil engineering and management of ancient monuments and cultural heritage artifacts, the science of materials being also a growing source of incentives and

suggestions. This is especially true as far as works of art are concerned, where the choice of methodology has been greatly influenced by the noninvasive characteristics of the methodologies of microgeophysics. In fact, microscopic methodologies that damage very small volumes provide a lot of information, but may turn out not to be representative of large volumes of the investigated artifact, whereas geotechnical macroscopic methodologies involving large volumes are generally more or less destructive.

As a matter of fact, over the last 30 years many different types of investigation have been implemented, often derived from other fields of study, for instance, the electrical resistivity tomography for stone columns, which in turn derives from medical diagnostics.

Microgeophysics noninvasive methods can be used in situ and are characterized by an resolution power that can be defined between “microscopic” and “macroscopic” investigations, ranging from a few centimeters to a few decimeters: such a resolution can be very useful for artifacts having dimensions from a few cubic decimeters to a few cubic meters. Therefore, the miniaturization of the methods of applied geophysics can well cover these kinds of small-sized targets (artifacts, columns, pillars, pottery, statues, museum objects, etc.), provided that investigations are integrated with other specific methodologies to evaluate particular physical and chemical aspects, sometimes also including the biological ones.

Even though there are not yet basic key papers on Microgeophysics but only papers regarding particular methodologies and/or case histories (some of them are included in the reference list), the involved methodologies are often applied to structures of civil engineering, ancient monuments, and cultural heritage items. The word “geo” is still present even though the investigated targets are not only sculptured rocks, but also include metallic, vitreous, ceramic, and even wooden artifacts. The main peculiarity of these investigations, compared with those of classical applied geophysics, is that the objects to be inspected generally offer more than one face, which can be looked into by injecting the necessary energy and by positioning the required external and/or internal probes in every point of the object. Therefore, they generally give better results if compared with those offered by classical geophysical investigations, which lose in resolution when the investigated depth increases.

2. Technical Problems

One of the main technical problems encountered by microgeophysics is related to the miniaturization of all the transducers, both transmitters and receivers. Obviously, there are some important differences regarding the methodology to be used, that is, potential fields (principally the electric fields) or wave fields, either mechanical or electromagnetic.

A normal assumption of geophysics is that both, transmitters and receivers, are punctiform with respect to the geometrical parameters of the model used. As in microgeophysics the models are undoubtedly small-sized with respect to those of geophysics, it is still harder to consider punctiform



FIGURE 1: Sandbags on the ECG electrodes (used only for potential measures) on the floor of the Ambulatory of the great hunt at the “Villa del Casale,” Piazza Armerina [30].

normal geophysical sources and probes, like geophones, hammers, steel pegs, GPR antennas, and so forth.

The problem has been faced in many ways, and different solutions have been studied to replace sources and probes with other small-sized ones.

The steel pegs having a length of 40–60 cm, normally used for geoelectrical survey, have been replaced by small steel nails (6–8 cm in length, 1.5–2 mm in diameter) and, where it is possible, by disposable electrocardiogram (ECG) electrodes (with a diameter of about 1 cm but with no extension in penetration inside the artifact) provided with external adhesive strips. The inconveniences of the ECG electrodes are two: (1) if they have to be put in roughly vertical or upside down positions (i.e., walls, columns, ceilings, etc.) the adhesion to the artifact is very critical or impossible, depending on the conditions of the surface of the artifact and (2) the contact resistance is rather high (higher than few $M\Omega$) and it is generally changing in time during some hours, that is the time that generally is necessary to place them on the wall—or floor or body—to be studied. This time can be up to 100 to 150 min, depending upon the number of electrodes and the type of object being studied. The final typical values of contact impedances range from 0.1 to 100 $M\Omega$ depending on the investigated lithotype and the treatment of its exposed surface. Obviously, these high contact impedances have to be suitably reduced in the current electrodes in order to inject an appropriate current intensity.

A lot of enterprises around the world produce these kinds of electrodes, but of the ones we tested the best we selected are those in Foam Ag/AgCl (adult-type F 9047 manufactured by FIAB). The main advantage of these electrodes consists in the relative time stability of their contact resistance: in fact, it is very important that the contact resistances remain more or less stable for the period of positioning all the set of electrodes in the artifact; otherwise, the electrodes would have contact resistance very different the one from the other, in such way inserting different errors in the electric potential measures. Unfortunately, large currents through these electrodes can burn them, so that it is sake to avoid to use them as current electrodes. Sometimes, when they have to be put on the floor (or on a horizontal surface), the adhesive stripes can be removed and a sandbag can be used as a weight to assure the contact (Figure 1). Alternatively, flat electrodes can be successfully used [6].

The geophones have been replaced by small or very small piezoelectric accelerometers, today very popular, which are



FIGURE 2: One transmitter and two ultrasonic receivers on the statue of Togato di Petrarà (2nd century A.D.) [31].



FIGURE 3: Transmitting and receiving GPR antennas (IDS, 1600 MHz) on the statue of S. Michele Arcangelo (Gagini's apprentices, 1530-50), at the Museum Abatellis, Palermo Italy [32].

also contained in many smartphones. Typical accelerometers have a shape similar to a thin drop with diameter about 1 cm, so that the correct positioning in microgeophysical survey can be considered reliable enough. The ones we selected for quality-to-price ratio are manufactured by Japanese Murata & Co (namely, type 6CC-10-3R9-1000). They have been successfully tested and used in many professional and research works. However, many other piezoelectric seismometers are manufactured around the world and are available on the world market (e.g., Kistler, STMicroelectronics, SensComp, etc.).

Generally, ultrasonic transducers (both, transmitters and receivers) are rather large (diameter about 3–6 cm, height about 4–8 cm). For microgeophysics surveys, it is a good rule to use cone-shaped extensions in order to considerably reduce the contact surface so improving the precision of the positioning (Figure 2).

As far as the GPR probes concerned, we can say that it is still a problem to handle the probes for microgeophysical surveys. In fact, the antennas manufactured and available are still too large, especially those which are in combined (transmitter-receiver) box (they are most of the commercial ones). Even those which are arranged in separated box (we use that manufactured by IDS, Italy, Figure 3) are rather large in size, because the boxes generally contain the electronics, too. However, the positioning of these antennas is more precise than the combined ones, where two dipoles are present.

Hopefully, in the future new separated antennas with an only shielded dipole connected by a semirigid cable with an easily handy box will be manufactured by Enterprises which will be heedful to this market segment.

Today, the multichannel instruments are being improved all over the world, increasing the sampling rate (higher sampling frequencies) and avoiding large multiplexing so to have a real simultaneous acquisition of all the channels. In particular, this should be made for microgeophysical instruments, for which the very short times to be measured impose larger and larger sampling rate.

3. Resolution

Resolution is one of the most important parameter of the tomographic approach. It should be faced very carefully, as it is primarily determined in the first phase of the survey, that is, the acquisition. In fact, the number and space density of the acquired data, both in potential field and in wave field tomography, are the main parameters can limit the maximum obtainable resolution.

It is important to remind the main differences of using energy sources given by potential fields, where geophysical responses are prevalently given by the investigated earth volumes, or by wave fields, where geophysical responses are prevalently given by the reflecting, refracting, and diffracting surfaces that separate different parts of the interior of the investigated artifacts. According to this important difference, body parameters are involved in the first case and surface-parameters are at stake in the second one. These differences heavily affect the tomographic approach, as the potential field tomography originates from an inversion of contributions given by volume units, while wave field tomography is based on the analysis and reconstruction of ray paths of the waves traveling into the investigated volume. However, in both cases tomography is carried out keeping a particular prearranged order among the places of the transmitting and receiving probes. Commonly, the number of transmitting and receiving probes is equal, leading to nearly-symmetrical arrangements. But sometimes the number of transmitting and receiving probes is different, especially in sonic and ultrasonic tomography, where transmitting and receiving probes are very alike and separated, so that for each ray they can be exchanged each other without any difference in the results.

In some cases, especially in ERT survey, places of transmitting and receiving probes are constrained by a particular kind of array which has been selected for acquisition. In particular, we would recommend the use of the MYG array [7] using a lot of receiving probes and few transmitting ones (without any precise geometrical constrain), especially for cases in which surfaces are vulnerable, then avoiding the employment of many nails because, although they are small, they can damage the surface.

When wave fields are concerned, another parameter can limit the resolution, that is, the frequency for the waves used, as in turn it is responsible of wave diffractions and consequent loss of energy. Therefore, higher resolution required by microgeophysics generally demands the use of higher frequencies, in spite of the smaller waves' penetration depth. A compromise, if possible, should be made between the increase in the resolution and the decrease in the penetration depth. On the contrary, if lower frequencies are

to be used to obtain a higher penetration depth, diffracted waves can be used to study small targets; however, the analysis of diffracted waves is complicated and represents an emerging field of microgeophysics.

However, the resolution attainable using a rich set of experimental data should be maintained with an appropriate inversion in order to obtain the final tomographic restitution both in a 2D or 3D model.

The preliminary choice of any inversion is the geometrical arrangement of the pixels (2D) or voxels (3D): it depends on many parameters and, primarily, on those already mentioned linked to the acquisition array. These parameters are essential in potential methods, like ERT, but they should be combined with the physical discriminating power of the used methodology.

In potential field methodologies this power is limited by the “distance” of the objects from the observation instruments (transmitters and receivers generally located on the surfaces), so that the distinguishable voxels (3D) or pixels (2D) should be larger and larger when the distance (depth) increases.

In wave field methodologies (sonic, ultrasonic, and GPR), the discriminating power is limited by the “frequency” of the waves arriving to the detecting probes (i.e., the used frequencies, as filtered by the investigated sample). The frequencies should be obviously transformed in wavelengths taking into account the velocity of the waves. The wavelength allows us to calculate the Fresnel zone radius and consequently the discriminating power (namely, the lateral resolution r) at various distances, following Cerveny and Soares [8], as

$$r = \left[L \frac{\lambda}{2} + \left(\frac{\lambda}{4} \right)^2 \right]^{1/2}, \quad (1)$$

where L being the ray length and λ the wavelength calculated using $\lambda = v/f$, v is the velocity of the wave, and f is the frequency.

In sonic survey, a pulse is generally used as energy source, and therefore its spectral content is practically very large (depending on the hammer used), going to very high frequencies. On the contrary, in both electromagnetic GPR and ultrasonic survey, a single frequency source is used: but, this frequency, which is also characteristic of the used transducer, is modulated by a squared shape pulse, producing a signal characterized by a large band. In this way in all the waves field methodologies we are able to send signals characterized by very high frequencies, which in turn will be subjected to the cruel attenuation law smoothing higher frequencies much more than the lower ones. However, we have to consider, when we keep the first arrival of the signals, the frequencies contained in the first rises of the arrivals, that is we have to look at the steep slope of the first arrivals. Our experience is that this part of the signals contains very high frequencies; anyhow, the maximum contained frequency of the signals decreases when the distances increase.

By the light of the above line of reasoning, in order to evaluate the lateral resolution we should use as frequency

f in (1) the maximum frequency retrieved in the picking of the first arrivals to the detecting probes, which are the real information sources in order to obtain a velocity tomography. Such maximum frequencies are generally much higher than the nonmodulated monochromatic frequency of the transmitter. However, these maximum frequencies also depend on the sampling rate, following the well known sampling rule given by the Nyquist-Shannon sampling theorem [9, 10].

4. Some Case Histories

A few cases histories regarding ERT, ultrasonic, and GPR tomography are reported in order to discuss the applications of such simple rules we presented in the previous paragraphs.

4.1. Electrical Resistivity Tomography. An example of “full-3D” electrical resistivity tomography carried out on a wall is here presented. The aim was to understand the cause of moisture on a wall of the fountain room of the Zisa Palace (Palermo, XII century A.D., Figure 4(a)), covered by a precious mosaic interested by an important detachment of tesserae (Figure 4(b)). Therefore, we placed a regular grid of 11×16 adhesive electrodes, covering an area of 2 m high and 3 m wide. In order to assure a very low impact on the mosaic structure, only 15 nails electrodes were used for the current injection, driven into very small holes (2 mm of diameter) drilled in the interstices among the mosaic tesserae.

For each current injection, 176 potential measurements were acquired simultaneously with the MRS256 instrument (GF Instruments), between each electrode of the acquiring grid and a reference electrode (for an amount of 38 different current dipoles). In this way, the set of 6688 experimental data is very flexible, so to allow any calculation of potential difference between any of the possible electrode couples of the grid.

Then, the apparent resistivity values were calculated selecting the potential dipoles as close as possible to the hypothetical current lines in the medium, using the Maximum Yield Grid methodology [7, 11]. 1769 data have been considered as outliers and 4919 data have been processed using Res3D inv software [12].

The geometrical model was made by ten layers with 6000 voxels (10×10 cm in each layer). The layer thicknesses increase with the depth from 0.05 m (1st layer) to about 0.12 m (10th layer) following the decrement of resolution with depth.

The resulting tomographic inverted model of resistivity distribution (Figure 4(c)) presents a large volume characterized by low resistivity values, that seems to be originated in the middle of the wall, in correspondence with the water-pipe of the fountain. The conductive anomaly has been interpreted (as successively confirmed by a direct inspection) as a accumulation point of water inside the masonry, now clogged towards the fountain. The deep high resistivity volumes surrounding the accumulation point could be explained by the difference between the two exposed sides of the wall: the internal surface is covered by the mosaic that

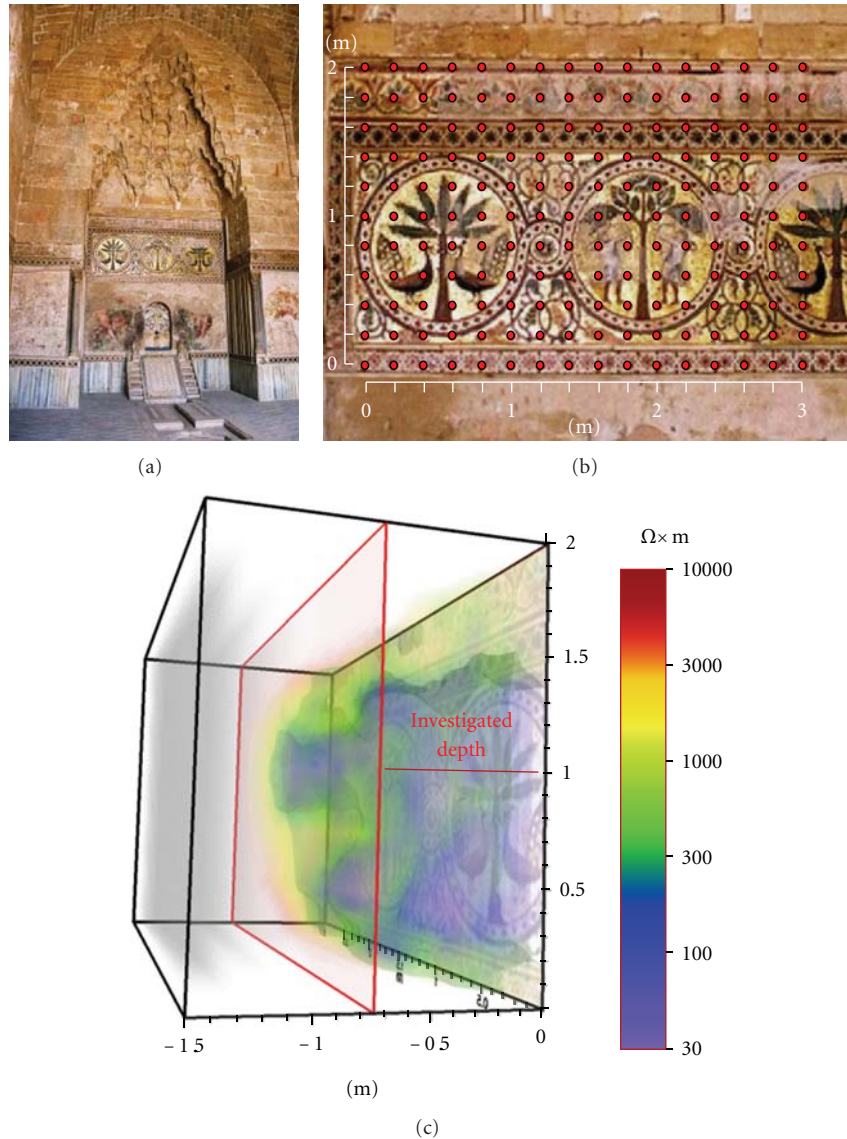


FIGURE 4: (a) Frontal wall of the Fountain Room of the Arabian Zisa Palace in Palermo; (b) part of the investigated mosaic wall where the grid of 176 potential electrodes was applied (red points). The 15 nails used to inject the current were inserted in as many selected points along the small, mortar-filled spaces between the tesserae of the mosaic; (c) 3D inversion model of the acquired data observed from the back of the wall (1.5 m thick). Due to the size of the grid used (2 m \times 3 m), the inversion model is limited to 0.75 m of depth. All dimensions are in meters (after [4], modified).

obstructs the moisture evaporation while the external one is not only mosaic free but also exposed to winds and sun (i.e., it is characterized by high drying capacity). It is evident how this substantially noninvasive investigation solved a serious restoration problem.

4.2. Ultrasonic Survey. Ultrasonic tomography for non-destructive tests and for characterization of artefacts has been applied in many case with good results [13–17]. In particular, 3D ultrasonic tomography has been recently used to study the structural continuity of the material [18–20].

We relate about the ultrasonic tomography carried out on the bust of Eleonora d’Aragona (sculptured by F. Laurana,

1468, Figure 5(a)), which is a beautiful work of art, finely carved from a block of white and microcrystalline marble. It is shown on the original support designed by the architect Carlo Scarpa in the 60s.

The cleanup of the sculpture has revealed a fracture that probably originated on a natural veining of the marble block in the central portion of the neck, involving the whole face of the lady. To better understand the nature of this feature, a 3D ultrasonic tomography, obtained from 157 measurement points identified along the surface of the work, was performed [21]. The measure points were spaced 2–5 cm, so that 1832 signals corresponding to as many paths were acquired using the TDAS 16 Boviar multichannel

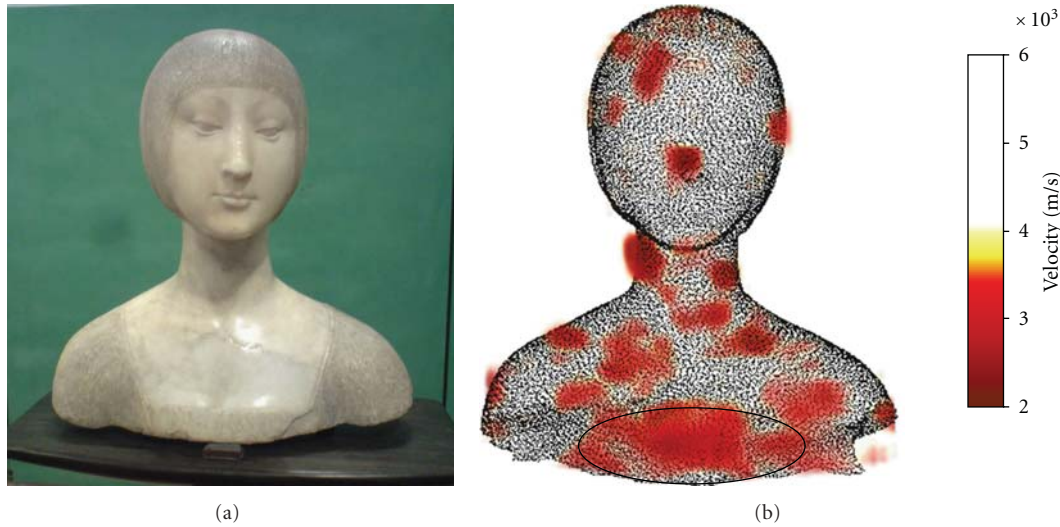


FIGURE 5: At left the bust of Eleonora d'Aragona (F. Laurana, 1468). At right the frontal 3D image with transparency of the investigated volume showing an area at low velocity, corresponding to the support point of the bust [21].

system, which acquires up to 16 channels using an electronic switch on four channels at a time with a maximum sampling rate of 1.25 MHz. The equipment is supplied with receiver and transmitter probes characterized by a central frequency of 55 kHz. 64 signals were discarded because considered outliers, while 1768 of these were processed. A comparison between results obtained using different cell dimensions were carried out and finally we decided to use a $1 \times 1 \times 1 \text{ cm}^3$ cell size for inversion process (Figure 5), performed with GeoTomCG software which performs inversions with the simultaneous iterative reconstruction technique (SIRT, [22]). Curved ray tracing was used with a revised form of ray bending, derived from the method given by Um and Thurber [23].

The model does not show significant discrepancies at the lesion on the face of the lady. Also the upper torso (head and neck) shows velocity values corresponding to a sufficiently homogeneous and well-preserved marble. However, the velocity model shows low values in the lower front portion of the trunk at the breast, according to the traveltime graph analysis.

This area bears the entire weight of the work; that is why the architect Carlo Scarpa designed the original support.

Even in this case, the noninvasive tomographic investigation solved a serious doubt raised by the restorers and our beautiful lady Eleonora continued travelling in the Museums all over the world.

4.3. GPR Surveys Integrated with Ultrasonic Tomography. The large size of the GPR antennas does not allow up to now a resolution similar to that of ultrasonic and ERT tomographies, especially when irregular surfaces are concerned. Therefore, GPR surveys are generally integrated with ultrasonic and/or electrical tomographies, substantially improving the obtained results. One of these cases is here discussed.

The archaeological Museum of Rome asked our group to inquire into the physical consistency of a marble slab (II-III century AD) that has recently fallen down during its travel for being part of an exhibition. We decided to use different methodologies to investigate the slab: namely, a pacometer (Protovale Elcometer) to individuate internal coupling pins, GPR (2000 MHz), and Ultrasonic (55 kHz) tomographic high-density surveys to investigate the internal extension of all the visible fractures and to search for the hidden ones.

4.3.1. Ultrasonic Tomography. The acquisition was realized using 65 measurement points, 40 distributed on the thickness of the slab side and 25 on the relief. The distance between two consecutive probe positions was set to 100 mm, for measurement points distributed on the external thickness of the slab side. Ultrasonic measures were carried out using the TDAS 16 Boviar multichannel system, which acquires up to 16 channels using an electronic switch on four channels at a time with a maximum sampling rate of 1.25 MHz. The equipment is supplied with receiver and transmitter probes characterized by a central frequency of 55 kHz.

A total of 961 signals were acquired and processed, on which the traveltimes of elastic waves were measured by picking procedures. Inversion process were carried out using $2 \times 2 \times 2 \text{ cm}^3$ cell size, with GeoTomCG software and curved ray tracing [23].

A total of 961 signals were acquired and processed, on which the traveltimes of elastic waves were measured by picking procedures.

The tomographic model (Figure 6) shows velocity values with a minimum of about 1500 m/s and a maximum of about 5000 m/s (that is probably the velocity of the original marble). This lack of homogeneity and the presence of low velocity values suggest that the state of the marble is poor, especially in correspondence of the injury of the slab

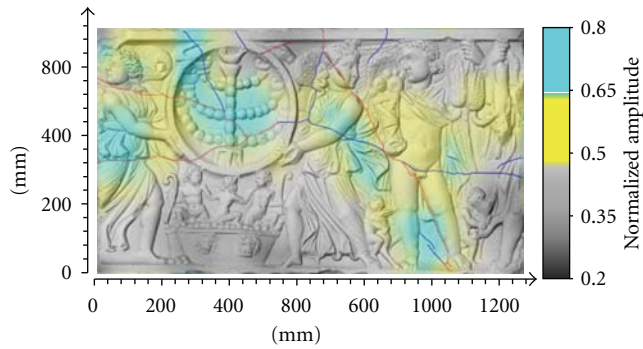


FIGURE 6: Smoothed 2D tomographic section, using $2 \times 2 \text{ cm}^2$ cell dimension, superimposed to slab image.

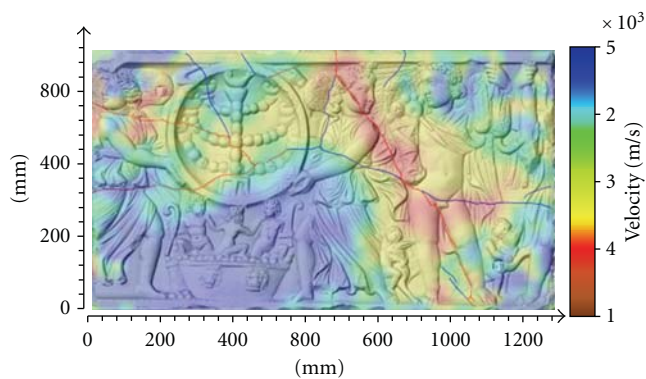


FIGURE 7: GPR tomography superimposed to slab image.

(recent or not) as evidenced by the superimposition of a tomographic ultrasonic image on the relief of the slab.

4.3.2. GPR Surveys. GPR method used to detect small discontinuities is not simple, but several studies have been carried out to locate subsurfaces fractures and all of them showed that GPR can give good results [17, 24–29].

GPR surveys to the roman marble slab were carried out using the Aladdin system (IDS), with a 2 GHz bipolar antenna. Considering the direction of the maximum elongation of the slab, 12 longitudinal and 7 transverse profiles were acquired. This configuration allowed us to obtain a good sampling of the data, achieving tomographic images with high detail.

GPR processed data were used to construct depthslices which were calculated with our procedure implemented in Matlab environment. The appropriate analysis window was chosen depending on the shape, size, and location of anomalies detected with ultrasonic surveys. In particular, we chose an analysis window of 0.25 ns along the time axis and 0.05 m along the distance axis. The depthslice presented in Figure 7 corresponds to the central depth of the slab. The scale of the amplitudes in the presented map was normalized to the maximum value recorded.

Even radar tomography shows a strong correlation with observable cracks in the slab, and therefore also with ultrasonic tomography. The detected anomalies correspond

to changes in em properties of the material as well as to metallic elements of reinforcement.

As regards the results given to the Museum, we affirmed that the slab was in very bad condition, having reduced physical-mechanical characteristics. The falling of the marble slab caused a weakening of the marble and a deterioration of its mechanical properties: beside the existing lesions, the development of new lesions practically covered the whole slab. The damage caused to the material was not easily remediable because the characteristics of the material cannot be reconstructed before undergoing such a trauma. The restorers proceeded to plan a steel containment belt, with reversible support, in order to raise the slab and let the artwork be admired both from the front side and the back one. Successively, a suitable consolidation project has been planned to reinforce the whole marble structure.

References

- [1] A. Apparao, "Model tank experiments on resolution of resistivity anomalies obtained over buried conducting dykes—inline and broadside profiling," *Geophysical Prospecting*, vol. 27, no. 4, pp. 835–847, 1979.
- [2] A. Apparao, A. Roy, and K. Mallick, "Resistivity model experiments," *Geoexploration*, vol. 7, no. 1, pp. 45–54, 1969.
- [3] A. Apparao and A. Roy, "Resistivity model experiments-II," *Geoexploration*, vol. 9, no. 4, pp. 195–205, 1971.
- [4] P. L. Cosentino, P. Capizzi, G. Fiandaca, R. Martorana, and P. Messina, "Advances in microgeophysics for engineering and cultural heritage," *Journal of Earth Science*, vol. 20, no. 3, pp. 626–639, 2009.
- [5] W. Goudswaard, "On the effect of the tank wall material in geoelectrical model experiments," *Geophysical Prospecting*, vol. 5, no. 3, pp. 272–281, 1957.
- [6] E. N. Athanasiou, P. I. Tsourlos, G. N. Vargemezis, C. B. Papazachos, and G. N. Tsokas, "Non-destructive DC resistivity surveying using flat-base electrodes," *Near Surface Geophysics*, vol. 5, no. 4, pp. 263–272, 2007.
- [7] G. Fiandaca, R. Martorana, P. Messina, and P. L. Cosentino, "The MYG methodology to carry out 3D electrical resistivity tomography on media covered by vulnerable surfaces of artistic value," *Il Nuovo Cimento B*, vol. 125, no. 5-6, pp. 711–718, 2010.
- [8] V. Cerveny and J. E. P. Soares, "Fresnel volume ray tracing," *Geophysics*, vol. 57, no. 7, pp. 902–915, 1992.
- [9] U. Grenander, *Probability and Statistics, Harald Cramér Volume*, Almquist & Wiksell, 1959.
- [10] H. L. Stiltz, *Aerospace Telemetry*, Prentice-Hall, New York, NY, USA, 1961.
- [11] G. Fiandaca, R. Martorana, P. Messina, and P. L. Cosentino, "3D ERT for the study of an ancient wall covered by precious mosaics," in *Proceedings of the Near Surface 15th European Meeting of Environmental and Engineering Geophysics*, Dublin, Ireland, 2009.
- [12] M. H. Loke, "Tutorial : 2-D and 3-D electrical imaging surveys," 2010.
- [13] L. Binda, A. Saisi, C. Tiraboschi, S. Valle, C. Colla, and M. Forde, "Application of sonic and radar tests on the piers and walls of the Cathedral of Noto," *Construction and Building Materials*, vol. 17, no. 8, pp. 613–627, 2003.
- [14] J. Blitz and G. Simpson, *Ultrasonic Methods of Non-Destructive Testing*, vol. 2 of *Non-Destructive Evaluation Series*, 1996.

- [15] K. A. Dines and R. J. Lytle, "Computerized geophysical tomography," *Proceedings of IEEE*, vol. 67, no. 7, pp. 1065–1073, 1979.
- [16] W. S. Phillips and M. C. Fehler, "Traveltime tomography: a comparison of popular methods," *Geophysics*, vol. 56, no. 10, pp. 1639–1649, 1991.
- [17] L. Sambuelli, G. Bohm, P. Capizzi, E. Cardarelli, and P. Cosentino, "Comparison among GPR measurements and ultrasonic tomographies with different inversion algorithms. An application to the basement of an ancient Egyptian sculpture," *Journal of Geophysics and Engineering*, vol. 8, pp. 1–11, 2011.
- [18] P. Capizzi, P. Cosentino, and S. Schiavone, "Ultrasonic tomographic analysis for getting information on the mechanical structure of ceramic tiles," *Environmental Semeiotics*, vol. 2, no. 2, pp. 110–119, 2009.
- [19] P. Capizzi, P. L. Cosentino, A. Danesi, G. Fiandaca, and S. Gambardella, "Indagini fisiche a supporto dell'intervento di restauro di una lastra marmorea del II-III d.C. Atti del," in *VII Congresso Nazionale IGHC—Lo Stato dell'Arte 7*, pp. 457–462, Napoli, Italy, October 2009.
- [20] E. Cardarelli and R. de Nardis, "Seismic refraction, isotropic anisotropic seismic tomography on an ancient monument (Antonino and Faustina temple AD 141)," *Geophysical Prospecting*, vol. 49, no. 2, pp. 228–240, 2001.
- [21] F. Agnello, M. Cannella, P. Capizzi, P. Cosentino, L. Pellegrino, and S. Schiavone, "Indagini 3D di dettaglio per l'analisi dell'integrità del busto di Eleonora d'Aragona (F. Laurana, 1468)," *Atti del 28° Convegno GNGTS*, vol. 28, 521–523, Novembre 2009.
- [22] J. E. Peterson, B. N. P. Paulsson, and T. V. McEvelly, "Applications of algebraic reconstruction techniques to crosshole seismic data," *Geophysics*, vol. 50, no. 10, pp. 1566–1580, 1985.
- [23] J. Um and C. Thurber, "A fast algorithm for two-point seismic ray tracing," *Bulletin of the Seismological Society of America*, vol. 77, no. 3, pp. 972–986, 1987.
- [24] M. Bavusi, F. Soldovieri, S. Piscitelli, A. Loperte, F. Vallianatos, and P. Soupios, "Ground-penetrating radar and microwave tomography to evaluate the crack and joint geometry in historical buildings: some examples from Chania, Crete, Greece," *Near Surface Geophysics*, vol. 8, no. 5, pp. 377–387, 2010.
- [25] P. Capizzi and P. L. Casentino, "GPR multi-component data analysis," *Near Surface Geophysics*, vol. 6, no. 2, pp. 87–95, 2008.
- [26] G. Grandjean and J. C. Gourry, "GPR data processing for 3D fracture mapping in a marble quarry (Thassos, Greece)," *Journal of Applied Geophysics*, vol. 36, no. 1, pp. 19–30, 1996.
- [27] V. Pérez-Gracia, O. Caselles, J. Clapés, R. Osorio, J. A. Canas, and L. G. Pujades, "Radar exploration applied to historical buildings: a case study of the Marques de Llió palace, in Barcelona (Spain)," *Engineering Failure Analysis*, vol. 16, no. 4, pp. 1039–1050, 2009.
- [28] S. J. Radzevicius, E. D. Guy, and J. J. Daniels, "Pitfalls in GPR data interpretation: differentiating stratigraphy and buried objects from periodic antenna and target effects," *Geophysical Research Letters*, vol. 27, no. 20, pp. 3393–3396, 2000.
- [29] M. Rashed, D. Kawamura, H. Nemoto, T. Miyata, and K. Nakagawa, "Ground penetrating radar investigations across the Uemachi fault, Osaka, Japan," *Journal of Applied Geophysics*, vol. 53, no. 2-3, pp. 63–75, 2003.
- [30] P. L. Cosentino, P. Capizzi, G. Fiandaca et al., "Diagnostica per il consolidamento del mosaico pavimentale dell'ambulacro nella Villa Romana del Casale (Piazza Armerina)," in *XXIII Convegno internazionale—IL Consolidamento Degli Apparati Architettonici E Decorativi: Conoscenze, Orientamenti, Esperienze*, pp. 91–98, Bressanone, Italy, July 2007.
- [31] S. Gambardella, A. Danesi, P. L. Cosentino, P. Capizzi, and G. Fiandaca, "L'indagine sonica ed ultrasonica come prassi necessaria alla conoscenza di strutture complesse. Il rimontaggio di una statua di epoca romana da Locri: un caso esemplare," in *Atti del VI Congresso Nazionale IGHC—Lo Stato dell'Arte*, pp. 689–694, Spoleto, Italy, October 2008.
- [32] P. Capizzi, P. L. Cosentino, G. Fiandaca, R. Martorana, P. Messina, and I. Razo Amoroz, "Misure microgeofisiche sulla Statua del S. Michele Arcangelo (Scuola Gaginiana, XVI Sec.)," in *V Congresso Nazionale IGHC Lo Stato dell'Arte*, pp. 317–324, Cremona, Italy, October 2007.

Research Article

Distributed Strain Measurement along a Concrete Beam via Stimulated Brillouin Scattering in Optical Fibers

Romeo Bernini,¹ Aldo Minardo,² Stefano Ciaramella,³
Vincenzo Minutolo,⁴ and Luigi Zeni⁵

¹*Istituto per Il Rilevamento Elettromagnetico Dell Ambiente, Consiglio Nazionale Delle Ricerche, Naples, Italy*

²*Department of Information Engineering, Second University of Naples, 81031 Aversa (CE), Italy*

³*Dipartimento di Ingegneria Civile, Seconda Università di Napoli, Via Roma, 29 81031 Aversa, Italy*

⁴*Seconda Università di Napoli, Via Roma, 29 81031 Aversa, Italy*

⁵*Istituto Nazionale per la Fisica della Materia, Trieste, Italy*

Correspondence should be addressed to Aldo Minardo, aldo.minardo@unina2.it

Received 18 January 2011; Accepted 25 February 2011

Academic Editor: Francesco Soldovieri

Copyright © 2011 Romeo Bernini et al. This is an open access article distributed under the Creative Commons Attribution License, which permits unrestricted use, distribution, and reproduction in any medium, provided the original work is properly cited.

The structural strain measurement of tension and compression in a 4 m long concrete beam was demonstrated with a distributed fiber-optic sensor portable system based on Brillouin scattering. Strain measurements provided by the fiber-optic sensor permitted to detect the formation of a crack in the beam resulting from the external applied load. The sensor system is valuable for structural monitoring applications, enabling the long-term performance and health of structures to be efficiently monitored.

1. Introduction

Structural health monitoring systems have the potential to reduce operational maintenance costs by identifying problems at an early stage, and to verify the effectiveness of repair procedures. Moreover, monitoring systems help increase understanding of the real behavior of a structure, such as a bridge, and aid in planning maintenance interventions. In the long term, static monitoring requires an accurate and very stable system, which can relate deformation measurements taken over long periods of time [1]. Strain measurement with a distributed Brillouin scattering-based sensor system provides excellent opportunity for the health monitoring of civil structures [2–4]. It allows measurements to be taken along the entire length of the fiber, rather than at discrete points, by using fiber itself as the sensing medium.

Distributed optical fiber sensors based on stimulated Brillouin scattering (SBS) rely on the interaction between two lightwaves and an acoustic wave in the optical fiber. The measurement principle is based on the characteristic that the Brillouin frequency of the optical fiber is shifted when strain as well as temperature changes occur. Spatial information along the length of the fiber can be obtained

through Brillouin optical time domain analysis (BOTDA) by measuring propagation times for light pulses travelling in the fiber. This allows for continuous distributions of the measurand to be monitored. This type of sensing has tremendous potential for structural monitoring. These systems offer unmatched flexibility of measurement locations and the ability to monitor a virtually unlimited number of locations simultaneously.

In this paper, we report a number of experimental measurements carried out along a 4 m-long concrete beam subjected to a variable load, by the use of a portable BOTDA sensor. A single-mode optical fiber was attached to the beam in order to detect both tensile and compressive strains. Two different adhesives were employed, in order to compare them as regards their efficiency in transferring the strain between the structure and the fiber core. The sensor was able to detect the formation of a crack in the midsection of the beam, consequent to the application of an external load.

2. Experimental Results

BOTDA measurements were carried out by using a portable prototype integrating all the optoelectronic equipment



FIGURE 1: Portable prototype for SBS-based distributed strain and temperature measurements.

necessary to perform distributed strain and temperature measurements in optical fibers. Details on the arrangement implemented can be found in [4]. Here, we focus on the characteristics of the realized prototype, a picture of which is shown in Figure 1. The main features of the instrument are, a relatively short acquisition time, a fully automatic operation and a high signal-to-noise (S/N) ratio of the measurements. An acquisition time in the order of about one minute was obtained by employing for data acquisition an analog-to-digital (A/D) converter with a field-programmable gate array (FPGA) device on the same board. The FPGA can process the output of the A/D converter in real time, we use it to perform an averaging on board of the acquired traces. This permitted to strongly reduce the aggregate data rate and therefore the latency time due to transfer of data to PC. A valuable consequence is that a high number of averages, and therefore a high S/N ratio can be obtained while keeping a short acquisition time. Both instrument control and data processing are performed by a central processing unit (CPU) mounted on a mini-ITX board placed internally. External communication with the instrument is realized by setting up a remote desktop control. The optical fiber used for sensing is connected to the prototype optical circuit by two FC adapters located in the front panel of the instrument. Dedicated software was developed by which the whole measuring process as well as post processing of the acquired data are fully automatic. The different measurement parameters can be easily set, and the results of the measurements are visualized and stored. The nominal resolution of the sensor is $\pm 1^\circ\text{C}$ for temperature sensing, and $\pm 20\ \mu\epsilon$ for strain sensing.

The laboratory tests described hereafter have been performed using a 4m-long “T” cross section pretensed concrete beam. Figure 2 shows a sketch of the beam, together with the positions where the sensing fiber was attached. The sensing fiber was a commercial standard single-mode fiber for telecommunication with polyvinyl chloride 900 μm tight-buffer outer jacket. Note that a single optical fiber was bonded four times along the structure along different longitudinal directions. In this way, the strain profiles were acquired simultaneously at each measurement. Two different adhesives were employed for comparison purposes: an epoxy resin for the leftmost positions (A and B), and a polyurethane-based adhesive for the rightmost positions

(C and D). A dial strain gauge was placed at the point of maximum deflection (midsection) in order to validate the measurements provided by the optical fiber sensor. Before application of external loads to the beam, a reference strain profile was acquired by the prototype. This reference profile was employed to subtract the strains induced by the bonding procedure from the successive measurements.

The beam was loaded by using a single-span arrangement and applying different weights at the center of the span. We applied an increasing weight from 50 daN to 200 daN at a step of 25 daN. External temperature was verified to keep constant during the experimental tests. Figure 3 reports a summary of the measurements performed during the whole loading cycle. In particular, Figure 3(a) reports the strains acquired along the two fibers bonded with epoxy resin (positions A and B), while Figure 3(b) refers to the fibers bonded with polyurethane adhesive (positions C and D). For each case, the positive (tensile) strains are relative to the lower fibers (B and D), while the negative (compressive) strains refer to the upper fibers (A and C). At first, we note that although the theory predicts a sharp turn of the strain profiles in the midsection, the measured distributions appear smoothed around their maximum. This has to be attributed to the limited spatial resolution of our optical sensor (1 m), as well as to the limited spatial sampling (20 cm). Note also that for each applied load the peak tensile strain is always lower than the maximum compressive strain. This was expected as it is directly related to the position at which the fibers were attached with respect to the neutral axis of the structure (see Figure 2(b)). Comparing Figures 3(a) and 3(b), we note that the fibers bonded with epoxy and subjected to tensile strain provide more regular strain profiles as compared to the fibers bonded with polyurethane, that is, the strain distributions are closer to the theoretical profiles. However, the absolute strain levels are highly comparable for the two adhesives. At the condition of maximum load (200 daN), a crack opened at the midsection of the beam. The effect of the crack on the strain profiles acquired by the optical fibers can be observed in Figure 3, showing a sudden increase in the maximum strain in the concrete when the crack develops.

The beam was then subjected to a progressively decreasing load. Figures 4 and 5 summarize the results of this new measurement cycle. In particular, Figure 4 refers to the fibers bonded with epoxy, while Figure 5 refers to the fibers bonded with polyurethane. Comparing the results with those obtained before crack formation, an increase of strain all over the loaded beam is clearly observable, such an increase being higher in the middle portion of the beam.

For example, referring to the fibers bonded with epoxy, the maximum strain measured at position B with an applied load of 150 daN increases from $\approx 125\ \mu\epsilon$ to $\approx 210\ \mu\epsilon$ after crack formation. Similarly, at position A the compressive strain at the midsection increases from $\approx 195\ \mu\epsilon$ to $\approx 300\ \mu\epsilon$. Note that, at zero load, a residual tensile strain upto $100\ \mu\epsilon$ and a compressive strain upto $30\ \mu\epsilon$ are measured by the two epoxy-glued fibers.

In order to show the effect of crack opening in a different perspective, we report in Figure 6 the maximum strain

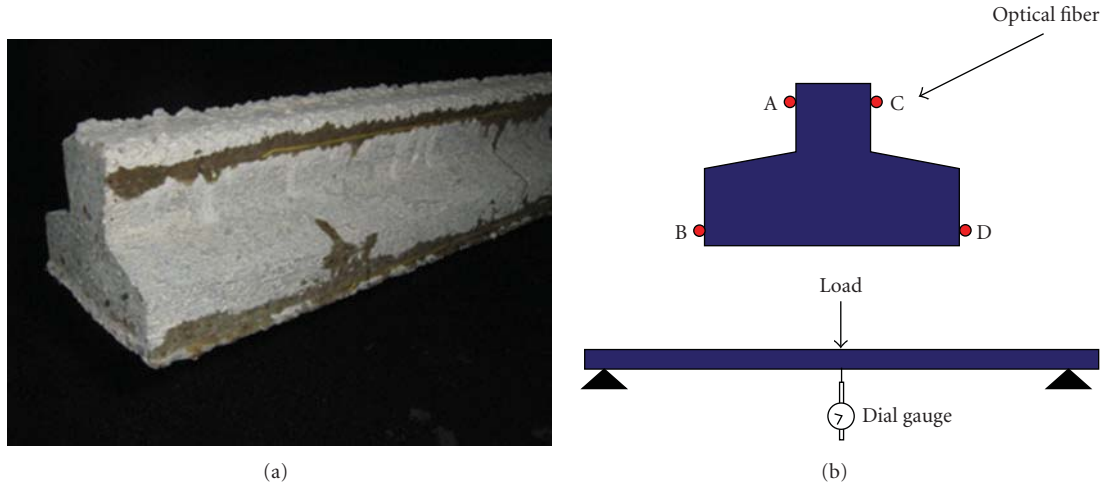


FIGURE 2: (a) Picture of the concrete beam used for the tests; (b) the crosssection and longitudinal view of the concrete beam used for the tests.

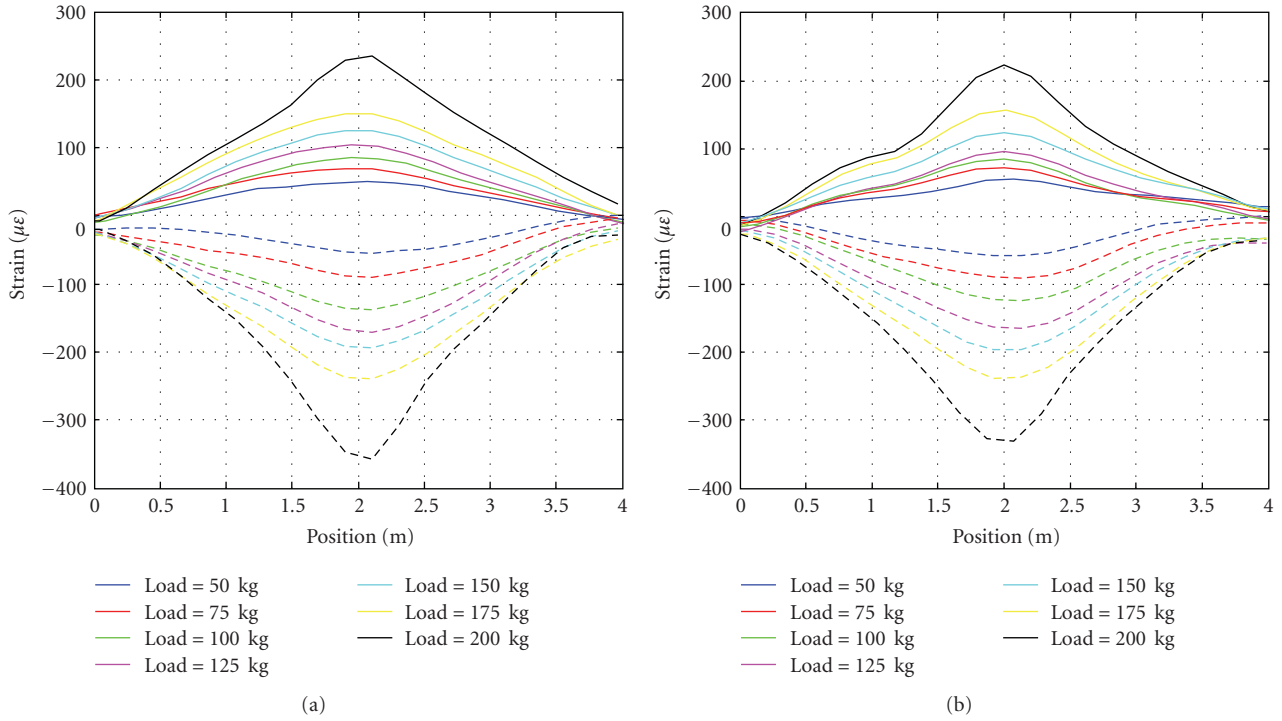


FIGURE 3: (a) Measured strain distribution along the length of the beam with fibers bonded with epoxy resin; (b) measured strain distribution along the length of the beam with fibers bonded with polyurethane.

measured during the first (loading) and second (unloading) cycles, for each monitored position and applied weight. It can be seen that, during the first cycle, the strain change increases abruptly when increasing the load from 175 daN to 200 daN. Also, during the unloading cycle, the maximum strain is always higher than the corresponding value measured before crack formation.

The crack formation produces an eigenstrain distribution in the cross section of the beam that is revealed by the residual strain values attained at complete unloading. The

residual strain distribution gives origin to a localized inelastic curvature given by

$$\chi_a = \frac{\epsilon_l - \epsilon_u}{h}, \tag{1}$$

where ϵ_l and ϵ_u are the strains measured at two different quotes distant h . We can use the curvature in order to compare data provided by the dial strain gauge, with data provided by the optical fiber sensors. In particular, we use (1) in order to calculate the curvature provided by the two

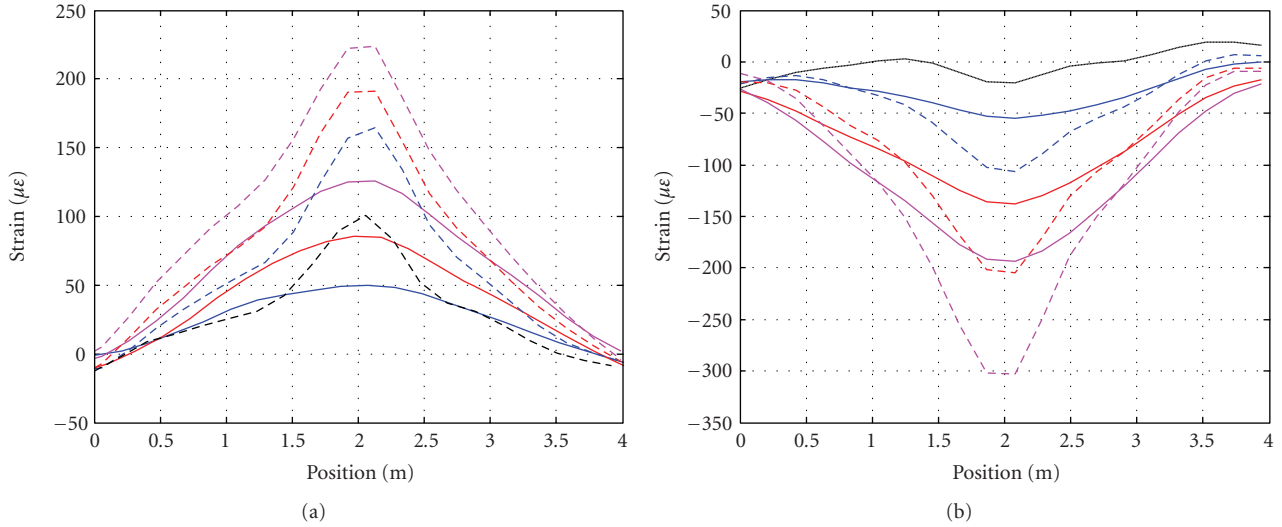


FIGURE 4: (a) Measured strain distribution along the length of the beam with fiber bonded with epoxy resin (position B); (b) measured strain distribution along the length of the beam with fiber bonded with epoxy resin (position A). Solid line = loading step. Dashed line = unloading step. Blue line = 50 daN. Red line = 100 daN. Magenta line = 150 daN. Black line = 0 daN.

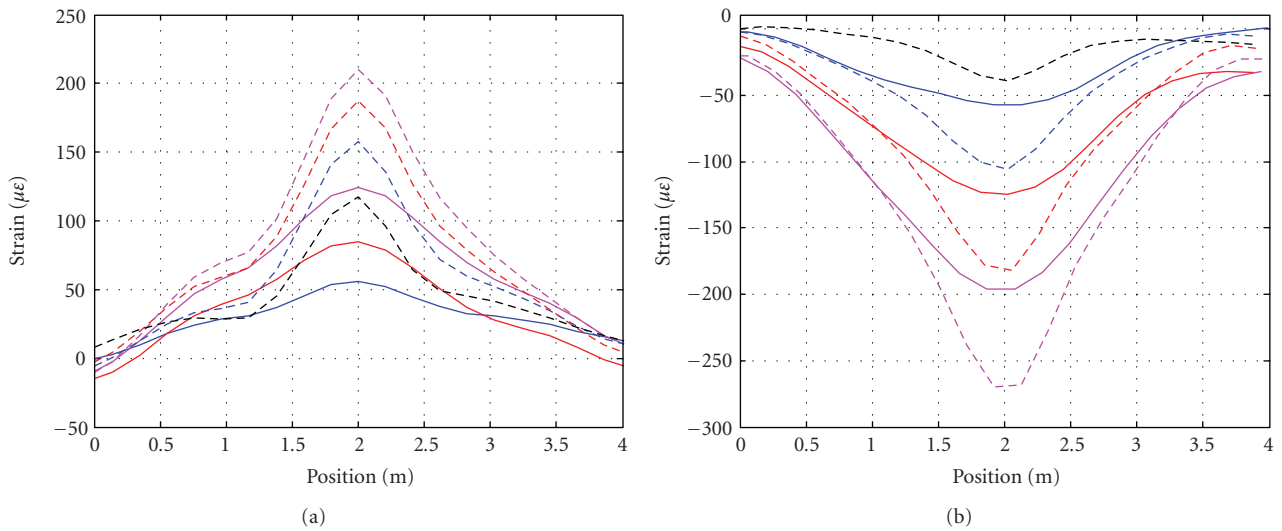


FIGURE 5: (a) Measured strain distribution along the length of the beam with fiber bonded with polyurethane (position D); (b) measured strain distribution along the length of the beam with fiber bonded with polyurethane (position C). Solid line = loading step. Dashed line = unloading step. Blue line = 50 daN. Red line = 100 daN. Magenta line = 150 daN. Black line = 0 daN.

sensors, using a height h of 10 cm for the dial gauge case, or $h = 8.1$ cm (i.e., the vertical distance between fibers A and B, or C and D) for the optical fiber case.

The results are shown in Figure 7. It is seen that a good agreement exists between the curvatures provided by the sensors, except from the measurements carried out after crack formation. The discrepancy can be explained by considering that the optical fiber sensor has a spatial resolution of ≈ 1 m, so the highly localized strains consequent to crack opening are spatially averaged. Therefore, the resulting curvature provided by the optical fiber sensor in the midsection is lower than the actual one, after crack formation. This limitation can be overcome either by the use of a sophisticated signal processing of data, permitting to detect more accurately the

crack-induced strains, [5], or by the use of an SBS sensor with improved spatial resolution. A cm scale spatial resolution has the clear advantage of permitting a precise localization of the crack within the monitored structure [6]. Work is in progress in order to push the spatial resolution of the portable instrument in the cm-range.

3. Conclusions

A portable distributed Brillouin scattering sensor has been used for structural health monitoring on a concrete beam. The experiments show the correlation of the distributed measured strain with local measurements provided by a dial strain gauge. It has been shown that the formation of a crack

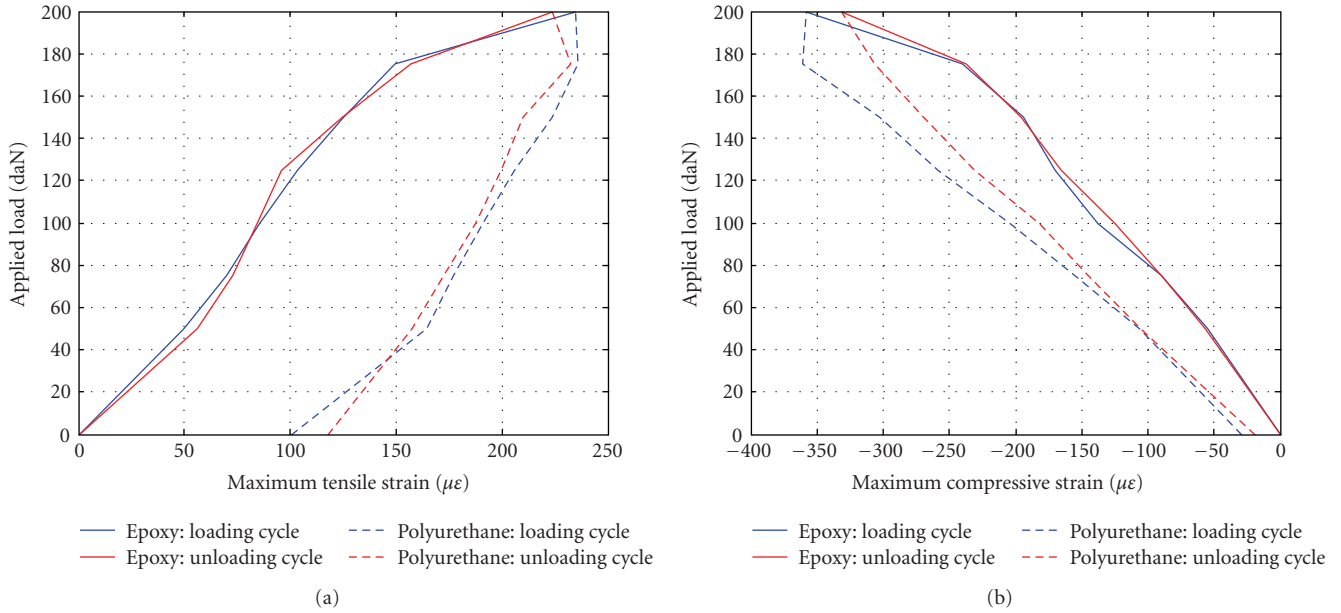


FIGURE 6: (a) Applied load versus maximum tensile strain; (b) applied load versus maximum compressive strain.

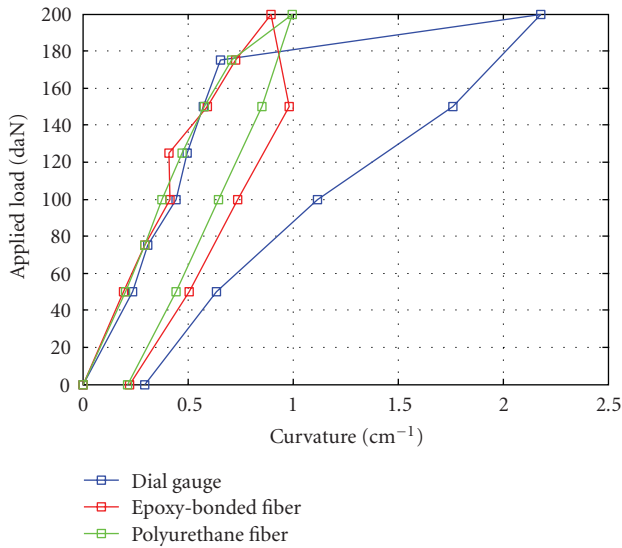


FIGURE 7: Applied load versus curvature. The latter was calculated at the midsection using the dial strain gauge or the optical fiber sensor measurements.

emerges as an increase of the beam curvature, successfully detected by means of the optical fiber sensor readings.

Acknowledgments

The research leading to these results has received funding from the European Community’s Seventh Framework Programme (FP7/2007-2013) under Grant Agreement no. 225663 Joint Call FP7-ICT-SEC-2007-1 and from Second University of Naples—PRIST 2009 Project.

References

- [1] O. Burdet, “Automatic deflection and temperature monitoring of a balanced cantilever concrete bridge,” in *Proceedings of The 5th International Conference of Short and Medium Concrete Bridges*, Calgary, Alberta, Canada, July 1998.
- [2] T. Horiguchi, K. Shimizu, T. Kurashima, M. Tateda, and Y. Koyamada, “Development of a distributed sensing technique using Brillouin scattering,” *Journal of Lightwave Technology*, vol. 13, no. 7, pp. 1296–1302, 1995.
- [3] M. DeMerchant, A. Brown, X. Bao, and T. Bremner, “Structural monitoring by use of a Brillouin distributed sensor,” *Applied Optics*, vol. 38, no. 13, pp. 2755–2759, 1999.
- [4] R. Bernini, M. Fraldi, A. Minardo et al., “Identification of defects and strain error estimating in bending steel beams through time-domain Brillouin distributed Optical Fiber Sensors,” *Smart Materials and Structures*, vol. 15, pp. 612–622, 2006.
- [5] F. Ravet, F. Briffod, B. Glisic, M. Nikles, and D. Inaudi, “Detection of sub-millimeter faults with a time domain distributed Brillouin sensor,” in *19th International Conference on Optical Fibre Sensors*, D. Sampson, S. Collins, K. Oh, and R. Yamauchi, Eds., vol. 7004 of *Proceedings of SPIE*, pp. 1–4, 2008, 700412.
- [6] M. Imai, R. Nakano, T. Kono, T. Ichinomiya, S. Miura, and M. Mure, “Crack detection application for fiber reinforced concrete using BOCDA-based optical fiber strain sensor,” *Journal of Structural Engineering*, vol. 136, no. 8, pp. 1001–1008, 2010.